

RADC-TR-88-160, Vol I (of two)
In-House Report
July 1988



AD-A206 704

PROCEEDINGS OF THE 1987 ANTENNA APPLICATIONS SYMPOSIUM

Peter R. Franchi

Sponsored by
DIRECTORATE OF ELECTROMAGNETICS
ROME AIR DEVELOPMENT CENTER
HANSCOM AFB, MA 01731
AIR FORCE SYSTEMS COMMAND


DTIC
SELECTED
28 MAR 1989

APPROVED FOR PUBLIC RELEASE; DISTRIBUTION UNLIMITED.

ROME AIR DEVELOPMENT CENTER
Air Force Systems Command
Griffiss Air Force Base, NY 13441-5700

**BEST
AVAILABLE COPY**

89 3 27 098

This report has been reviewed by the RADC Public Affairs Division (PA) and is releasable to the National Technical Information Service (NTIS). At NTIS it will be releasable to the general public, including foreign nations.

RADC-TR-88-160, Vol I (of two) has been reviewed and is approved for publication.

APPROVED:



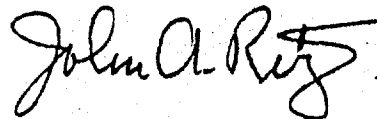
ROBERT J. MAILLOUX
Antennas & Components Division
Directorate of Electromagnetics

APPROVED:



JOHN K. SCHINDLER
Acting Director of Electromagnetics

FOR THE COMMANDER:



JOHN A. RITZ
Directorate of Plans & Programs

If your address has changed or if you wish to be removed from the RADC mailing list, or if the addressee is no longer employed by your organization, please notify RADC (EEAS) Hanscom AFB MA 01731-5000. This will assist us in maintaining a current mailing list.

Do not return copies of this report unless contractual obligations or notices on a specific document require that it be returned.

SECURITY CLASSIFICATION OF THIS PAGE

REPORT DOCUMENTATION PAGE				
1a. REPORT SECURITY CLASSIFICATION Unclassified		1b. RESTRICTIVE MARKINGS		
2a. SECURITY CLASSIFICATION AUTHORITY		3. DISTRIBUTION/AVAILABILITY OF REPORT Approved for public release; Distribution Unlimited		
2b. DECLASSIFICATION/DOWNGRADING SCHEDULE		4. PERFORMING ORGANIZATION REPORT NUMBER(S) RADC-TR-88-160 (Vol I)		
4. PERFORMING ORGANIZATION REPORT NUMBER(S) RADC-TR-88-160 (Vol I)		5. MONITORING ORGANIZATION REPORT NUMBER(S)		
6a. NAME OF PERFORMING ORGANIZATION Rome Air Development Center	6b. OFFICE SYMBOL (if applicable) EEAS	7a. NAME OF MONITORING ORGANIZATION		
6c. ADDRESS (City, State, and ZIP Code) Hanscom AFB Massachusetts 01731-5000		7b. ADDRESS (City, State, and ZIP Code)		
8a. NAME OF FUNDING / SPONSORING ORGANIZATION Rome Air Development Center	8b. OFFICE SYMBOL (if applicable) EEAS	9. PROCUREMENT INSTRUMENT IDENTIFICATION NUMBER		
8c. ADDRESS (City, State, and ZIP Code) Hanscom AFB Massachusetts 01731-5000		10. SOURCE OF FUNDING NUMBERS		
		PROGRAM ELEMENT NO. 62702F	PROJECT NO. 4600	TASK NO. 14
				WORK UNIT ACCESSION NO. 01
11. TITLE (Include Security Classification) Proceedings of the 1987 Antenna Applications Symposium				
12. PERSONAL AUTHOR(S)				
13a. TYPE OF REPORT In-house	13b. TIME COVERED FROM _____ TO _____	14. DATE OF REPORT (Year, Month, Day) 1988 July	15. PAGE COUNT 236	
16. SUPPLEMENTARY NOTATION Volume I consists of pages 1 through 230; Volume II consists of pages 231 through 420				
17. COSATI CODES		18. SUBJECT TERMS (Continue on reverse if necessary and identify by block number)		
FIELD	GROUP	SUB-GROUP		
			Antennas Microstrip Multibeam Antennas	
			Satellite Antennas Reflector Array Antennas	
			Broad Antennas HF, VHF, UHF	
19. ABSTRACT (Continue on reverse if necessary and identify by block number) The proceedings of the 1987 Antenna Applications Symposium is a collection of state-of-the-art papers relating to phased array antennas, multibeam antennas, satellite antennas, microstrip antennas, reflector antennas, HF, VHF, UHF and various other antennas. (5)				
20. DISTRIBUTION / AVAILABILITY OF ABSTRACT <input type="checkbox"/> UNCLASSIFIED/UNLIMITED <input checked="" type="checkbox"/> SAME AS RPT. <input type="checkbox"/> DTIC USERS		21. ABSTRACT SECURITY CLASSIFICATION Unclassified		
22a. NAME OF RESPONSIBLE INDIVIDUAL PETER R. FRANCHI		22b. TELEPHONE (Include Area Code) (617)-377-3067	22c. OFFICE SYMBOL RADC/EEAS	

Accession For	
NTIS GRA&I	<input checked="" type="checkbox"/>
DTIC TAB	<input checked="" type="checkbox"/>
Unannounced	<input type="checkbox"/>
Justification	
By _____	
Distribution/	
Availability Codes	
Dist	Avail and/or Special
A-1	



Contents

- * Keynote Speaker: "MMICs - The Key to Affordable Arrays," J. Schindler,
Rome Air Development Center, Hanscom AFB, MA

WEDNESDAY, SEPTEMBER 23, 1987

PHASED ARRAYS

- | | | |
|------|--|----|
| 1. | "MMIC Phased Arrays," A. I. Zaghloul and R. J. Mailloux | 1 |
| * 2. | "Wideband Active Phased Array," C. D. Pepe, M. J. Povinelli, and
J. J. Komiak | |
| 3. | "A Ku-Band Hemispherical Array Antenna for Possible Space Station
Application," R. W. Shaw, J. R. Carl, and G. D. Arndt | 31 |
| 4. | "Antenna Subsystem for Aviation Satellite Communications," S. Y. Peng,
H. H. Chung, and W. Foy | 47 |

* NOT INCLUDED IN THIS VOLUME

Contents

- * 5. "A Cavity-Backed Twin-Slot Array for IFF Applications," W. Foy,
H. H. Chung, and S. Y. Peng
- * 6. "Single Reflector Shaping Technique," A. R. Cherrette, and S. W. Lee

CONFORMAL ANTENNAS

- 7. "Analysis of Finite Phased Arrays of Circular Microstrip Patches," 63
M. D. Deshpande and M. C. Bailey
- 8. "An Experimental Investigation of Parasitic Microstrip Arrays," 91
R. Q. Lee, R. Acosta, J. S. Dahele, and K. F. Lee
- 9. "A Multi-Layer Multi-Band Symmetrical Microstrip Antenna," S. Sensiper 109
- * 10. "Conformal Microstrip Antennas," V. Clark and Y. T. Lo
- 11. "Slot-Coupled Microstrip Constrained Lens," D. T. McGrath, Capt, USAF 139
- * 12. "Resonance Frequency of a Rectangular Microstrip Patch," W. C. Chew
and Q. Liu
- * 13. "Microwave Antenna Arrays as Contact Applicators for Clinical
Hyperthermia," A. F. Peterson and E. C. Burdette

THURSDAY, SEPTEMBER 24, 1987

ADAPTIVE ANTENNAS

- 14. "On the Behavior of Adaptive Lens and Feed Antennas," M. Santana and 169
R. Blau
- 15. "A Stochastic Conjugate Gradient Algorithm for Adaptive Arrays," 181
H. M. Ibrahim and N. M. Ibrahim
- 16. "Adaptive Transform Feed Test Results," M. Hayes, Capt, USAF 201
- * 17. "Adaptive Antenna Analysis Using the Method of Moments," G. C. Thorpe,
J. L. Fath, W. P. Baker, and A. J. Terzuoli
- 18. "Polarization Multiplexing Systems," T. D. Moran and B. J. Lamberty 231
- 19. "Interference Suppression Using an Adaptive Polarization Combiner," 247
B. J. Lamberty and R. P. Friedman
- * 20. "Moment Method Resolution Enhancement for Scanning Antennas," G. Marcus
and W.T. Carey

* NOT INCLUDED IN THIS VOLUME

BROADBAND ANTENNAS

Contents

- | | | |
|-------|--|-----|
| 21. | "Performance Characteristics of Notch Array Elements Over a 6/1 Frequency Band," G. J. Monser | 263 |
| * 22. | "Broadband Feeds for Vivaldi Antennas," K. Frantz and P. Mayes | |
| * 23. | "Improved Endfire Log-Periodic Dipole Array Antennas," S. C. Kuo | |
| * 24. | "Discone Design Using Simple N-Connector Feed," T. S. Rappaport | |
| 25. | "An Orbiter - ACTS Communications Experiment," G. D. Arndt, L. Leopold, S. H. H. Chen, Y. C. Loh, Y. S. Kuo, R. Shaw and J. Carl | 277 |
| 26. | "MOM Analysis of a Finite Length Slot in an Infinite Conducting Sheet," H. A. Karwacki | 297 |
| * 27. | "On the Service Area of AM Broadcast Stations: The Optimum AM Broadcast Antenna," V. Trainotti | |

FRIDAY, SEPTEMBER 25, 1987

ANTENNA MEASUREMENTS AND ANALYSIS

- | | | |
|-------|---|-----|
| 28. | "Near-Field Bistatic RCS Measurement at BDM," R. Rogers and E. Farr | 321 |
| 29. | "Field Uniformity Criteria for the Design of a Two-Wire EMP Simulator," C. Zuffada and N. Engheta | 345 |
| 30. | "A Unified Method of Antenna System Analysis Based on the Parametric Modeling of Component Scattering Coefficients," W. Milroy, R. Lewis, M. Thomas, and S. Drost | 361 |
| 31. | "Solving Maxwell Equations by Matrix Formulation in Antenna Design and Applications," F. C. Chang | 391 |
| * 32. | "Scattering From the Interior of a Corner Reflector Using the Spectral Domain Technique," G. P. Saramadis and S. R. Laxpati | |

* NOT INCLUDED IN THIS VOLUME

MMIC PHASED ARRAYS

A. I. Zaghoul
COMSAT Laboratories
Clarksburg, MD 20871

R. J. Mailloux
Rome Air Development Center
Hanscom AFB, MA 01731

With Contributions by:

R. Stockton, Ball Aerospace; J. N. LaPrade, RCA Astro;
B. J. Edward, GE Electronics Laboratory; L. Nystrom, Anaren
Microwave; H. Ahn, Sedco; and K. C. Gupta, University of Colorado.

ABSTRACT

The present status of MMIC-fed phased-array antennas, or monolithic phased arrays, is reviewed through the results of a workshop on the subject. Problem areas are identified and recommendations for future developments are presented. The paper addresses five aspects of the MMIC phased-array design: array architecture, MMIC-to-radiating-element interface, RF signal distribution, performance monitoring and fault isolation, and computer-aided design tools for MMIC arrays.

1. INTRODUCTION

The advent of monolithic microwave integrated circuit (MMIC) technology has introduced new promise, as well as challenges, in the area of phased-array designs and their use in radar and communications systems. Application of this technology raises new problems associated with fabrication, packaging, and design methods. The AP-S Workshop held at the 1987 IEEE/AP Symposium in Blacksburg, Virginia, addressed the present status of MMIC-fed phased-array antennas (or monolithic phased arrays). It acted as a forum to identify the problems encountered in design and fabrication of such arrays, and to suggest possible solutions.

Two survey presentations reviewing the present status of MMIC phased arrays and describing some existing systems were made by H. Weber of the Air Force's Wright Aeronautical Laboratories and R. Stockton of Ball Aerospace Systems Division. Working subgroups were then formed to study in greater detail the major topics associated with the design of MMIC-fed phased arrays: architectures for MMIC-fed phased arrays, circuit-to-radiating-element

interfaces, RF signal distribution systems, performance monitoring and fault isolation, and computer-aided design (CAD) tools for MMIC arrays. This paper presents an overview of these topics and discusses key areas within each.

2. ARRAY ARCHITECTURE

The topic of array architecture is difficult to address in a general sense because it is highly dependent upon mission requirements. For example, a large space-based radar will have substantially different architecture requirements than a ground-based satellite communications antenna. In order to focus on common problems, the topic can be divided into configuration issues and performance issues.

Array configuration is defined as the way in which an array is constructed, including materials, level of integration, and packaging techniques. The level of integration and packaging areas can be further subdivided into the following:

- Modules--both perpendicular and planar to the aperture surface;
- Monolithic--with the radiators and active circuits on the same surface;
- Multilayer--with the radiators, active circuits, and feed network residing on different layers; and
- Bootlace lens--with active modules sandwiched between two radiating surfaces.

Performance requirements that affect the architecture include polarization diversity, sidelobe levels, directivity, scanning region, gain-to-noise-temperature ratio (G/T), and e.i.r.p. Almost without exception, performance issues dominate the architecture tradeoffs and constrain the configuration.

Among the applications which drive both performance requirements and configuration are satellite communications; airborne, ground, and space-based radars; and multifunction broadband arrays. This partial list encompasses the major systems-level requirements that impact array architectures.

2.1 Configuration Issues

The traditional module which extends behind the radiating aperture will remain a viable architecture as long as module size can be made compatible with array lattice constraints. Both the physical size and cost of this configuration can be reduced by replacing hybrid MIC components with MMIC chips. Further reductions in size and cost can be realized by increasing the level of integration. This is accomplished by replacing element modules with multi-element or subarray modules. Eventually, module size will be limited by the number of RF, DC, and control-line interconnections. This problem can be largely alleviated by partitioning and integrating portions of the control electronics within the module. An alternate approach is to replace control-line interconnects with fiber optics. In either case, decreasing the number of interconnects results in improved reliability.

Another module issue which requires a new conceptual approach is the development of improved, higher density transitions to both the radiating element and the feed network. Such techniques will

increase in importance if the module concept is extended up to the K_u -band.

Planar modules offer obvious advantages in thin or conformal array applications. As with any multilayer structure, RF interconnects are a major concern. A two-layer structure with the radiators above, and MMIC chips below, a common ground plane is the preferred approach. This technique doubles the unit cell area while avoiding complex ground-plane-to-ground-plane interconnections. Planar, multilayer modules with more than one ground-plane layer require improved interconnect technologies to prevent moding and high-inductance feedthrough paths. These factors may preclude the use of modules with more than one ground plane above X-band.

Monolithic subarrays, or "phased arrays on a chip," are viable configurations for half-duplex communications applications. Separate chips are required for transmit and receive functions, for two reasons. Since the radiators, amplifiers, phase shifters, bias and control lines, and a portion of the feed network are on the same surface, area limitations are acute. The unit cell cannot accommodate more than a single element, amplifier, and phase

shifter. Even if the transmit and receive components could be made small enough to share the unit cell, the additional isolation and attendant filtering requirement at each element would make this approach impractical.

The practical application of the monolithic approach is limited to roughly 15 GHz and above, where useful levels of integration can be achieved on wafers of 4-in. diameter or smaller. With a monolithic configuration, both the cost effectiveness and feasibility of this approach are directly related to yield. However, if the level of integration is commensurate with the maturity of GaAs MMIC processing technology, monolithic arrays should become a practical architecture.

In an active lens configuration, all of the module issues mentioned above are applicable, in addition to concerns regarding control signal and DC power bus distribution and heat removal. The impact of these issues varies in direct relation to aperture size and frequency of operation.

A final configuration problem involves broadband arrays. For an active broadband array, the element lattice is determined by the highest frequency of

operation, while the physical size of the components and modules is dictated by the lowest frequency of operation. A fundamental problem which appears to have received little attention is whether the modules can be made compatible with the lattice. At the low end of the spectrum the problem is less severe, since MMIC components with lumped elements can be made much smaller than the halfwave element spacings. This issue is of greater concern at the higher frequencies, where chip and module size no longer scale linearly with wavelength. This subject warrants additional detailed investigation.

2.2 Performance Issues

Of the various performance issues discussed, the following four topics emerged as having a major impact on overall array architecture:

a. Dynamic Output Control of Power Amplifiers.

This is an important requirement for active radar arrays. Present amplifier designs provide acceptable phase and amplitude tracking from module to module when operated in compression. However, when the

amplifiers are taken out of saturation to reduce output power, phase and amplitude tracking become unacceptably poor. One solution is to operate in compression, using an attenuator to reduce the output power. Although this is an effective approach, it is undesirable because it reduces overall efficiency and increases the heat load which must be dissipated. Better techniques must be developed to provide acceptable tracking without sacrificing efficiency.

b. Efficiency. It was concluded that the most beneficial performance improvement would be higher power-added efficiency for solid-state devices.

c. True Time-Delay Networks. With increased emphasis on broadband phased arrays, this technology area should receive more attention. Much work is needed in both component design and techniques for integration into array feed networks.

d. Repairability and Performance Upgrading. This involves the ability to retrofit the active components within the array to enhance performance; it is also a configuration issue when repairability is considered. As systems become more expensive, and service lifetimes are extended to compensate, ease of maintenance and performance upgrading should be

important requirements in the selection of array architecture design and packaging concepts. Ideally, something as simple as a replaceable plug-in module or subarray assembly could be implemented.

3. MMIC-TO-RADIATING-ELEMENT INTERFACE

Attention was focused on two aspects of the MMIC-to-radiating-element interface: the case where the radiating element is printed during the GaAs MMIC fabrication process, and all other cases where the radiating element is off-substrate. Requirements for the radiating element, and the MMIC interface to that element, are clearly interdependent and are identified as system-driven. Four aspects determining element/interface requirements are frequency of operation, bandwidth, application, and test requirements.

Frequency of operation permits a first-level tradeoff in determining whether to print the radiating element integrally with (and planar to) the MMIC. The millimeter waveband is generally the lowest frequency at which this arrangement is economical in terms of GaAs real estate and associated overall circuit yield.

The bandwidth of the system drives selection of the interface and the element. Broadbanding (a relative term) has been achieved for printed radiators by the addition of off-substrate loading to effectively double-tune the resonant structure. Very broadband elements are available; however, the matching circuitry is often incompatible with high-density monolithic interface requirements. If the MMICs are to be separately packaged for the element interface, then the transition may be integrated with the package. Figure 1 shows a package design sponsored by NASA which features a broadband microstrip interface. In this case, conventional microstrip-to-coaxial or microstrip-to-waveguide transition techniques are suitable for the MMIC-to-radiating-element interface.

The system application is a strong determinant of the MMIC/element interface. Three separate applications were considered: transmit only, receive only, and transmit/receive (T/R). In the transmit-only case, a direct interface from the MMIC to the radiating element is straightforward. Minimum path length and low VSWR will ensure maximum radiated

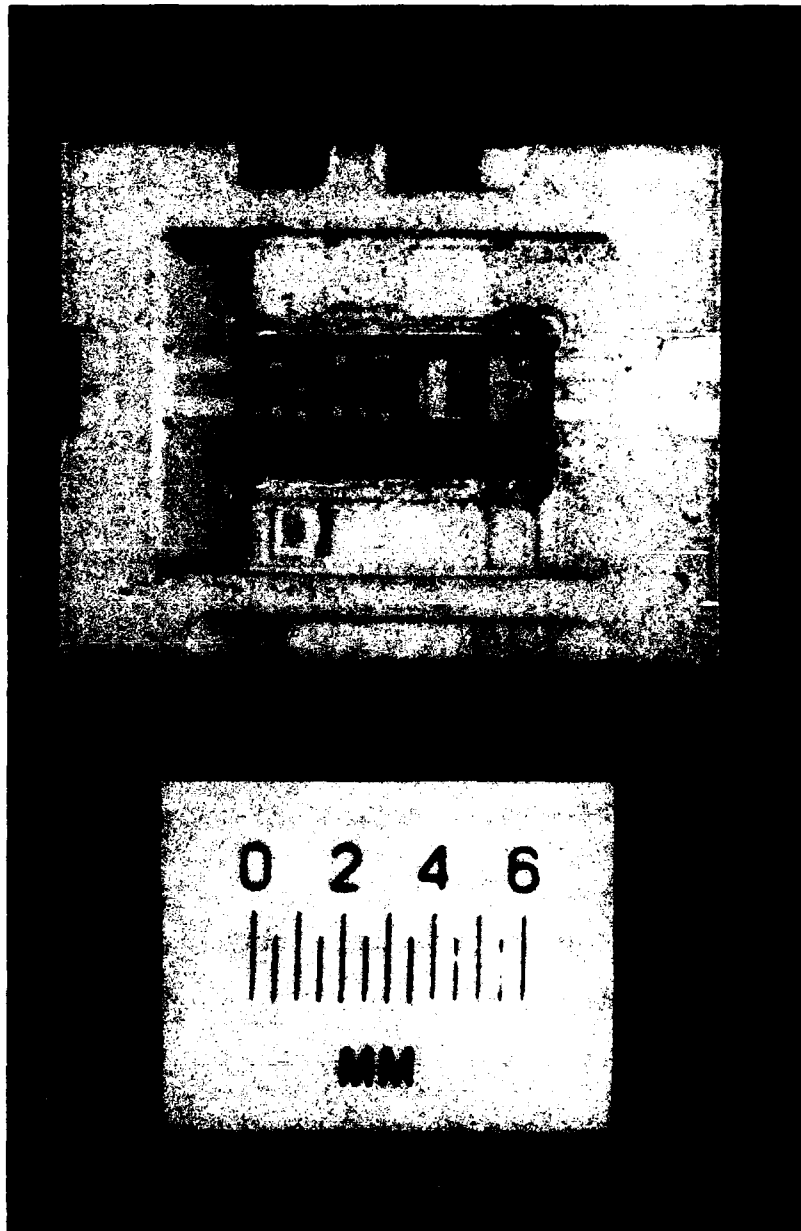


Figure 1. Typical MMIC Package

power from the MMIC. In the receive-only case, filtering is more likely to be required between the MMIC and the radiating element. This filtering can be inserted on-substrate for low-Q applications. However, if narrow bandwidths are selected or sharp filter characteristics are required, significant insertion loss and component complexity may be introduced between the MMIC (packaged) output and the corresponding receiving antenna element.

In the case of T/R antenna systems, the lack of a monolithic nonreciprocal device such as a circulator is apparent. For radar applications, a switch may be the output circuit element on the MMIC, thereby allowing for direct transition to the radiating element. However, simultaneous transmit and receive systems will require a nonreciprocal device or a diplexing filter structure, which leads to increased complexity for the interface.

Test requirements imposed at levels of assembly below that of the full-up array can impact the MMIC-to-radiating-element interface. MMICs packaged as shown in Figure 1 are ideally suited for high reliability applications. When steps are taken to integrate the radiating element with the package, or to

integrate the transition to the element with the package, unique requirements are introduced which may limit or preclude testing at the MMIC (packaged) level. In the case of a fully monolithic active antenna, only full-up antenna testing will indicate individual MMIC/element performance.

The advantages of integrating the radiating element on the GaAs substrate increase with increasing frequency. The ability to achieve the greatest interconnect repeatability and reliability is a constant advantage, and the potential exists to achieve a low-cost design where human contact during the production process is minimal. Several as yet unreported areas of development may bring further advantages to a monolithic approach. One approach may be to center the ground plane within the monolithic structure in a way that provides for closer element spacing and therefore higher circuit density than is currently achieved in monolithic active arrays.

Several disadvantages of integrating the element on the MMIC substrate have already been identified, including the wavelength/frequency relationship to GaAs real estate and circuit yield (and hence greater

cost), as well as the lack of MMIC process-compatible circulators. Other disadvantages include degraded printed-circuit radiating element performance due to the high relative permittivity of GaAs and associated substrate thinning. The significant lack of experimental data for various element configurations on GaAs limits the ability of a designer to predict array performance, particularly with regard to radiative and phonon coupling between radiating elements, and between elements and other circuitry present on the monolithic array.

4. RF SIGNAL DISTRIBUTION SYSTEMS

A variety of networks have been developed for distributing (feeding) RF signals to the radiating elements of a phased-array antenna. To fulfill the electrical and mechanical requirements, these networks have capitalized on various architectures, media, and materials. Locating active MMIC T/R modules with each radiating element promises to increase the performance and functional flexibility of the array, and as a result greater demands are placed on the feed network. Depending on its mission, the

active phased array may require a feed system that accommodates the following:

- independent transmit and receive signal distribution,
- sum and difference receive beams for target tracking,
- simultaneous multiple beams,
- dual polarization,
- coherent local oscillator signal distribution, and/or
- module calibration signal distribution.

The feed system for the active array must also compete for volume with the prime DC power (bias) distribution system, the MMIC module control signal distribution system, the array thermal management system, and the mechanical support structure.

Historically, the media that have been considered for the distribution of array RF signals are variations of microwave circuitry and space. Microwave circuitry techniques include waveguide, coaxial, and channel line, as well as the printed approaches

such as stripline, microstrip, and coplanar waveguide. Waveguide exhibits low loss and good phase tracking; however, its volume and weight can be prohibitive when multiples of the above-listed feed functions are required. Coaxial-type line is limited by its loss, plus the difficulty of realizing such components as splitters and couplers. In contrast, the printed transmission line approaches offer a great deal of flexibility in the realization of splitters, couplers, etc.; however, they can be unwieldy when multiple feed functions are required.

Space feed techniques, where the array is an active lens illuminated from some central location, can be particularly attractive for use at higher frequencies because the difficulty of mechanically interfacing to extremely closely spaced elemental modules is eliminated. Inefficiency due to RF energy spillover is not of significant consequence in the active array. However, the space feed approach also is limited when multiple feed functions are required.

Optical fiber technology is currently being investigated as a possible medium for distributing microwave signals to the elemental T/R modules of an

active phased array. Fiber optic techniques appear promising, particularly when employed in conjunction with digital beam forming. Figure 2 depicts a possible system architecture. The transmit signal amplitude modulates the optical frequency carrier of one or more lasers. This modulated carrier is divided using fiber optic splitters and distributed to the elemental modules. Note that the lengths of these optical fibers need only be toleranced with respect to the microwave wavelength to maintain signal coherency. In the receive mode, the signal is down-converted and digitized within the elemental module. The digital format signal modulates an optical carrier, which is sent via fiber to a central location for detection and combination with the signals from other modules.

The attractive characteristics of optical fibers include their light weight, small physical size, and mechanical flexibility. They are also immune to electromagnetic interference (EMI) and electromagnetic pulse (EMP), and exhibit extremely low fiber-to-fiber cross coupling.

The present limitations of fiber optic techniques are associated with the losses and frequency

limits inherent in the modulation/demodulation process. The level of microwave frequency transmit signal that may be extracted from an optic link and applied to the input of an elemental module is typically lower than desired. Similarly, for an analog receive signal fiber optic link, modulation and demodulation losses limit the dynamic range. The current upper frequency extreme for direct modulation of a laser diode optical source is in the neighborhood of 10 GHz. It is fully expected that advances in optical source and detector technology will relieve these limitations.

Techniques for simplifying the array feed network by leveraging the electrical sophistication of the T/R modules are being investigated. For example, the inclusion of phase and amplitude error detection and compensation circuitry within the modules enables relaxation of the feed network tolerance requirements. Performing signal multiplexing within the module may permit a simple one-channel feed network to accommodate multiple beams or polarizations. Modules that accommodate multiplexing of RF and control signals on the feed system alleviate the competition

for array volume that normally occurs between these two distribution networks.

To ensure the successful design of active phased arrays, accurate modeling and analysis tools that address the interaction of the feed, modules, and radiating elements are required. For example, the transmit mode radiated power and efficiency is a function of the active element impedance presented to the modules' MMIC power amplifiers. In the receive mode, the radiating element serves as the source for the receive amplifiers, and therefore its impedance influences the system gain and noise figure. The designer must possess good knowledge of both the circuit fabrication process and the module and feed assembly operation in order to predict performance and identify potential problems.

5. PERFORMANCE MONITORING AND FAULT ISOLATION

In order to examine the incorporation of performance monitoring and fault isolation (PMFI) into MMIC arrays, it is first necessary to compare array architectures that include subarrays fabricated in the plane of the aperture with those having subarrays

fabricated in the plane orthogonal to the aperture. The in-plane type of fabrication is clearly very difficult to repair. Even if the in-plane array is composed of subarrays, a radome (often hermetically sealed) generally must be removed in order to accomplish repairs. In contrast, the orthogonal subarray configuration seems to offer the possibility of removing one row or column from behind the array in order to replace the failed element or subarray. The main conclusion in this area is that fault detection leads to replacement of the subarray, instead of repair.

The various PMFI approaches can be classified in two categories: internal techniques which are accomplished within the array and calibration network, and external techniques which involve the measurement of radiated or received signals. The internal techniques include RF sampling at the aperture by using a directional coupler, and time domain reflectometry. The external techniques, which are mainly measurements of radiated fields, include probing and near-field measurement, far-field measurement, and phase shifter bit toggling.

Some PMFI techniques can be implemented with the array system in the field, while others are limited to use on the antenna range. The distinction depends in part on the amount of data involved in the PMFI, and in part on physical constraints such as the availability of an antenna to measure the far fields in the external case.

From a PMFI viewpoint, MMIC (or at least photolithographically produced) arrays appear to have the following advantages:

- a. Built-in on-board or on-chip circuits to act as PMFI calibrators.
- b. Built-in on-board or on-chip processing for PMFI. (Presumably this is digital circuitry that could be manufactured directly on the board.)
- c. The capability of using amplification to inject modulation into various levels of the circuits.
- d. The capability to correct amplitude performance using an MMIC variable attenuator, probably on the same board or chip.

e. The ability to switch elements over a wide dynamic range, and to effectively switch off all elements but one. (This capability is not available with current arrays.)

6. CAD TOOLS FOR MMIC ARRAYS

The CAD tools required for MMIC phased arrays may be discussed separately for two possible types of MMIC phased-array configurations. The first type uses conventional radiating elements driven by MMICs, such as phase shifters, switches, power amplifiers (for transmitting), and low-noise amplifiers (for receiving). The second group deals with truly monolithic arrays in which the radiating elements are fabricated on the same substrate (usually GaAs) used for monolithic circuits.

There is an urgent need to develop accurate CAD tools for both types of MMIC phased arrays. Successful implementation of MMIC antenna arrays would be difficult (if not impossible) without the appropriate CAD tools.

6.1 CAD for Monolithic Microwave Circuits

Several CAD packages for microwave circuit design are available commercially; however, most of these were developed for hybrid microwave circuits (on alumina or polystyrene-based substrates) and do not possess the accuracy needed for designing monolithic microwave circuits on GaAs. Currently, several groups are working to improve microwave circuit CAD techniques, and a second generation of CAD tools should be available within the next few years. Improvements are being sought in the following areas:

a. Improved models for passive circuit elements (such as spiral inductors) and transmission line discontinuities, especially at frequencies above 12 GHz. Rigorously accurate characterizations of these elements are obtained from numerically intensive algorithms. There is a need to develop techniques for using the numerically derived results in circuit analysis and optimization algorithms so that adequate accuracy and speed requirements are met.

b. More accurate models for the nonlinear behavior of active devices (such as MESFETs).

c. Nonlinear circuit analysis using the harmonic balance technique or its variations.

d. Models and analysis techniques for incorporating spurious coupling between various components or portions of monolithic integrated circuits.

e. Integration of sensitivity analysis, tolerance analysis, and yield analysis in CAD packages.

f. Use of expert-system concepts to make CAD tools more user friendly, especially in the area of circuit synthesis.

6.2 CAD for Monolithic Microstrip Antenna Arrays

In monolithic microstrip arrays, radiating microstrip antenna elements are fabricated on the high-resistivity GaAs substrates used for monolithic circuit fabrication. Thus, an integrated CAD software is needed which could be used for analysis and optimization of radiating, as well as nonradiating, components.

CAD tools for radiating microstrip antenna elements are still in the preliminary stages of development. It has recently been reported¹ that a

modified version of a cavity model, called a multi-port network model, is suitable for CAD of microstrip antennas. Using this approach, the CAD techniques developed for multiport networks can be extended to microstrip patches and arrays. Another software development effort is taking place in West Germany,² in which rectangular and circular microstrip patches are analyzed using a CAD package which should soon be commercially available.

The CAD of monolithic microstrip arrays requires the same tools used for MMICs, as discussed in the preceding subsection. In addition, techniques must be developed for CAD of microstrip patches and arrays. For this purpose, research efforts are needed in the following areas:

- a. Accurate CAD-oriented models for microstrip radiating elements and for mutual coupling between these elements.

- b. Synthesis algorithms for microstrip arrays, taking into account conductor and dielectric losses.

- c. Convenient modeling of surface wave effects and their influence on microstrip array design.

d. Evaluation of the effect of radiation generated from "nonradiating" parts of the arrays, such as the circuit components and the feed network.

e. Development of sensitivity analysis and optimization techniques applicable to microstrip patches and arrays.

f. Design tools for both broadband and electromagnetically coupled microstrip patches.

6.3 Related CAD Issues

Two related areas for which CAD tools must be developed were identified. One of these involves computer-aided measurements for both MMICs and monolithic phased arrays, while the other is related to evaluating the thermal and mechanical performance of MMIC arrays. Research efforts should be encouraged in these areas.

7. REFERENCES

1. Gupta, K. C. (1987) "Multiport network modeling approach for computer-aided design of microstrip patches and arrays," IEEE AP-S International Symposium, Blacksburg, Virginia, Digest 2:786-789.
2. Wolff, I. (1987) Private communications.

**A KU-BAND HEMISPHERICAL ARRAY ANTENNA
FOR POSSIBLE
SPACE STATION APPLICATION**

**R. W. Shaw, J. R. Carl; Lockheed Engineering and Management Services
Company**

**G. D. Arndt; National Aeronautics and Space Administration –
Johnson Space Center**

ABSTRACT

The Space Station communication system will use microwave frequency radio links to carry digitized information from sender to receiver. The ability of the antenna system to meet stringent requirements on coverage zones, multiple users, and reliability will play an important part in the overall multiple access communication system. This paper will describe a hemispherical array with non-uniformly spaced active radiating elements to meet the solid angle gain/coverage requirements associated with the Space Station communication midzone region.

1. INTRODUCTION

It can be shown that an array of radiating elements distributed in some fashion over a doubly curved surface is usually better suited than a planar array for applications requiring moderate gain over wide solid

angle coverage.¹ The ability of such an antenna to achieve a given spatial gain/coverage characteristic while minimizing the number of radiating antenna elements, thereby lowering hardware costs, is considered one of the more important requirements of this application.

The system itself is a multichannel, full duplex, Ku-band, frequency division multiple access scheme which will allow communications from 200 m to 185 km from the Space Station structure. Figure 1 shows the antenna system configuration and its major functional blocks. The implementation of the array has been tailored to the unique coverage

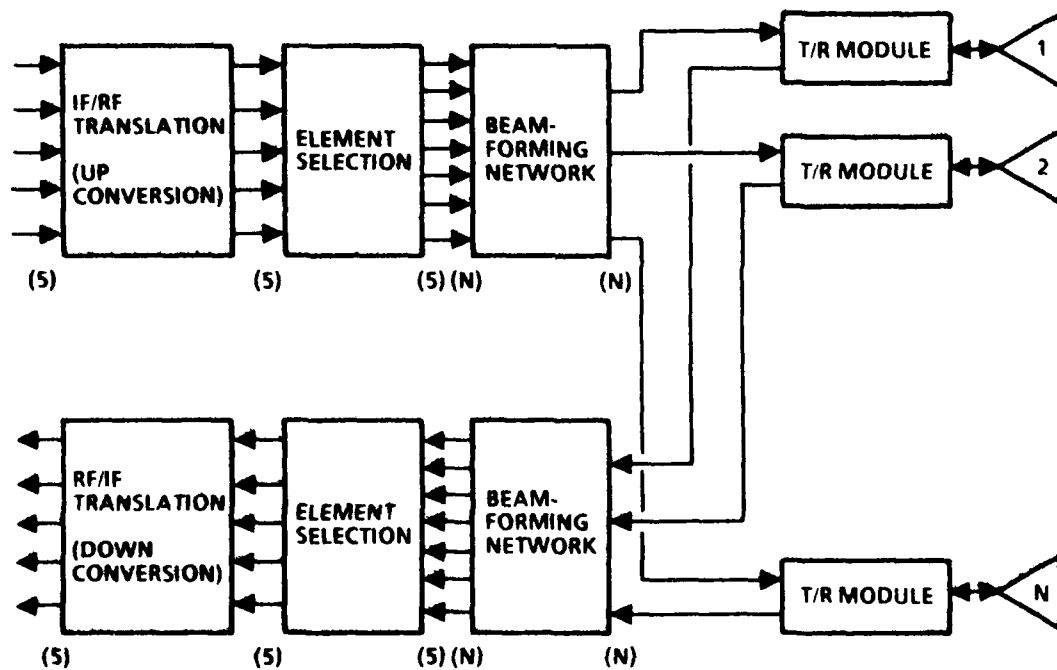


Figure 1.- System configuration.

zone requirements of the Space Station multiple access midzone region and incorporates moderate gain horn elements in a hemispherical arrangement.

The design of the array also encompasses the mechanical and electrical integration of transmit/receive (T/R) modules colocated at each element. It is the T/R module which then sets the transmit power level and receiver noise figure of the system and allows the optimum performance of the array to be obtained.

2. ARRAY DESIGN

The first step in determining the antenna gain, pattern, and the subsequent array configuration is deciding the coverage zone needs. This specific antenna system is required to serve the users located in the midzone region of the multiple access network. The midzone region extends from 200 m to 185 km from the Space Station structure with varying scan angle requirements for given distances.

Figure 2 shows a pictorial representation of the gain/coverage requirement. The first region of interest encompasses a sphere that extends from 200 m to 1 km away from the structure. In this region, the elevation angle can vary up to $\pm 180^\circ$, and the scan angle (the angle from the velocity vector) can vary up to $\pm 90^\circ$. Users in this region may require telemetry and command information (low data rate) or high resolution television (high data rate). The second region

of interest encompasses a disc shape that extends from 1 km to 37 km out from the structure. This region requires an elevation angle variation of $\pm 180^\circ$ but a scan angle variation of only $\pm 20^\circ$. Again, users in this region may require telemetry and command or high resolution television. The final sector of interest is a rectangular region which extends from 37 km to 185 km along the velocity vector and is 74 km high by 18 km thick. In this region, users require only low data rate telemetry and command information.

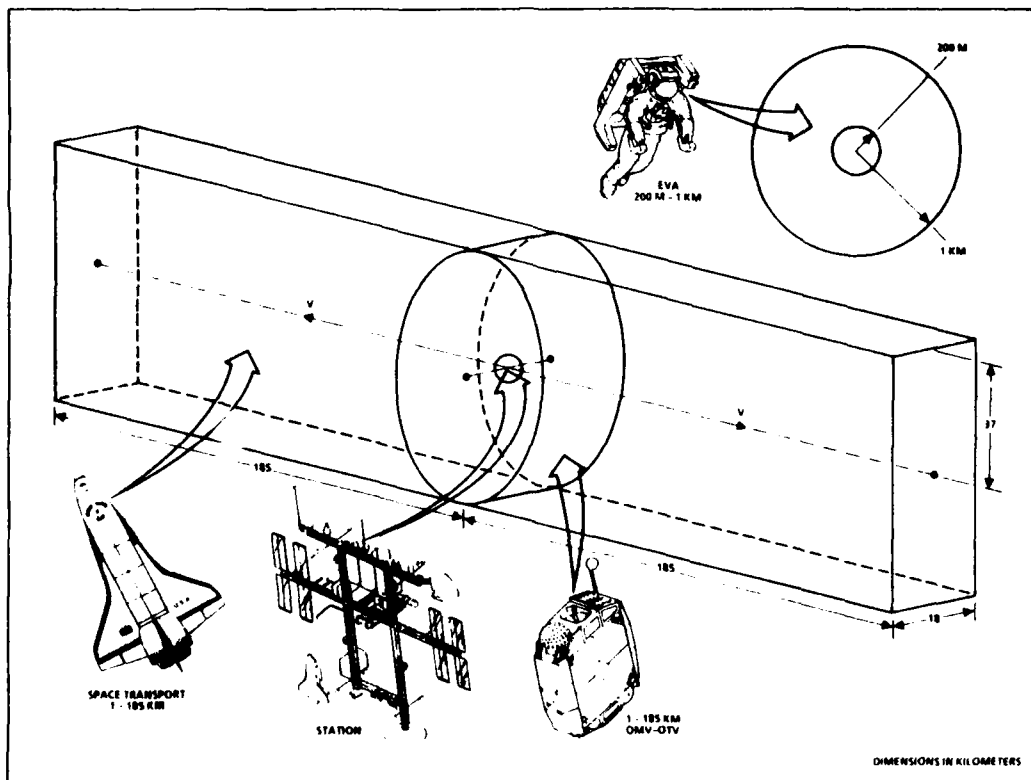


Figure 2.- Coverage zones.

The most stringent requirement on the array design is the spherical antenna coverage zone. However, the most stringent link margin for the system is the farthest distance requirement of 185 km. By blending the requirements of each coverage zone with the required effective isotropic radiated powers (EIRP's) and link margins, a gain taper can be determined on the array to allow spherical close-in antenna coverage with maximized array gain in the velocity vector (orbital plane) direction. Such a gain taper is shown in figure 3, where a somewhat constant gain is maintained within 20° of the orbital plane, with a decreasing gain rolloff at 90° from the orbital plane.

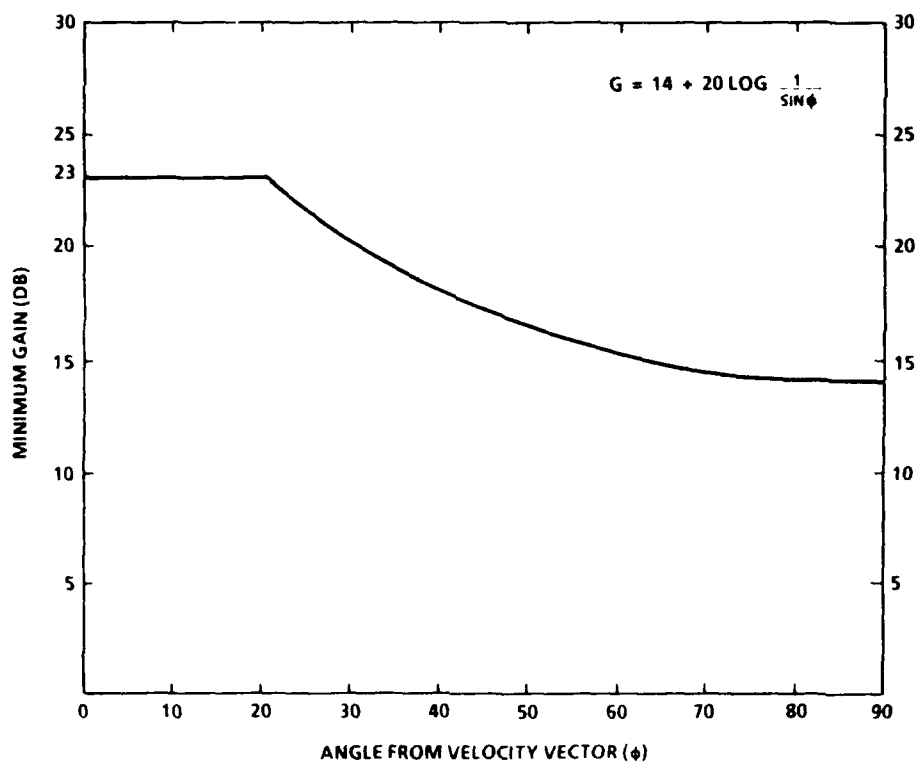


Figure 3.- Array gain taper.

Interest in spherical arrays for achieving spherical or hemispherical antenna coverage is based on the natural ability of spherical arrays to provide uniform pattern and gain over wide angular regions. Other array configurations, such as planar arrays, suffer from beam degradation as the beam is steered over wide angular regions. Cylindrical or conical arrays can reduce beam variations in elevation but still suffer beam variations in the scan angle direction. Figure 4 shows a predicted gain versus scan angle plot of a spherical and a cylindrical array. Therefore, an array of elements conforming to a spherical pattern can be used for hemispherical coverage, provided the

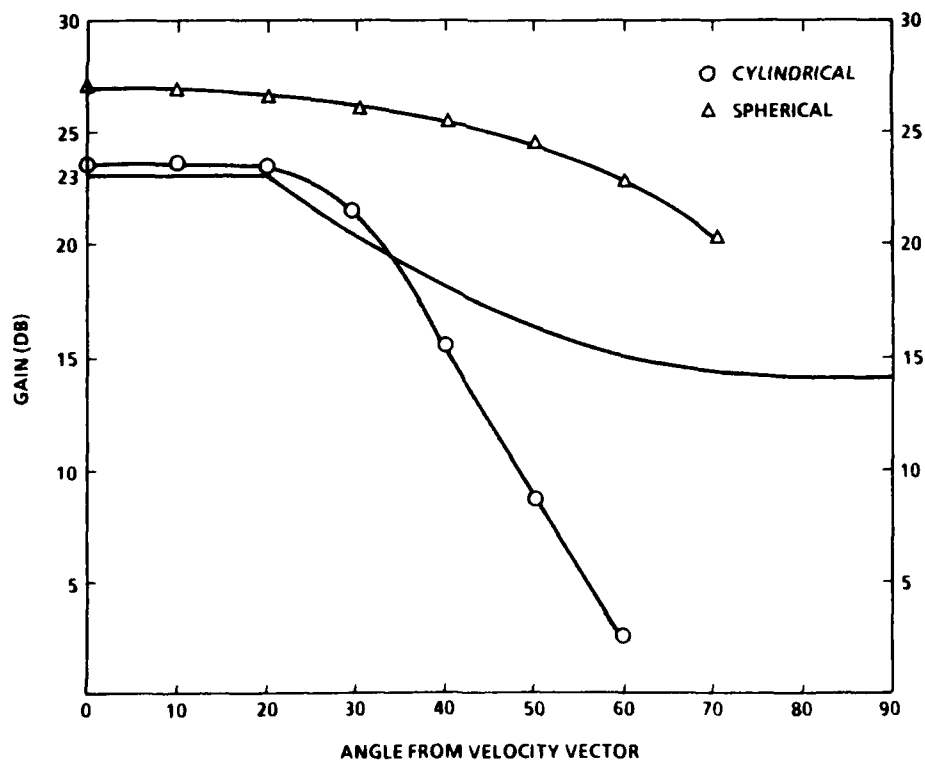


Figure 4.- Spherical and cylindrical comparison.

array is large in terms of wavelength. In addition, the individual elements may be tilted toward the velocity vector to maximize the contribution of the elements in that direction with a corresponding decrease in contribution toward the scan angle direction.

The overall gain of the planar array antenna is a function of the individual element gain and the total number of elements in the array. This is also a good approximation for a spherical antenna provided that the "active" elements point near the line-of-sight vector.

$$G_{ARRAY} = G_{IND} + 10 \log N \quad (1)$$

ELEM

where

- G_{ARRAY} = gain of the array (in dB)
- G_{IND} = gain of identical elements in the array
- ELEM
- N = total number of elements in the array

Therefore, for a desired array gain, incorporating individual high gain elements results in a fewer number of elements for the array. However, the real benefit in this reduction of elements is the corresponding decrease in components. Recent interest in array development has been in terms of microwave monolithic circuits integrated into an array of microstrip patch antennas. Typically, these patch antennas have gains ranging from 0 dBi to 6 dBi at Ku-band

frequencies. Thus, an array of 23 dBi would require 100 elements (3 dBi). As a contrast to this, using elements of 8 dBi gain would require an array of only 32 elements. This threefold decrease in elements and active components is extremely beneficial to the reliability and cost of the system.

In this array application, the elements are waveguide horns with gains of approximately 8.5 dBi and beamwidths of 58°. The integration of this waveguide component to the T/R module is done via a fin-line waveguide-to-microstrip transition. This technique allows an end launch into the waveguide assembly for a more desirable mechanical configuration. Figure 5 shows a picture of the transition/element assembly and the corresponding measured input impedance. Figure 6 shows the measured antenna pattern of a gold-plated aluminum assembly.

3. COMPUTER-ASSISTED DESIGN

A computer program has been written to calculate and graphically display the radiation patterns of a wide variety of possible conformal array antennas. If the curvature of the array can be approximated by the surface of any ellipsoid, or a section thereof, the program is applicable. By specifying the dimensions of the three major axes of an ellipsoid, a wide variety of surface curvatures are possible including a sphere, cylinder, or plane. Once the surface is defined, the radiating

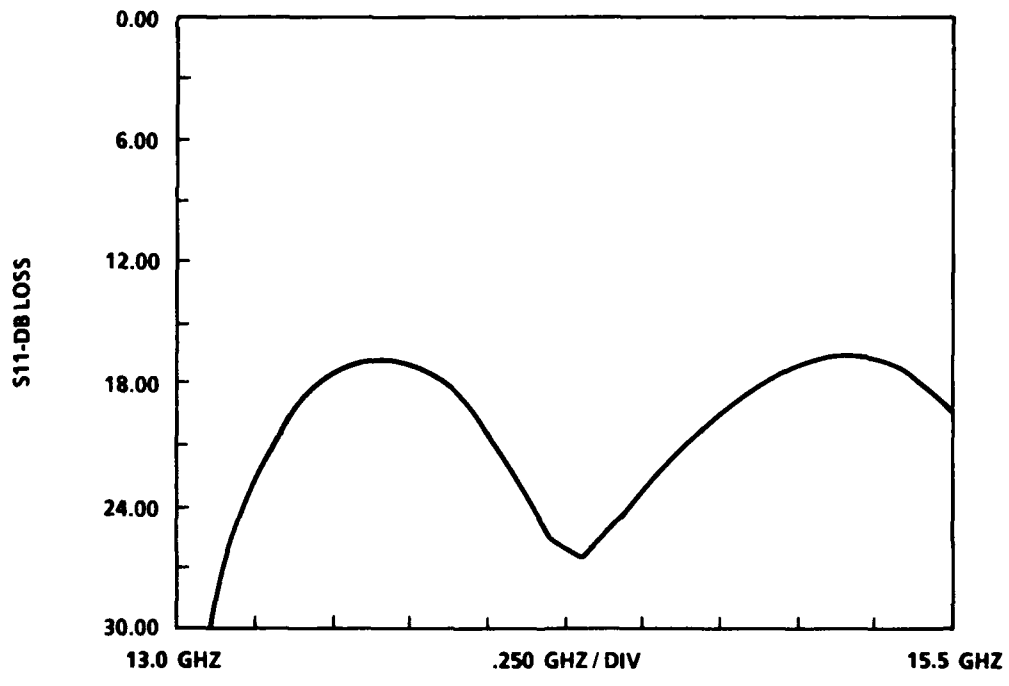
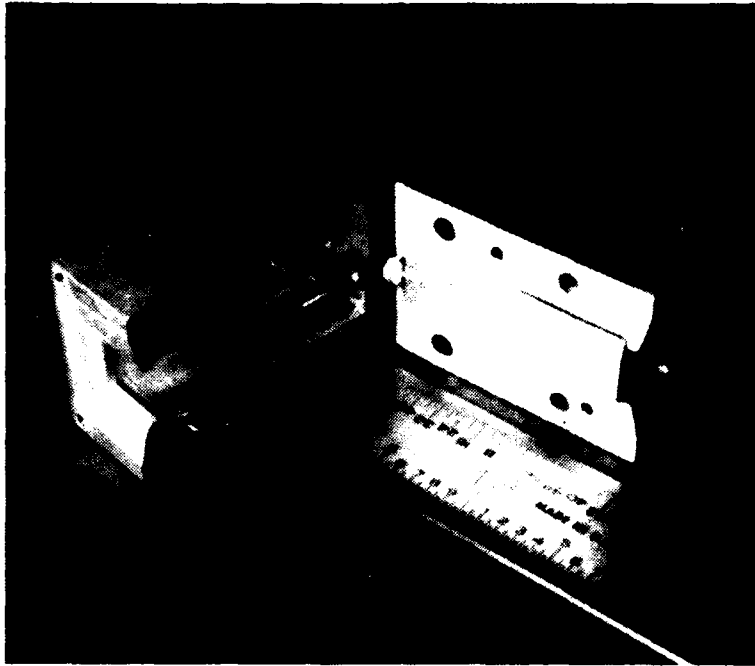


Figure 5.- Transition/horn element.

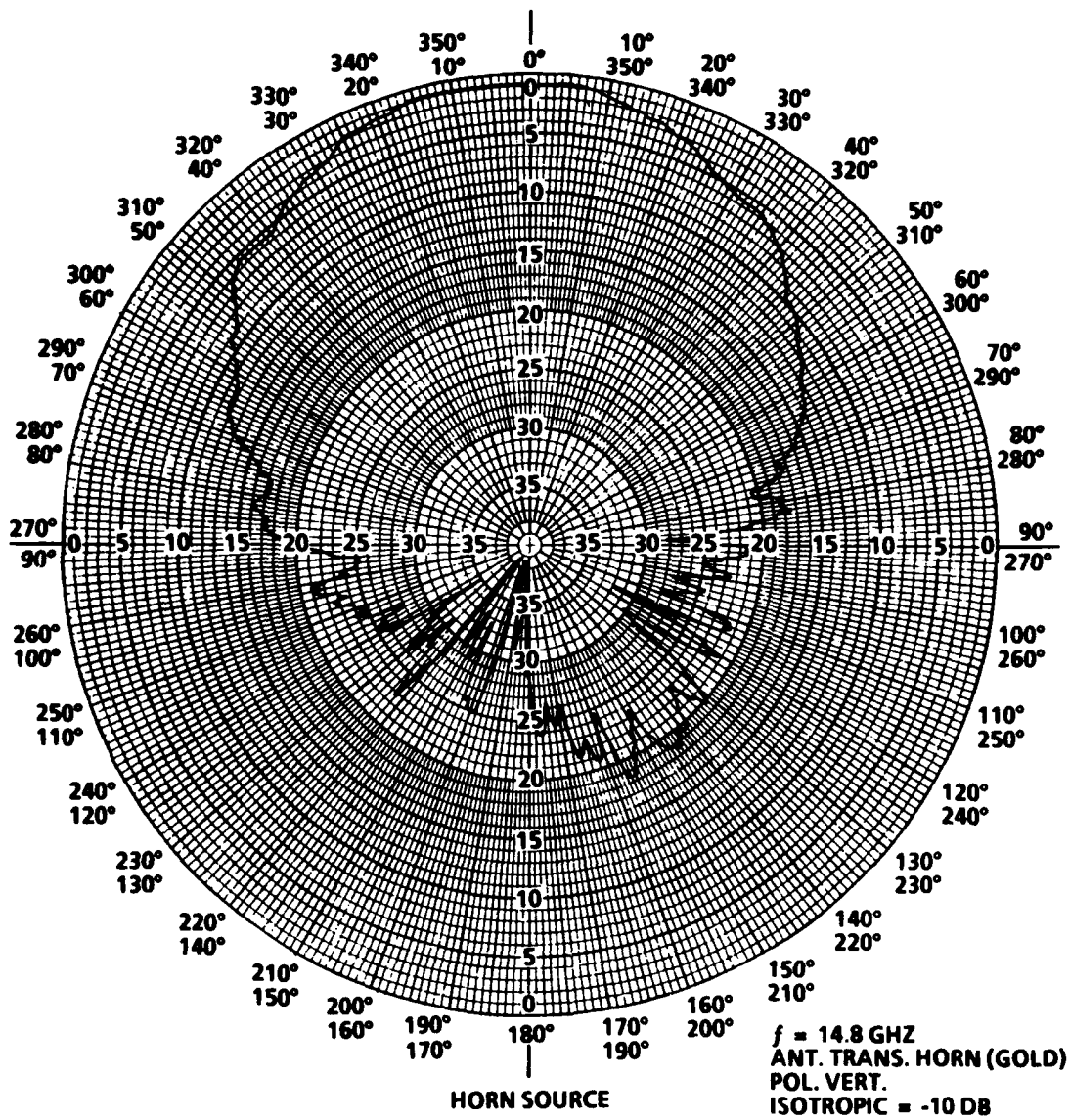


Figure 6.- Transition/horn antenna pattern.

elements can be layed out on it, and the location of each phase center can be specified.

The program calculates the far field radiation pattern of the array by the element summation:

$$\hat{E} = \sum_{i=1}^N \hat{A}_i e^{-jk(\vec{s}_i \cdot \vec{r})} \quad (2)$$

where

\hat{E} = the field intensity at some point in the multibeam radiation pattern

\hat{A}_i = the complex amplitude and phase at some element location "i" on the array, which is the superposition of the requirements for M beams of the multibeam pattern

that is

$$\hat{A}_i = \sum_{j=1}^M \hat{A}_j \quad (3)$$

k = the propagation constant

\vec{s}_i = the element location vector

\vec{r} = the direction in space where the field is being summed

Whether or not an element is active is based on the permitted angular difference between the element's normal vector and the beam direction. This permitted angular difference is an input. The contribution of each active element is a vector sum at some point in space. The phase of each element's contribution is based on its precise

location on the ellipsoid, and the amplitude is based on the direction of the element's normal vector and the element pattern factor. These summations are systematically performed one point at a time, over the sector of space of interest, and provides the data for the radiation pattern plot.

3.1 COMPUTER-PREDICTED RADIATION PATTERNS

With the use of this computer-generated theoretical radiation pattern data, analysis of several array anomalies can be investigated. Figure 7 shows the predicted radiation pattern of the beam when it is located in the orbital plane.

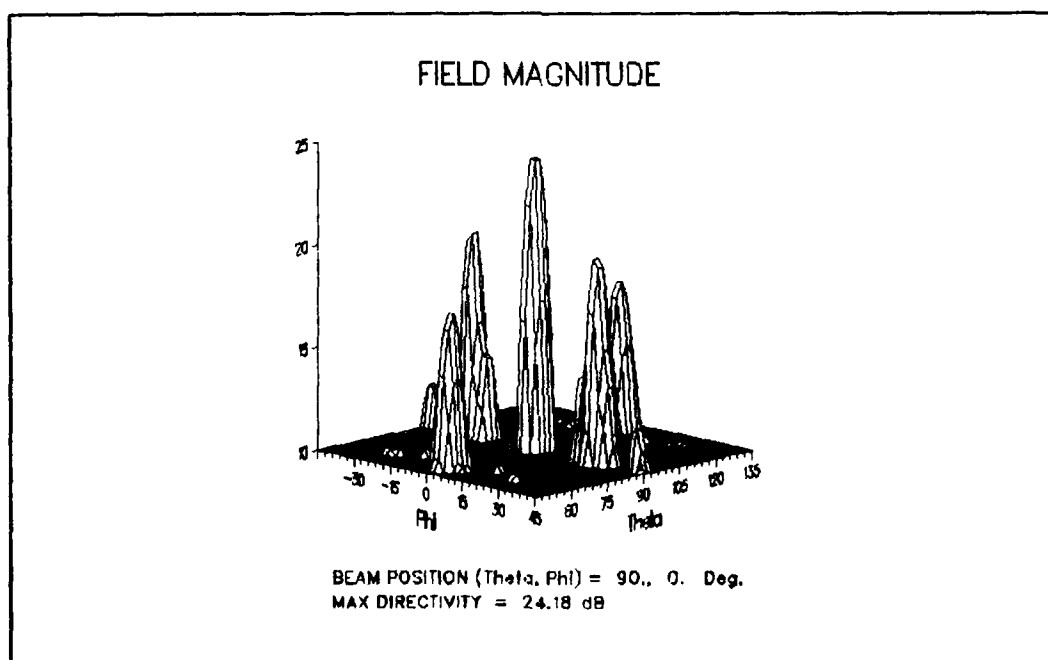


Figure 7.- Array radiation pattern.

3.1.1 EFFECTS OF PHASE QUANTIZATION

Phase shift is supplied to the radiating elements in discrete amounts and is digitally controlled from the beam-forming network. One bit (0 or 1) of control will permit either 0° or 180° of phase shift at each element. Two bits (00, 01, 10, 11) will permit 0° , 90° , 180° , 270° , etc. Plots have been made to show how the reference radiation pattern is affected by a degree of control from 1 bit to 5 bits. The data shows that little (0.02 dB) is gained by going from 4 bits to 5 bits. Therefore, 4 bits was chosen for control of this antenna.

3.1.2 ELEMENTAL PHASE ERRORS

The phase errors associated with the element phase shifters and other components are assumed to be gaussian in nature. Figures 8, 9, and 10 show how the reference radiation pattern is affected as elemental phase error is increased from a standard deviation (1σ) of 22.50° to 90° . The patterns show that the former is acceptable, and the latter is not.

3.1.3 ELEMENT FAILURES

A cursory investigation has been made on the effects of element failures. In figures 11 and 12 the effects of 5 and 12 failures are shown respectively. There are normally 31 active elements in the reference pattern. The failed elements have been randomly chosen and made to be completely "dead." These plots show that graceful degradation occurs and that several hard failures do not severely degrade the performance of the antenna.

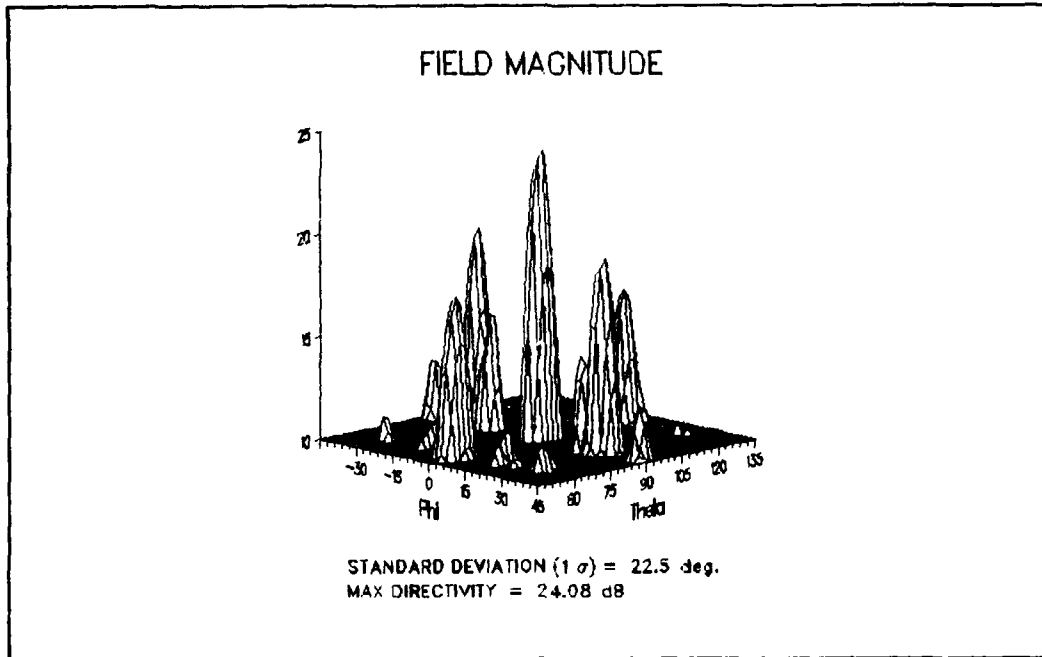


Figure 8.- Radiation pattern with
22.5° elemental phase error.

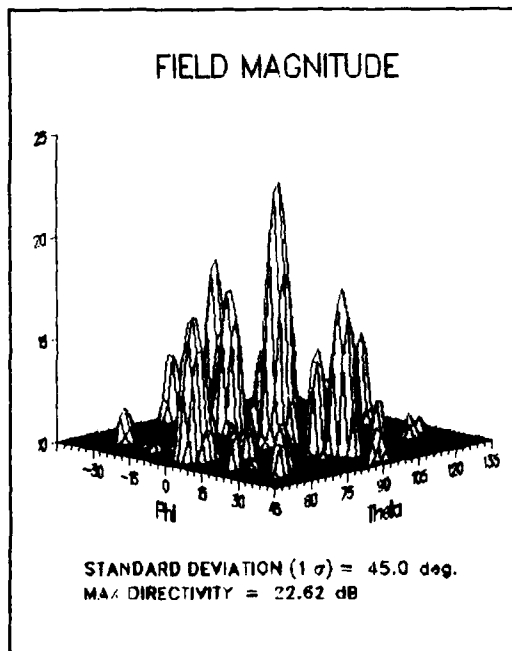


Figure 9.- Radiation pattern with
45° elemental phase error.

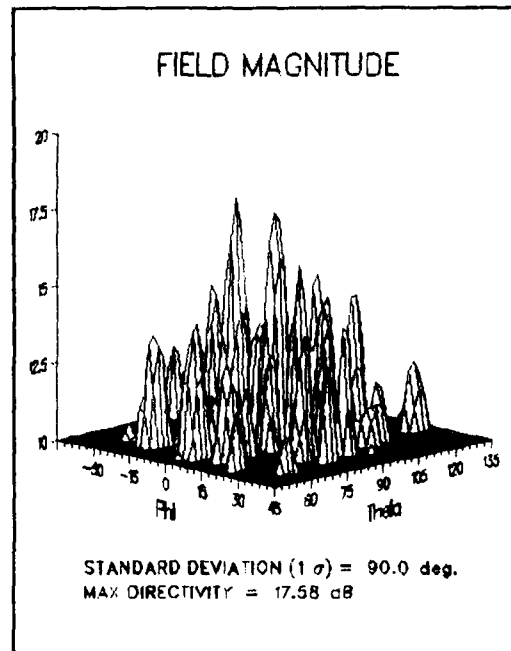


Figure 10.- Radiation pattern with
90° elemental phase error.

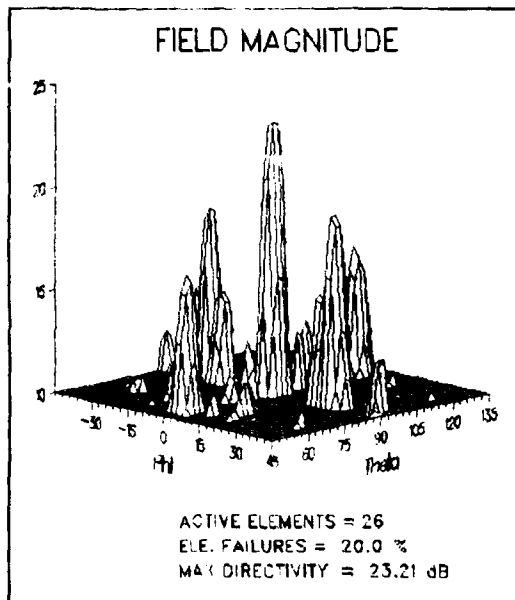


Figure 11.- Radiation pattern with five element failures.

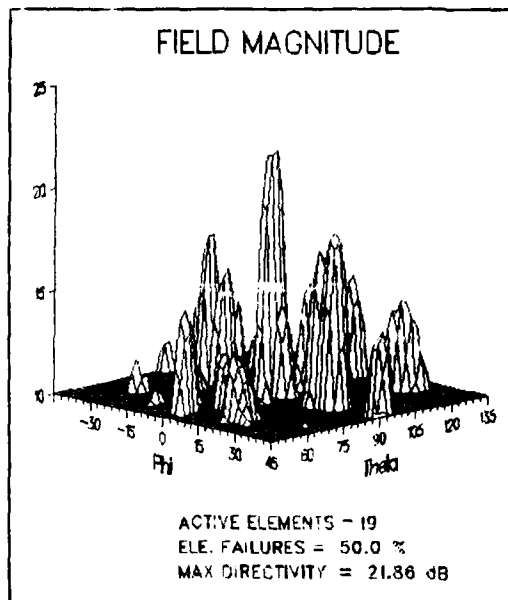


Figure 12.- Radiation pattern with 12 element failures.

4. CONCLUSION

The array design for a full duplex multibeam antenna has been presented. This communication antenna system utilizes a spherical conformal array of high gain elements to achieve the gain/coverage requirement of the Space Station midzone region. The design configuration and the anticipated performance of the array have been optimized using an in-house computer program. This program also allows the variation of key parameters in the antenna design which enables absolute phase errors, phase quantization errors, and element failures to be simulated.

ACKNOWLEDGMENTS

This work has been performed under the sponsorship of the National Aeronautics and Space Administration (NASA), Lyndon B. Johnson Space Center (JSC), Houston, Texas, contract number NAS 9-17900. The authors wish to thank Dr. G. Raffoul and B. P. Lu for assistance in the antenna analysis and array design.

REFERENCES

1. Schrank, H. E. (1970) Basic theoretical aspects of spherical phased arrays. Paper presented at the 1970 Phased Array Antenna Symposium: June 2-5, 1970.
2. Shaw, R. W., Kovitz, J. K. (1986) A distributed array antenna system. 1986 Microwave Theory and Techniques Symposium Digest: 315-318.

**ANTENNA SUBSYSTEM FOR
AVIATION SATELLITE COMMUNICATION**

S.Y. Peng, H.H. Chung, and W. Foy
Teledyne Ryan Electronics
San Diego, California

ABSTRACT

There is a tremendous need for a low cost phased array antenna subsystem for satellite communication. This low cost antenna subsystem will be either installed on top of motor vehicles, on the side of airplanes, or may be inside homes to provide telephone service, traffic control, and many other needed functions. This paper presents a newly developed L-band phased array antenna subsystem for aviation satellite communication.

The proposed Antenna Subsystem consists of two high gain antennas, one low gain antenna, 3 low-noise amplifiers, 3 diplexers, and associated electronics. Each high gain antenna is a phase array, consisting of 19 crossed-slot elements designed to be conformally mounted on each side of the fuselage. Each array main beam will be electronically steered by 3-bit diode phase shifters.

The overall physical size of each array is a 20 inch by 20 inch square that is 0.4 inch thick. The low gain antenna is a single

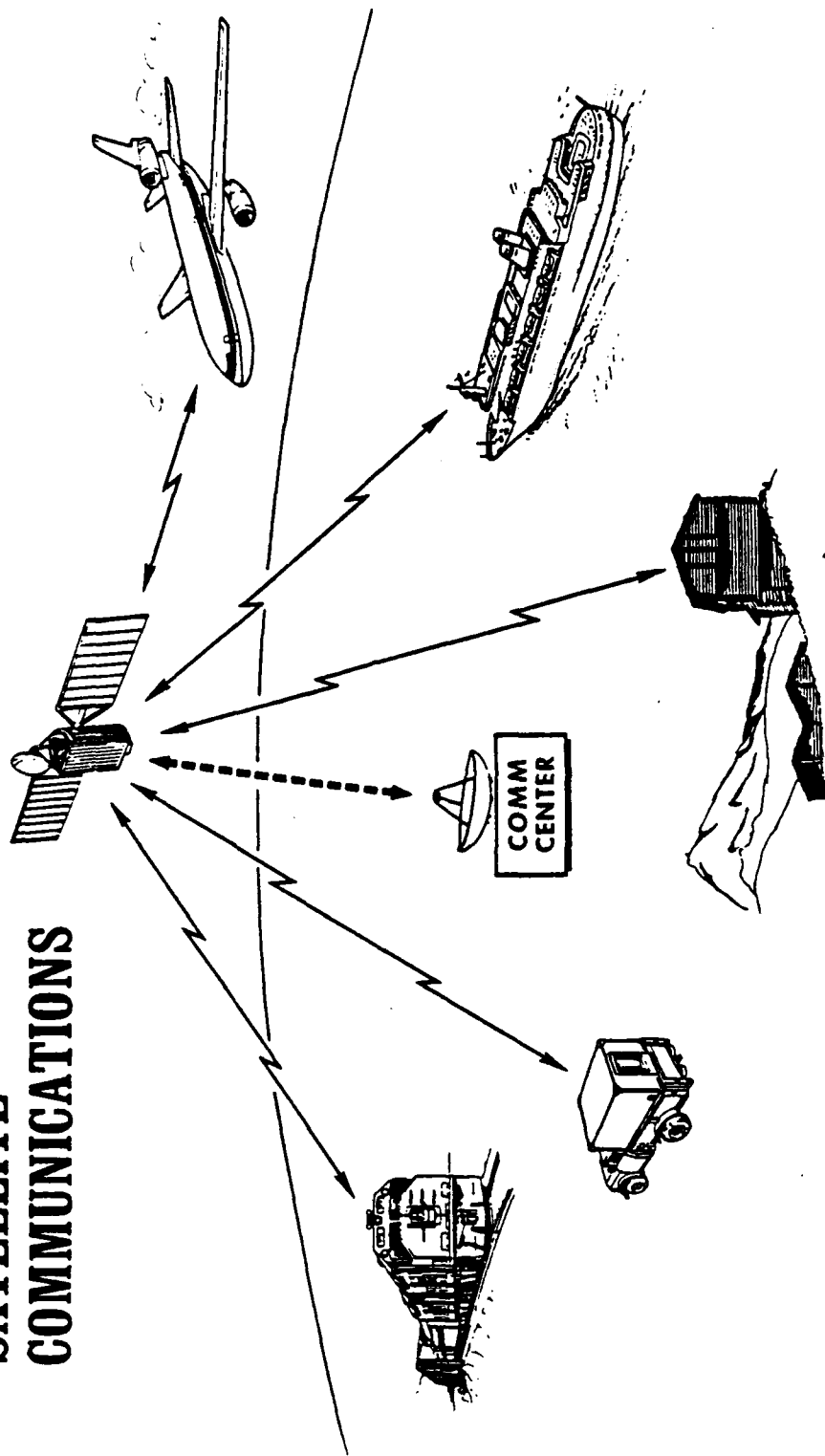
crossed-slot, flush mounted on the top of the fuselage. The key features of the presently developed phased array are low profile, low cost, lightweight, highly reliable, and maintainable. The printed cross-slot array elements newly developed provide the ideal element pattern, greater spatial coverage, for satellite communication. The array pattern performance and installation concept will be discussed.

1.0 INTRODUCTION

Teledyne Ryan Electronics (TRE) has broad experience in the development of Phased Array Antennas. Currently, TRE is developing an L-Band Phased Array for the NASA Mobile Satellite (MSAT) vehicular communication program. An overall concept of mobile satellite communications is shown in Figure 1. Under this program TRE will develop and deliver an antenna system with characteristics very similar to those required by Aviation Satellite (AVSAT) Communication System. Because the MSAT antenna requirements are very close to those of AVSAT, TRE strongly believes that the proposed Antenna Subsystem is a low risk solution to the ARINC AVSAT specifications. TRE has more than a 30 year history of developing and producing highly reliable electronic and RF avionics equipment.

The proposed Antenna Subsystem consists of two high gain antenna, one low gain antenna, 3 low-noise amplifiers, 3 diplexers, and

MOBILE SATELLITE COMMUNICATIONS



TELEDYNE RYAN ELECTRONICS
E8427

Figure 1. Overall Concept of Mobile Satellite Communications

associated electronics. Each high gain antenna is a phase array, consisting of 19 crossed-slot elements designed to be conformally mounted on each side of the fuselage. Each array main beam will be electronically steered by 3-bit diode phase shifters. The overall physical size of each array is a 20 inch by 20 inch square that is 0.4 inch thick. The low gain antenna is a single crossed-slot, flush mounted on the top of the fuselage.

Key features of the proposed Antenna Subsystem include the use of crossed-slot elements etched in stripline material to provide a low profile, low cost, lightweight, highly reliable and maintainable design. Major advantages of using the crossed-slot design over microstrip patch antennas include greater spatial coverage, broader frequency bandwidths, and less sensitivity to manufacturing tolerances. Commonality of design in each of the three antennas also aids in cost reduction. In addition, the selection of a 19-element circular aperture design over a 16-element rectangular aperture is to improve sidelobe performance at large scan angles. One of the two side-mounted fuselage conformal phased array is shown in Figure 2 thru 3 which is a photo of a mockup built for this year's Paris Air Show. The concept of the TRE's Antenna Subsystem is to minimize the total number of Line Replaceable Unit (LRU), to provide the ease of maintainability and to simplify installation procedure.

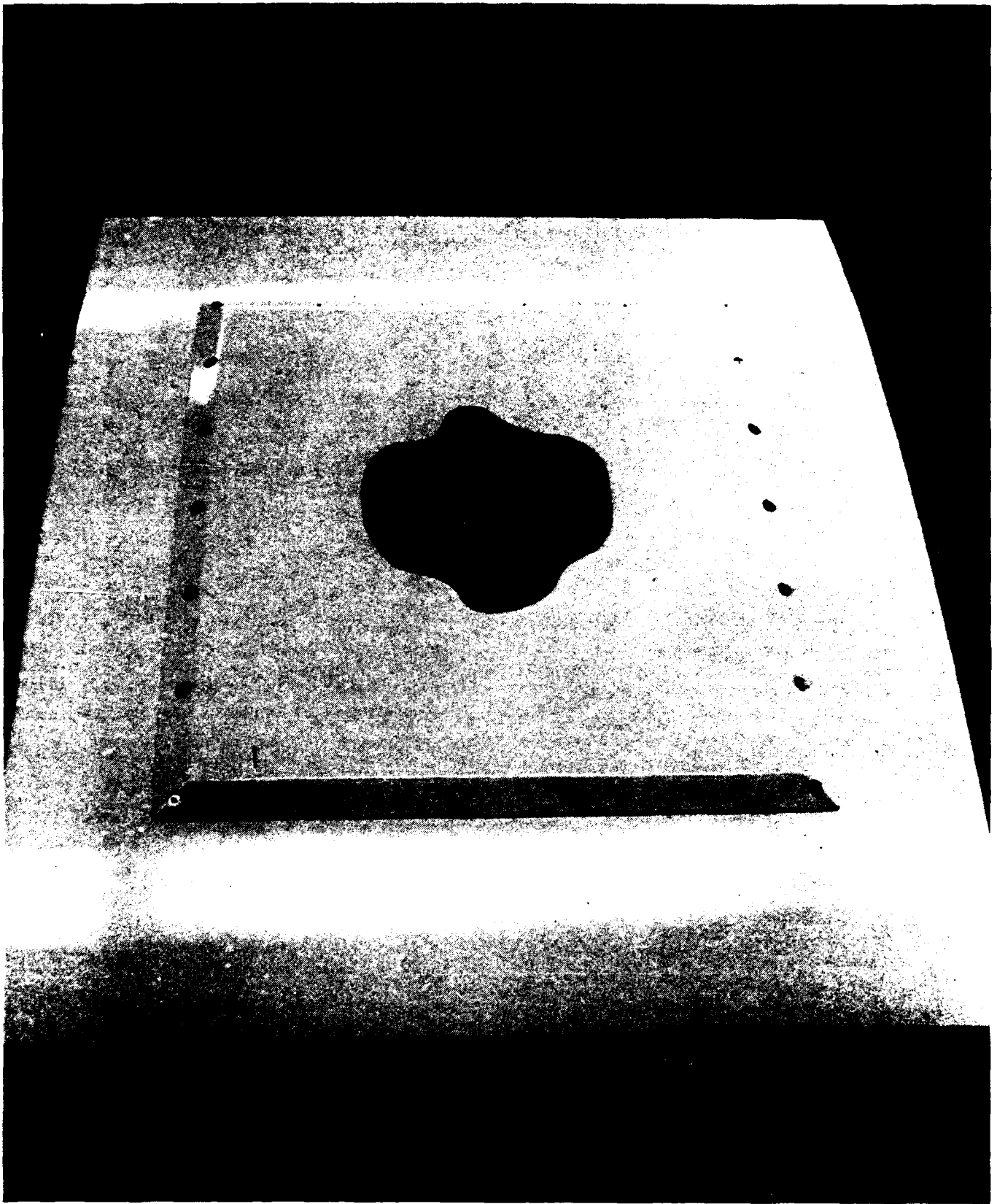


Figure 2. A Photo to Show the Top View of a Side-Mounted Array Mockup

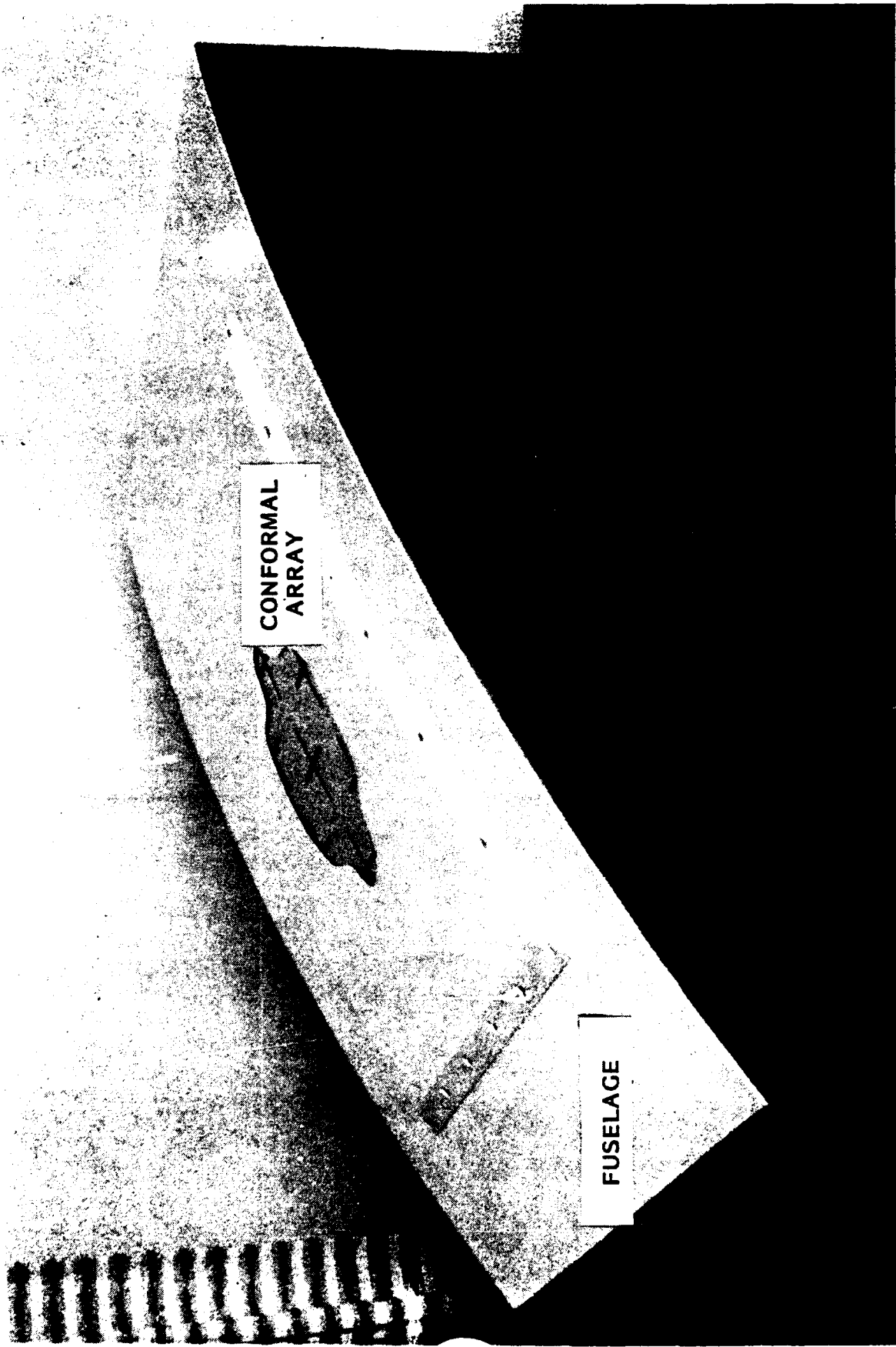


Figure 3. A Photo to Show the Side View of a Side-Mounted Array Mockup

2.0 ANTENNA SUBSYSTEM CHARACTERISTICS

The antenna subsystem includes two high gain array antennas and one low gain antenna utilizing printed circuit crossed-slot elements. These antenna radiating elements are conformal to the fuselage skin using tapered edges to reduce aerodynamic drag. The normal to the array aperture is about 45 degrees above horizon which allows the maximum elevation scan coverage to be -20 to +90 degrees relative to the horizon.

Detailed trade-off analysis were performed to maximize array gain, satellite isolation and to minimize backlobe and sidelobe levels. The resulting Antenna Subsystem characteristics are summarized in Table 2-1. The trade-off parameters investigated included array size, the number and spacing of array elements, and the distribution of losses.

Table 2-1. Antenna Subsystem Characteristics

Frequency of Operation	
Transmit	1625.5 to 1660.5 MHz
Receive	1530.0 to 1559.0 MHz
Gain	
Broadside	15 dBic
At +60 scan angle	12 dBic
Coverage	
Elevation	-20 degrees to +90 degrees
Azimuth	360 degrees
Sidelobe Discrimination	13 dB at 45 degrees separation
Satellite Isolation	<u>>20 dB</u>

The high gain antennas are electronically steered by 3-bit diode phase shifters controlled by the beam forming network and microcomputer. For the low gain antenna, there is no phase shifter requirements. Both phase shifter and control electronics are contained on a microstrip circuit board. Coaxial RF cables, through a special high density connector, are used to interconnect radiating elements and phase shifters circuits. The phase shifter drive circuits, microcomputer, and low noise amplifiers are powered by a low cost D.C. power supply. The diplexer and Low Noise Amplifier (LNA) are physically integrated to form a single unit to reduce RF loss. The definition of each LRU for the proposed antenna subsystem is given in Table 2-2.

Table 2-2. Antenna Subsystem

- | | |
|-------|---|
| A-1* | First of a 19-element high gain antenna flush-mounted on one side of fuselage. |
| A-2* | Second unit of a 19-element high gain antenna flush-mounted on the other side of fuselage. |
| B-1 | A single element low gain antenna flush-mounted on the top of fuselage, and a diplexer and Low Noise Amplifier (LNA) unit to feed the low gain antenna. |
| C-1** | First high gain antenna electronic units consisting of a phase shifter circuit board. Beam forming network, diplexer, Low Noise Amplifier (LNA) and its associated electronics circuits and power supply. |

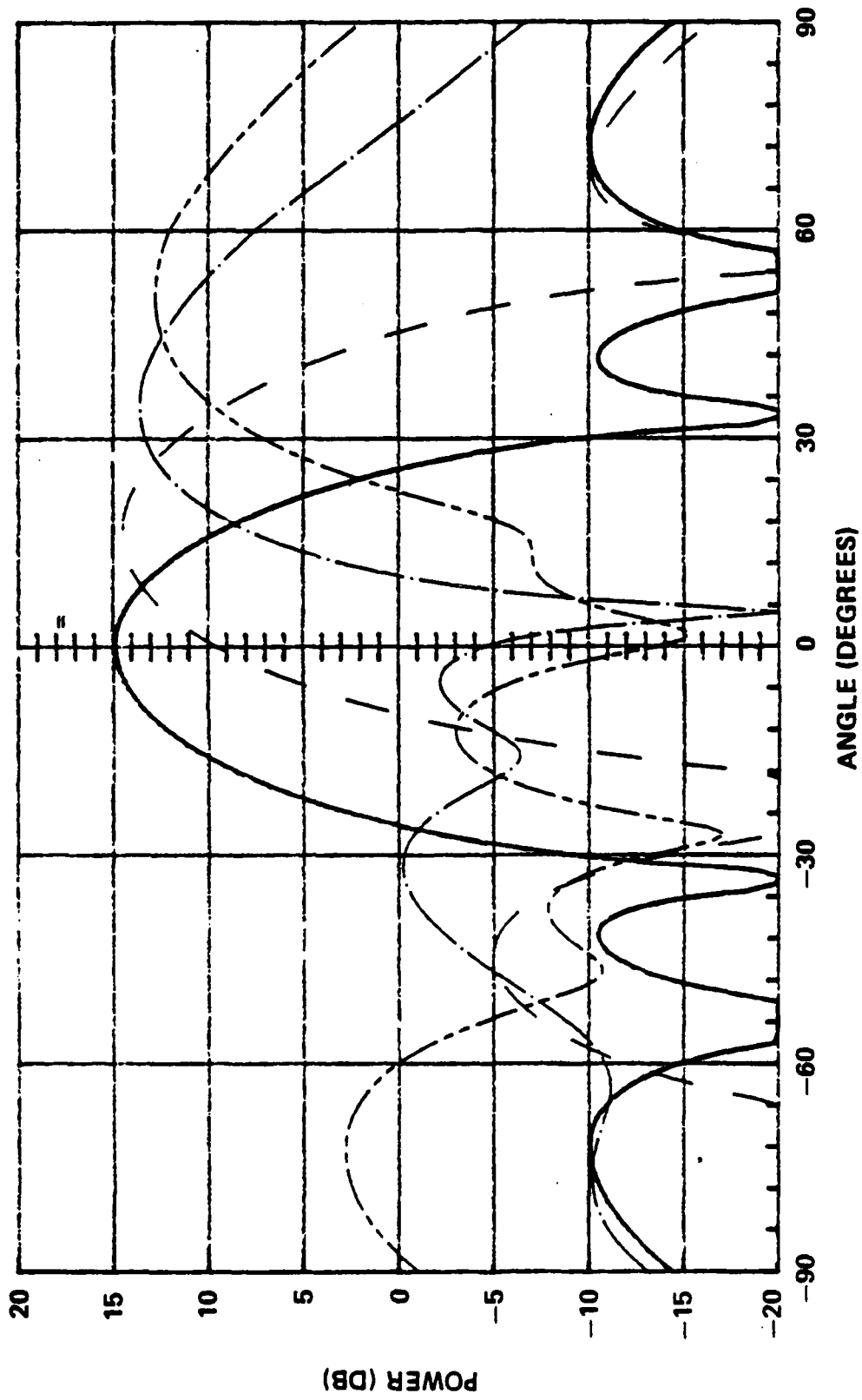
C-2** Second high gain antenna unit consisting of a phase shifter circuit board, beam forming network, diplexer, Low Noise Amplifier (LNA) and its associated electronics circuits and power supply.

Typical array antenna patterns were calculated for frequencies of 1660 and 1545 MHz as shown in Figures 4 through 7. Note that within +60 degrees scan angles in both azimuth and elevation planes, the 12 dBic gain requirement is met. In addition, the azimuth and elevation angles stated here are referenced to the array aperture. The calculated 3 dB beamwidths are 30°, 34°, 38°, and 44°, corresponding to the scan angle of 30°, 40°, 50°, and 60° respectively.

The high gain antenna beam forming network consists of 18 3-bit pin diode phase shifters. These phase shifters are fed by a 1:19 reactive stripline power divider. One of the 19 ports is used as the reference port, which eliminates one 3-bit phase shifter and provides phase stable conditions as the beam is steered off broadside.

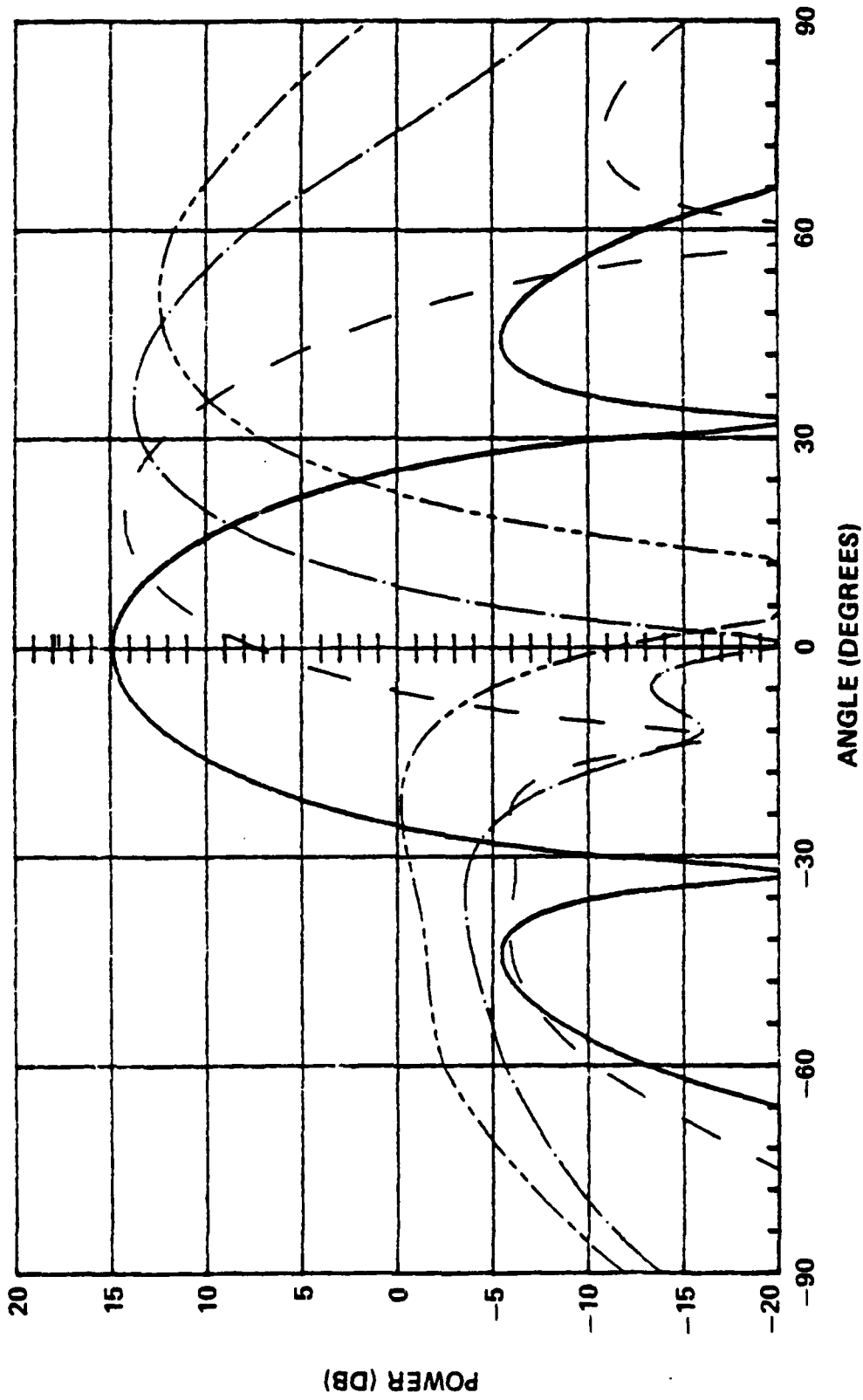
3.0 INSTALLATION CONCEPT

The antenna subsystem installation concept is aimed to simplify procedure, to reduce cost, to ease accessibility for maintenance, and to enhance system reliability. Based on above concept, it is



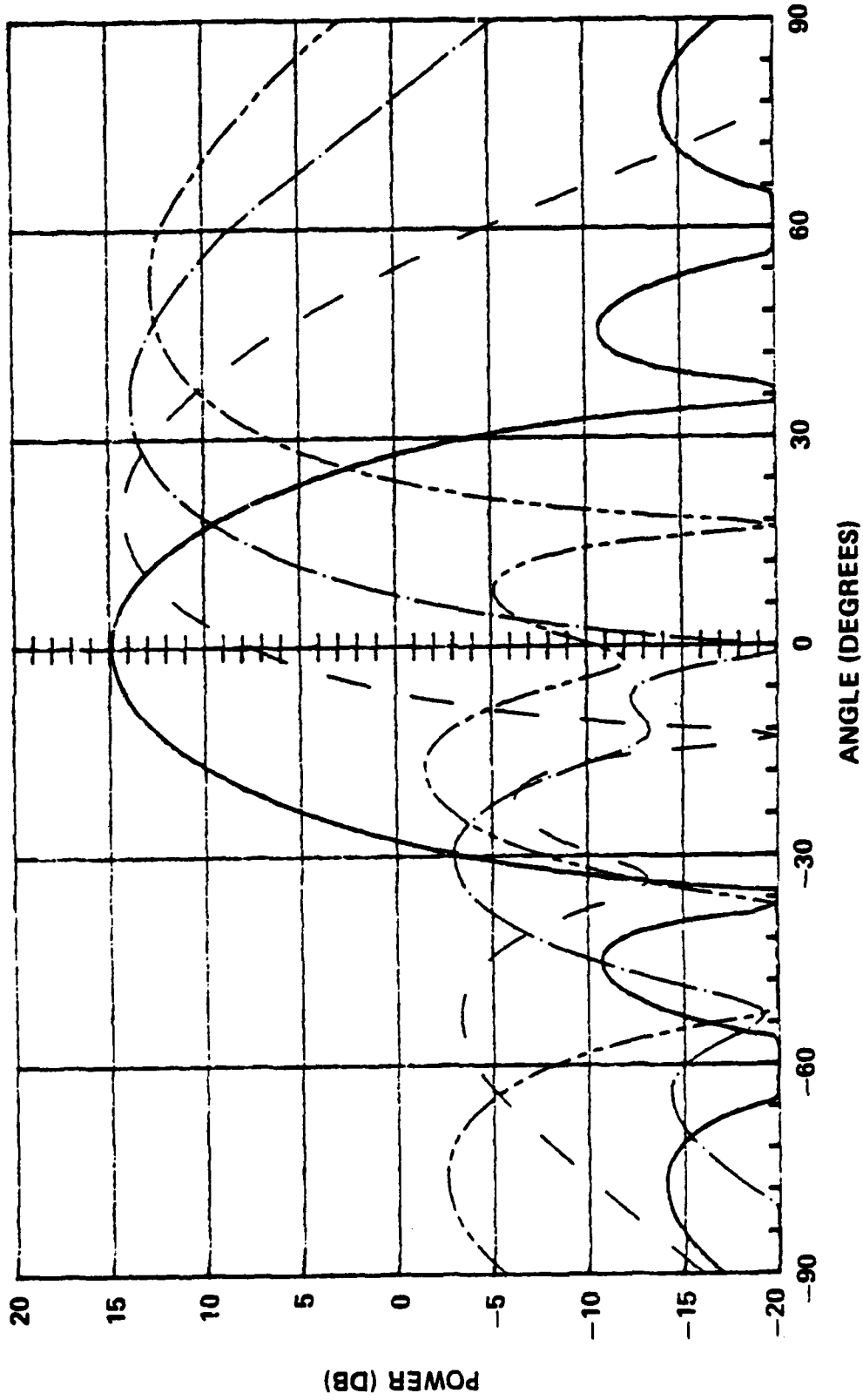
TELEDYNE RYAN ELECTRONICS
E8776

Figure 4. (FORE-AFT) Azimuth Array Pattern at 1660 MHz



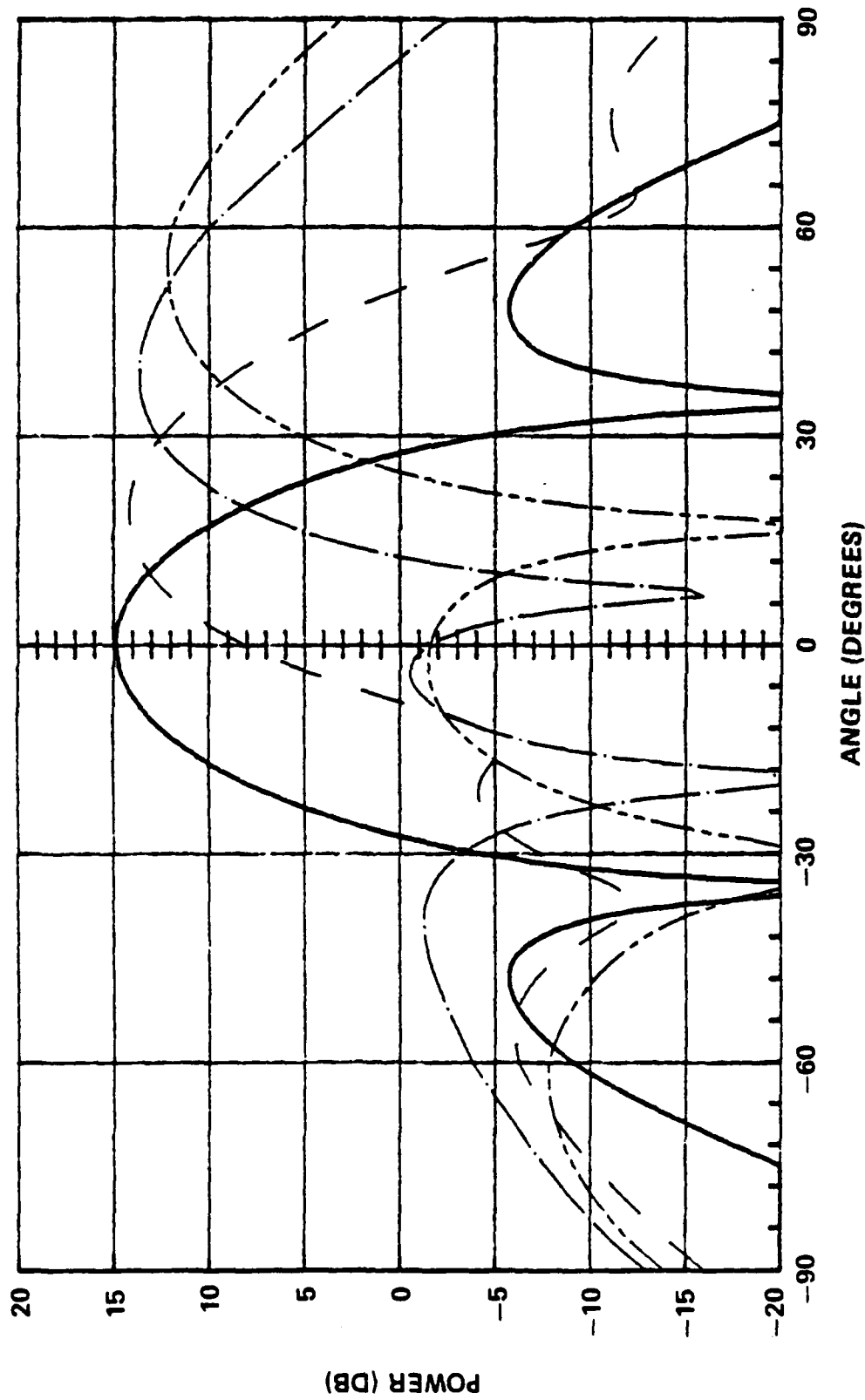
TELEPHONE RYAN ELECTRONICS
E8777

Figure 5. (PORT-STARTBOARD) Elevation Array Pattern at 1660 MHz



TELEDYNE RYAN ELECTRONICS
E8778

Figure 6. (FORE-AFT) Aximuth Array Pattern at 1545 MHz



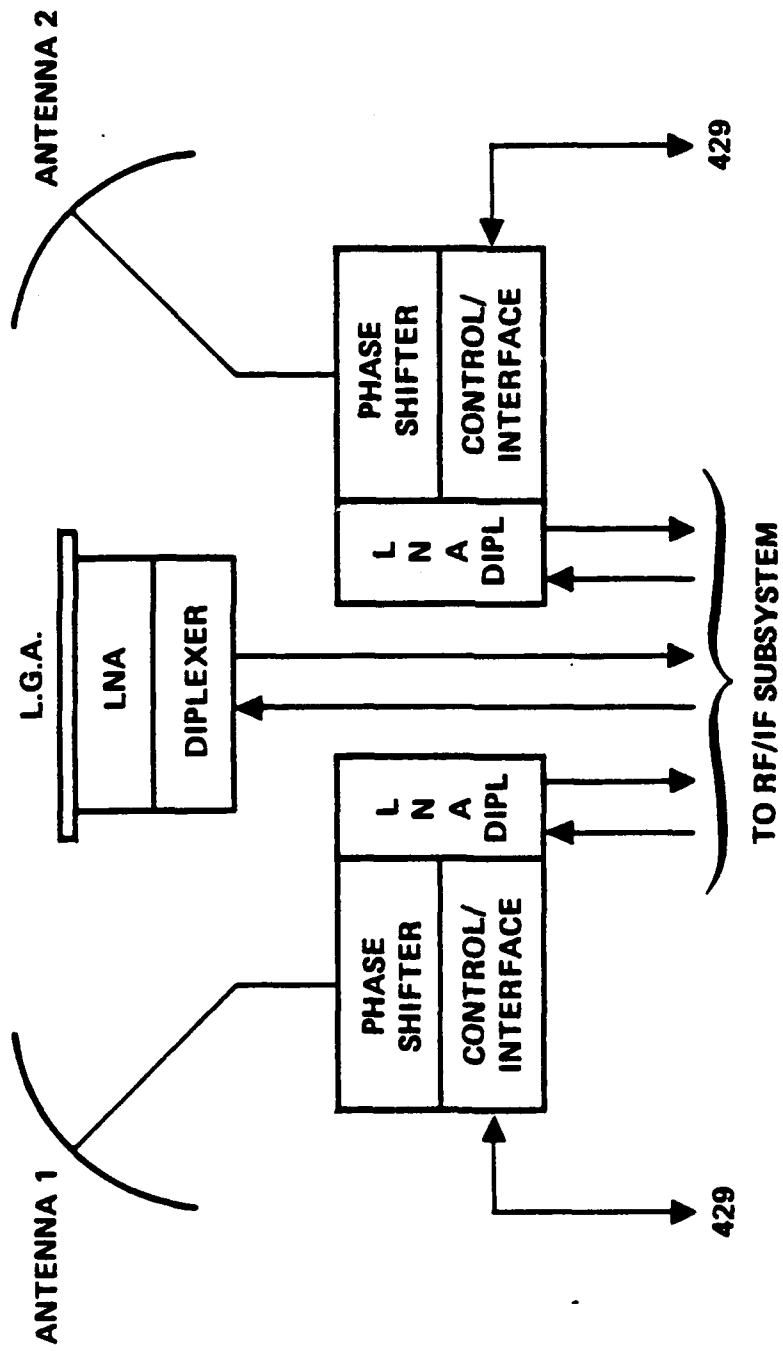
TELEDYNE RYAN ELECTRONICS
ER779

Figure 7. (PORT-STARTBOARD) Elevation Array Pattern at 1545 MHz

suggested that the total LRU (Line Replaceable Unit) will be housed in one electronics box with the phase shifter and electronics control interface for the high gain antennas as shown in Figure 8. To protect electronics circuit and phase shifters, the electronics box will be installed inside the aircraft. Based on the limited drawings obtained for the aircraft structures and overhead luggage compartment, we recommend to mount the electronics box inside the overhead compartment for the ease of maintenance. However, it should be emphasized that the proposed location is only one of many possibilities. For example, for wide body aircrafts, there is sufficient space behind the modified panels where the electronics box can be attached.

The high gain array radiating elements and their associated feed circuit will be mounted on each side of aircraft fuselage with tapered edges and solid grounding to reduce air drag and to protect array from lightning.

The array elements are connected to the beam forming network with a common connector which contains 19 coaxial cables through a common hole with the diameter complying with ARINC 741 Spec. The beam forming network is contained in the electronics box and connected to a diplexer/LNA unit.



TELEDYNE RYAN ELECTRONICS
E8782

Figure 8. Antenna Subsystem Installation Grouping Concept

It should be pointed out that the estimated overall weight for one high gain antenna subsystem is 44.21 lbs. For one array alone is about 20 lbs. It also should be mentioned that the location of the electronic units in the overhead compartment is our preliminary recommendation and will be subjected to change for other better locations.

4.0 CONCLUSIONS

In conclusion, the TRE (Teledyne Ryan Electronics) Antenna Subsystem has the following nice features:

- Desired Array Elements - crossed-slot, which provides better low angle space coverage, low profile (0.4"), low drag, high reliability, low maintenance and low cost.
- Optimized Array Design, which minimized sidelobe level at large scan angles and maximizes intersatellite isolation.
- Minimized Number of LRU, which simplifies installation procedure, reduces installation cost, and provides high maintainability.

ANALYSIS OF FINITE PHASED ARRAYS OF CIRCULAR
MICROSTRIP PATCHES

Manohar D. Deshpande and M. C. Bailey

NASA Langley Research Center, Hampton VA

Abstract:

A method is presented to analyze a finite planar array of circular microstrip patches fed by coaxial probes. The self and mutual impedances between array elements are calculated using the method of moments with the dyadic Green's function for a dielectric layer on a ground plane. The patch currents are determined by using the reaction integral equation. The active input impedance as well as the active element pattern of the arrays are computed from a knowledge of the resultant patch currents.

The calculated results for 2-element and 8-element linear arrays are in good agreement with experimental data. The active reflection coefficient and element pattern for the center and edge elements of a two dimensional planar array as a function of scan angle are also presented.

1.0 Introduction:

Use of phased arrays of printed antennas is becoming increasingly popular mainly due to monolithic MIC concept, where active devices and radiating elements are integrated on the same layer of a dielectric substrate. Recently some attempts have been made to

analyze this new class of phased arrays of printed antennas. The scan blindness in an infinite phased array of printed dipoles were studied in [1] using the moment method. The effects of substrate parameters and grid spacing on the performance of an infinite array of rectangular microstrip patches were reported in [2]. However, the infinite array model is only valid for elements which are well away from the edges of a finite array. Furthermore, the infinite array solution does not account for edge effects of a finite array. Thus the study of finite phased arrays yields more practical information than the study of infinite arrays. Using an element by element approach, various aspects like reflection coefficient, element patterns, effect of dielectric cover and efficiency of finite phased arrays of rectangular microstrip patches are studied in [3,4].

This paper describes a solution to the problem of a finite planar array of circular microstrip patches fed by coaxial probes. The self and mutual impedances between the elements of an array antenna are calculated using moment method. Assuming that only one patch is excited at a time and other feed probes open circuited, the patch currents are determined using a reaction

integral equation in conjunction with the method of moments. Following the principle of superposition, the resultant patch currents when all patches are excited are then calculated. The active input impedance and element pattern of the array are computed from a knowledge of the resultant patch currents. The computed results on the mutual admittance and the mutual coupling between two circular patches are compared with experimental data. The active reflection coefficient and the element pattern as a function of scan angle for four array sizes are computed.

2.0 Theory:

Fig.1 shows the geometry of a finite array of circular microstrip patches excited by coaxial probes. The patches are assumed to be placed in a skewed coordinate system and covered with a dielectric slab of thickness $(d-z')$. The effect of multiple interaction between the radiating patches can be studied from a knowledge of the mutual impedance between the patches. Consider the i^{th} and j^{th} patches as shown in Fig.2. The mutual impedance between these two patches can be expressed as

$$Z_{ij} = \frac{j120\pi\kappa_0 z'}{(2\pi)^2 \epsilon_r \kappa_0^2} \iint \left[F(\beta) \psi_{\beta m} \psi_{\beta n}^* + \epsilon_r \zeta_1(\beta) \psi_{\alpha m} \psi_{\alpha n}^* \right] \cdot e^{j\kappa_0 \rho_{ij} \beta \cos(\phi_{ij} - \alpha)} \beta d\beta d\alpha \dots\dots\dots(1)$$

$$F(\beta) = \left[(\epsilon_r - \beta^2) \zeta_1(\beta) - j(\epsilon_r - 1)\beta^2 \zeta_2(\beta) \right]$$

where $\zeta_1(\beta)$ and $\zeta_2(\beta)$ are defined in [5, eqs. (19) and (20)], $\psi_{\beta m}$ and $\psi_{\alpha m}$ are the radial and circumferential components of the Fourier transforms of m^{th} expansion mode current on the i^{th} patch, $\psi_{\beta n}$ and $\psi_{\alpha n}$ are the components of the Fourier transform of the n^{th} expansion mode current on the j^{th} patch.

Since the microstrip patch is a high Q circuit, near the first resonance the current distribution over the patch can be well approximated by a single dominant mode. However for a circular patch all modes are degenerate, hence the current expansion on the i^{th} patch can be written as

$$\vec{J}(\rho, \phi) = \vec{J}_i(\rho, \phi) + \vec{J}_{ic}(\rho, \phi) \dots\dots\dots(2)$$

where

$$\vec{J}_i(\rho, \phi) = -C_e \hat{i}_i \left[\hat{\rho} \frac{x'_{11}}{a} J_1\left(\frac{x'_{11}\rho}{a}\right) \cos(\phi) - \hat{\phi} \frac{1}{\rho} J_1\left(\frac{x'_{11}\rho}{a}\right) \sin(\phi) \right]$$

$$\vec{J}_{ic}(\rho, \phi) = -C_e \hat{i}_{ic} \left[\hat{\rho} \frac{x'_{11}}{a} J_1\left(\frac{x'_{11}\rho}{a}\right) \sin(\phi) + \hat{\phi} \frac{1}{\rho} J_1\left(\frac{x'_{11}\rho}{a}\right) \cos(\phi) \right]$$

In the above equations $C_e = \sqrt{2/\pi(x'_{11}{}^2 - 1)} \frac{1}{J_1(x'_{11})}$, $J_1'(\cdot)$ is the first derivative of $J_1(\cdot)$, $J_1(\cdot)$ is the Bessel function of first kind of order one, x'_{11} is the first root of $J_1(\cdot) = 0$.

Substituting the Fourier transforms of $J_i(\rho, \phi)$ and $J_{ic}(\rho, \phi)$, the mutual impedances between the patch currents are obtained as

$$Z_{ij} = \frac{-jn_0 k_0 z'}{\epsilon_r} \frac{2}{(x'_{11}{}^2 - 1)} \int_0^\infty \left[F(\beta) \frac{(x'_{11})^4}{(k_0 a)^2} \left[\frac{J_1'(k_0 a \beta)}{(x'_{11}/k_0 a)^2 - \beta^2} \right]^2 S_1 + \epsilon_r \zeta_1(\beta) \left[\frac{J_1(k_0 a \beta)}{\beta} S_2 \right]^2 \right] \beta d\beta \quad (3)$$

$$Z_{ijc} = \frac{jn_0 k_0 z'}{\epsilon_r} \frac{2}{(x'_{11}{}^2 - 1)} \int_0^\infty \left\{ F(\beta) \frac{(x'_{11})^4}{(k_0 a)^2} \left[\frac{J_1'(k_0 a \beta)}{(x'_{11}/k_0 a)^2 - \beta^2} \right]^2 - \epsilon_r \zeta_1(\beta) \left[\frac{J_1(k_0 a \beta)}{\beta} \right]^2 \right\} S_3 \beta d\beta$$

.....(4)
'5'

$$Z_{cjc} = Z_{ij}$$

where

$$S_1 = J_0(k_0 \rho_{ij} \beta) - J_2(k_0 \rho_{ij} \beta) \cos(2\phi_{ij})$$

$$S_2 = J_0(k_0 \rho_{ij} \beta) + J_2(k_0 \rho_{ij} \beta) \cos(2\phi_{ij})$$

$$S_3 = J_2(k_0 \rho_{ij} \beta) \sin(2\phi_{ij})$$

It should be noted that when $j=i, Z_{ijc}=0$.

Let the patch elements be numbered as shown in Fig.1. The column p and row q in the array for the location of the k^{th} element is given by

$$\begin{aligned} p &= 1 + (k-1)/N \\ q &= k - (p-1) \cdot N \end{aligned} \quad \dots \dots \quad (6)$$

For scanning at angle (θ, ϕ) , the probe excitation current at the k^{th} patch should be

$$I_k^p = \text{Exp.} \left[-jk_0 d_x (p-1) + k_0 d_y (q-1) \cos(\alpha_0) \right] u \cdot \text{Exp} \left[-jk_0 d_y (q-1) \sin(\alpha_0) \right] v \quad (7)$$

where $u = \sin(\theta) \cos(\phi)$ and $v = \sin(\theta) \sin(\phi)$

Let the k^{th} patch be excited and the probes at the other patches be open circuited. Now selecting J_j with $I_j=1$ on the j^{th} patch as a test current, the reaction integral equation in conjunction with the moment method yields

$$\sum_{i=1}^{N^2} \left(Z_{ij} I_i^k + Z_{icj} I_{ic}^k \right) + v_j^k = 0 \quad (8)$$

$$\sum_{i=1}^{N^2} \left(Z_{ijc} I_i^k + Z_{icjc} I_{ic}^k \right) + v_{jc}^k = 0 \quad (9)$$

where $j=1, 2, \dots, N^2$, $Z_{ic,j} = Z_{j,ic}$, $v_{jc} = 0$ for all j and v_j^k is zero for all $j \neq k$ and for $j=k$, v_j^k is given by

$$v_k^k = I_k^p \frac{j \eta_0 k_0 z'}{\epsilon_r} \sqrt{\frac{2}{\pi(x_{11}^2 - 1)}} \int_0^\infty \left[\xi_1 - j(\epsilon_r - 1) \xi_2 / \beta^2 \right] \beta^2 d\beta$$

$$\frac{x_{11}^2}{k_0^2} \left[\frac{J_1'(k_0 a \beta)}{(x_{11}^2 / k_0^2) - \beta^2} \right] J_1(k_0 a \beta) J_0(k_0 d_0 \beta / 2) \quad (10)$$

The equations (8) and (9) can be solved for the unknown patch currents $I_1^k, I_2^k, \dots, I_{N^2}^k$ and $I_{1c}^k, I_{2c}^k, \dots, I_{N^2c}^k$ due to excitation at the k^{th} patch. Using the

principle of superposition, the resultant current on the i^{th} patch when all patches are excited is obtained as

$$I_i = \sum_{k=1}^{N^2} I_i^k \quad (11)$$

$$I_{ic} = \sum_{k=1}^{N^2} I_{ic}^k \quad (12)$$

(a) Active Input Impedance:

Using eqns.(10) and (12), the active input impedance at the i^{th} patch is then obtained from

$$Z_{in}^i(\theta \phi) = \frac{V_i^i I_i}{|I_i^p|^2} + jX_L \quad (13)$$

where X_L is the probe reactance. The input reflection coefficient at the i^{th} patch can be calculated from

$$R(\theta \phi) = \frac{Z_{in}^i(\theta \phi) - Z_{in}^i(0 \ 0)}{Z_{in}^i(\theta \phi) + Z_{in}^{i*}(0 \ 0)} \quad (14)$$

where * indicates complex conjugate.

(b) Active Element Pattern:

The active element pattern of the i^{th} element is obtained by considering the probe excitation at the i^{th} patch only (i.e. $I^p=1$ amp.). The eqns.(8)-(9) are then solved for the patch currents I_j . The element

pattern of the i^{th} patch is obtained in the form

$$\vec{E}^i(\theta, \phi) = \vec{E}_0(\theta, \phi) \sum_{j=1}^N I_j^i \begin{matrix} \text{Exp. } [jk_0 d_x (p-1) + d_y (q-1) \cos(\alpha)] u. \\ \text{Exp. } [jk_0 (q-1) d_y \sin(\alpha)] v. \end{matrix} \quad (15)$$

where $E_0(\theta, \phi)$ is the radiation pattern of the isolated patch.

3.0 Results & Discussion:

In order to verify the present theory, a few examples for which the results are already available are considered first.

(a) Mutual Admittance between two Circular Patches:

Using expression (3), the mutual and self impedances between two circular patches with dimensions as shown in Fig.3 are computed. The normalized mutual admittance calculated using

$$Y_{12} = \frac{Z_{12}}{Z_{11}} \quad (16)$$

is plotted in Fig.3 along with the experimental results [6]. Note that expression (16) is independent of the probe position and its dimensions. However the probe dimensions are taken into account by following the method given below. For a two-element array antenna eqns.(8)-(9) reduce to

$$\begin{aligned} Z_{11} I_1^1 + Z_{12} I_2^1 + V_1^1 &= 0 \\ Z_{21} I_1^1 + Z_{22} I_2^1 &= 0 \end{aligned} \quad (17)$$

In eq.(17) it is assumed that only patch # 1 is excited. The port impedance matrix is then obtained as

$$[Z^P] = -(V_1^1)^2 [Y] \quad (18)$$

where

$$[Y] = \begin{bmatrix} Z_{11} & Z_{12} \\ Z_{21} & Z_{22} \end{bmatrix}^{-1} \quad (19)$$

The normalized mutual admittance is calculated from a knowledge of the port impedances by using

$$Y_{12} = \frac{Z_{12}^p}{Z_{11}^p} \quad (20)$$

and is plotted in Fig.4 along with the results reported earlier [6]. From Figs.3-4 it should be noted that inclusion of the probe in the formulation gives closer agreement with the experimental results. Using eq.(20), the mutual admittance in the H-plane is also calculated and presented in Fig.5 along with the experimental data [6].

(b) Mutual Coupling between two Circular Patches:

A scattering matrix for a two-element array is given by

$$[S] = [Z^P + Z_C][Z^P - Z_C]^{-1} \quad (21)$$

Where

$$[Z_c] = \begin{bmatrix} Z_0 & 0 \\ 0 & Z_0 \end{bmatrix}$$

Using eqn.(21), S_{12} is computed for E- and H-planes and presented in Fig.6 along with the experimental results [7].

(c) Mutual Coupling in 8-Element Linear Array:

Extending the analysis to an 8-element linear array of circular patches, mutual coupling for the E-and H-planes are computed and compared with the experimental data [7] in Fig.7. There is good agreement between the mutual coupling calculated by the present method and the experimental data as far as the E-plane is concerned. However the results for the H-plane coupling could not be compared with experimental results due to non-availability of measured data.

(d) Reflection Coefficient & Element Pattern of Two dimensional Planar Array:

Figs.8-10 show computed results for the active reflection coefficient and element pattern of finite arrays on a dielectric substrate with $\epsilon_r = 2.5$, $\tan(\delta) = 0.002$, $d = z' = 0.16\text{cm}$, $d_x = d_y = 2.66\text{cm}$, $\alpha_0 = 90^\circ$, $f_0 = 5.6375$

GHz. The reflection coefficient magnitude versus scan angle for the center element of four different array sizes (3X3, 5X5, 7X7, and 11X11) are computed for three principal planes (E-, H- and D-planes) and presented in Figs. 8(a) - 8(c). For comparison the reflection coefficient magnitude for an infinite array is also presented in Figs. 8(a) - 8(c). It is observed that at small scan angles there are ripples in the curves for the finite arrays. The number of ripples increase with the array size. The active reflection coefficient magnitude for several off centered elements is also presented in Fig. 9.

Using expression (15), the active element pattern of center element for four different array sizes is computed and presented in Fig. 10. It is observed that there are few ripples in the element pattern. These ripples may be attributed to the constructive and destructive interference between the elements of the finite array.

4.0 Conclusion:

An element by element approach has been used to analyze a finite array of circular patches. Assuming

the current distribution of TE_{11} and TE_{11c} type on the circular patches, expressions for the active reflection coefficient and element pattern are obtained. The experimental data for two element and 8-element linear arrays has been compared with the calculated results. Numerical data on the active reflection coefficient and element pattern for various array sizes have been presented and compared with the results for an infinite array antenna. From these results it may be concluded that a finite array of size (7X7) or more may well be approximated by an infinite array.

5.0 References:

1. D. M. Pozar & D. H. Schaubert (1984). Scan blindness in infinite phased arrays of printed dipoles, IEEE Trans. AP-32(No.6):602-610.
2. -----(1984), Analysis of an infinite array of rectangular patches with idealized probe feeds, IEEE Trans. AP-32(No.10):1101-1107
3. D. M. Pozar(1986), Finite phased arrays of rectangular microstrip patches, IEEE Trans. AP-34(No.5) (No.5):658-665
4. M. D. Deshpande and P. D. Prabhakar, Analysis

of dielectric covered infinite array of rectangular patches, IEEE Trans.AP. to appear.

5. M. C. Bailey and M. D. Deshpande(1982), Integral equation formulation of microstrip antennas, IEEE Trans.AP-30, (No.4) :651-656.
6. Misao Haneishi, et.al.(1981) ,A design of back feed type circularly polarized microstrip disk antenna having symmetrical perturbation element by one point feed, Electronics and Comm. in Japan, Vol.64, (No-7) :52-60
7. M. C. Bailey and P. G. Parks(1978) Design of microstrip disk antenna arrays, NASA Technical Memorandum, 78631.

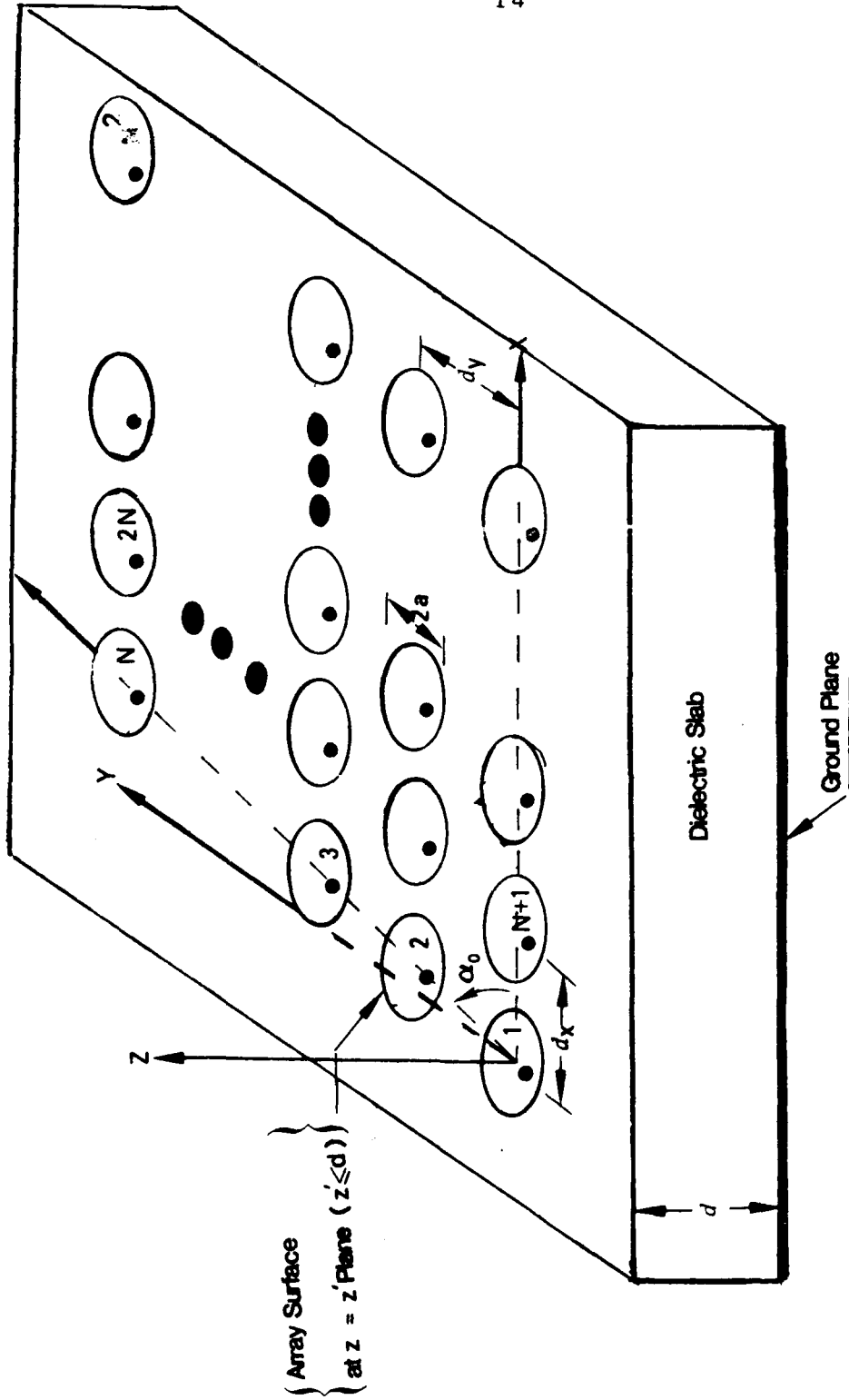


Fig.1 Geometry of Finite Array of Circular Microstrip Patches.

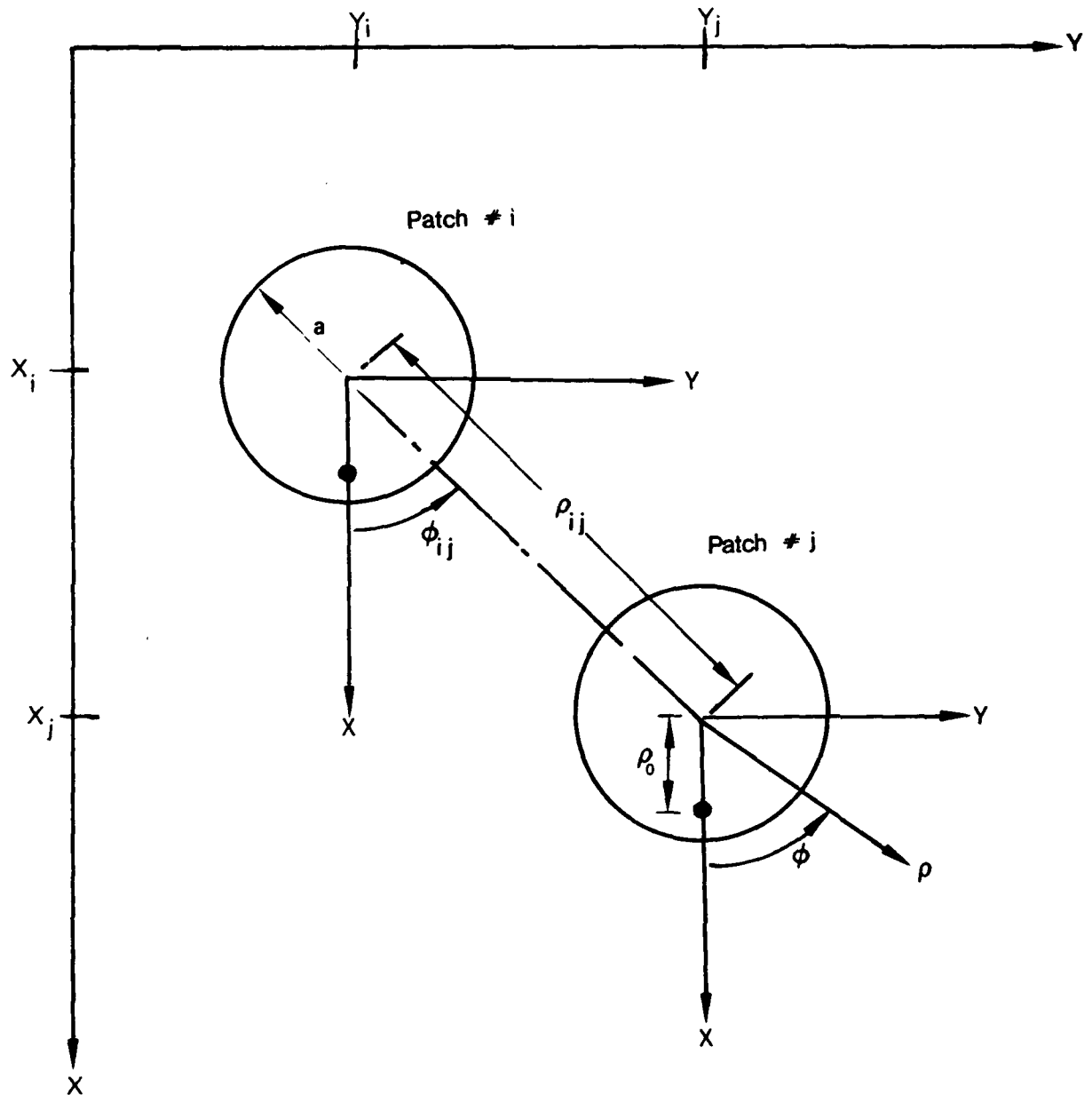


Fig 2 Geometry of i^{th} and j^{th} Patches.

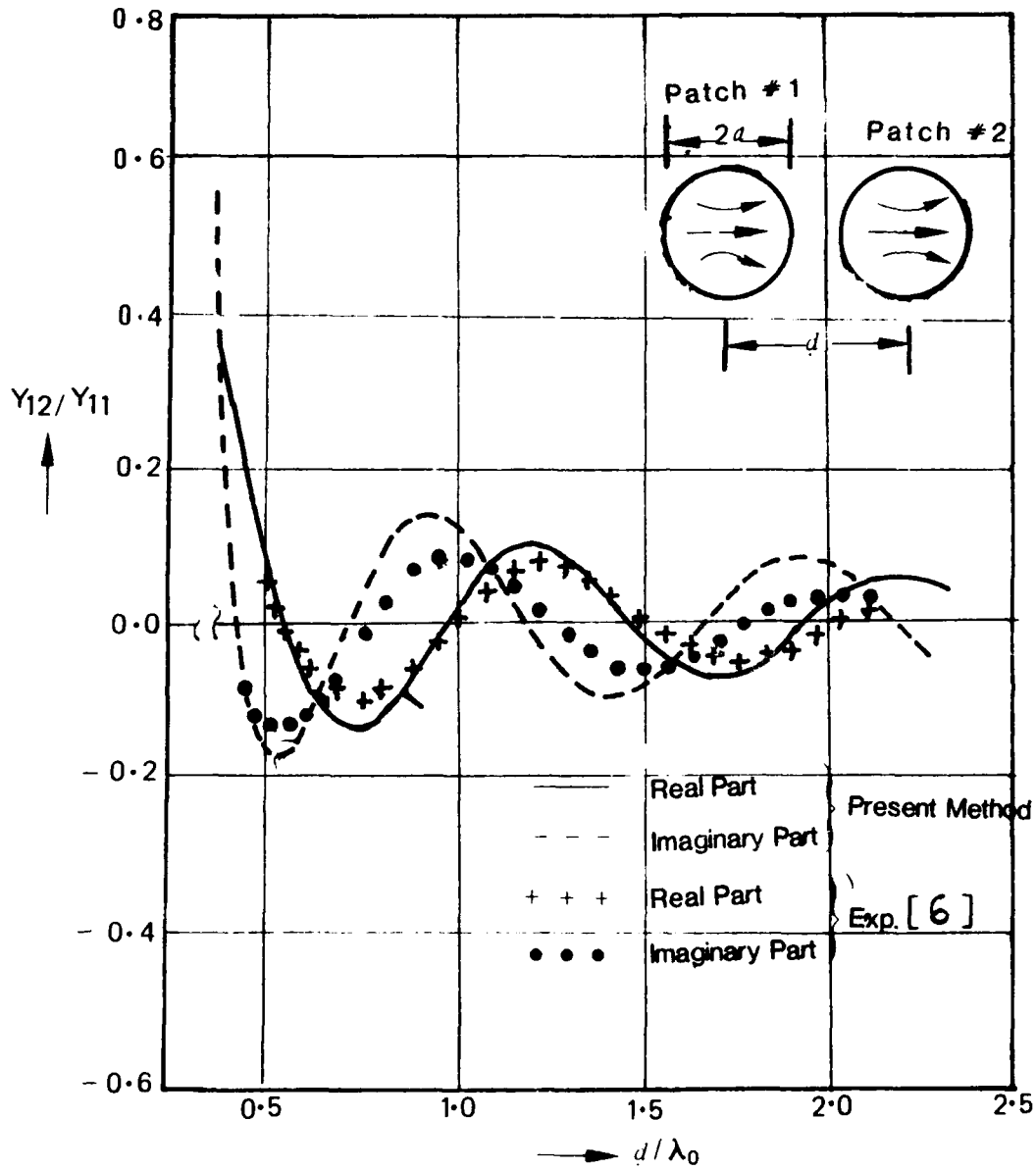


Fig.3 E-Plane Mutual Admittance between two Microstrip Disk Antennas with $2a = 1.01$ cms,
 $d = z' = 0.118$ cms, $\epsilon_r = 2.55$, $\tan(\delta) = 0.002$, $R_0 = 0.11$ cms (Probe effect not included)

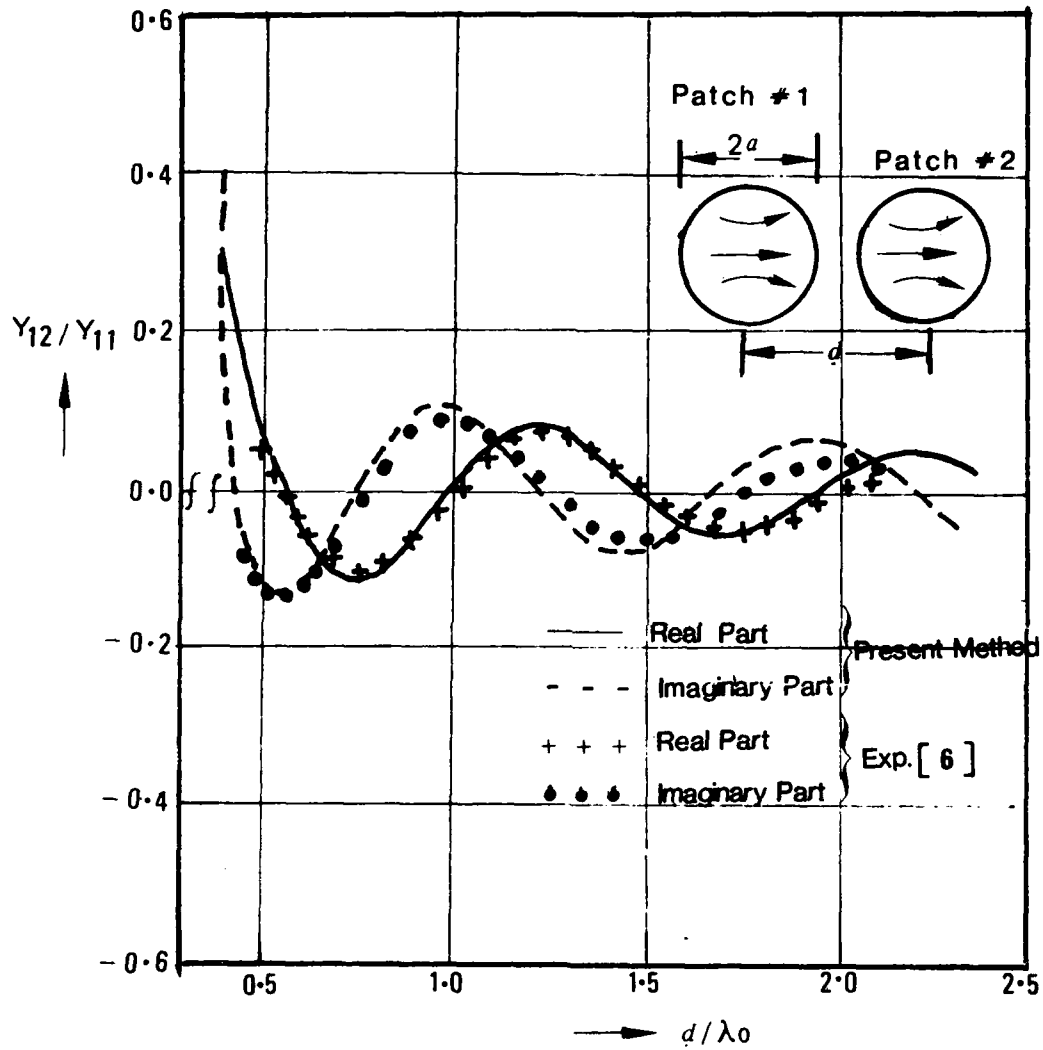


Fig.4 E-Plane Mutual Admittance between two Microstrip Disk Antenna with $2a=1.01$ cms;
 $d = z' = 0.118$ cms, $\epsilon_r = 2.55$, $\tan(\delta) = 0.002$, $\rho_0 = 0.11$ cms (Probe effect included)

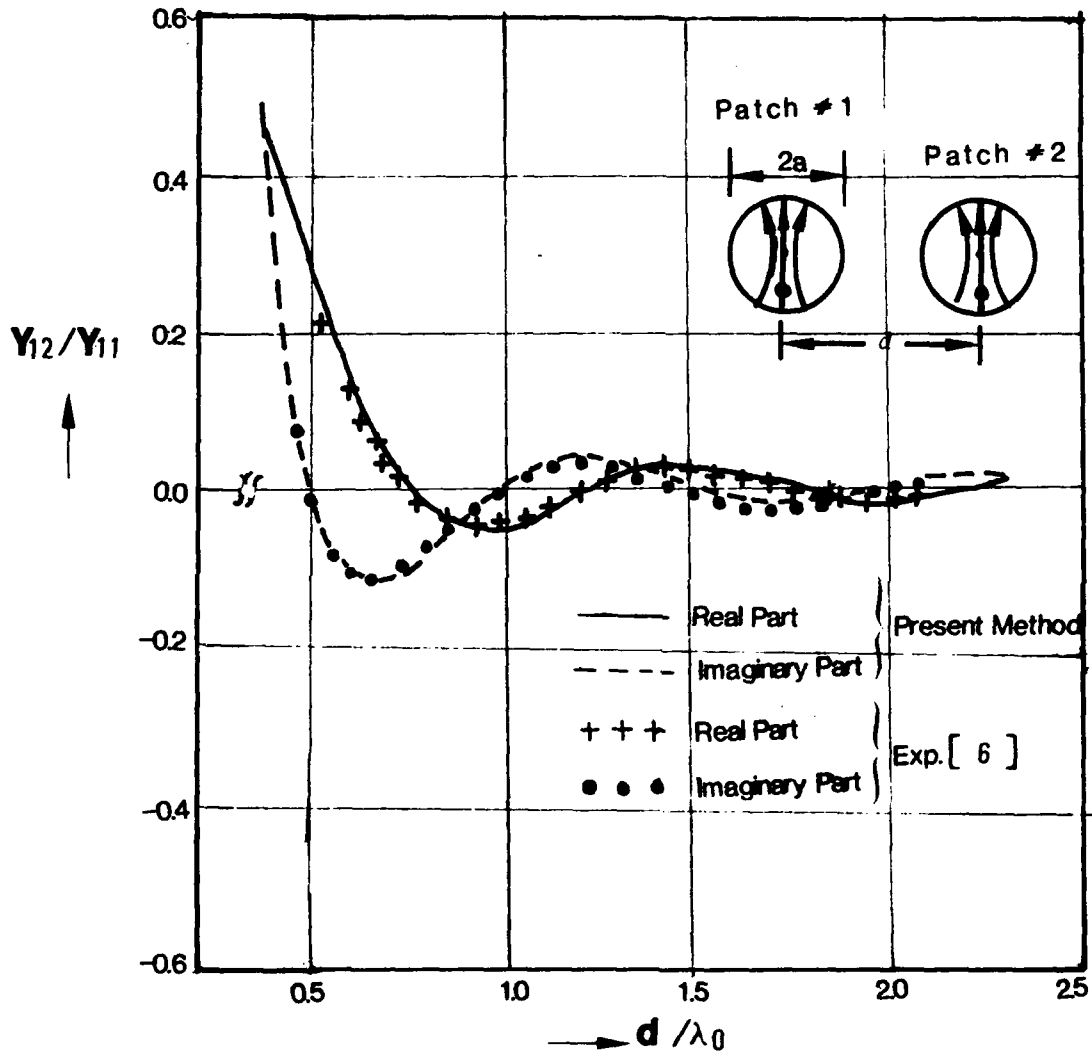


Fig.5 H-Plane Mutual Admittance Between two Microstrip Disk Antennas with $2a = 1.01$ cms.

$d = z' = 0.118$ cms, $\epsilon_r = 2.55$, $\tan(\delta) = 0.002$, $\rho_0 = 0.11$ cm

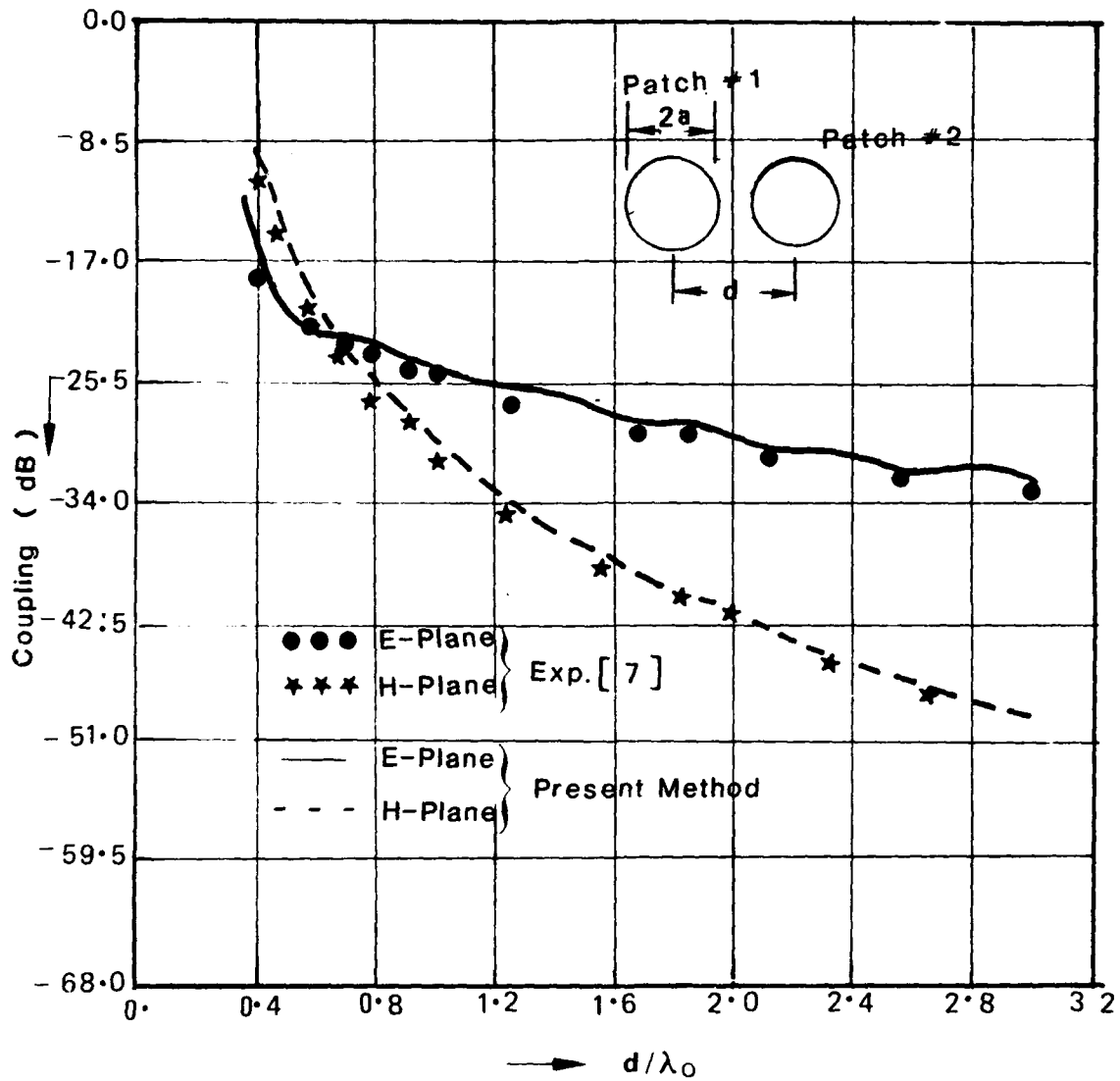


Fig. 6 Mutual Coupling between two Circular Microstrip Disk Antennas with dimensions $2a = 1.86$ cms, $d = z' = 0.16$ cms, $\epsilon_r = 25$, $\tan(\delta) = 0.002$

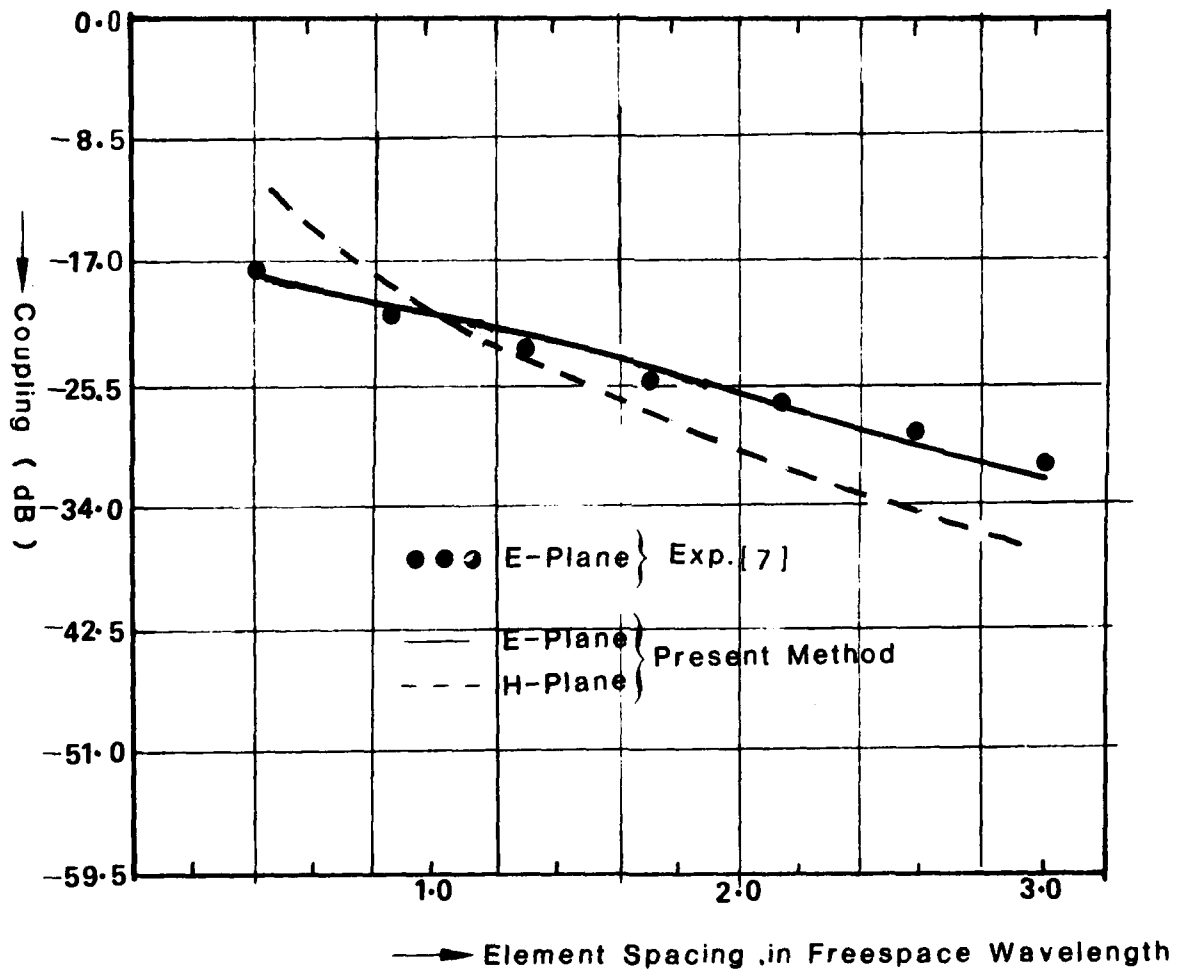


Fig.7 Mutual Coupling between the Elements of an 8-Element Linear Microstrip Disk Array with left most Element Excited and $2a = 1.86$ cms. $d = z = 0.16$ cms. $\epsilon_r = 2.5$, $\tan(\delta) = 0.002$, $f_0 = 5.6375$ GHz. l Element Spacing = 2.24 cms.

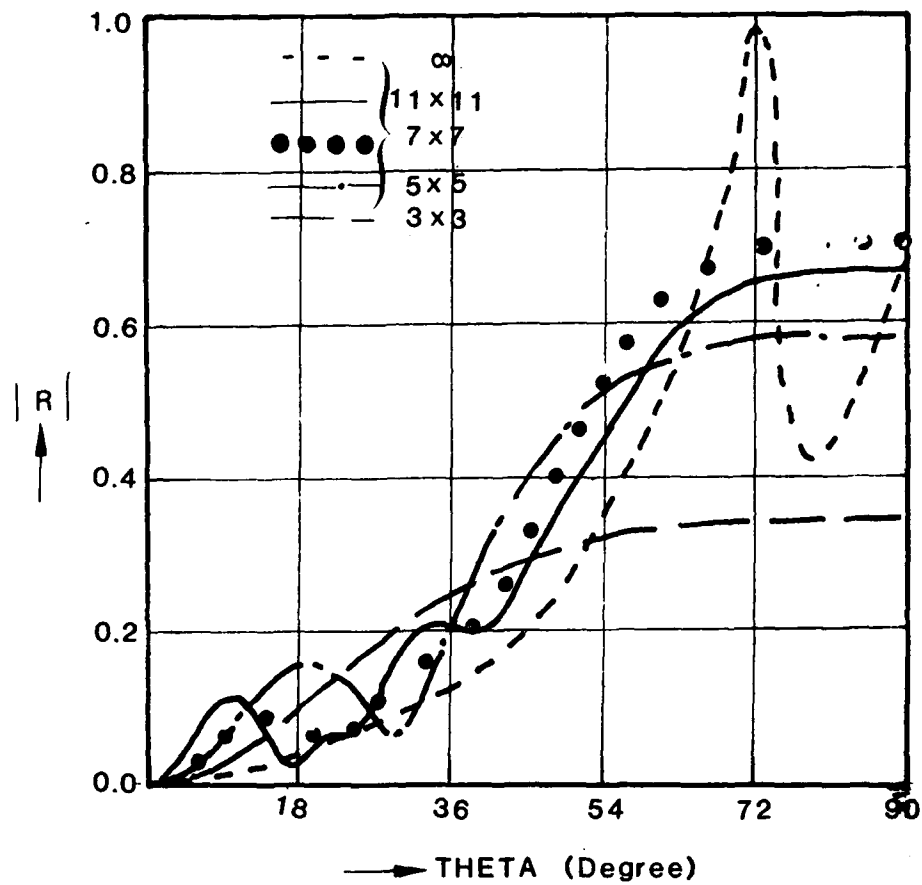


Fig. 8(a) E-plane reflection coefficient magnitude versus scan angle for patch arrays of various sizes. $2a = 1.86\text{cm}$, $d = z' = 0.16\text{cm}$, $\epsilon_r = 2.5$, $\tan(\delta) = 0.002$, $\rho_0 = 0.193\text{cm}$.

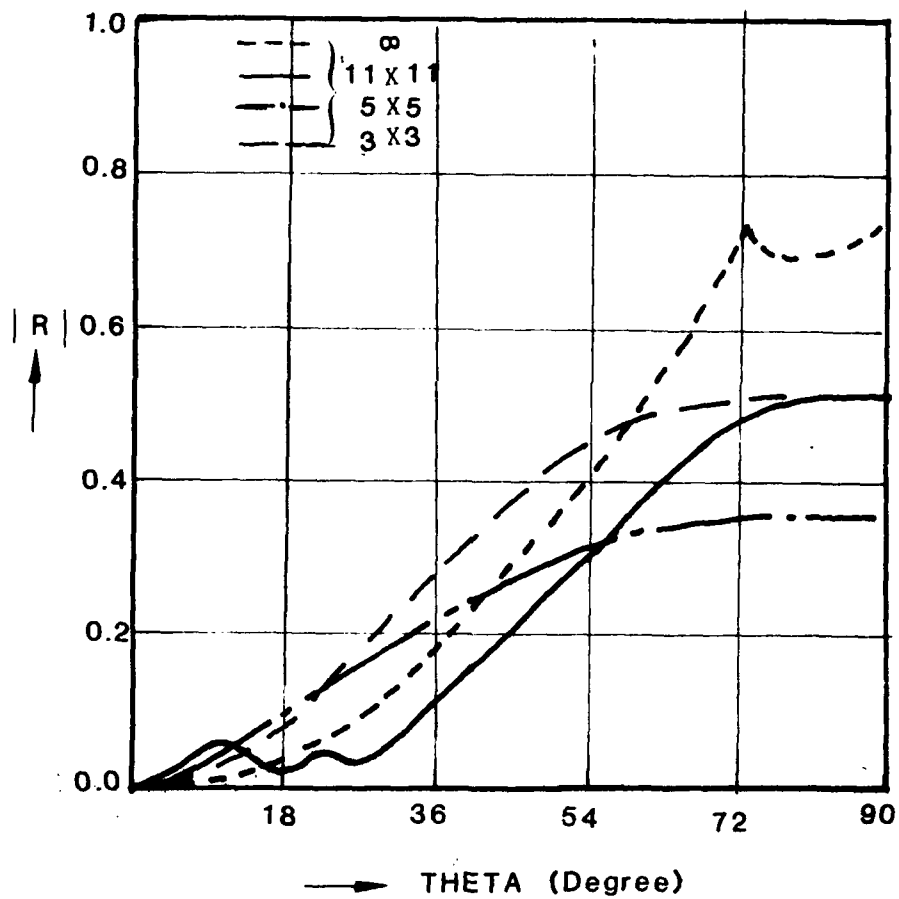


Fig.8(b) H-plane reflection coefficient magnitude versus scan angle for patch arrays of various sizes. $2a = 1.86\text{cm}$, $d = z' = 0.16\text{cm}$, $\epsilon_r = 2.5$, $\tan(\delta) = 0.002$, $\rho_o = 0.193\text{cm}$.

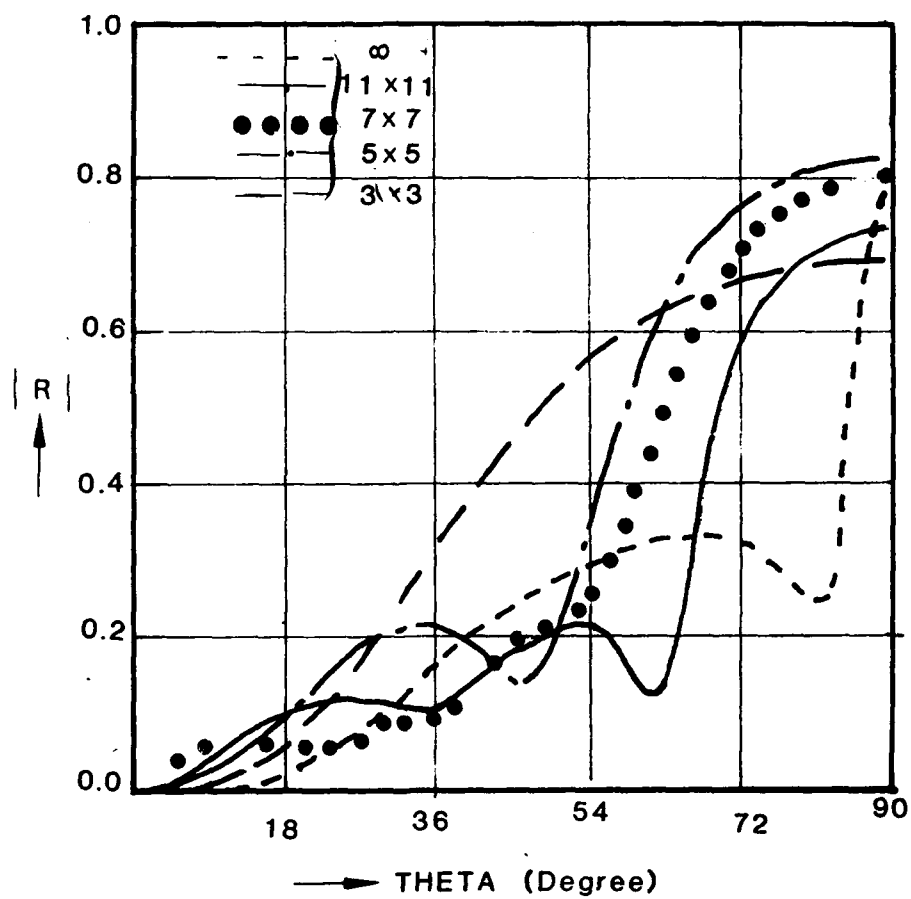


Fig.8(c) D-plane reflection coefficient magnitude versus scan angle for patch arrays of various sizes. $2a = 1.86\text{cm}$, $d = z' = 0.16\text{cm}$, $\epsilon_r = 2.5$, $\tan(\delta) = 0.002$, $\rho_o = 0.193\text{cm}$.

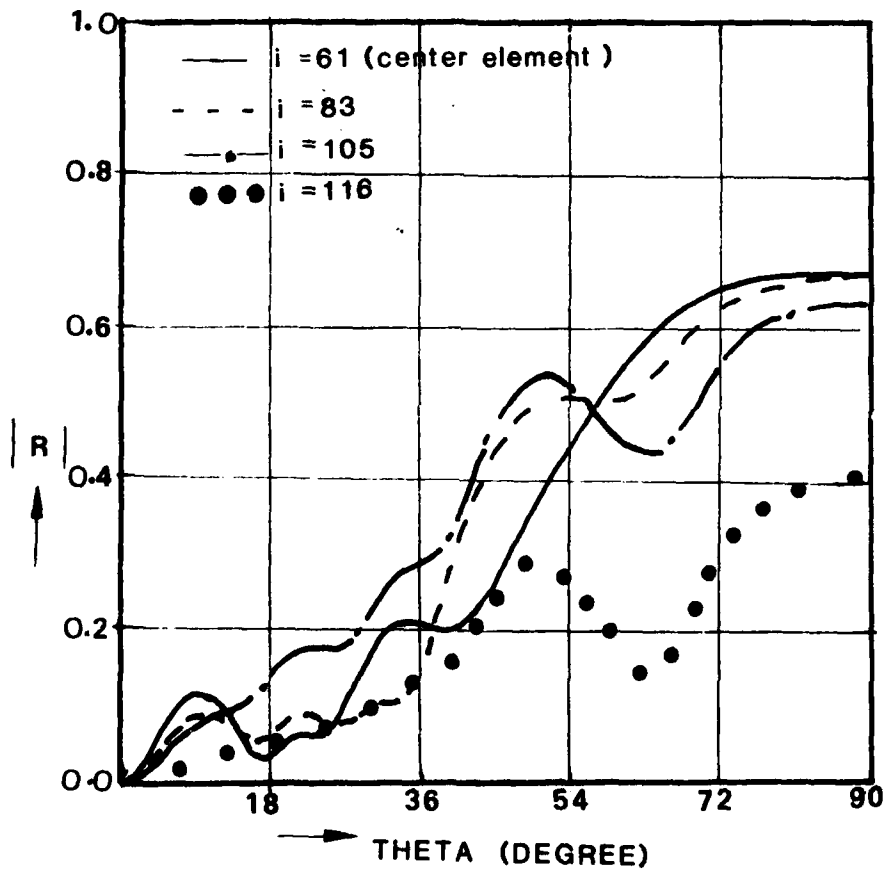


Fig.9(a) E-Plane, reflection coefficient magnitude versus scan angle for various elements of a finite 11×11 patch array. $2a = 1.86\text{cms}$, $d = z' = 0.16\text{cms}$, $\epsilon_r = 2.5$, $\tan(\delta) = 0.002$, $\rho_0 = 0.193\text{cms}$.

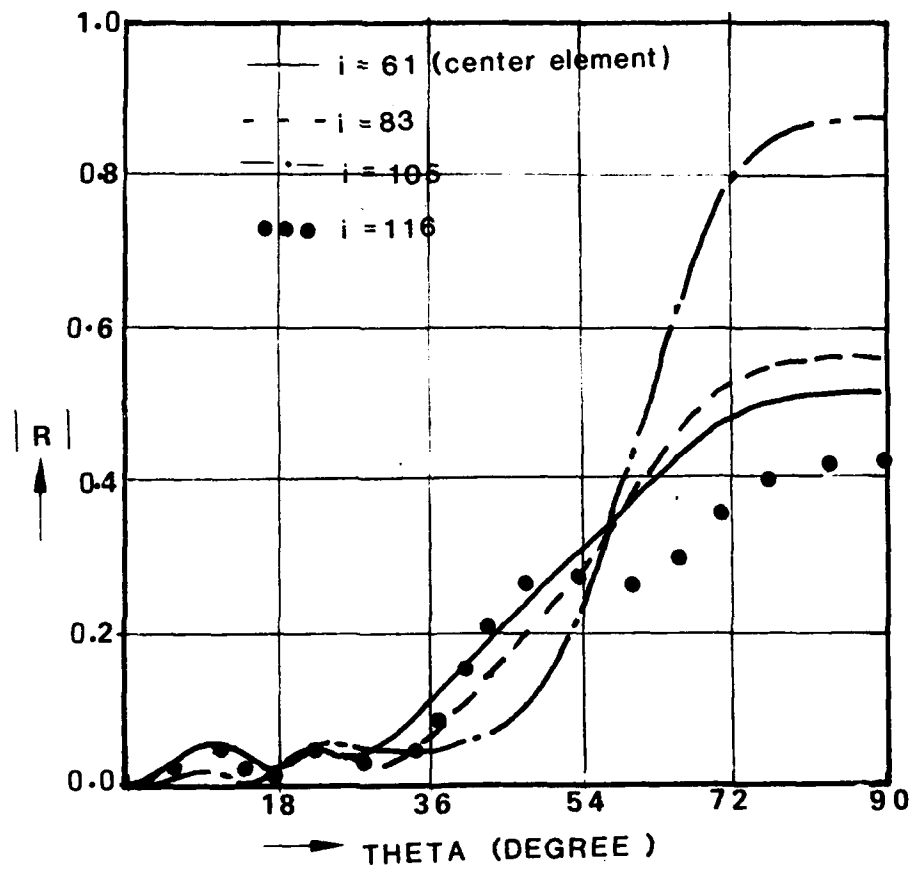


Fig.9(b) H-Plane reflection coefficient magnitude versus scan angle for various elements of a finite 11×11 patch array. $2a = 1.86$ cms. $d = z = 0.16$ cms. $\epsilon_r = 2.5$. $\tan(\delta) = 0.002$. $\rho_0 = 0.193$ cms.

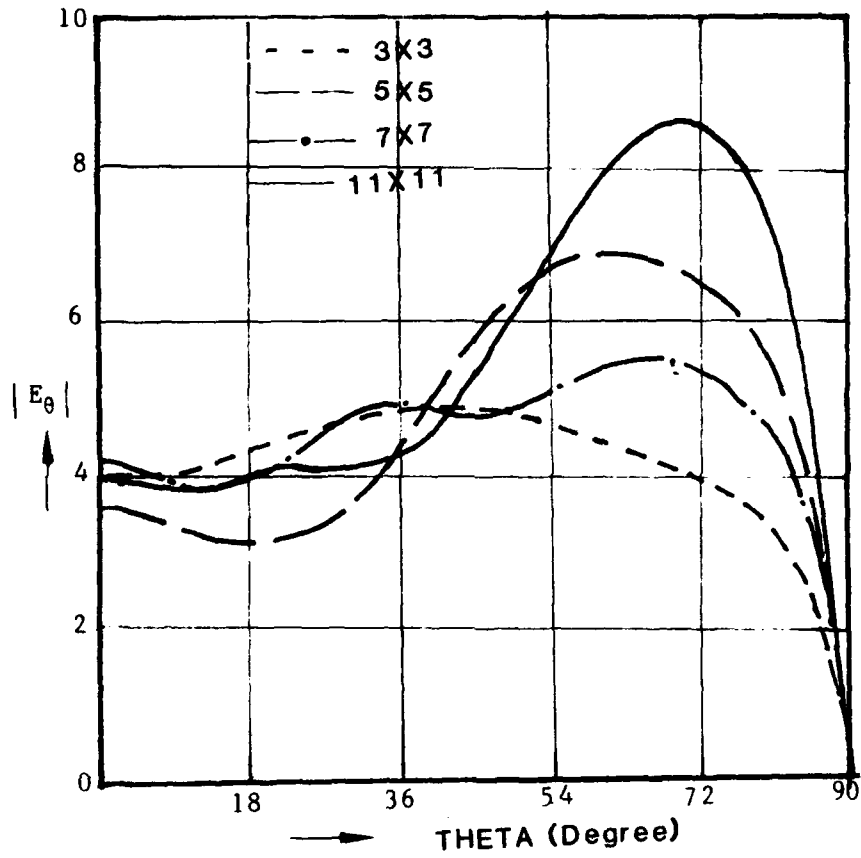


Fig. 10(a) E-plane active element pattern for patch arrays of various sizes. $d_x = d_y = 2.66 \text{ cm}$, $\alpha_0 = 90^\circ$, $2a = 1.86 \text{ cm}$, $d = z = 0.16 \text{ cm}$, $\epsilon_r = 2.5$, $\rho_0 = 0.193$.

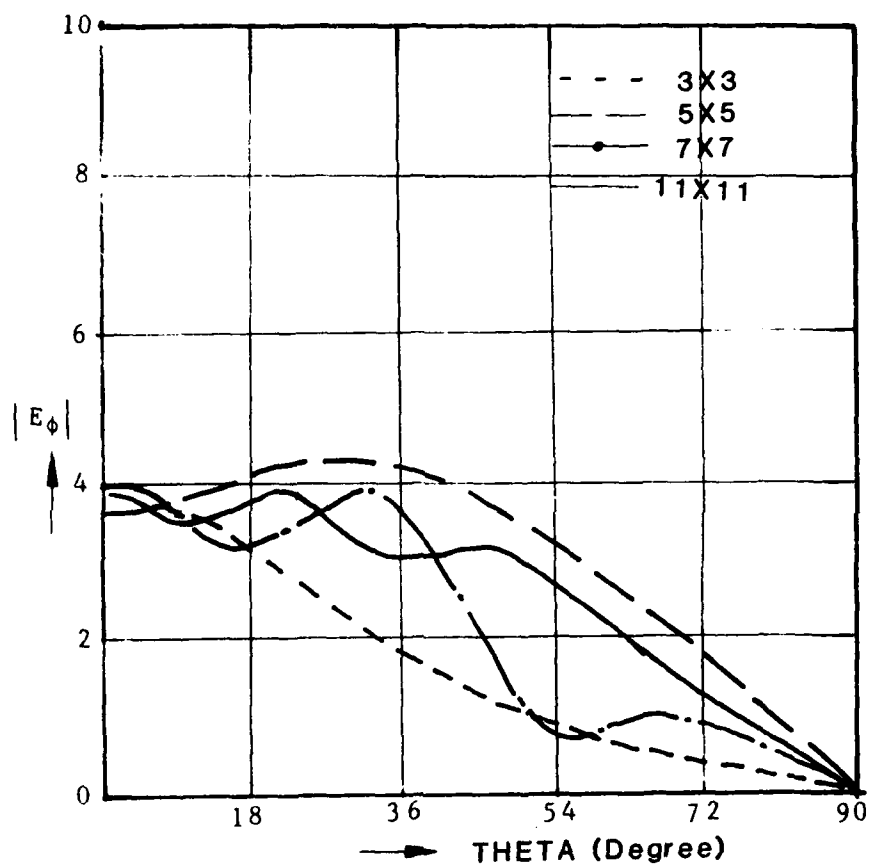


Fig.10(b) H-plane active element pattern for patch arrays of various sizes. $d_x=d_y=2.66\text{cm}$, $\alpha_0=90^\circ$, $2a=1.86\text{cm}$, $d=z=0.16\text{cm}$, $\epsilon_r=2.5$, $\rho_0=0.193\text{cm}$.

AN EXPERIMENTAL INVESTIGATION OF PARASITIC
MICROSTRIP ARRAYS

by
Richard Q. Lee and Roberto Acosta
NASA Lewis Research Center
Cleveland, Ohio 44135

J.S. Dahele
School of Electrical Engineering and Science
Royal Military College of Science
United Kingdom

K.F. Lee
Department of Electrical Engineering
The University of Akron, Akron, Ohio 44325

Abstract

The characteristics of a parasitic microstrip antenna array with a center-fed patch are experimentally investigated. The parasitic array is composed of identical parasitic patches which are symmetrically arranged and electromagnetically coupled to a center-fed patch. The shape and dimensions of the parasitic patches and their positions relative to the center-fed patch are parameters in the study. To show mutual coupling effects between radiating and nonradiating edges of adjacent patches, the impedance and radiation characteristics of a three-element parasitic array excited with (0,1) mode are examined, and compared to that of a single patch. Experimental data indicate that the presence of parasitic patches has significant effects upon the gain, resonant frequency and impedance bandwidth of the array.

Introduction

Using parasitic elements to enhance the bandwidth of a microstrip antenna patch have been studied by numerous researchers.¹⁻³ The antenna configurations generally consist of a center-fed patch with one or more adjacent parasitic patches of different resonant lengths. Such an arrangement improves the bandwidth, but is usually accompanied by a degradation of the pattern characteristics over the impedance bandwidth of the antenna.¹⁻²

Very little work has been reported in the literature regarding the use of parasitic elements to enhance the gain of the antenna. Entschladen and Nagel⁴ showed experimentally that enhancement in gain can be achieved with parasitic patches of identical sizes. This conclusion is supported by a theoretical model of Lee et al.,⁵ who also point out the potential advantages of using parasitic subarrays as the basic unit for a large antenna array with MMIC (monolithic microwave integrated circuit) phase and amplitude controls.

The aim of this paper is to present some experimental results of impedance and radiation characteristics for a center-fed parasitic antenna array with identical parasitic elements.

Experimental Results

In the experiment, three antenna configurations were tested: a five-element cross (Fig. 1(a)), a three-element and a seven-element linear array of square and rectangular patches (Fig. 1(b)).

The rectangular patch having dimensions $a = 0.78$ cm and $b = 0.519$ cm was etched on a Cufion substrate with $\epsilon_r = 2.17$, and the 2 by 2 cm square patch was etched on a fibreglass substrate with $\epsilon_r = 4.1$. In both cases, only the center patch was driven via a coaxial feed.

First, the impedance characteristics of a three-element square patch array consisting of a center-fed patch and two adjacent parasitic patches were investigated. The feed location was confined to the center-line along the y -axis at a distance, y_0 , from the edge (Fig. 2) to ensure a single mode (TM_{01}) operation. For this feed position, the edges along the x -axis correspond to the radiating edges. The antenna configurations of Fig. 2(b) and (c) were tested to study the electromagnetic coupling between the radiating and the nonradiating edges respectively. In general, the parasitic elements enhance the impedance bandwidth as clearly indicated in the resistance curves (b) and (c) of Figure 2. The interaction is stronger between the nonradiating edges than the radiating edges. As a consequence, the impedance bandwidth of Fig. 2(c) is considerably broader compared with the bandwidth of Fig. 2(b), and is more than double the bandwidth of a single antenna. For the antenna configuration (c), the measured resonant frequency is about 3.46 GHz, and the impedance bandwidth with 10 dB return loss is about 6 percent.

The impedance loci for a five-element cross and a three-element linear parasitic array of rectangular patches are displayed on Smith chart in Figure 3. All patches are etched on 10 mil Cufion substrates with 0.08 cm element spacing. Figure 3 shows that the presence of parasitic patches introduces loops in the impedance loci. The loop decreases in size and eventually degenerates into a cusp as the coupling between the parasitic patches and the driven patch is reduced. As indicated in curve (c) for the five-element cross, the impedance locus shows a large loop indicating a strong interaction between the nonradiating edges; a small loop and a cusp from weak coupling between the radiating edges. The appearance of the loops suggests that the parasitic elements behave like coupled multiple tuned circuits. Figure 4 shows the impedance loci for a five-element cross and a three-element linear parasitic array of rectangular patches etched on a 30 mil Cufion substrate with 0.25 cm element spacing. Because of wider spacing and lower antenna Q associated with thicker substrates, the parasitic effect on the impedance characteristics is small. In Figures 3 and 4, the impedance loci for a single patch are also included for comparison purpose.

For antenna configurations of 3, 5, and 7 rectangular elements etched on 10 mil Cufion substrates, the results of the gain and pattern measurements are summarized in Table 1 for the lowest mode (TM_{01}). As noted before, the presence of parasitic elements

shifts the resonant frequency slightly. The increase in gain and decrease in beamwidth are quite obvious. This happens because the parasitic elements derive energy from the excited patch through near field coupling, and re-radiate as discrete elements in an array. The interaction is stronger for closer spacing, as is evident from the data for $d = 0.24$ cm and $d = 0.08$ cm. For $d = 0.08$ cm, the gain increases from the single patch value of 4.9 to 8.6 db for the five-element cross and to 10 db for the seven-element linear array. The 3 db beamwidths are 50° by 55° and 80° by 16° respectively compared with 100° by 80° for the single patch.

The H and E plane patterns for the antenna configurations of Figure 1 were measured. The patterns for the thin rectangular patch (10 mil) with $d = 0.08$ cm are shown in Figures 5 and 6, and the patterns for the thick rectangular patches (30 mil) with $d = 0.08$ and $d = 0.25$ cm are shown in Figures 7 to 10. The patterns of the single patches are also provided for comparison. It appears that the presence of identical parasitic elements does not cause any serious degradation in the radiation patterns.

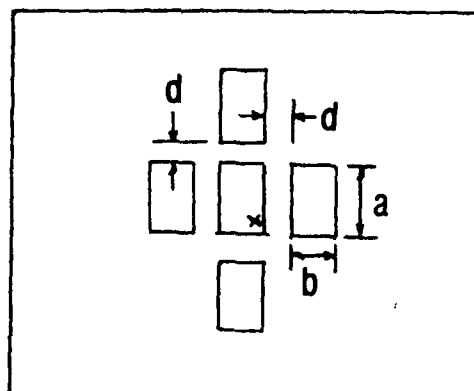
Conclusions

Experimental results indicate that, by placing identical parasitic patches adjacent to a driven patch, a broadside radiation pattern with significant enhancement in gain is obtained without any degradation of the pattern characteristics. The

impedance bandwidth is also broadened considerably, particularly, when the coupling is between the nonradiating edges of the antennas. The presence of parasitic elements introduces loops in the impedance loci, and thus, the parasitic elements act like coupled multiple tuned circuits. The loop reduces in size, and degenerate into a cusp as a result of weak coupling with wider element spacing and lower antenna Q. In general, the presence of parasitic patches alters the resonant frequency and the input impedance of the antenna.

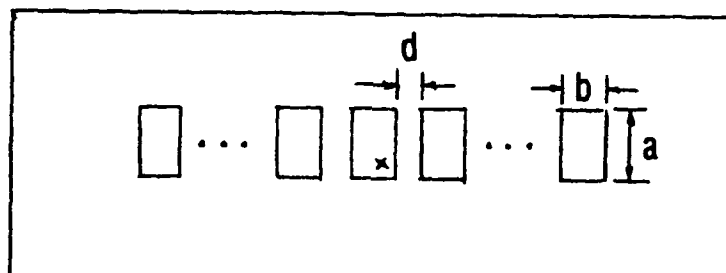
TABLE 1. - RADIATION CHARACTERISTICS OF MICROSTRIP
ARRAYS WITH PARASITIC ELEMENTS

Antenna configuration	Interelement spacing $d = 0.25$ cm			Interelement spacing $d = 0.08$ cm		
	Resonant frequency, GHz	Gain, dB	3 dB beamwidths, deg	Resonant frequency, GHz	Gain, dB	3 dB beamwidths, deg
Single patch	12.7	4.9	100 x 80	12.7	4.9	100 x 80
3 element linear array	12.98	7.0	100 x 60	12.95	8.1	95 x 47
7 element linear array	12.84	7.8	81 x 57	13.0	10.0	80 x 16
5 element cross	12.87	6.5	100 x 60	13.19	8.6	50 x 55



(A) 5-ELEMENT CROSS.

x - COAXIAL FEED



(B) 3 AND 7-ELEMENT LINEAR ARRAY.

FIGURE 1. - GEOMETRIES OF (A) A 5-ELEMENT CROSS AND (B) A 3 AND 7-ELEMENT LINEAR ARRAY FOR: $\epsilon_r = 2.17$,
 $a = 0.78$ cm, $b = 0.519$ cm, $d = 0.08$ cm
 AND 0.25 cm.

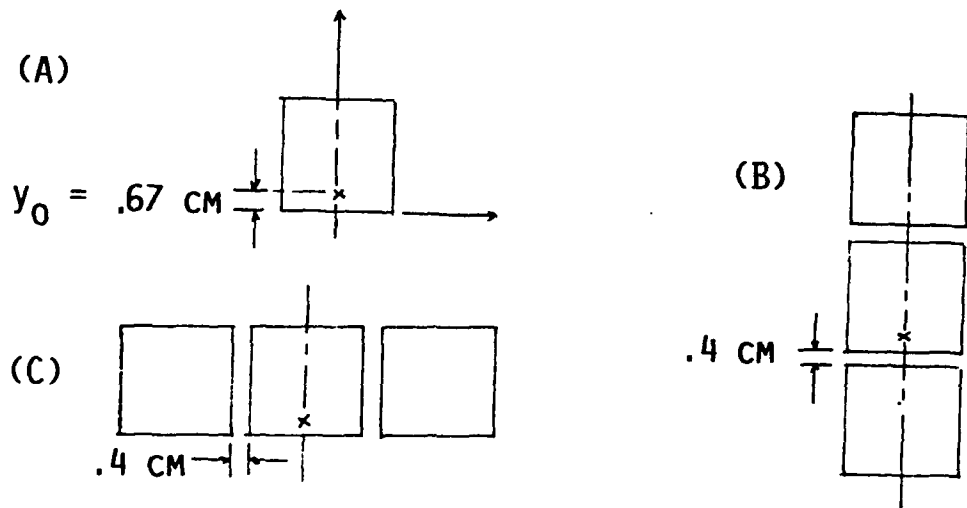
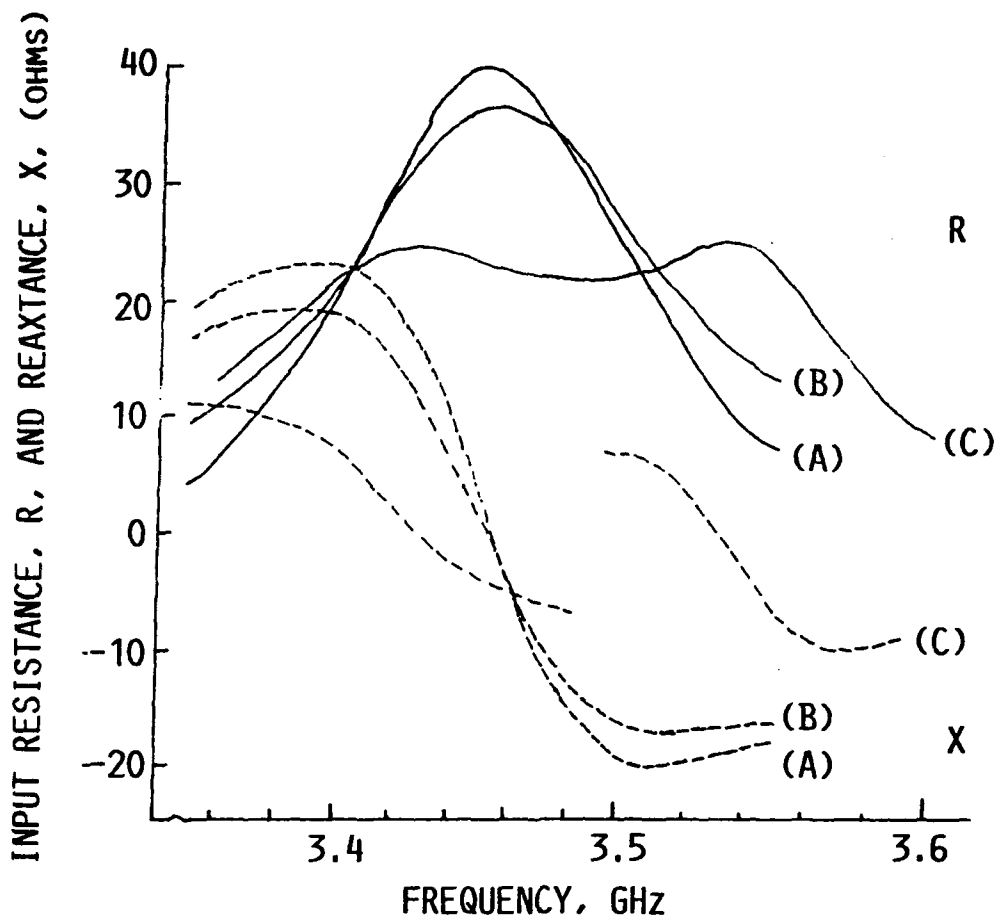


FIGURE 2. - IMPEDANCE PLOT FOR (A) 2x2 cm SQUARE PATCH, (B) AND (C) 3-ELEMENT LINEAR ARRAY.

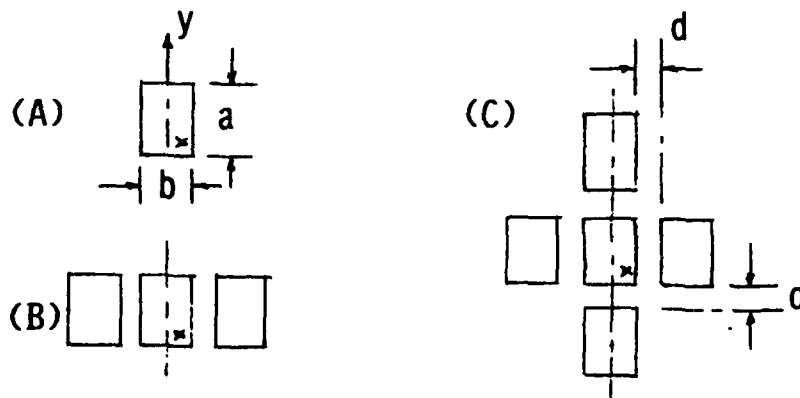
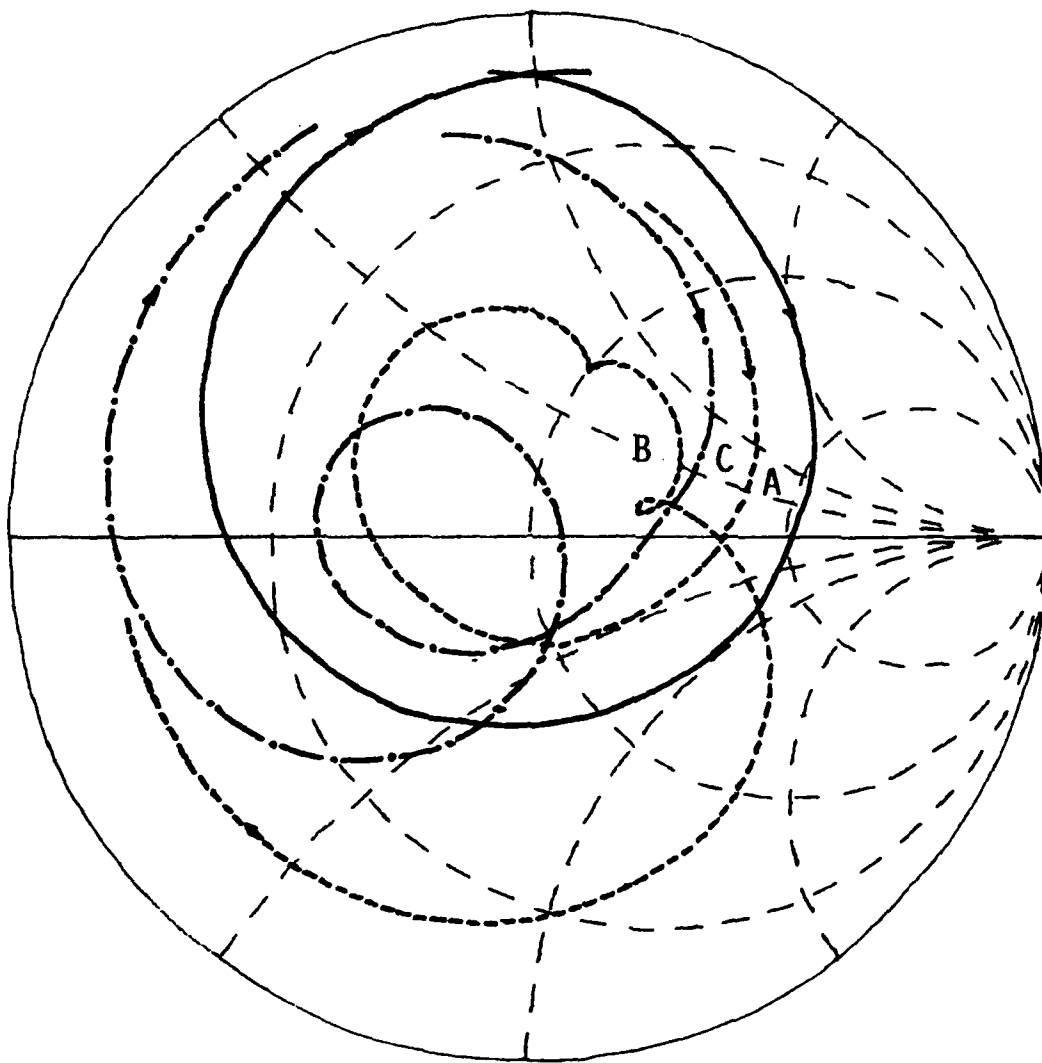


FIGURE 3. - IMPEDANCE LOCI FOR (A) A SINGLE MICROSTRIP PATCH, (B) A 3-ELEMENT PARASITIC ARRAY AND (C) A 5-ELEMENT CROSS FOR: $\epsilon_r = 2.17$, $a = 0.78$ cm, $b = 0.519$ cm, $d = 0.08$ cm AND SUBSTRATE THICKNESS = 10 MIL.

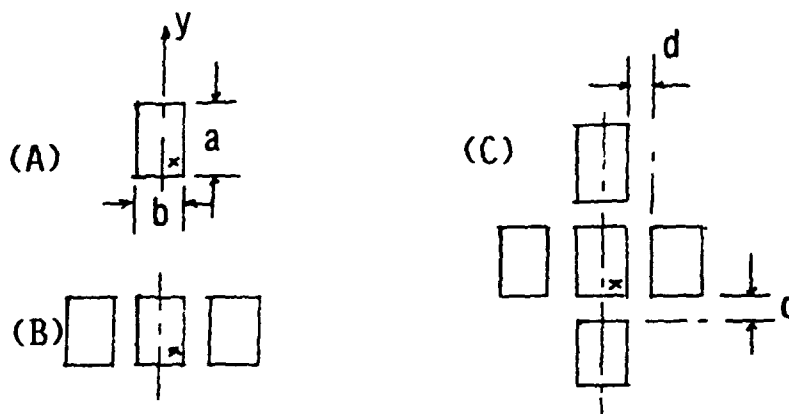
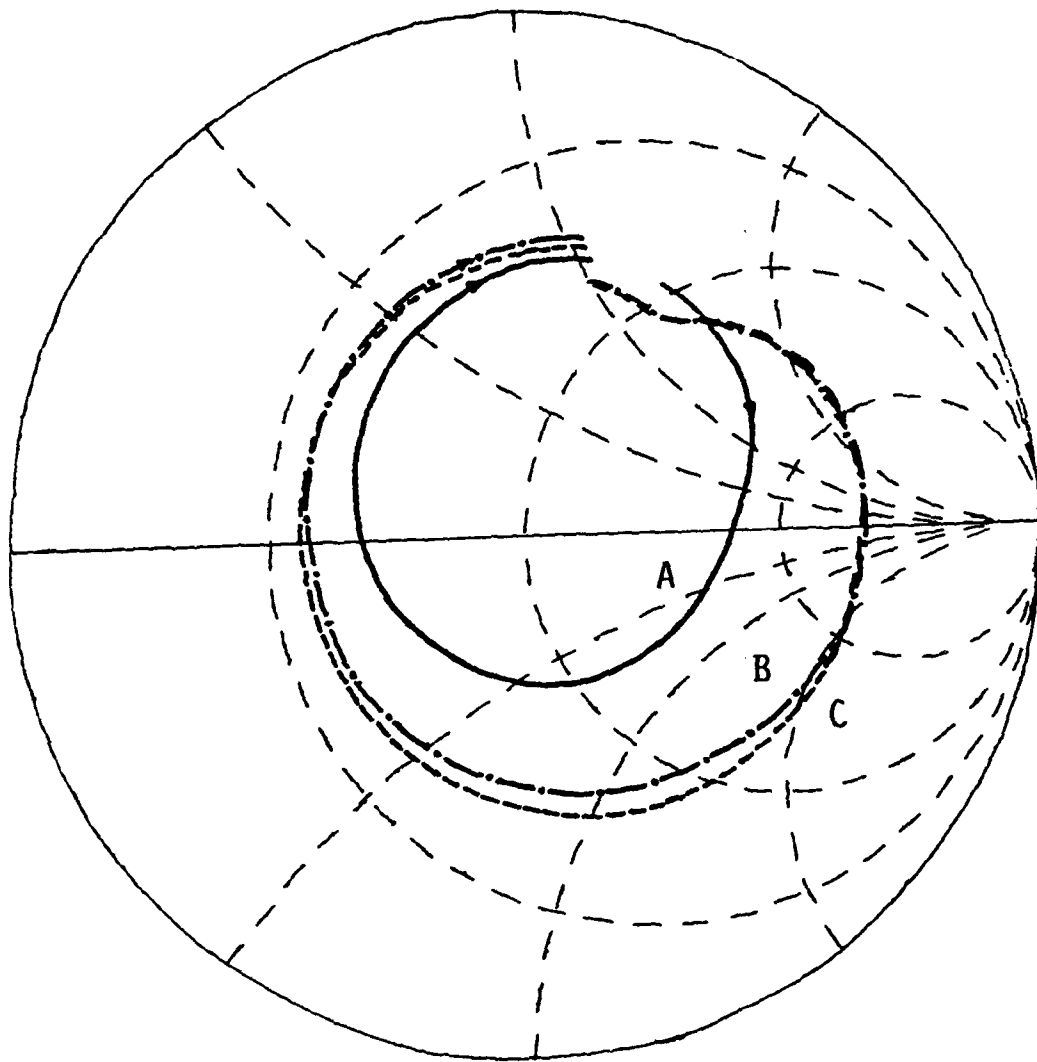


FIGURE 4. - IMPEDANCE LOCI FOR (A) A SINGLE MICROSTRIP PATCH, (B) A 3-ELEMENT PARASITIC ARRAY AND (C) A 5-ELEMENT CROSS FOR: $\epsilon_r = 2.17$, $a = 0.78$ cm, $b = 0.519$ cm, $d = 0.25$ cm AND SUBSTRATE THICKNESS = 30 MIL.

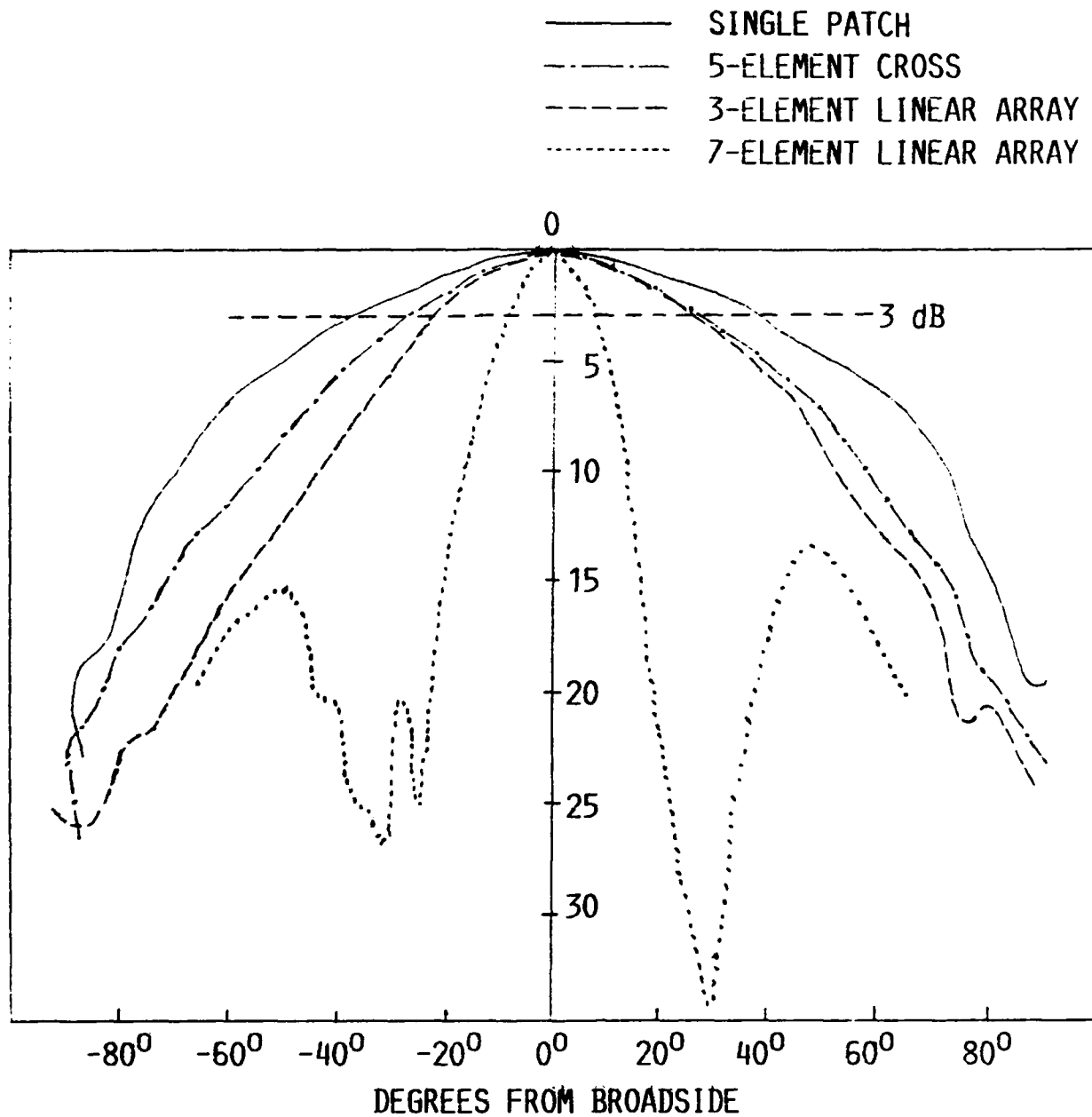


FIGURE 5. - H-PLANE PATTERNS FOR: $\epsilon_r = 2.17$, $d = 0.08$ cm, AND SUBSTRATE THICKNESS = 10 MIL.

- SINGLE PATCH
- - - - 5-ELEMENT CROSS
- - - - 3-ELEMENT LINEAR ARRAY
- · - · 7-ELEMENT LINEAR ARRAY

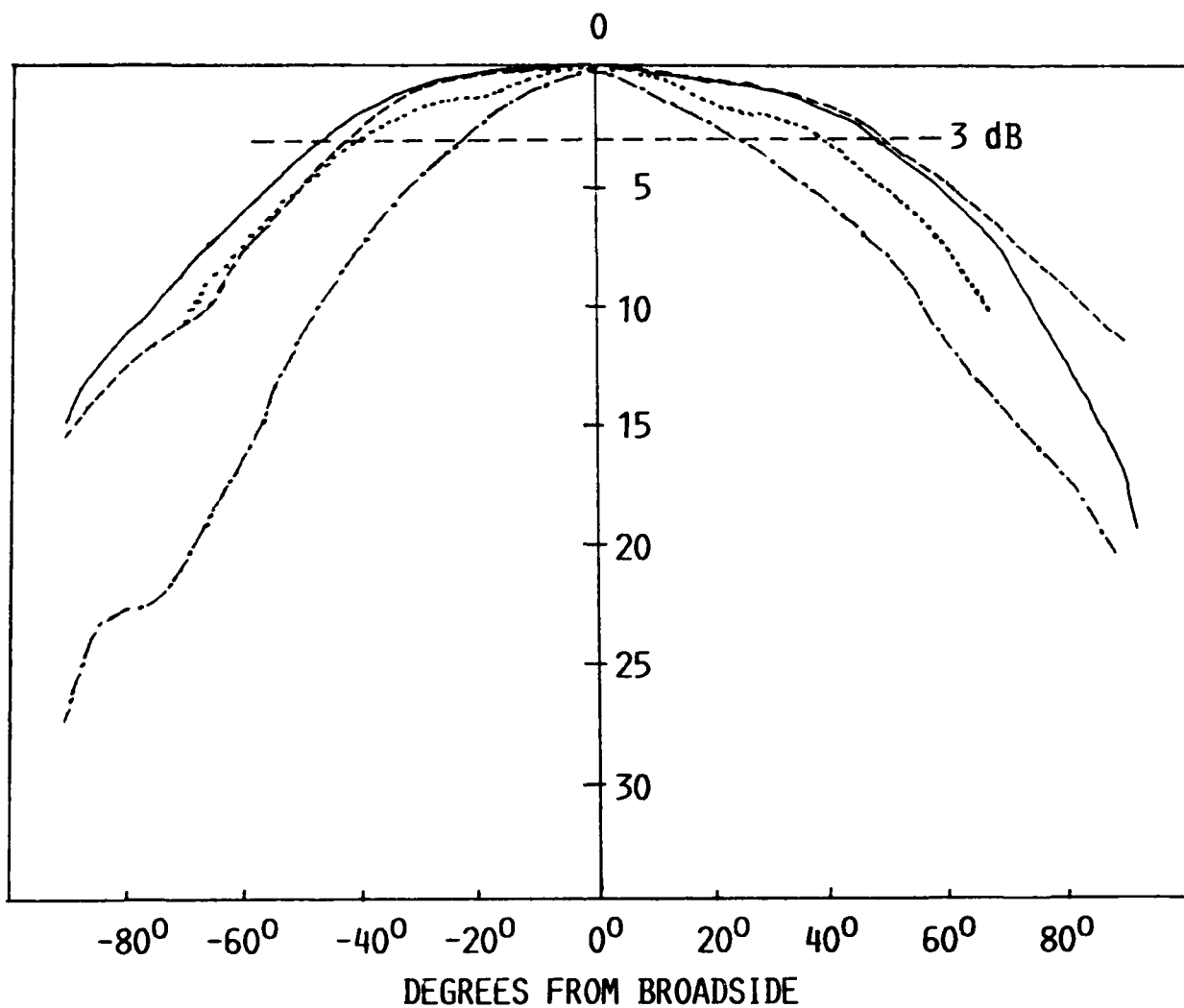


FIGURE 6. - E-PLANE PATTERNS FOR: $\epsilon_r = 2.17$, $d = 0.08$ cm, AND SUBSTRATE THICKNESS = 10 MIL.

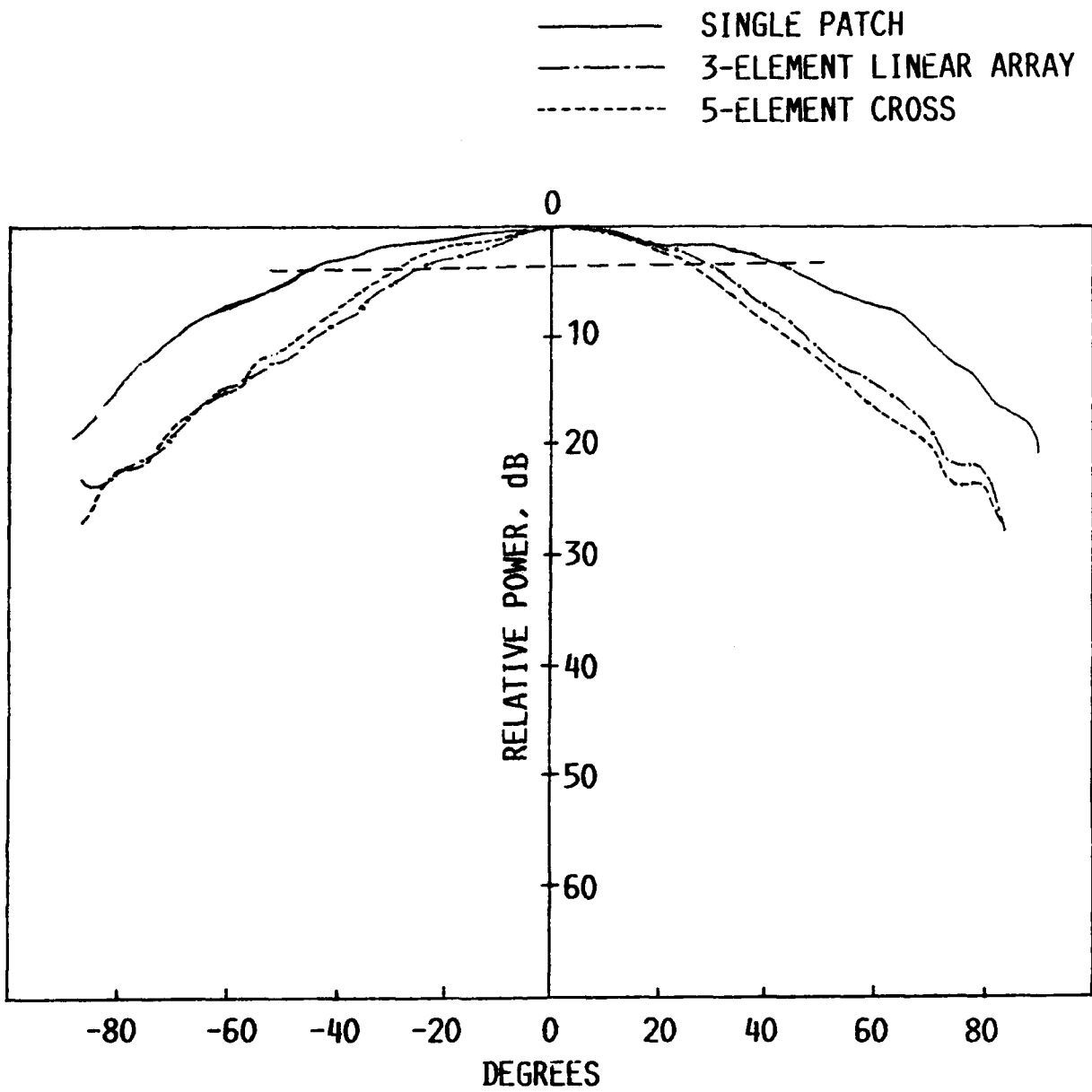


FIGURE 7. - H-PLANE PATTERNS FOR: $\epsilon_r = 2.17$, $d = 0.08$ CM AND SUBSTRATE THICKNESS = 30 MIL.

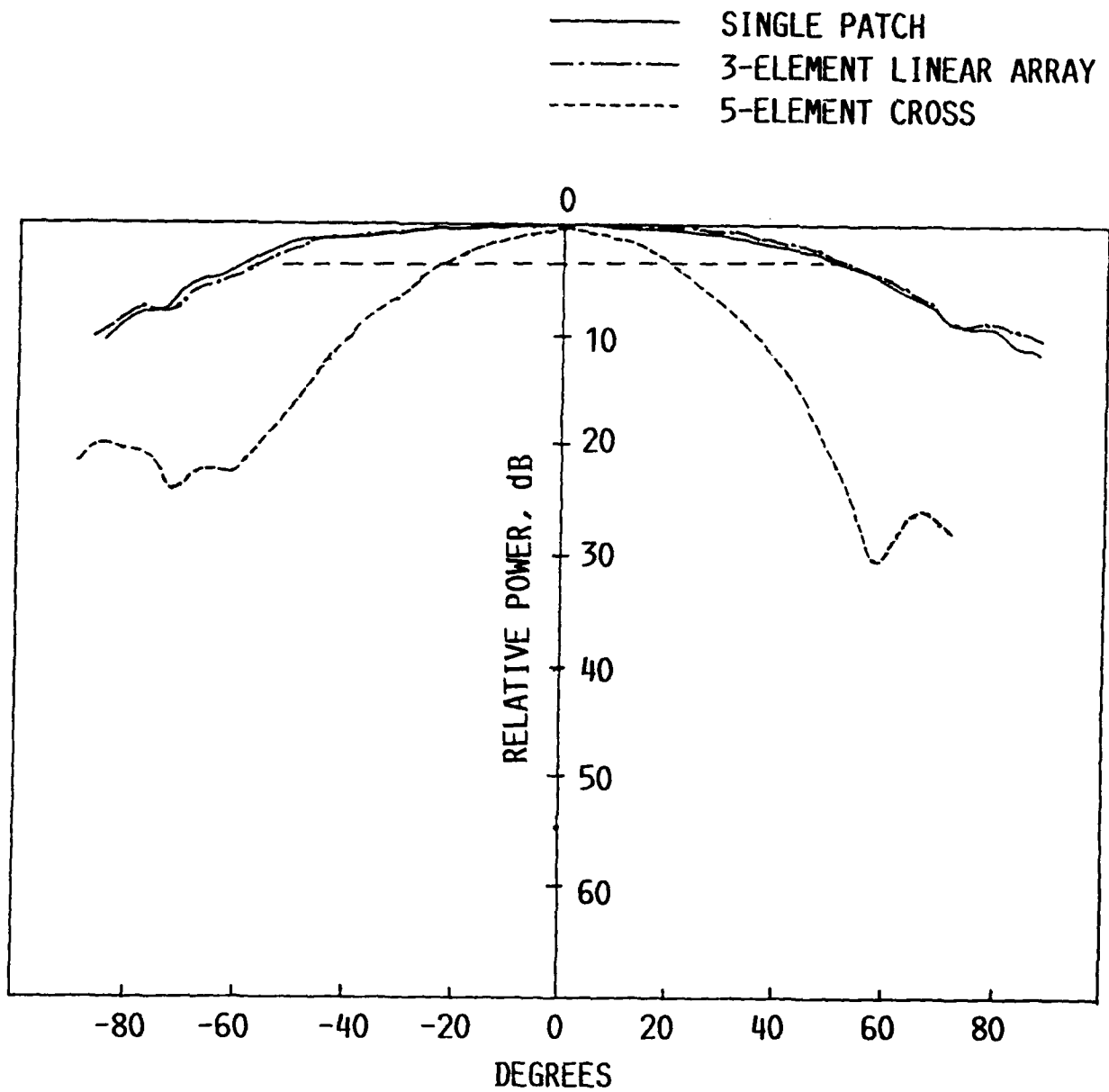


FIGURE 8. - E-PLANE PATTERNS FOR: $\epsilon_r = 2.17$, $d = 0.08$ cm AND SUBSTRATE THICKNESS = 30 MIL.

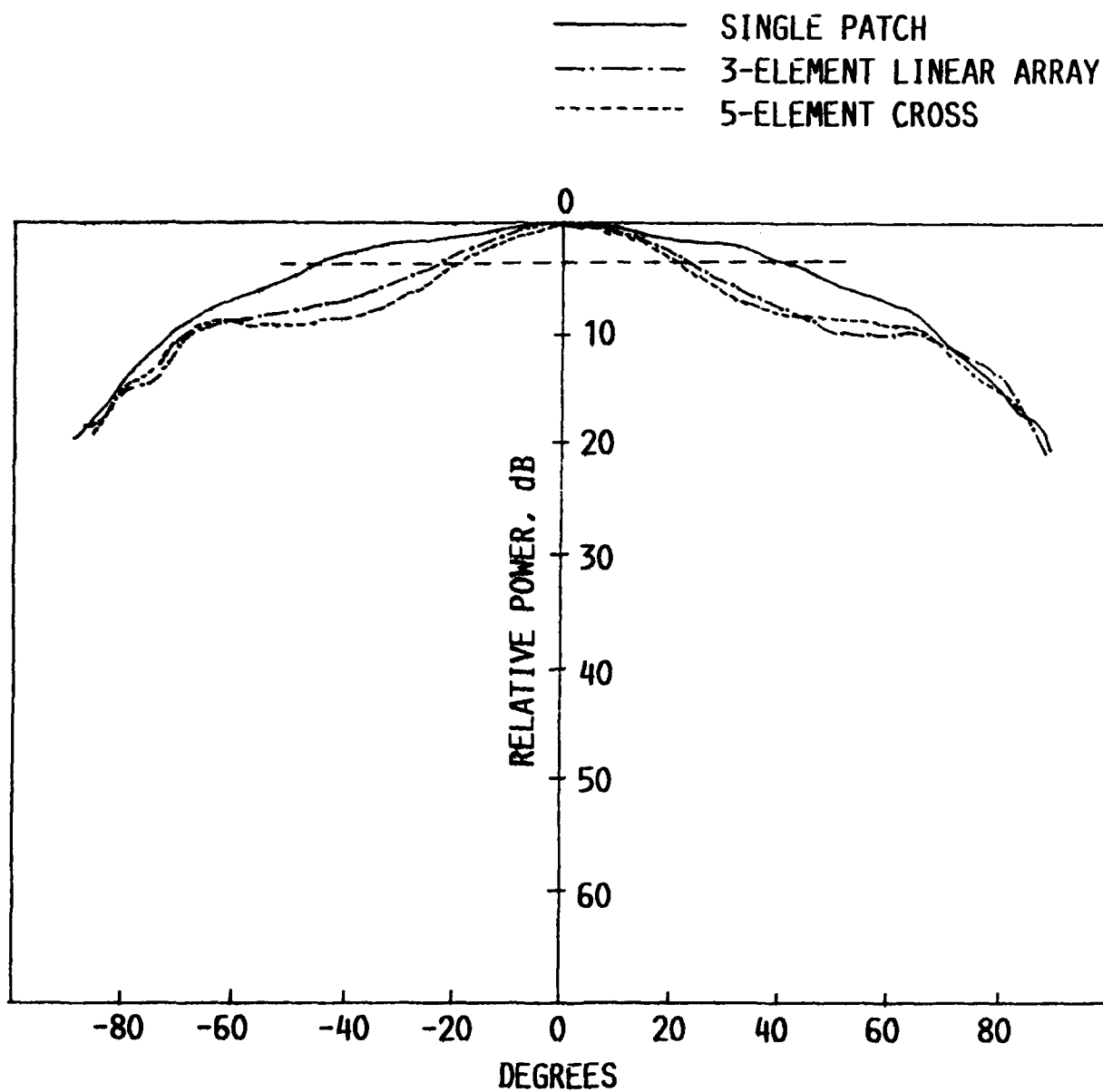


FIGURE 9. - H-PLANE PATTERNS FOR: $\epsilon_r = 2.17$, $d = 0.25$ cm AND SUBSTRATE THICKNESS = 30 MIL.

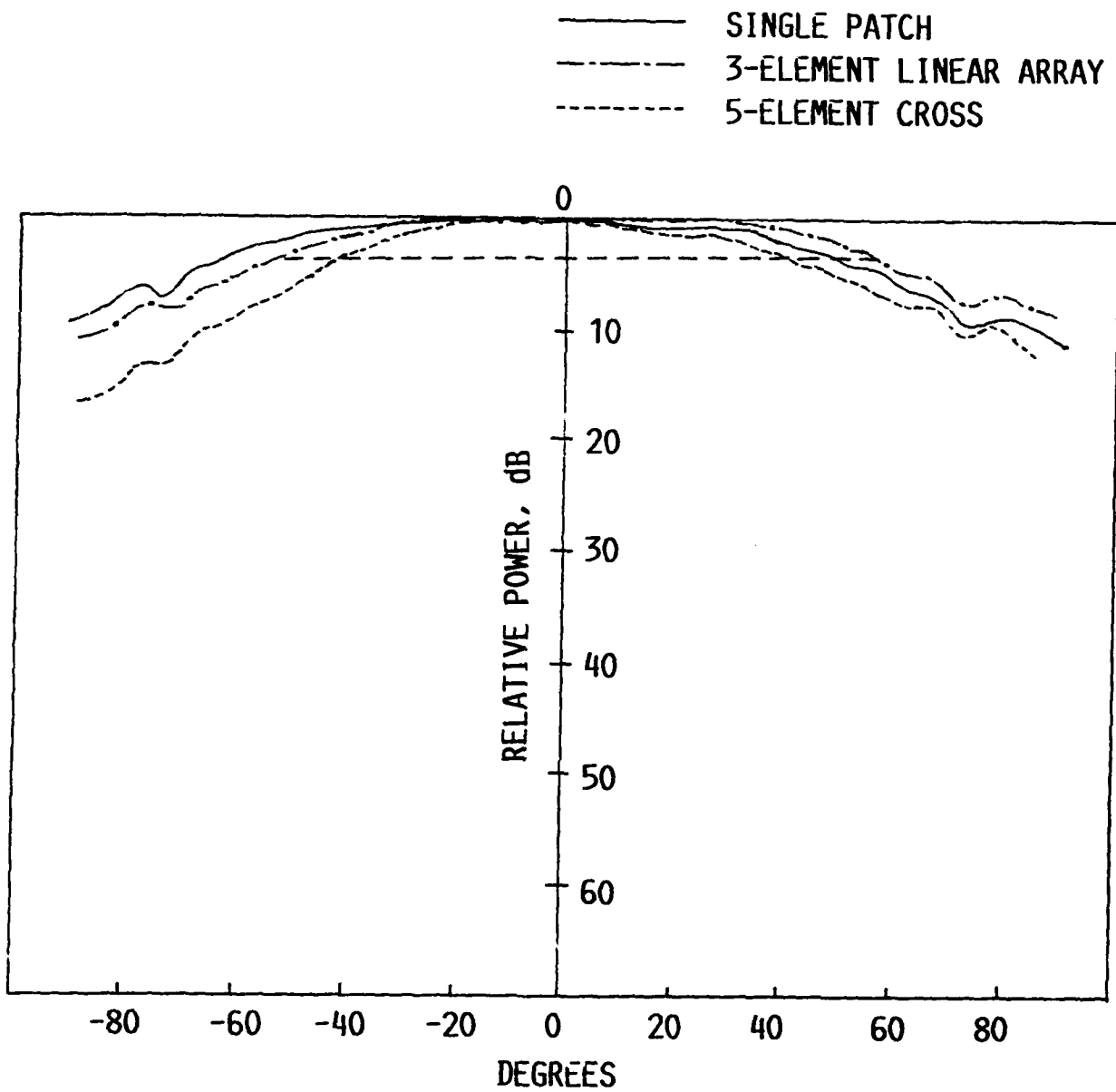


FIGURE 10. - E-PLANE PATTERNS FOR: $\epsilon_r = 2.17$, $d = 0.25$ cm AND SUBSTRATE THICKNESS = 30 MIL.

A MULTI-LAYER MULTI-BAND
SYMMETRICAL MICROSTRIP ANTENNA

Samuel Sensiper
Consulting Engineer
Culver City, CA 90230

ABSTRACT

A novel antenna feed scheme is described for independently exciting two or more microstrip antenna elements one placed over the other in a symmetrical manner. Applications where two or more relatively narrow bands rather than one very wide band are required are candidates for this approach. These include GPS, MOBILSAT, and INMARSAT. The feed design is illustrated by hardware built, tested, and used for GPS applications with excellent pattern, gain, axial ratio, and phase center properties in the L1 and L2 bands. Comparison of some pattern data with theoretical predictions shows good agreement. Among the features of the feed approach is the ease of design using available single patch data. High isolation between the signal ports suggests transceiver applications. Other applications are considered including the use of higher mode configurations. Areas for further work conclude the report.

1.0 INTRODUCTION

Many applications require an antenna that operates in two or more narrow frequency bands which are relatively widely spaced. Examples are the Global Positioning System (GPS),^{1,2} the International Maritime Satellite System (INMARSAT),³ and the Mobile Satellite System (MOBILESAT).^{4,5} Such requirements can be met by an antenna whose performance bandwidth covers the entire frequency span between the upper and lower bands of the system, or by an antenna which has the appropriate performance only in the bands of interest.

A microstrip type antenna element with its feed scheme which is of the multi-band response type is described here. It has been successfully used for GPS applications.⁶ The results obtained in this example are shown to illustrate the concept, and applications to other cases are suggested. Advantages which accrue from this approach as well disadvantages are noted. Suggestions for further work are also indicated.

2.0 TWO LAYER MICROSTRIP ANTENNA

2.1 BACKGROUND

The motivation which led to the multi-layer concept was to achieve a low cost easily manufactured antenna that could be integrated with a low noise ampli-

fier for man-carried field GPS (dual-band) applications. Reception is required in two bands for maximum GPS utilization. These are at 1575 MHz (L1) and at 1228 MHz (L2) with a useful bandwidth of 20 MHz for each. An antenna covering the entire span between L1 and L2 would need a performance bandwidth of 26% whereas an antenna covering each band separately needs a performance bandwidth of only 1.6% in each band.

The two band response microstrip scheme with the top patch only fed through the lower patch as described several years ago was the initial design choice.⁷ Adequate impedance matches were obtained but system performance implied unacceptable pattern imbalance.

2.2 THE PHYSICAL CONFIGURATION

Consideration of these results as well as the original objectives including the need for circular polarization reception for GPS applications led to another arrangement which gives excellent performance. In this case a hollow conducting tube centrally located penetrates both the lower and upper patches and is connected to the respective patches and ground planes. The lower patch acts as the immediate ground plane for the upper patch. The centered hollow tube allows feeding the upper patch independently of the lower one and in

the usual way for circular polarization, i.e., at two orthogonal locations with two signals in quadrature.

This is achieved by passing two short small diameter coaxial cables from a power divider-phasing network under the extended ground plane through the tube and feeding the upper patch from above. The lower patch is fed in the usual manner from underneath from a power divider-phasing network which is also under the extended ground plane. Thus the upper and lower patches have their centers on the same axis. Figure 1 is a close-up top view of the patches and the upper feed.

Figure 2 is a view of the disassembled antenna with the removed radome. The radome is a thin plastic shell in the form of a low profile truncated spherical cap with a flat lip for attachment to the extended ground plane. In Figure 2 the microstrip antenna is a single band one demonstrating the use of this standard ground plane configuration for either dual or single band application.

The single patch assembly of Figure 2 or the dual patch assembly of Figure 1 is mounted on the extended circular ground plane seen in Figure 2. Here several nylon screws are used around the periphery of the lower patch substrate to insure a good electrical connection

of the lower patch ground plane to this extended circular ground plane. This mode of attachment has no evident influence on the electrical characteristics of the antenna. On the back side of the extended ground plane are shielding cavities for the power divider-phasing networks as well as for the low noise amplifiers for the two GPS bands and the associated power supply. These devices are of well known form, have been described elsewhere, and are not of major interest here.⁶

As seen in Figure 1 the substrate for the top L1 patch extends beyond the patch edge for one substrate thickness, 0.32 centimeters. Beyond this is the lower patch. The lower patch operates at L2; its substrate extends considerably beyond the edge of the lower patch. The substrate for both is a teflon-glass cloth laminate material with $\epsilon_r = 2.55$. The dimensions of the patches agreed with the dimensions calculable from the available theory for isolated patches to less than 1%.⁸ The changes from the small diameter central tube are evidently very small as would be expected since the center of the patches is an electric field null point.

2.3 FEED, MATCH, AND TEMPERATURE EFFECTS

The feed for the patches in all cases is the probe formed by the extension of the center conductor of

the small coaxial lines with the outer conductors appropriately connected in the usual manner. Matching is obtained by locating the probes along lines bisecting the patch sides at the location that gives the best match at band center for the band of interest. The individual feeds are matched to a return loss of less than -10 db over a bandwidth of 22 MHz for L1 and L2. Calculated bandwidths for isolated patches with the dimensions and substrate used here are 23 MHz at 1228 MHz (L2) and 38 MHz at 1575 MHz (L1).⁸ Later measurements suggest that the particular model chosen for measurements did not have the best probe location for the optimum match at band center for the L1 band. This could result from the manner in which the antennas were adjusted for the small production run utilized. This may explain why an adequate but not the maximum available bandwidth was obtained for L1. Another possible explanation is the influence of the short extension of the substrate beyond the L1 patch which would alter the edge admittance to some degree. However this did not appear to alter the resonance patch size significantly.

Temperature tests for L1 showed that the frequency/temperature coefficient is $0.09 \text{ MHz}/^\circ\text{C}$. From -40 to +60 $^\circ\text{C}$ the band center moved from -4 to +5 MHz

with the bandwidth remaining the same. Similar results are expected for L2. In view of the characteristics of the GPS signals this variation is thought to be acceptable particularly as a result of field tests over wide temperature ranges^{9,10,11}. In other applications wider bandwidths at the mid-operating temperature may be required to avoid signal loss because of acceptance band motion over the operating temperature range.

2.4 ISOLATION BETWEEN SIGNAL PORTS

Although not of too much significance for the GPS receive only application a useful property of this arrangement for other applications is the isolation between the L1 and L2 ports. Tests on one unit showed -47 db isolation between the L1 and L2 ports with 1575 MHz into the L1 port. It was -33 db with 1228 MHz into the L2 port.

2.5 RADIATION PATTERNS AND PHASE CENTER

Figures 3 and 4 show radiation patterns obtained with the dual frequency arrangement of Figure 1 mounted on the standard extended ground plane shown in Figure 2. This extended ground plane has a diameter of 28 centimeters. The rotating linear polarization gain data shown in Figures 3 and 4 taken with a gain standard in an anechoic chamber can be used to derive dbic-

db isotropic circular - values.¹² These are shown in TABLE 1 for some specific elevation angles. The gains

TABLE 1 - GPS DUAL BAND ANTENNA - GAIN (dbic)

Angle (degrees)	L1	L2
0 (zenith)	6	7
.....		
60	4	0
70	1.5+	-1.5+
80	-1 +	-4 +
90 (horizon)	-4 +	-6 +

were derived using the lower of the values at the indicated angles either side of boresight. Asymmetries in the data result from test mount asymmetry, boresight misalignment, and other factors including possible higher mode effects. As indicated by the + the gain is possibly 1 to 2 db more particularly beyond 70°. Other pattern data not presented here indicates that the gain variation in azimuth is less than 1 db down to about 50° below the zenith.

For GPS applications and possibly for many other applications the positional stability of the apparent phase center of the antenna as a function of the eleva-

tion and azimuth angles is of importance. An independent measurement of this characteristic yielded results which can be summarized as follows: "Four tested Global Positioning Satellite Antenna-Low Noise Amplifier units showed less than $\pm 3^\circ$ variation from 30° above the horizon to zenith for all azimuths. Phase centers were within ± 0.08 centimeters in three axes for all units for L1 and L2."¹³

3.0 RELATED EXPERIMENTAL RESULTS

3.1 OTHER DIAMETERS AND OTHER PERMITTIVITIES

System field tests with the particular GPS receiver for which the antenna with the 28 centimeter ground plane had been designed demonstrated that the elevation coverage was quite adequate. However other users stated a possible requirement for more near horizon gain. This might be needed for applications on a vehicle with roll and pitch. Of course this low angle coverage could aggravate the problems resulting from multipath reception. Some brief experiments were performed to examine the influence on the radiation pattern particularly of the ground plane diameter and the substrate permittivity value since it was clear from general principles that these parameters would have a major influence on the elevation pattern.

Figure 5 shows the pattern of an L1 only round patch with the same substrate material and thickness as before with a ground plane diameter of 15 centimeters. The patch was fed for circular polarization in the same way as for the previous square patches. The substrate in this case extended two times the substrate thickness beyond the patch edge, with the ground plane edge some distance beyond this point. The patch size for resonance agreed to within less than 1% from that predicted from available theory.¹⁴ Probe feed locations were not optimized for maximum bandwidth here; narrower bandwidths can be expected generally for round patches than for square patches, other parameters being equal.¹⁴

The zenith gain is the same as with the larger ground plane, i.e., 6 dbic, but improved near horizon gain is observed, -2 dbic instead of -4 dbic. Better horizon coverage is expected for L2 also, although no tests have been made yet on an L1 and L2 combination. Comparison may not be appropriate since the patch was round in this case compared to square patches with the larger ground plane. Other pattern data not displayed here indicate negligible gain variation-less than 1/4 db-in azimuth over most of the elevation angle range from zenith to back lobe-a 180 degree range-except for a

few regions. Such uniformity in azimuth would be expected in view of the azimuthal symmetry of the antenna. The major deviations noted are thought to be a result of various experimental errors.

Figure 6 illustrates the pattern of a round patch again for L1 only on a ground plane 10 centimeters in diameter. The substrate in this case was a ceramic filled material 0.16 centimeters thick with $\epsilon_r = 10.2$. Circular polarization was achieved by the same feed arrangement as before. The zenith gain in this case is only 4 dbic possibly because of the increased back radiation, which is to be expected, as well as antenna losses, particularly dielectric losses. The result is that the near horizon gain is actually less than for the 15 centimeter case. The patch size for resonance agreed with the theoretically predicted value within 1%. The substrate extended beyond the patch edge for about two times the substrate thickness with the substrate edge radius about one-half the ground plane radius. As expected the bandwidth of this antenna was substantially less than the other models although no attempt was made to optimize it for these preliminary tests.

3.2 ANOTHER CONSTRUCTION TECHNIQUE

The configuration shown in Figure 1 met sub-

stantially all of the objectives originally required. However the possibilities of reduced cost and a higher level of antenna/low noise amplifier integration for application here as well as to other areas led to some exploratory tests and preliminary results worth noting here.

These refer to the use of thick film techniques for low cost construction of patch antennas on ceramic material. Results of these tests suggest that the application of the usual thick film metallization methods on 96% alumina are generally not suitable for creating patch antennas since dielectric and metallic losses are too large. The use of lapped surface purer alumina substrates and higher density metallization may be required to reduce such losses. Of course the other constraints such as available bandwidth, pattern coverage, etc. influenced by the dielectric constant would have to be considered.

4.0 THEORETICAL PATTERN PREDICTIONS

4.1 INFINITE GROUND PLANE

Early analyses to determine the radiation pattern from a microstrip antenna element assumed the element located on an infinite conducting ground plane with an infinite substrate. Field calculations were made

with increasing degrees of accuracy and sophistication. The simplest of these came from the use of the equivalent magnetic currents method, where the magnetic currents are related to the gap or assumed slot electric fields obtained via transmission line or cavity solutions appropriately modified.^{14,15} The more sophisticated solutions came from a full wave analysis.¹⁶ Although adequate for some cases where the ground plane is large, insufficient accuracy and detail results for the finite ground plane situation.

4.2 FINITE GROUND PLANE

Recently published work have demonstrated solutions for two microstrip antenna configurations with finite ground planes. For the square patch on a square ground plane case the often used geometrical theory of diffraction (GTD) was applied to the field from the patch equivalent slot fields yielding good agreement with experimental results in the E and H planes for the case considered.¹⁷ The dielectric substrate was assumed thin enough to permit neglecting any possible surface wave effects. It was noted that patterns other than those in the principal planes could be determined using the corner diffraction solutions.

For the round patch on a round ground plane case an

exact radiated field solution for this rotational symmetric geometry was determined via equivalent electric and magnetic surface currents over the entire included volume excited by a vertical electric dipole simulating a coaxial probe feed in the patch-ground plane region.¹⁸ The level of excitation of the various modes as well as the influence of the patch radius and the substrate thickness and radius, taken equal to the ground plane radius, were determined for a range of these parameters normalized to the wavelength. Good agreement was shown with some experimental results in the E and H plane for a typical case, except possibly in the back lobe region.

Unfortunately no published analysis for the radiated fields for the square patch on a round ground plane case seems available. It would appear in this case, particularly for thin substrates, that the GTD method is the most appropriate solution approach. Integration over the equivalent magnetic current source at the patch perimeter and summation of the direct geometric optics, the singly diffracted, and the slope diffracted fields would be required, where the diffracted fields are from the circular ground plane edge. This approach would yield closed form analytic expressions for the fields and permit relatively simple numerical evaluation of the

parameter variation influence.

4.3 PUBLISHED THEORY VS. PRESENT MEASUREMENTS

The equivalent current approach requires very extensive numerical evaluation and closed form solutions for the radiated field are not possible or practical. However over a reasonably wide range in wavelength normalized parameters the results of the published calculations allow examination of the influence of the parameters, at least for the one fixed value of permittivity assumed. Indeed, one set has wavelength normalized parameters very close to the antenna whose results are shown in Figure 5. They are compared in TABLE 2.

TABLE 2 - WAVELENGTH NORMALIZED PARAMETER COMPARISON

FIGURE 5 HERE WITH REFERENCE 18

	Ground Plane Radius	Substrate Thickness	Patch Radius
Figure 5	0.40	0.0165	0.175
Reference 18	0.4	0.02	0.1806

	Substrate Radius	Feedpoint Radius	Substrate ϵ_r
Figure 5	0.21	0.042	2.55
Reference 18	0.4	0.045	2.32

In view of the symmetry of the configuration as well as the excellent phasing evident from the nearly zero axial ratio at boresight the single feed E and H plane patterns can be deduced. It should also be noted that the pattern measurement was made in the feed point-boresight plane. All this permits direct comparison with the calculated pattern data published in the reference. The results are shown in TABLE 3.

TABLE 3 -PATTERN COMPARISON -E AND H PLANE

FIGURE 5 HERE VS REFERENCE 1B

θ	-180°	-135°	-90°	-45°	0°	45°	90°	135°	180°
Em	-15	-20	-9.5	-3.5	0	-3.0	-9.0	-17	-15
Ec	-17	-20	-10.5	-3.5	0	-3.5	-11	-21	-17
Hm	-19	-29	-13	-4.0	0	-4.0	-14.5	-25	-19
Hc	-17	-25	-13.5	-3.5	0	-3.5	-13.5	-25	-17

In Table 3 θ is the elevation angle taken from -180° to -180° through θ at zenith or boresight to conform with the notation in the reference. Em, Ec, Hm, and Hc are the relative values in db of the E plane and H plane measured and calculated values respectively normalized

to 0 db at $\theta = 0$ for comparison.

Note the excellent agreement nearly everywhere even in the back hemisphere. The major difference between the measured model and the analytical model is in the substrate radius. The disagreements between the calculated and measured results may be a result of this, although with a small substrate thickness/wavelength ratio the difference in these radii is thought to have only small influence. Even the permittivity difference is small and the other differences are quite small indeed. Some of the possible disagreement may result from inaccuracies in interpolating from the reference graphical data as well from the experimentally obtained pattern data.

5.0 OTHER CONFIGURATIONS

5.1 MULTI-BAND APPLICATION

The dual band antenna described above for GPS suggests that the same approach might be used where three or more separate frequency bands are required. In this case the top and bottom patches would be fed as before with intermediate patches fed along or through the respective patch material. As an example a possible arrangement is shown in Figure 7 for a three band case. It should be clear how this can be extended for even

more bands although no multi-band antennas for more than the two band case have been built and tested.

In Figure 7 the patch for the f2 band acts as the ground plane for the f1 band; the patch for the f3 band acts as the ground plane for the f2 band. The f3 band ground plane is adjusted for radiation pattern control or for array use. The f2 band feed is shown associated with the f2 patch with the probe extended downward. It could be in the f3 patch with the probe extending upward. Similar combinations are possible for other bands with appropriate feed lines as noted below.

The feed scheme suggested in Figure 7 for the f2 patch could be achieved by a coaxial line impeded in the f2 patch or f1 ground plane. Better and more easily constructed would be a stripline conductor in which the top and bottom surfaces of the chosen patch are separated to form the ground planes for the feeding stripline. This type of construction would be particularly attractive since it might allow some stripline circuitry such as filters, phasing network, etc. to be incorporated as well as permitting an integral rugged layered assembly. Incidentally a microstrip type feed line might be used for the top patch via an additional substrate, but possible spurious radiation from this

might not be desirable.

Any of these feeds or others will increase the effective thickness of the patch or patches between the top and bottom ones. If this increase is quite small compared to a wavelength it is expected that the radiation patterns will be influenced very little although modification of the patch edge admittance will probably influence the patch size and bandwidth somewhat. Other factors which would clearly influence the design are the number of bands and the frequency separation with wider spacing yielding more independence.

A possible limitation on the number of bands is the number of feed lines which can be practically passed through the central hollow tube. This can be quite large since a desired mode for the required radiation pattern can be obtained even with large tube diameters. Increased perturbation of the center field will alter the patch size for resonance.^{19,20} Spurious mode generation may put a practical limit on size and number of bands.

5.2 MULTI-MODE APPLICATIONS

Since the arrangement here permits independent feeding of two or more stacked microstrip antennas with common axes, application where this feature might offer some advantages have been briefly considered. For ex-

ample it may be desired to have an antenna combination with one pattern having a null at boresight with the other having a maximum. This could be achieved with one circular patch operating in the dominant TM₁₁ mode with the other in the TM₂₁ mode.^{15,18} Further these can be at the same frequency since the modes are orthogonal and the two parts of the antenna will not couple to each other.

The above combination or some variation including additional patches would appear to have some promise in a direction finding arrangement or in a monopulse configuration. However the brief review to date indicates that the polarization of the radiated field is not satisfactory for this application. Also no combining circuit arrangement has yet been devised from which boresight deviation signals can be derived. Further work may eliminate or reduce these deficiencies.

6.0 DISCUSSION AND SUMMARY

6.1 DISCUSSION

One major feature of the feed concept described above is simplicity of design and freedom in parameter choice particularly if the central tube diameter is small. The perturbation of the electric null field is also small permitting the usual single isolated

patch design information to be used with little error. Even if the central tube is not small the top feed scheme can be useful. Incidentally although in the examples noted so far the electric null point is the patch center, modes other than the TM₁₁ will have electric field null points at other radial locations. This will allow some design choices when it is desired to excite some of the stacked patches in other modes.

A significant advantage for the case here results from the common axis obtained for each band for microstrip type antennas with consequent excellent phase performance for GPS applications.^{13,21} This property might be useful in other applications, for example in phased arrays, or combined with shaped ground planes.

Perhaps a major feature of the approach is the retention of the advantages of a microstrip type antenna where only band pass rather than broad band performance is required. But in addition to not needing the usual broadband physical features, i.e., thick substrate, matching networks, etc., which can have several disadvantages, other electrical advantages accrue. For example in the GPS case the band pass feature leads to rejection of noise and interference that would result from signals in the spectrum between L1 and L2 in a broadband response

device without any additional equipment.^{9,10}

As a corollary the isolation between the signal ports can be very useful in a transceiver application since any additional filtering for the receiver for full duplex operation need have less rejection capability and can operate at lower power level. In applications like MOBILSAT AND INMARSAT where the band spacings are about 6% the isolation can be expected to be less than the over 30 db obtained in the GPS L1-L2 case where the band spacing is 25%. Use of different permittivities for the patches with consequent additional physical separation between the patch apertures may improve the isolation.

A further advantage of this feed scheme is that since the patches are operating with substantial isolation and with independent ports, many of the various techniques useful for individual microstrip antennas are applicable here with only little modification.^{14,15}

One possible disadvantage is some increase in construction complexity although this has not been significant for the example cited. A possible disadvantage is the small extension of the feed coaxial line over the top patch which in a sense increases the total height somewhat although in a limited region. Other feeds, such as microstrip or stripline would also do this.

Another disadvantage in some cases, which in others would be an advantage, is that each frequency band has its own port. This can be a disadvantage if all the signals must be carried across a single line interface.

Among the possible areas for further work would be those which answer the following questions. How does the isolation between ports vary as a function of frequency separation, number of bands, and physical parameters—including permittivity, patch and substrate thickness and radii, as well as feed point? How is the patch size for resonance altered as a function of these same parameters, i.e. number of bands, etc., and how is the Q or bandwidth changed? Similarly what is the effect on the radiation patterns in the various bands as a function of these variables?

6.2 SUMMARY

The fact that a microstrip antenna can be probe fed from either side of the substrate leads to a stacked configuration in which the patches can be placed over each other on a common axis. These in turn are fed through hollow tubes placed in electric field null regions in the appropriate microstrip antenna "cavities". Successfully applied to a dual band GPS antenna where relatively narrow bands widely spaced in frequency are

required, this approach avoids the need for a wide band response antenna and also leads to further advantages. Other applications are suggested and extensions of the concept are noted. The advantages and disadvantages of this approach are reviewed and suggestions for further work are noted.

7.0 ACKNOWLEDGEMENT

The author acknowledges D. Williams and J.P. McKone of Wilmanco, Northridge, CA for ably translating a concept into working hardware.

REFERENCES

1. Janiczek, P.M., Ed., (1980) (1984) Global positioning system, Navigation, I:1-246, II:1-257.
2. National Geodetic Information Center, NOAA, (1985) Positioning with GPS-1985, 1:1-508, 2:509-946, Rockville, MD.
3. da Silva Curiel, A. (1983) The first generation INMARSAT system, Satellite Systems for Mobile Communications and Navigation, IEE Conference Publication No.222, pp. 1-7, London, UK.
4. Schmidt, F. W. (1987) Low-cost microstrip phased

- array antenna for use in mobile satellite telephone communication service, IEEE Antenna and Propagation Soc. Symp. Dig. pp. 1152-1155, Paper presented in Blacksburg, VA.
5. Chung, H. H. (1987) Analysis of low cost conformal phased array for MSAT-X applications, IEEE Antenna and Propagation Soc. Symp. Dig. pp. 1156-1159, Paper presented in Blacksburg, VA.
 6. Sensiper, S., Williams, D. and McKone J. P. (1987) An integrated global positioning satellite antenna-low noise amplifier system, Fifth Int'l. Conf. on Antennas and Propagation (ICAP 87), IEE Conference Publication No. 274, Part 1: Antennas pp. 51-54, London, UK.
 7. Long, S. A. and Walton, M. D. (1978) A dual-frequency stacked circular antenna, IEEE Antenna and Propagation Soc. Symp. Dig. pp. 260-263, Paper presented in College Park, MD.
 8. Carver, K. R. and Mink, J. W. (1981) Microstrip antenna technology, IEEE Trans. Antennas and Propagation 29 (No. 1):2-24.
 9. MacDoran, P. F., Whitcomb, J. H. and Miller, R. B. (1984) Codeless GPS positioning offers sub-meter accuracy, Sea Technology October.

10. Whitcomb, J. H. (1986) The ISTAC difference, Professional Surveyor 6 (No.5).
11. Fellas, C. N. (1987) Configuration like Figure 2 used successfully in telex via INMARSAT on Virgin transatlantic hot-air balloon flight July 1987, informal message from British Telecom International.
12. Ludwig, A. C. (1976) A simple graph for determining polarization loss, Microwave Journal 19 (No. 9):63.
13. Clark, T. (1986) Informal communication, NASA Goddard, Greenbelt, MD.
14. Bahl, I. J. and Bhartia, P. (1980) Microstrip Antennas, Artech House, Dedham, MA.
15. James, J. R., Hall, P. S. and Wood, C. (1981) Microstrip Antenna, Peter Peregrinus Ltd., Stevenage, UK.
16. Araki, K. and Itoh, T. (1981) Hankel transform domain analysis of open circular microstrip radiating structures, IEEE Trans. Antennas and Propagation 29 (No. 1):84-89.
17. Huang, J. (1983) The finite ground plane effect on the microstrip antenna radiation patterns, IEEE Trans. Antennas and Propagation 31 (No. 4):649-653.
18. Kishk, A. A. and Shafai, L. (1986) The effect of various parameters of circular microstrip antennas on their radiation efficiency and the mode excitati-

tion, IEEE Trans. Antennas and Propagation 34
(No. 8):969-978.

19. Yasunaga, M., Wantanabe, F., Shiokawa, T. and Yamada, M. (1987) Phased array antennas for aeronautical satellite communications, Fifth Int'l. Conf. on Antennas and Propagation (ICAP 87), IEE Conference Publication No. 274, Part 1: Antennas pp. 47-50, London, UK.
20. Goto, N. and Kaneta, K. (1987) Ring patch antenna for dual frequency use, IEEE Antenna and Propagation Soc. Symp. Dig. pp.944-947, Paper presented in Blacksburg, VA.
21. Tranquilla, J. M. and Colpitts (1987) Groundplane shaping techniques for use with satellite positioning systems, electromagnetics 6 (No. 4):369-386.

Note: Other references on microstrip antennas related to the work here are given below. For still others and particularly for other type antennas related to GPS applications see reference 6 above.

22. Jones, H. S. Jr., (1978) Some novel techniques for conformal antennas, Int'l. Conf. on Antennas and Propagation, IEE Conference Publication No. 169, Part 1: Antennas pp. 448-452, London, UK.

23. DeVries, J. M. (1983) A physically small circular microstrip antenna, International Telemetry Conference, 19:19-30.
24. Kishk, A. A. and Shafi, L. (1986) Experimental and numerical investigation of stacked circular microstrip antennas, ANTEM 1986 Conf. Proc., University of Manitoba, Winnipeg, Manitoba.
25. Henderson, A., James J. R. and Hall C.M. (1986) Bandwidth extension techniques in printed conformal antennas, Conf. Proc. Military Microwaves '86 pp.329-334, Microwave Exhibitions and Publishers, Kent, UK.
26. Paschen, D. A. (1986) Practical examples of integral broadband matching of microstrip antenna elements, Proc. of the Antenna Applications Symp. Paper presented at Robert Allerton Park, University of Illinois, Urbana, IL.
27. Hall, P. S., Dahele, J. S. and James, J. R. (1987) Wide bandwidth microstrip antenna for mobile earth stations, IEE Colloquium Digest No. 1987/62 pp.10/1-10/3, London, UK.



Figure 1
L1/L2 patches-L1 feed



Figure 2
Disassembled view

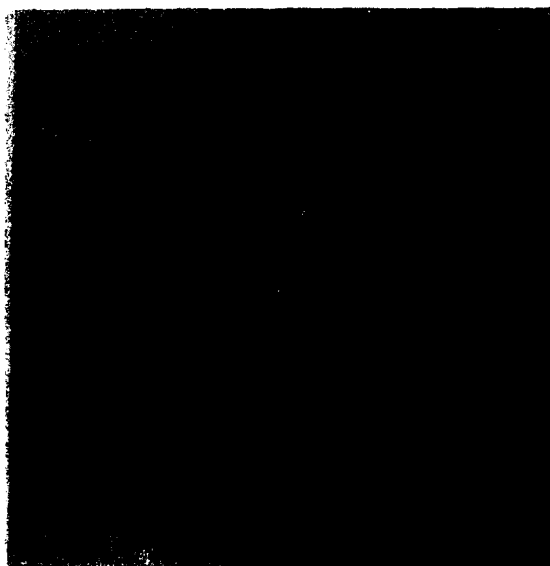


Figure 3
L1 pattern-L1/L2 combination

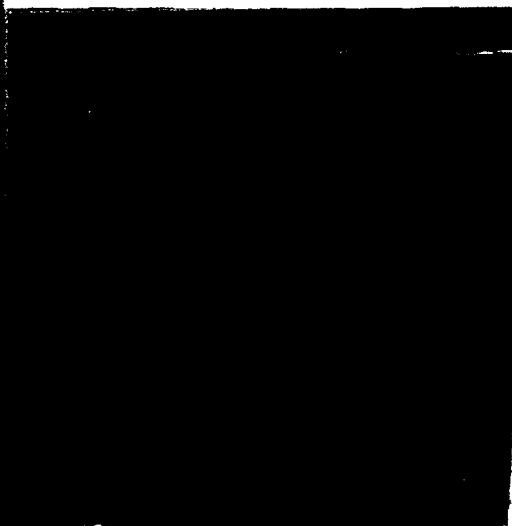


Figure 4
L2 pattern-L1/L2 combination

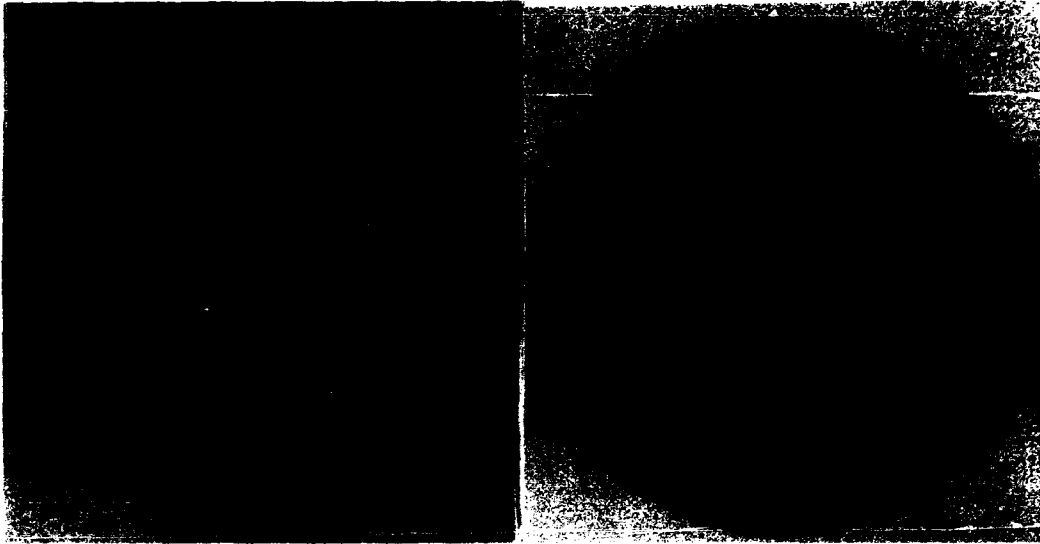


Figure 5
 L1 pattern- $\epsilon_r = 2.55$
 Ground plane diameter=15 cm

Figure 6
 L1 pattern- $\epsilon_r = 10.2$
 Ground plane diameter=10 cm

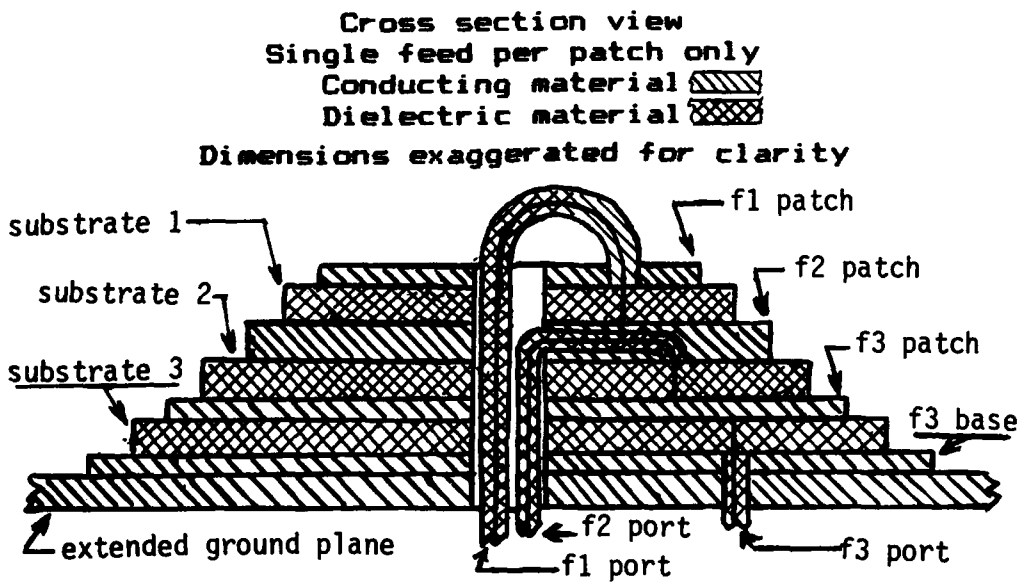


Figure 7
 N layer symmetrical microstrip antenna
 N = 3 example shown

SLOT COUPLED MICROSTRIP CONSTRAINED LENS

Daniel T. McGrath, Capt, USAF
Rome Air Development Center
Electromagnetics Directorate
Hanscom AFB, MA 01731

Abstract

The microstrip constrained lens is a three-dimensional beamformer comprised of two printed circuit layers. The two circuit boards contain planar arrays of microstrip patches that face in opposite directions, to respectively collect and re-radiate energy from a feed suspended behind the structure. It is a wide angle beamformer due to its use of two geometric degrees of freedom: the length of line joining front and back face lens elements varies with radius; and the back face elements are displaced radially instead of being placed directly behind their front face counterparts.

Experimental versions of the MCL were reported at this meeting last year, demonstrating its wide angle properties. This paper discusses a substantial improvement to the device: the feed thru pins of the first model were replaced with a solderless slot coupler, or capacitive coupler. Without the need to solder the many hundreds of feed thrus, the device is much easier to fabricate. But also, its performance is better because there is no degradation introduced by misalignment of the feed thru pins. This paper will discuss the theory, and experimental results for both an 8 GHz and a 12 GHz lens. It includes a discussion of potential improvements in future models.

1. INTRODUCTION

The microstrip constrained lens (MCL) is a focusing device for pencil beams. It is both lightweight and inexpensive since it is comprised entirely of two printed circuit boards. It is capable of moderately-wide angle scanning because it incorporates two geometric degrees of freedom. Figure 1 is a photograph of the first experimental model, which was discussed at this symposium in 1986 [1].

The front lens face is an equilateral triangular lattice of microstrip patches, and the back face is similar. Each front face is connected to a back face element by a microstrip transmission line that feeds through the ground plane separating the lens faces. In the first model, those feed thrus were pins centered in small holes in the ground plane and soldered to the transmission lines, as illustrated in Figure 2a.

This paper describes a modified design that uses a slot coupler for the feed thru mechanism. Its geometry is depicted in Figure 2b. Its obvious advantage is in manufacturability, since there are no pins to be soldered, but its performance is generally better, because the slots are less sensitive to alignment errors. This paper will first review the theory behind this lens design to show the rationale for our choices of design parameters. The two experimental slot-coupled models (8 GHz and 12 GHz) will be discussed, with measured data illustrating their performance.

2. THEORY

There are four theoretical aspects important to this lens design. First, its wide angle scanning properties result from the incorporation of two geometric "degrees of freedom:" the transmission lines joining front and back face elements vary in length according to the elements' radius from the center of the lens; and the back face elements do not lie directly behind their front face counterparts, but are displaced radially, with the amount of displacement also being a function of radius. Second, it will be shown that even though it is possible to design this kind of lens with two perfect focal points, better overall scan performance is obtained when it has only one focus. The third and fourth aspects of theory that will be discussed are, respectively, the element design and the slot coupler design.

2.1. Constrained Lens Design

The MCL is a "bootlace" lens of the general type conceived by Gent [2]. Each back face (feed side) element is connected to a front face (aperture side) element by a transmission line. A feed is positioned behind the lens, and the back face captures its radiation. The front face reradiates that energy, after it is collimated by the relative difference in line lengths between the lens center and lens edges. The addition of a second geometric variable ensures good focusing (or collimation) of feeds in a fairly large focal region around the lens axis. That variable is the relative position of front and back face radiators, r and p , respectively:

$$\rho = r \sqrt{\frac{F^2 - r^2 \sin^2 \theta_0}{F^2 - r^2}} \quad (1)$$

where F is the focal length and θ_0 is the focal angle. If this were two-dimensional structure such as a Rotman lens, it would have two perfect focal points at $\pm\theta_0$. The 3D structure does not, however, have any perfect foci unless $\theta_0=0$, in which case it has only one. The next section will discuss this in more detail.

The transmission line lengths, w , are given by:

$$w = F + w_0 - .5[\sqrt{F^2 + \rho^2 - 2\rho F \sin \theta_0} - \sqrt{F^2 + \rho^2 + 2\rho F \sin \theta_0}] \quad (2)$$

where w_0 is an arbitrary offset length. Details of this derivation are given in [3].

A limitation on the allowable F/D ratio is implicit in (1). Since the maximum aperture coordinate, r , must be less than F , F/D is restricted to .5 or greater. A practical limit is $F/D=1$, else the separation between front and back face element pairs near the lens edge becomes quite large, making it difficult to route the transmission lines.

The focal surface is a necessary part of the lens design because it specifies the feed locations. It is expressed as a function of θ :

$$\theta(\theta) = F \left[1 + .25 \frac{\sin^2 \alpha \sin^2 \theta}{(1 - \sec \alpha)(1 + \sin \alpha \sin \theta / \sqrt{2})} \right] \quad (3)$$

where $\alpha = \sin^{-1}(D/2F)$. Figure 3 shows the cross sectional shape of these focal surfaces for a few choices of F/D . Similar curves were shown in [1], but those were for a 2D lens structure.

2.2. Axial Symmetry vs. Bifocal

There are two ways to design a three dimensional lens (one that forms beams in two planes - azimuth and elevation). The easiest is to first derive a two dimensional design, then replace lateral coordinates with radial coordinates. This results in an axially-symmetric design. Equations (1)-(3) were derived in that fashion. As pointed out earlier, the axially-symmetric lens does not generally have any perfect foci, regardless of how many its two dimensional counterpart had.

The second design method is to solve the path length equality conditions in three dimensions. Transmission line lengths and back face element locations will then be a function of the axial coordinate, ϕ in the plane of the lens [3]:

$$\rho = r \left[\frac{F^2 - r^2 \sin^2 \theta_0 \cos^2 \phi}{F^2 - r^2} \right]^{1/2} \quad (4)$$

$$w = F + w_0 - .5 \left[\sqrt{F^2 + \rho^2 - 2\rho F \sin \theta_0 \cos \phi} - \sqrt{F^2 + \rho^2 + 2\rho F \sin \theta_0 \cos \phi} \right] \quad (5)$$

These design equations will yield a lens with perfect focal points at $\pm \theta_0$ in the $\phi=0$ plane.

Path length error is a common indicator of a lens' scanning performance, and we have used it to compare the ϕ -symmetric and bifocal designs. When a feed is placed anywhere on the focal surface other than at a perfect focus, it does not produce a planar phase gradient in the aperture (corresponding to a scanned beam). The difference between the actual and desired aperture phase is the path length error, and it usually looks something like Figure 4, which is a contour plot of the

error in wavelengths normalized to the design focal length, F . The root mean square value of that error, ϵ_{rms} is a good measure of its effect on the antenna gain. Figure 5 shows ϵ_{rms} vs. scan angle for two axially-symmetric lenses, with $\theta_0=0^\circ$ and $\theta_0=10^\circ$. The latter is slightly better outside 10° , but much worse inside that angle. This is an important result because it shows there is little advantage to choosing the focal angle as anything but $\theta_0=0$ in the axially symmetric case. It is important to note that the single-focus lens defined by (1)-(3) with $\theta_0=0^\circ$ is a wide angle scanning lens because it makes effective use of two degrees of freedom, including the element displacement $\rho-r$. Thus, a single-focus lens is not necessarily confined to limited scan. Figure 5 also shows the rms error vs. scan angle for a one degree of freedom lens. Such a lens would use only line lengths for focusing. Its much higher error shows the advantage of using two degrees of freedom.

Figure 6 shows similar error contours for a bifocal lens with $\theta_0=10^\circ$. Here, ϵ_{rms} depends on the scan plane, with the lowest error in the plane containing the focal points, and the greatest in the orthogonal plane. The curves for the axially symmetric case are overlaid (dashed) to show that the bifocal design only has the advantage inside $\phi=45^\circ$. Defining the effective scan region as that range of angles for which ϵ_{rms} is below a predetermined value, Figure 7 shows what those regions would be for bifocal and ϕ -symmetric designs for three different values. From this, it does not appear that a bifocal lens has any advantage in terms of the size of its scan region. The axially-symmetric lens can scan over approximately the same number of beamwidths, even though it only has one focal point.

The most important conclusion to be drawn from this analysis is that there is no strong justification for choosing a bifocal (or multifocal) lens over an axially-symmetric lens. That is our rationale for using the latter in our experimental microstrip lens models. From the standpoint of constrained lens design in general, the important conclusion is that wide angle scanning results from employment of two or more degrees of freedom, and not the existence of multiple focal points.

2.3. Patch Radiator

Both experimental models use inset-fed rectangular microstrip patch radiators. The front and back face radiators are identical. The inset feed provides the degree of control needed for impedance matching by moving the feed point inward from the edge, where the input impedance is very high (200-250 Ω).

The transmission line's characteristic impedance must be chosen carefully. It should be wide enough to be drawn fairly accurately by the mask plotter, but narrow enough that it can be routed between array elements. Reasonable values for this substrate material are 70-100 Ω .

The transmission line model [4],[5] was used to determine the resonant patch length. The patch width is $.65\lambda_d$ where $\lambda_d = \lambda_0 / \sqrt{\epsilon_r}$, resulting in an aspect ratio of about 1.3 to 1. The patch and transmission line dimensions for the 8 GHz and 12 GHz lenses are summarized in Table 1.

2.4. Slot Coupler

Each pair of elements is electrically connected by a narrow slot oriented transverse to the transmission line ends (Figure 2b). The three important parameters are the slot length, the slot width, and the length of transmission line extending past the slot. The slot length and width are based on preliminary results of experimental data by Franchi (unpublished), which we then scaled for the difference in frequency and dielectric constant between those experiments and our lens parameters. In the MCL, the slot must be made shorter than that of an optimum coupler so that it does not run underneath any of the patch elements or other parts of the transmission line.

The transmission lines should extend $\lambda_g/4$ past the center of the slot, where λ_g is the guide wavelength, minus a "length extension," Δl . The length extension is due to fringing at the end of the open-circuited line, which makes the line appear electrically longer. Hammerstad derived a very close approximate expression for that extension [6]:

$$\Delta l = .412h \frac{(\epsilon_{eff} + .3)(W/h + .264)}{(\epsilon_{eff} - .258)(W/h + .8)} \quad (6)$$

where ϵ_{eff} is the effective dielectric constant, W is the line width and h is the substrate thickness. The slot dimensions for the couplers are listed in Table 1.

3. EXPERIMENT

Figure 8 is a photograph of the circuit board that makes up the front lens face and the ground plane (8 GHz lens). In Figure 9 it is illuminated from the rear so that the slots are visible. The board that makes up the back face is similar, but does not have a ground plane. When the two boards are cemented together (with contact adhesive) the clad side of the front board serves as the common ground plane. Figure 1 shows the earlier version in the test fixture. During all pattern measurements an absorber shroud is placed over the region between the feed horn and the lens to prevent spillover multipath. The fixture allows the lens to be rotated $\pm 30^\circ$ on its baseplate while the feed remains fixed to scan the feed relative to the lens. The feed can be moved along its support, toward the lens, to change the focal length.

3.1. Mask Generation

Mask artwork for the experimental lenses was drawn on a Calcomp plotter with a 30" drum and a .015" liquid ink pen. The transmission line impedance was chosen so that its width would be at least twice the pen width to ensure reasonable accuracy. The masks were drawn on a 1:1 scale.

It can be difficult for a plotter to maintain precise accuracy over a large travel. That created a misalignment problem in the pin-coupled lenses: the feed thru holes were drilled by a computer-controlled milling machine, which had a very slight scale difference in one direction relative to the mask plotter. Consequently, the mask did not line up precisely with the pre-drilled holes and some of the feed thru

pins were not centered in the holes in the ground plane. This is one very important reason for going to the slot-coupled design - all three levels of the mask are drawn by the same machine, in sequence, and scale errors will affect them all the same, with no resulting misalignment.

3.2. 8 GHz Lens

The new 8 GHz lens was intended to directly replace the earlier pin-coupled version, so it has the same 40" focal length and 20" aperture diameter. Figure 10 shows scanned patterns of that earlier lens. Although these tended to demonstrate its wide angle scanning properties, the pattern shape is poor, and the peak gain indicated an overall efficiency of only 29%.

The new lens is only slightly better in the latter respect (31%). This tends to indicate that the feed thru mechanism has the same amount of loss. The H-plane scanned patterns shown in Figure 11 are much better focused than those in Figure 10. We attribute this to better alignment of the feed thrus, which was a major source of error in the pin-coupled lens. The new lens has about 8% bandwidth, measured between -3 dB gain points.

The E-plane scans are shown in Figure 12. Their asymmetry may be due to the close proximity of the feed lines to patch radiating edges, which is worse in some regions of the array than others. This could be avoided by using smaller transmission line bends. Stray radiation from the feed thrus is another possible source - since they all lie on the same side of the patches in the E plane they would tend to corrupt the patterns more in that plane.

Reflection from the feed thru can be estimated by the relative strength of the back lobe, which we observed by scanning the feed to about 2° off axis, and measuring the pattern in the direction opposite the main beam (with the absorber shroud removed). In the very first lens version, we had observed a well-focused back lobe. Since the total transmission line length is divided equally between the two faces, energy that is received by one face and reflects from the feed thru to be reradiated by the same face will tend to be focused. By contrast, energy that reflects directly from the surface will radiate with the unfocused feed horn pattern. In this new version the back lobe is 4 dB lower than the main beam. Thus, the feed thru and surface reflection together account for about 1.5 dB of the total loss. Another 1.5 dB is lost in the transmission lines - the circuit board material is epoxy-fiberglass, which is fairly lossy. Use of low loss substrate would improve the lens efficiency by up to 10%.

The conclusions we draw from this experiment is that the slot coupled lens performs at least as well as the pin coupled lens in all respects, but that the coupler design still needs some improvement to reduce its reflection.

3.3. 12 GHz Lens

The 12 GHz lens was a much more demanding case. Its focal length is 30", with the same 20" aperture diameter. The reduced F/D ratio increases the disparity in line lengths between the center and edges. That effect is evident in Figure 13, a photograph of the back face.

The reduced focal length also increases the distance between front

and back face elements, $p-r$. Near the edges, that distance was so large that the mask layout problem was intractable. To make that job easier, we chose to expand the front face lattice (after calculating the back face element locations and transmission line lengths) by a constant. The "K" factor, the inverse of the expansion constant, was about .96. Its side effect is that it changes the beam scan angle. A feed located at angle θ will produce a beam at a different angle, ψ [7]:

$$\sin \psi / \sin \theta = K. \quad (7)$$

The initial front face coordinates, r , were calculated for an equilateral lattice with slightly reduced element spacing to prevent grating lobes with the later expanded lattice.

This lens was fed with a pyramidal horn whose aperture dimensions are 2.1"x2.5", and gave an edge taper of about -6 dB. The lens' gain was measured at 22.7 dBi, which was the peak at 11.8 GHz. The bandwidth between 19.7 dBi gain points is about 9%. Feed horn losses, taper loss and spillover loss are estimated at 6.5 dB. The estimated efficiency is 18%. Of the losses in the lens, 2.5 dB is dissipated in the transmission lines. Since the back lobe is 1.1 dB higher than the main beam, the feed thru and surface reflection losses account for over half the total loss.

H plane and E plane scanned patterns are shown in Figures 14 and 15, respectively. The sidelobes in these are considerably higher than they should be, which is due to two factors: first, the transmission lines come too close to the patch radiating edges, and that is much more severe a problem than it was in the 8 GHz lens because the smaller

inter-element spacing leaves less room for the lines. Second, there is appreciable radiation from the slot couplers. Figure 16 is the cross polarized pattern, whose peak is only 14 DB below that of the co-polarized pattern. Evidently, the feed thru will capture cross polarized energy from the far field and route it along the transmission lines to be re-radiated by the back face. Since it has then gone through the differential line lengths, it is partially focused.

From these experiments, we draw the following conclusions: (1) the microstrip constrained lens can form beams to at least 12 beamwidths off axis in any ϕ plane; (2) a better feed thru design and a low loss substrate would increase efficiency substantially; and (3) close proximity of transmission lines to patch radiating edges needs to be avoided, although it will further complicate the mask layout.

4. CONCLUSIONS

These experimental models have shown that the microstrip constrained lens is a viable antenna concept. It is very lightweight and inexpensive and easy to construct, especially with the slot type feed thrus. It can scan to moderately wide angles due to the use of two degrees of freedom, and thus lends itself to electronic scanning applications. Although the experimental models had fairly low efficiencies, minor improvements can raise that substantially, and those are suggested areas for further research: efficient slot couplers; wide angle impedance matching to reduce surface reflection; and low loss substrate to reduce transmission line attenuation.

REFERENCES

1. Daniel T. McGrath, "A Lightweight Constrained Lens for Wide Angle Scan in Two Planes," Proceedings of the 1986 Antenna Applications Symposium, Sep. 1986.
2. Hubert Gent, "The Bootlace Aerial," Royal Radar Establishment Journal, pp. 47-57, Oct. 1957.
3. Daniel T. McGrath, "Planar Three-Dimensional Constrained Lenses," IEEE Transactions on Antennas and Propagation, Vol. AP-34, pp. 46-50, Jan. 1986.
4. D. H. Schaubert, F. G. Farrar, and A. Sindoris, "Microstrip Antennas with Frequency Agility and Polarization Diversity," IEEE Transactions on Antennas and Propagation, Vol. AP-29, pp. 118-123, 1981.
5. Daniel A. Mullinix and Daniel T. McGrath, "Rectangular Microstrip Patch Antenna Arrays," RADC-TR-86-151, Oct. 1986. ADA179170
6. K. C. Gupta, R. Garg and R. Chadha, Computer Aided Design of Microwave Circuits, Artech House, 1980.
7. George D. M. Peeler, "Lens Antennas," Antenna Engineering Handbook, pg. 16-20, McGraw-Hill, 1984.

Table 1. Lens Design Parameters

Parameter	8 GHz Lens	12 GHz Lens
Aperture Diameter, D	20"	20"
Focal Length, F	40"	30"
On-Axis Beamwidth	5.2°	3.5°
Microstrip Patch		
Length, b	.327"	.213"
Width, a	.457"	.258"
Inset, d	.095"	.062"
Transmission Lines		
Width, w	.060"	.039"
Impedance, Z ₀	71Ω	85Ω
Slot Coupler		
Slot Length	.240"	.160"
Slot Width	.050"	.033"



Figure 1. Microstrip Constrained Lens in Test Fixture with Pyramidal Horn Feed.

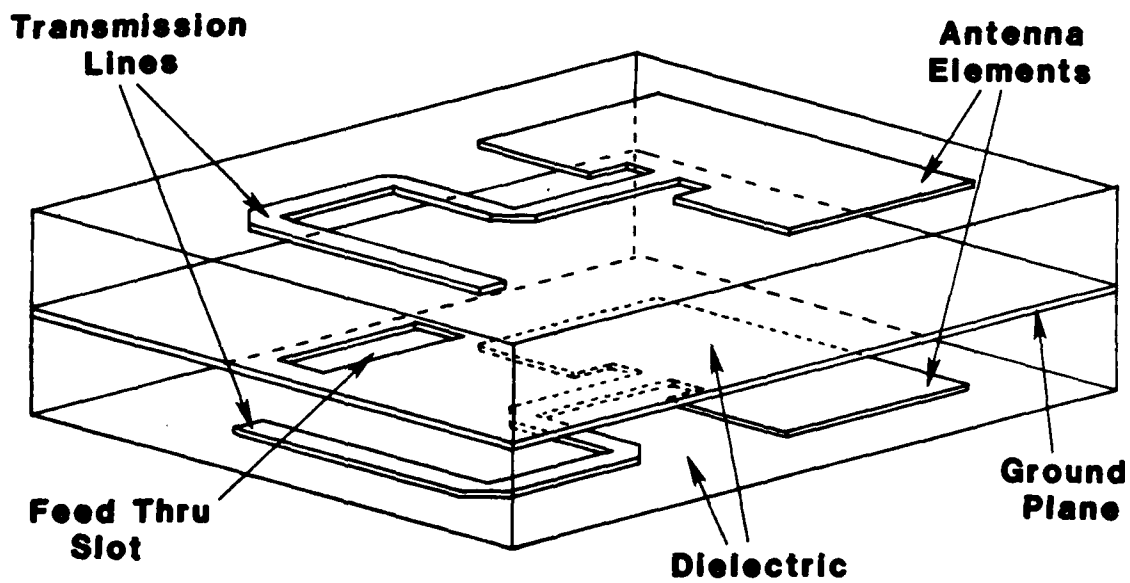
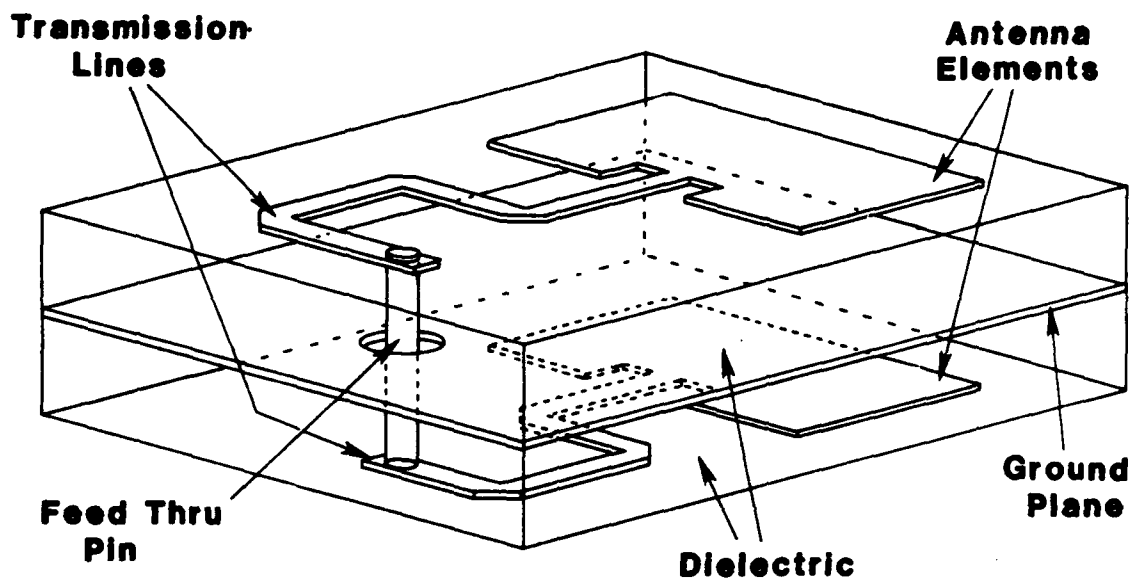


Figure 2. Cutaway Views of the Two Lens Types: (a) Pin Type Feed Thru; (b) Slot Type Feed Thru

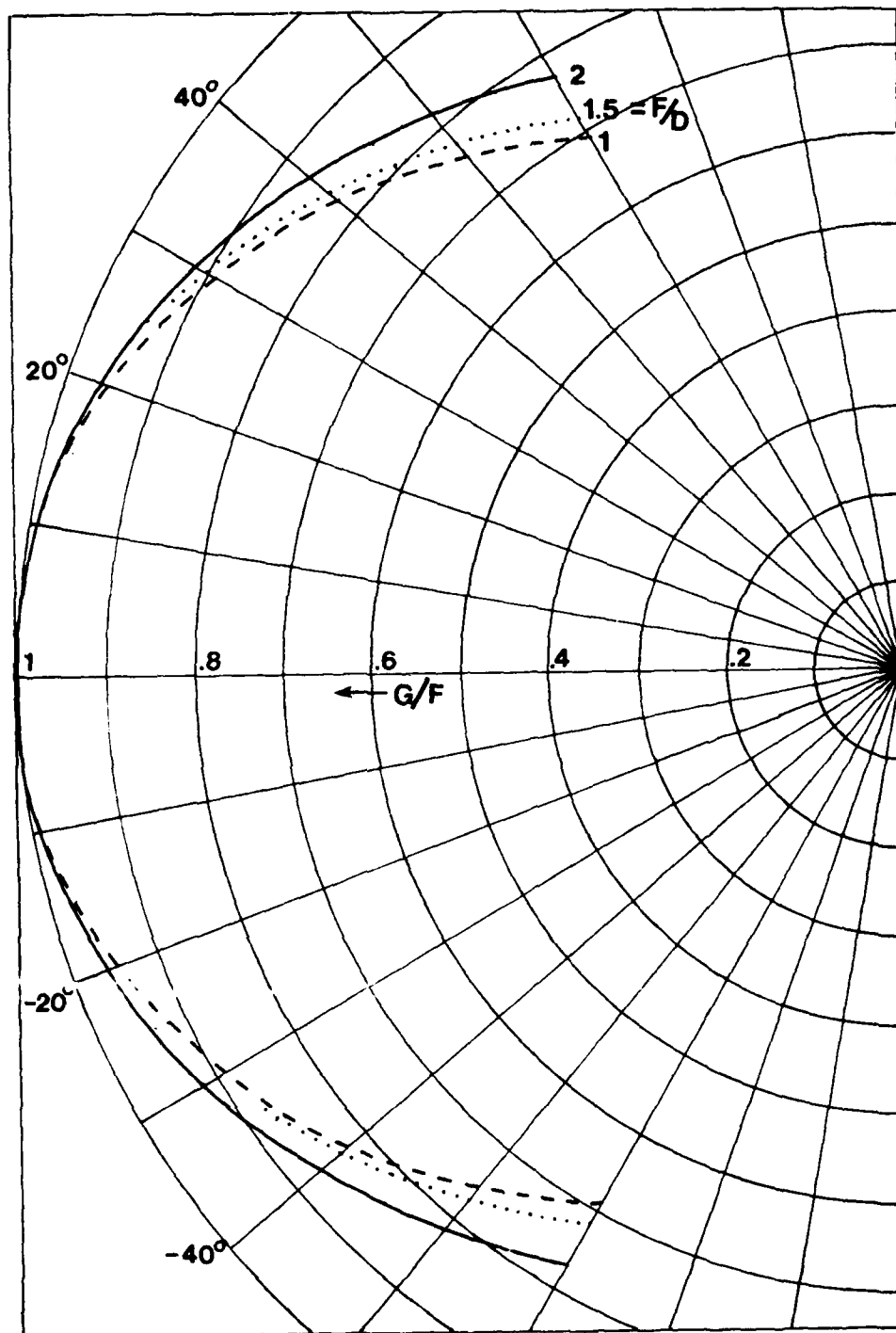


Figure 3. Focal Arc Contours (G/F vs. θ) for Three F/D Ratios

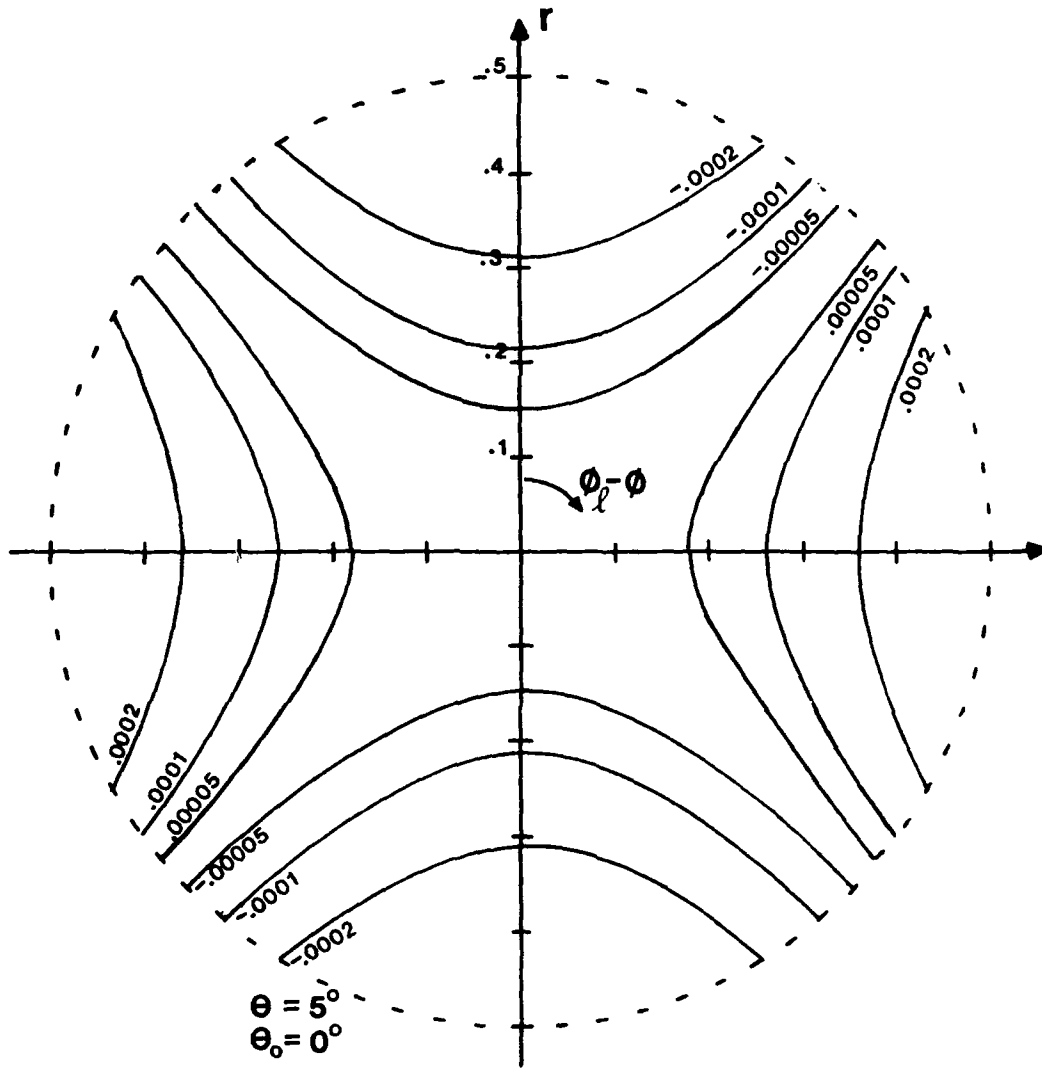


Figure 4. Path Length Error Contours ($\Delta l/F$) in the Aperture Plane for a Two Degree of Freedom Lens with $\theta_0 = 0$, $F/D = 1$, and Feed Scanned to 5°

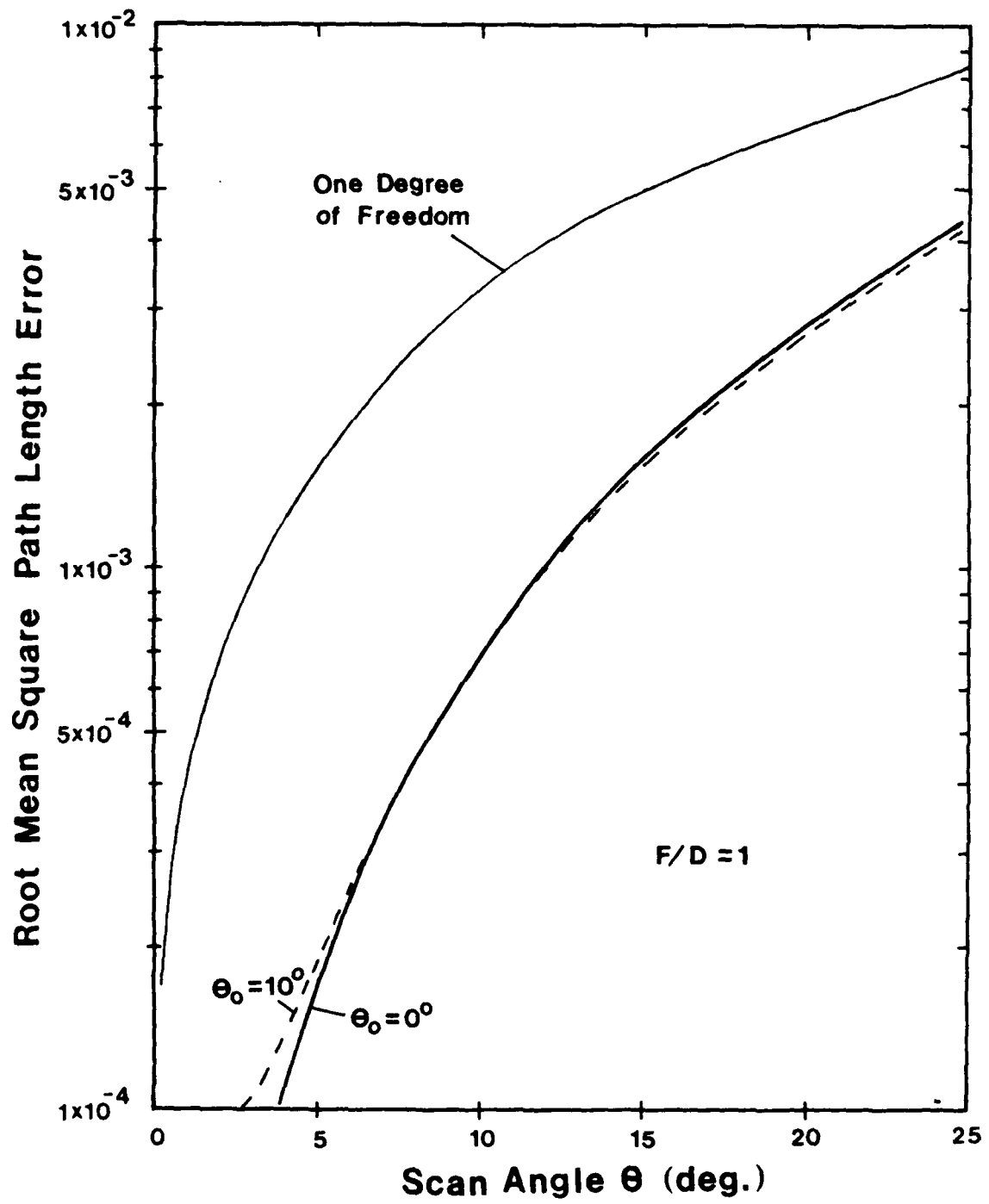


Figure 5. Root Mean Square Path length Error vs. Scan Angle for Axially-Symmetric Lens Designs

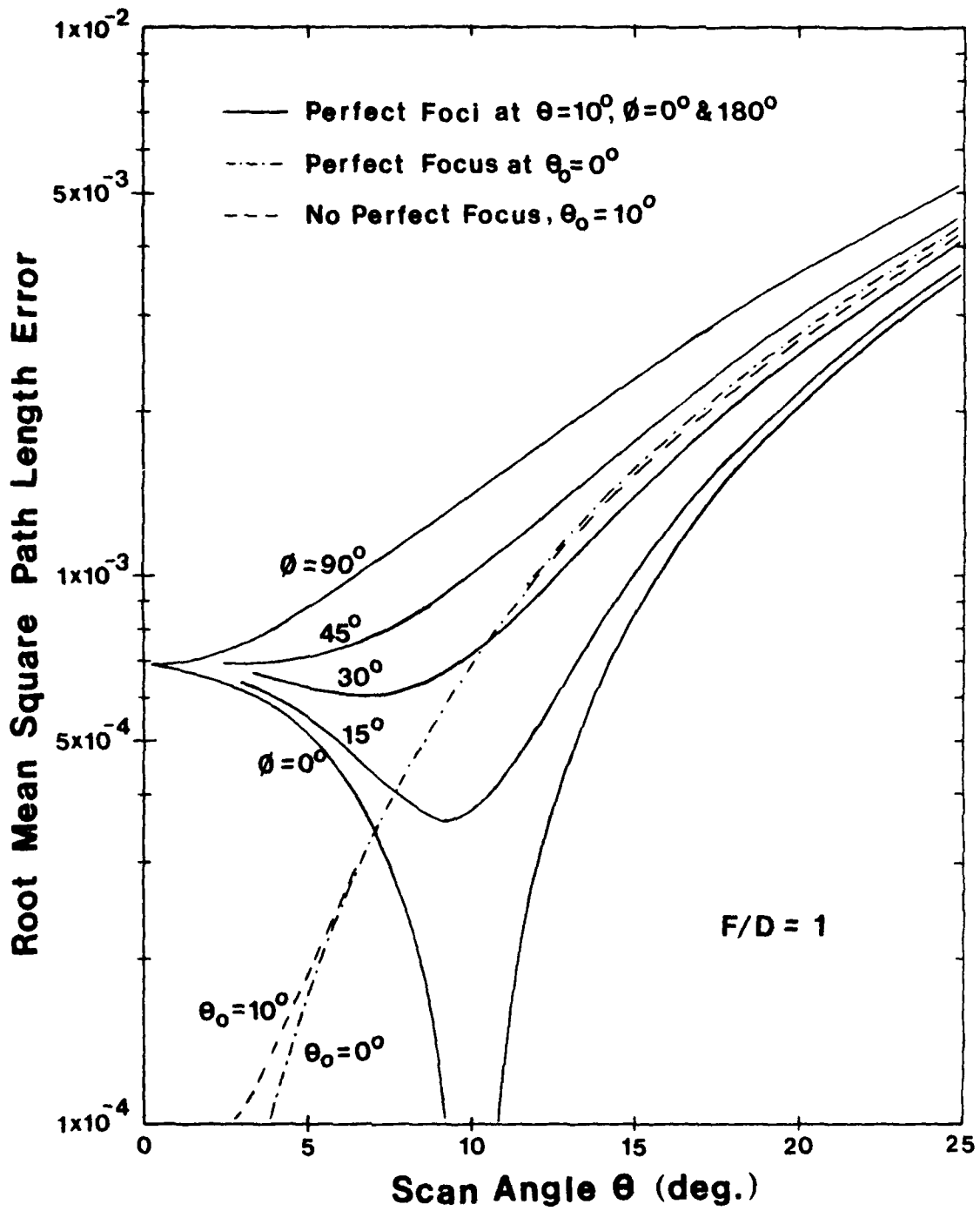


Figure 6. Root Mean Square Path Length Error vs. Scan Angle for a Bifocal Lens with Focal Points at $\theta_0 = \pm 10^\circ$

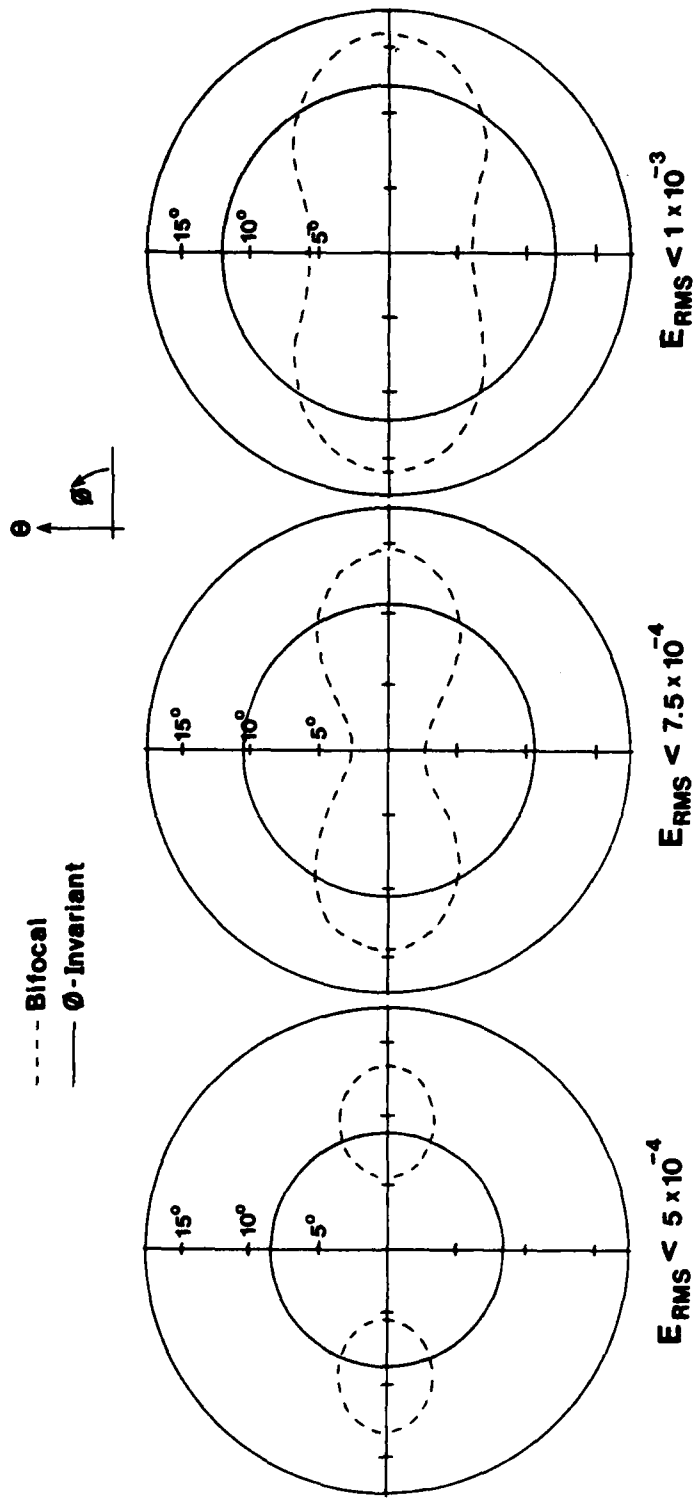


Figure 7. Comparison of Scanning Regions for Bifocal (dashed) and Axially-Symmetric Lens Designs



Figure 8. Photograph of the 8GHz Lens Front Face



Figure 9. Photograph of the 8GHz Lens Front Face Circuit Board. (It is lighted from the back so that the slot coupler apertures are visible.)

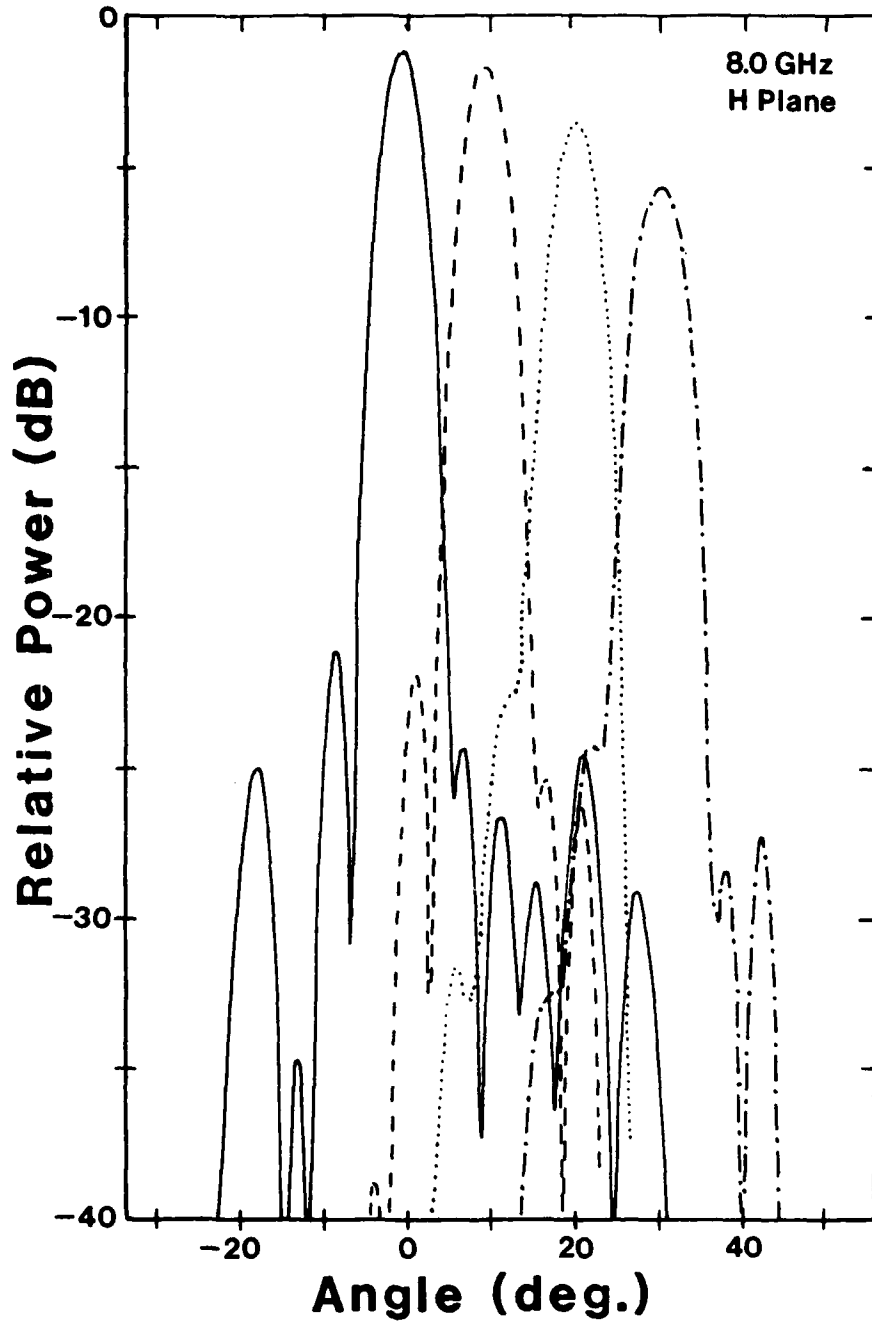


Figure 10. H Plane Patterns of the Earlier (Pin-type couplers) 8 GHz Lens.

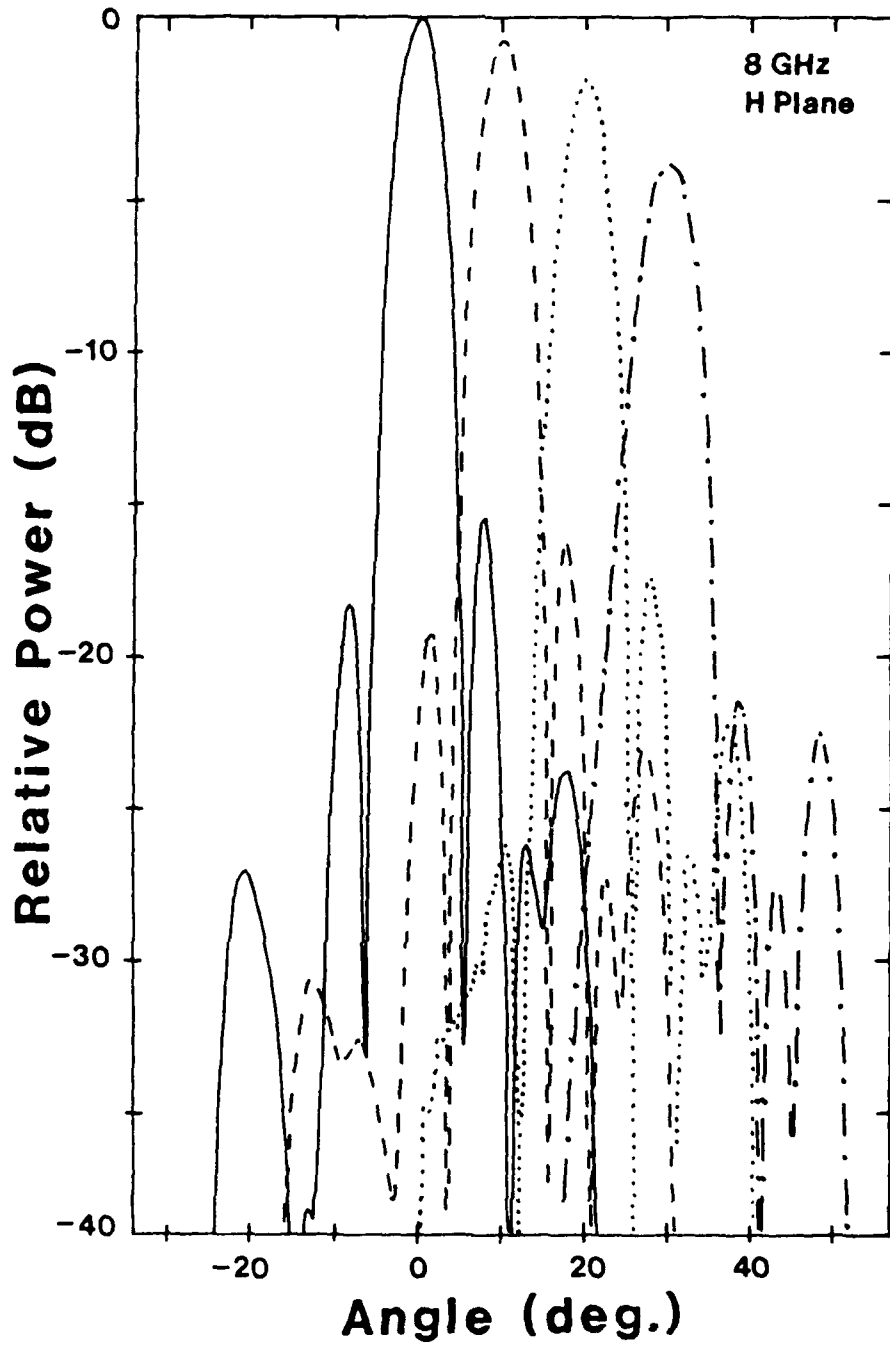


Figure 11. H Plane Patterns of the New 8GHz Lens (slot type couplers)

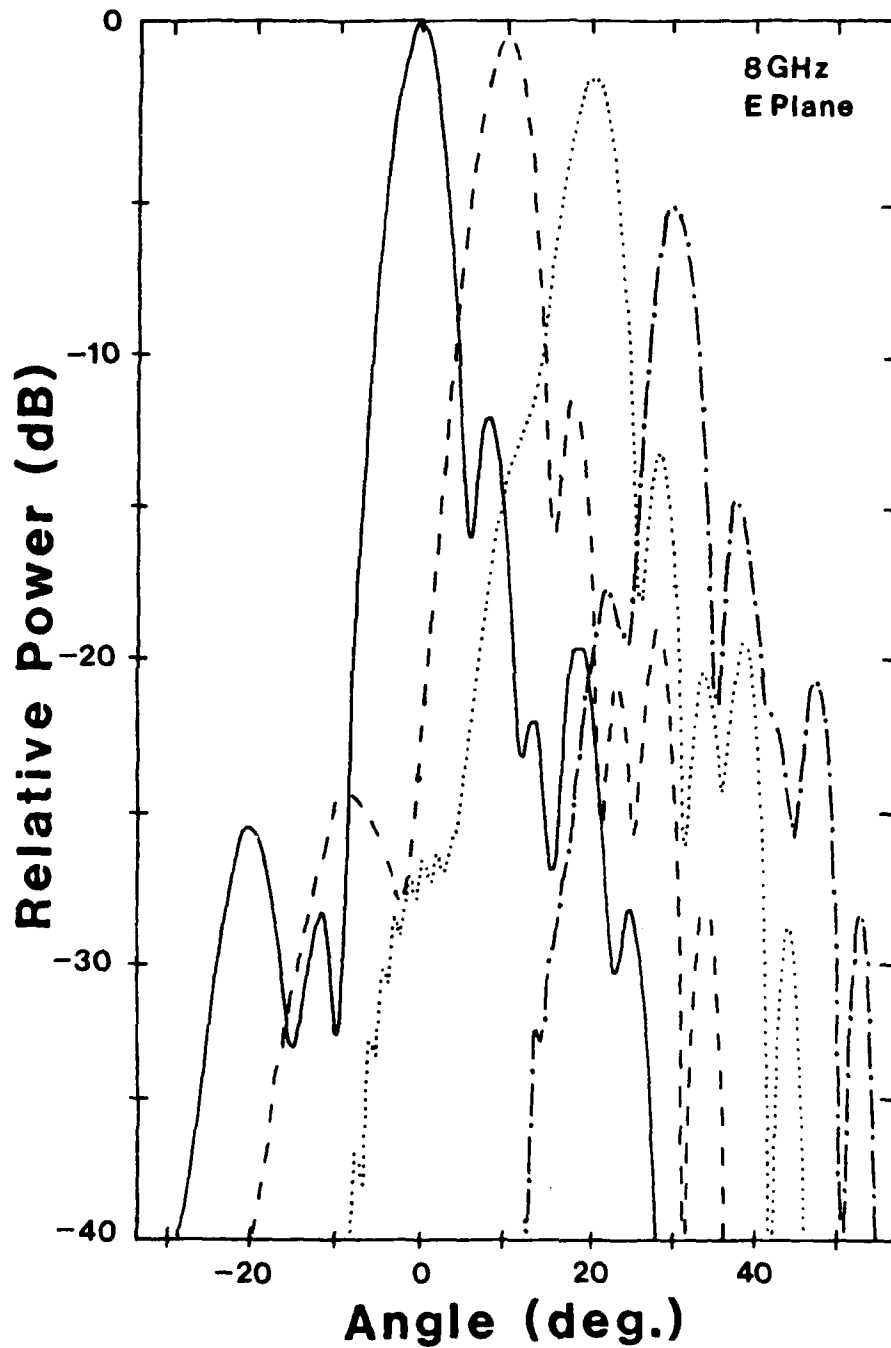


Figure 12. E Plane Patterns of the New 8 GHz Lens.

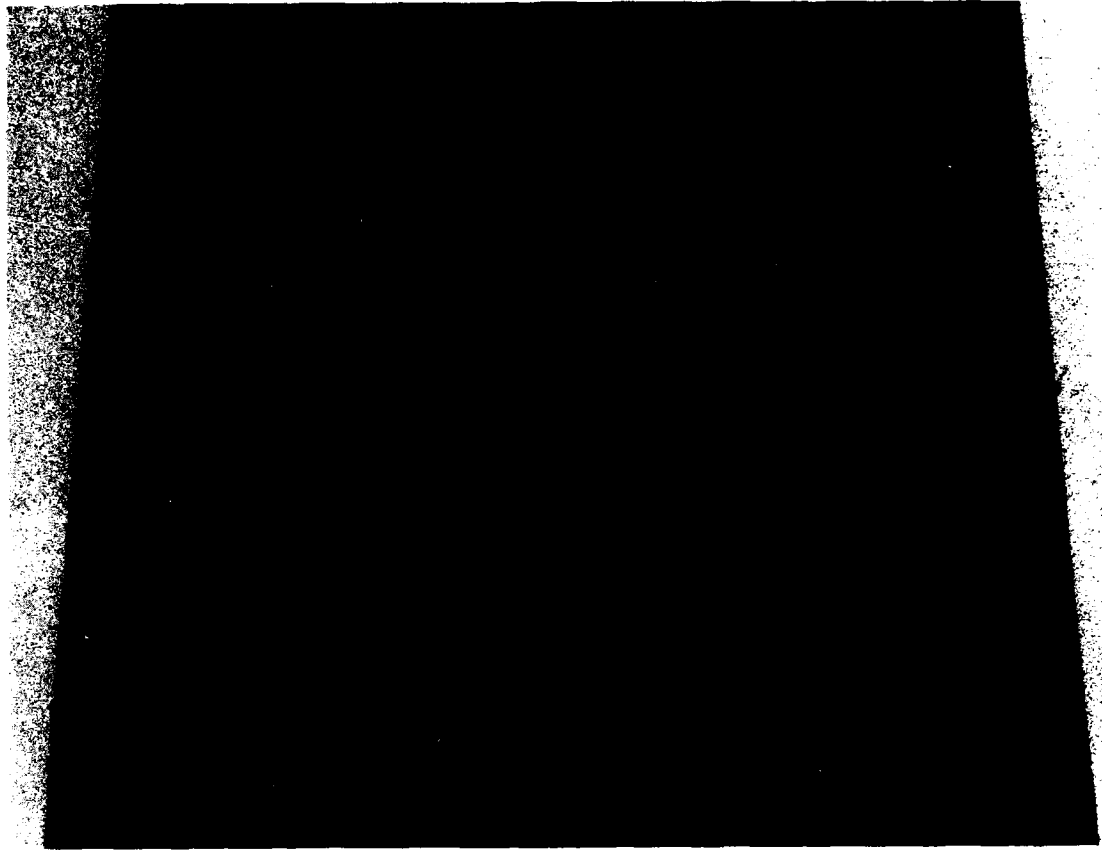


Figure 13. Photograph of the 12GHz Lens Back Face.

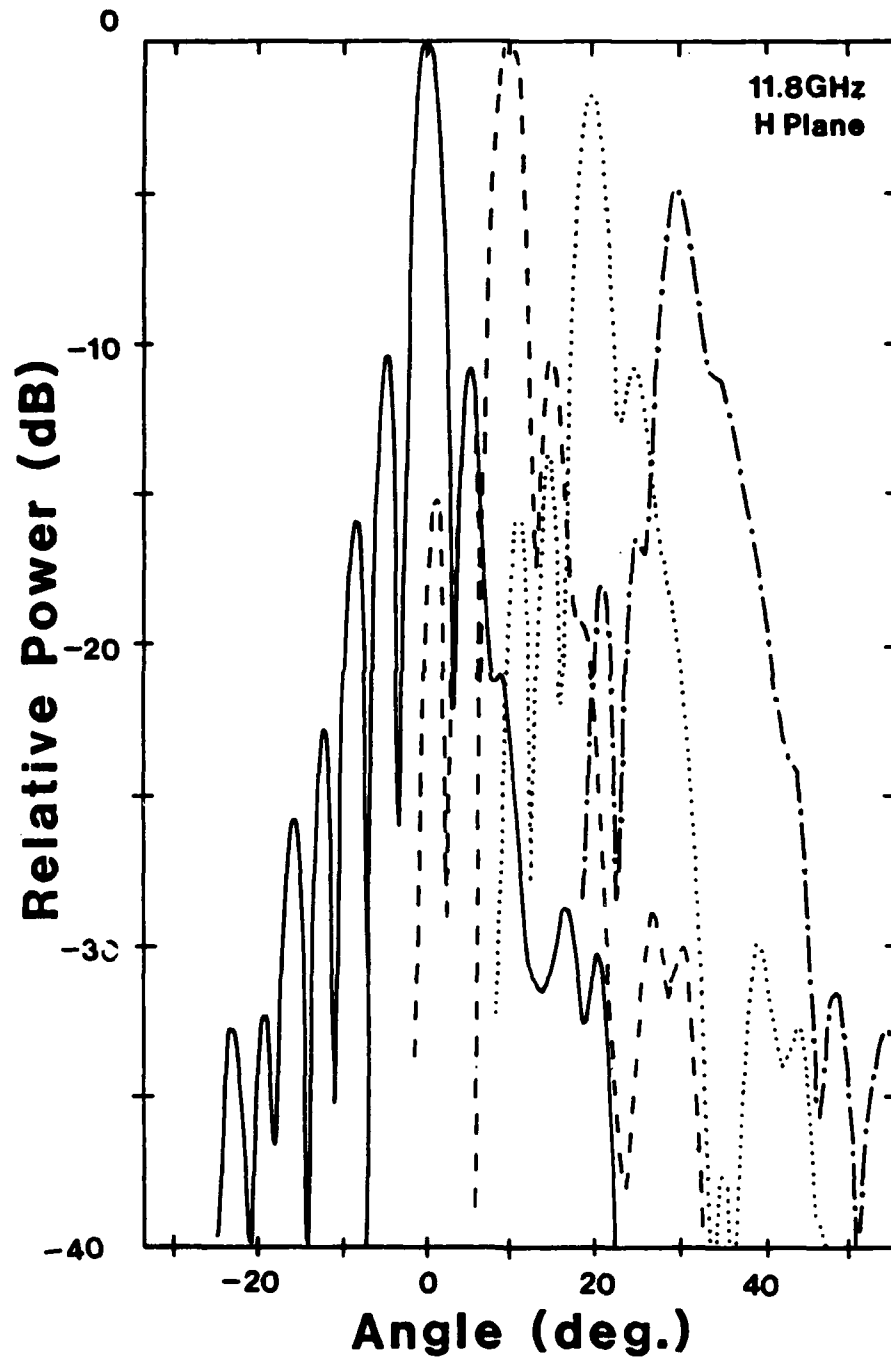


Figure 14. H Plane Patterns, 11.8 GHz.

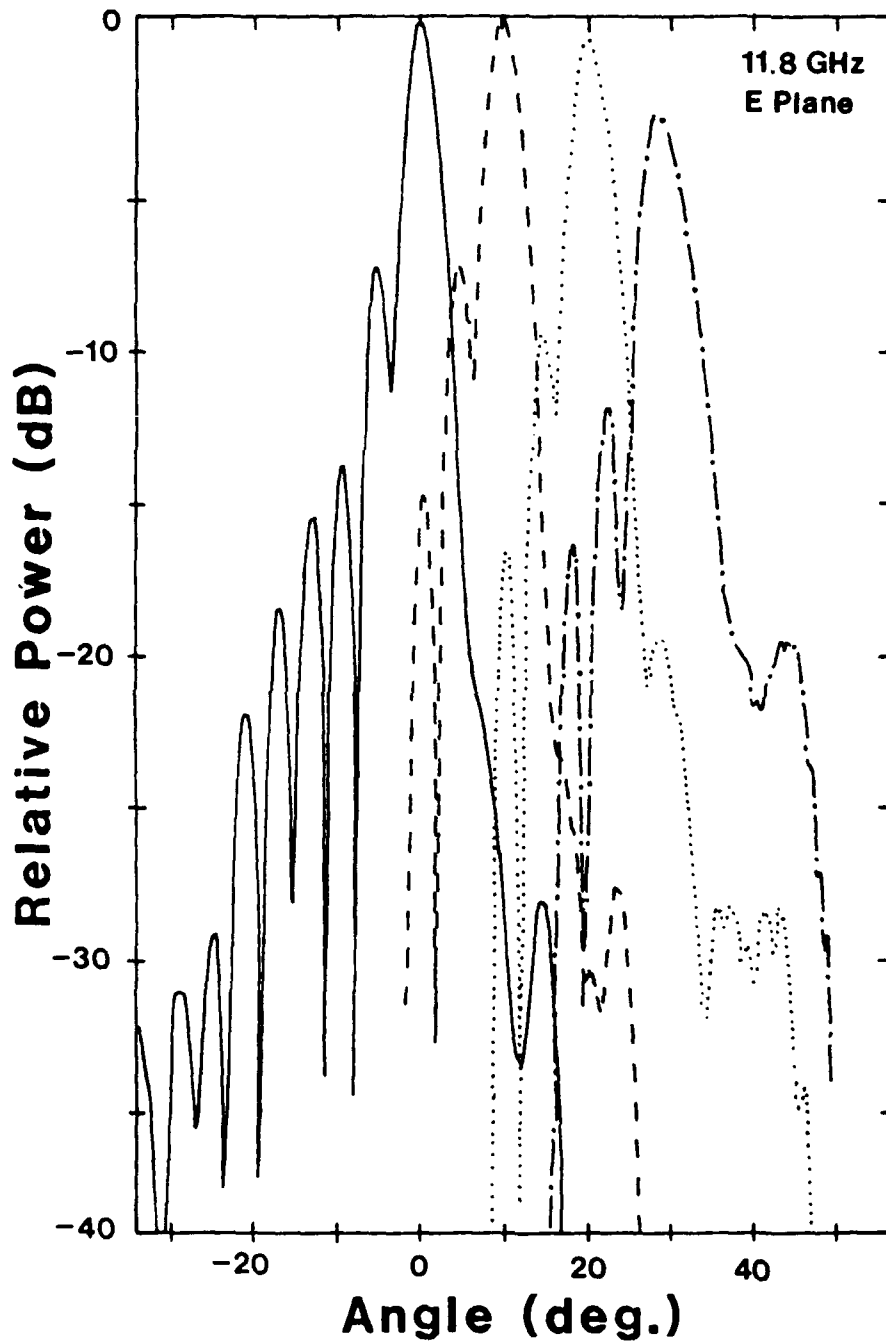


Figure 15. E Plane Patterns, 11.8 GHz.

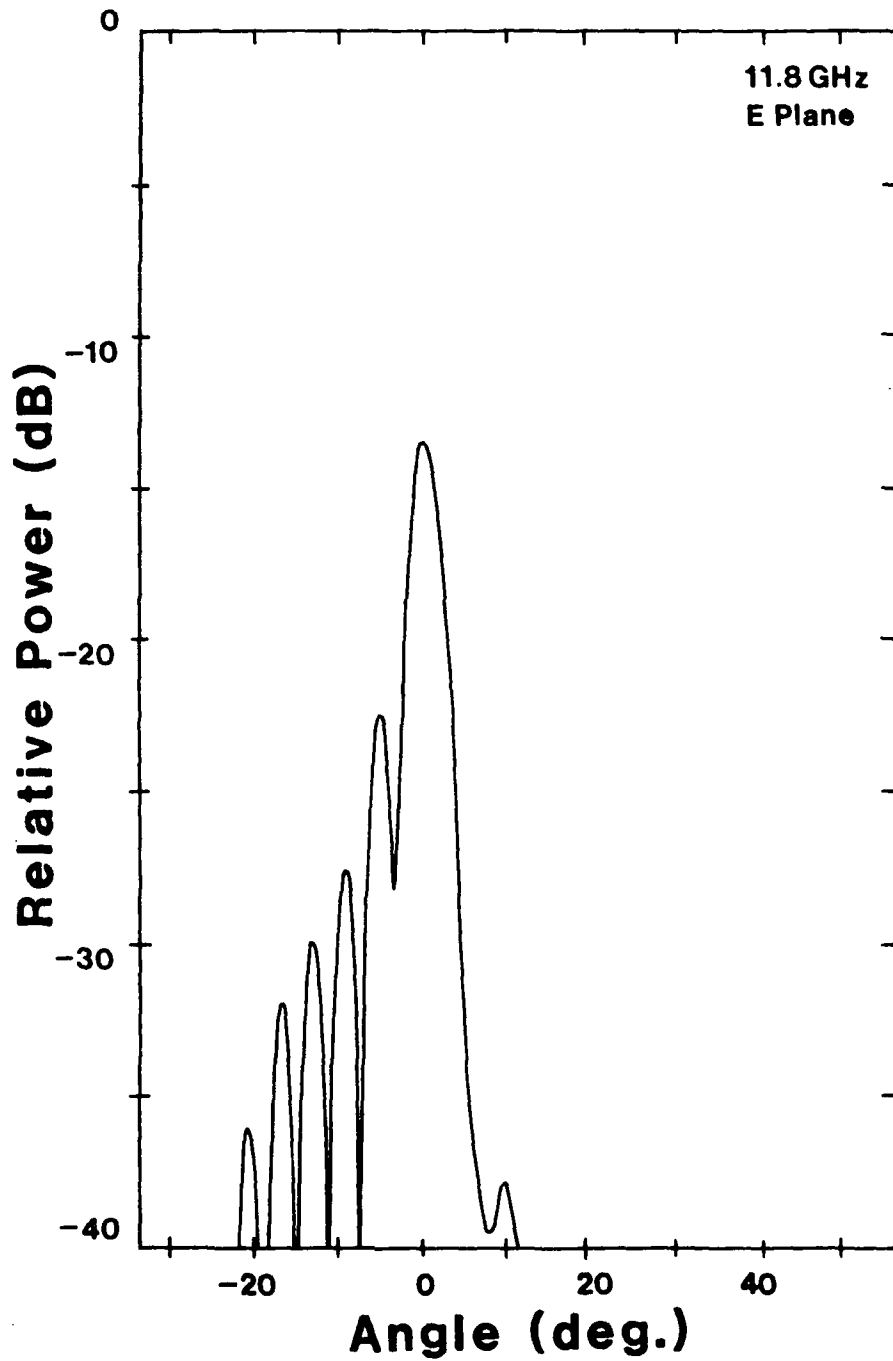


Figure 16. Cross Polarized E Plane Pattern, 11.8 GHz.

ON THE BEHAVIOR OF ADAPTIVE LENS AND FEED ANTENNAS

M. SANTANA AND R. BLAU

RAYTHEON COMPANY

ABSTRACT

The behavior of a conventional adaptive planar array in the presence of more than one interfering signal has been studied extensively (1). If the signals arrive with widely differing amplitudes, the covariance matrix has eigenvalues that also differ widely in amplitude, and convergence can be very slow. Two signals that arrive with the same amplitude exhibit no such convergence problem.

On the other hand, a space-fed antenna system (whether the lens is of the array type or not) behaves quite differently. There appears to be a "barrier angle": Two equal amplitude signals both arriving at one side or the other of this angle are readily nulled. However, if the two signals straddle the barrier angle, the eigenvalue spread is large, and convergence is slow.

This phenomenon, surprising when first encountered, is readily explained in terms of the geometry of the lens and feed systems. For lenses much larger than the feed, the barrier angle is a function of the beamwidth of the antenna, plus the angle subtended by the feed at the focal point. As with other types of antennas, eigenvalue spread is more troublesome for algorithms of the steepest descent types than for those employing some approximation to direct matrix inversion.

DISCUSSION

Simple adaptive phased array systems have been studied in detail by Widrow et. al. (2), Mayhan (3), and others. For the case of a planar array of point sources, the convergence time to null a pair of equal magnitude interferences, for example, is independent of the two directions of arrival. Each element receives equal amplitudes from each of the incident plane waves,

and the corresponding covariance matrix has eigenvalues of comparable magnitude. For a lens and feed system, however, this is not necessarily true. The covariance matrix of a weighted feed system can exhibit significant eigenvalue spread, depending on the directions of the two equal magnitude interferences.

Consider, for example, the miniature lens and feed array in two dimensions of Figure 1 for which extensive computer simulations have been run. Each lens element is considered to have a phase shifter which focuses a wave on boresight at the center of the feed, and each feed element has a complex weight. Numerous nulling algorithms all related to gradient based methods were tried, principally algorithms derived from the well known Widrow Least Mean Square (LMS) algorithm⁽⁴⁾.

Versions of this algorithm were tried with and without a mainbeam constraint⁽⁵⁾, and similar results were obtained for all of them. The simplest form of such algorithms, without a mainbeam constraint, can be written:

$$W_{K+1} = W_K - 2\mu \frac{\langle W_K, X \rangle}{\langle X^*, X \rangle} X. \quad (1)$$

In Equation (1), assuming there are M feed elements, W_K is the set of M complex numbers representing the Kth set of weights, X is the set of M interference voltages, μ is a real convergence factor, and the inner product notation is defined by:

$$\langle W_K, X \rangle = \sum_{i=1}^M W_K(i) X(i).$$

(The weighted sum $\langle W_X, X \rangle$, the entire signal environment, represents an error which the iterations of Equation (1) attempt to drive to zero. This is valid in, for example, a radar system which nulls before it transmits.)(6)

In the presence of two interfering sources of equal magnitude the system under Equation (1) in 2-dimensional space exhibits a barrier angle. This is an angle, symmetric about boresight, which determines the degree of eigenvalue spread in the covariance matrix due to the two interferences. If the interference of signals are both on one side or both on the other side of the barrier angle, the magnitudes from each source received at the feed are comparable, and the eigenvalue spread is small. On the other hand, if the two straddle the barrier angle, the magnitudes from each of them (as received at the feed) differ widely, the eigenvalue spread is large, and convergence is roughly 1000 times slower. In three dimensional space one has, instead of an angle, a right cone of elliptical cross-section.

When first encountered, the barrier angle comes as a surprise; for example, it is not related in any simple way to the features of the far field pattern. As a matter of fact, it is approximately equal to half the angle subtended by the lens at the center of the feed plus half the beamwidth.

Its existence can be understood in the following way. If the feed elements are connected to a simple sum network, power reaching the receiver is proportional to the square of:

$$|V| = \left| \sum_{i=1}^M W_i X_i \right| \quad (2)$$

As the weights change, this magnitude changes also. However, for normalized weights, an upper bound to this power is, according to Schwarz's inequality,

$$|v|^2 \leq \sum_{i=1}^M |x_i|^2 \quad (3)$$

Figure 2 shows a plot of the right hand side of (3) in arbitrary units, as a function of the angle of a single interference source. The barrier angle for this case was found to be ± 13 deg. Two signals arriving at the lens with equal power and straddling the barrier angle reach the feed with markedly different power levels. It is well known⁽⁷⁾ that such a power differential causes eigenvalue spread and slow convergence in gradient-based algorithms. The 3 dB beamwidth of the antenna, for pre-adaption weights, is approximately 5 deg. There is no contradiction here; Figure 2 is not an antenna pattern. It is a plot, for a source of a given magnitude, of the maximum power, as a function of angle, that can output the feed network for any set of weights. The comparable plot, for a simple phased array, would be a horizontal straight line.

For the purposes of illustration, the same antenna with the same two-source source scenario, was adapted via a different type of algorithm. It is well known⁽⁸⁾ that methods which invert the covariance matrix, either exactly or approximately, are much less sensitive to eigenvalue spread problems than steepest descent type algorithms. This remains true so long as the smallest eigenvalue lies well above the noise level⁽⁸⁾. One such algorithm, the Weighted

Least Squares⁽⁹⁾ (WLS) is compared with the LMS algorithm of Equation (1) in Figure 3. For each algorithm, two sets of two jammers straddling the barrier angle were used.

The algebra of the WLS method may be summarized as follows: the (t+1)'th sum and difference weights are given by

$$W_{t+1}(i) = W_t(i) - \frac{\sum_{k=1}^M P_t(i,k) X_{t+1}(k)}{C} - \sum_{\ell=1}^M W_t(\ell) X_{t+1}(\ell)$$

where the complex number C is given by

$$C = \alpha + \sum_{k=1}^M \sum_{\ell=1}^M X_{t+1}(k) P_t(k,\ell) X_{t+1}(\ell)$$

and where α is a real number between 0 and 1.

The (t+1)th update of the matrix P is given by

$$P_{t+1}(i,j) = \frac{1}{\alpha} P_t(i,j) - \frac{\sum_{k=1}^M \sum_{\ell=1}^M P_t(i,k) X_{t+1}(k) X_{t+1}(\ell) P_t(\ell,j)}{C}$$

For the miniature antenna described above, P_0 was chosen as the unit matrix, the starting sum weights were 1,0,0,0 whereas the starting difference weights were 0,0,0,1.

Referring to Figure 3, it is apparent that, for equal magnitude signals on opposite sides of the barrier angle, the LMS algorithm requires 1000 times more iterations than the WLS. (For signals on the same side of the barrier angle, the number of iterations is about the same.) Of course, each iteration of the WLS involves considerably more algebra than the LMS. However, no direct matrix inversions are involved, and the net gain in processing time in many cases of practical importance is substantial.

-
- (1) Monzingo, R. A. and Miller, T. W. (1980) Introduction To Adaptive Arrays, John Wiley and Sons, N.Y., Chapters 4 and 7.
 - (2) Widrow, B., Mantey, P. E., Griffiths, L. J. and Goode, B. B. (1967) Adaptive Antenna Systems, Proceeding IEEE 55 (No. 12): 2143 - 2159.
 - (3) Mayhan, J. T. (1978) Bandwidth Limitations on Achievable Cancellation For Adaptive Nulling Systems, Technical Note 1978-1, MIT Lincoln Laboratory, MA., Appendix I.
 - (4) Widrow, B. (1966) Adaptive Filters I: Fundamentals, Tech. Report 6764-6, Stanford Electronics Laboratories, CA, Rept. SEL-66-126.
 - (5) Appelbaum, S. P. and Chapman, D. J. (1976) Adaptive Arrays with Mainbeam Constraints, Trans. IEEE, AP-24 (No. 5); 650 - 662.
 - (6) In some cases, independent sets of weights are necessary. See, for example, Haupt, R. L. (1984) Simultaneous Nulling in the Sum and Difference Patterns of a Monopulse Antenna, Trans. IEEE, AP-32 (No. 5): 486 - 493.

(7) Monzingo, R. A. and Miller, T. W. (1980) Introduction to Adaptive Arrays, John Wiley and Sons, NY, 390.

(8) *ibid.*, Chapters 6 and 7.

(9) *ibid.*, P 319 ff.

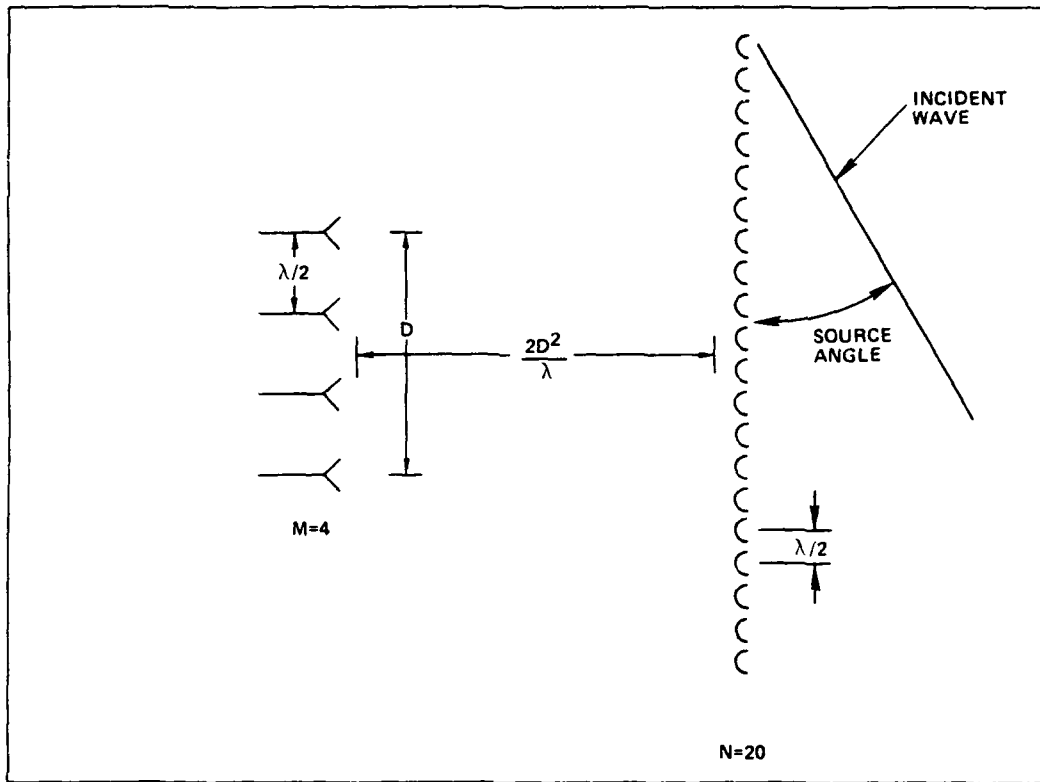


Figure 1. Two-Dimensional Miniature Lens and Feed System

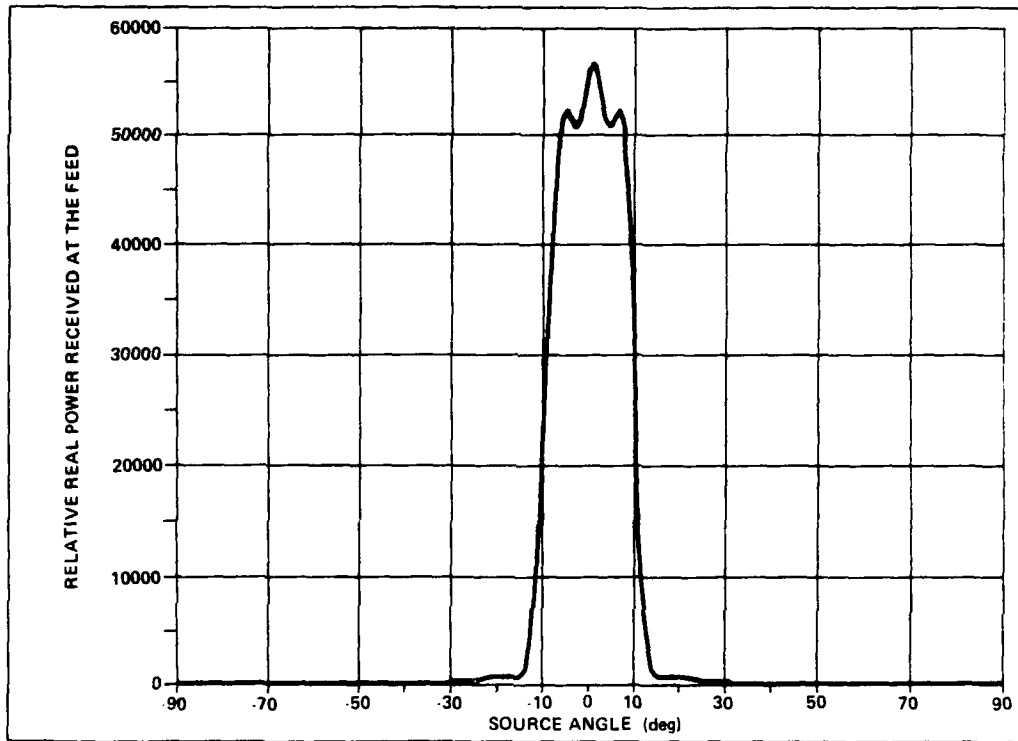


Figure 2. Total Real Power into the Feed vs Source Angle

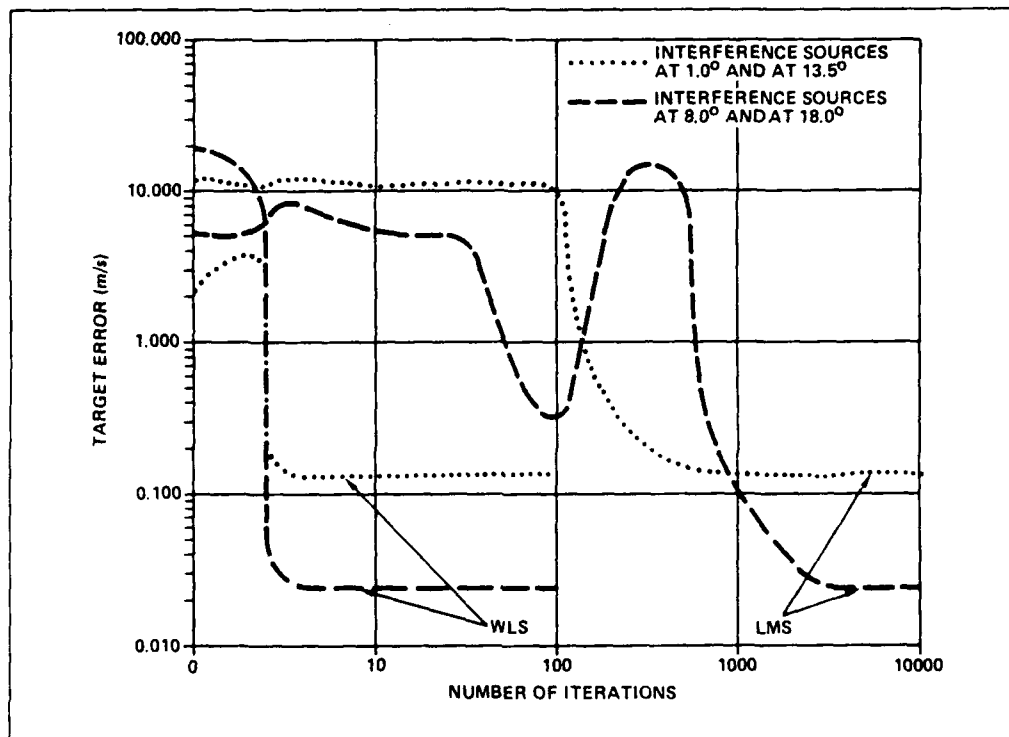


Figure 3. Convergence of the WLS Algorithm vs the LMS Algorithm

A STOCHASTIC CONJUGATE GRADIENT ALGORITHM FOR ADAPTIVE ARRAYS

Hosny M. Ibrahim, Nour El-Din M. Ibrahim

Faculty of Engineering, Electrical Dept., Assiut University,
Assiut, Egypt

ABSTRACT

In the present paper, a version of the conjugate gradient (CG) algorithm which has been used extensively in minimization problems is utilized for application in adaptive arrays. This algorithm is characterized by its fast convergence characteristics; in fact its convergence is quadratic. The mean square error (MSE) criterion is adopted. An analysis of the convergence characteristics and the excess MSE (misadjustment) for the CG algorithm under stochastic signal environments is presented.

Simulation results which show the different characteristics of the CG algorithm compared with the least mean square (LMS) algorithm are given.

1. INTRODUCTION

During the past two decades, many algorithms have been developed and utilized in the field of adaptive antenna system.¹⁻⁴ Due to its simplicity and ease of implementation,

the least mean square (LMS) algorithm developed by Widrow¹ has found widespread use in this area. However, the LMS suffers slow convergence especially when the spread of the eigenvalues of the signal covariance matrix is large.

Although the CG algorithm, developed by Hestenes and Stiefel⁵ to solve a set of simultaneous equations, is characterized by quadratic convergence and can overcome the problem of eigenvalue spread, it did not find widespread use in adaptive arrays. This is due to the hardware complexity, increase in computation, and memory requirements over the LMS algorithm. However, it is believed that due to the fast progress in the area of large and very large scale integrated circuits, these problems will recede in favor of the fast convergence of the CG algorithm.

In the present paper, a version of the CG algorithm developed by Fletcher and Reeves⁶ is utilized.

Section 2 introduces the conjugate gradient algorithm under stochastic signal environments. Section 3 presents the convergence analysis and the excess mean square error (MSE). Section 4 presents simulation results and discussion, and section 5 is a conclusion.

2. THE STOCHASTIC CONJUGATE GRADIENT ALGORITHM

The basic arrangement for the adaptive antenna system utilizing the mean square error (MSE) criterion is shown in Fig. 1. The signal from each element is multiplied by a variable weight before it is summed to give the array output. This output is compared with a reference or desired signal to give an error signal. The adaptive algorithm varies the weights in such a

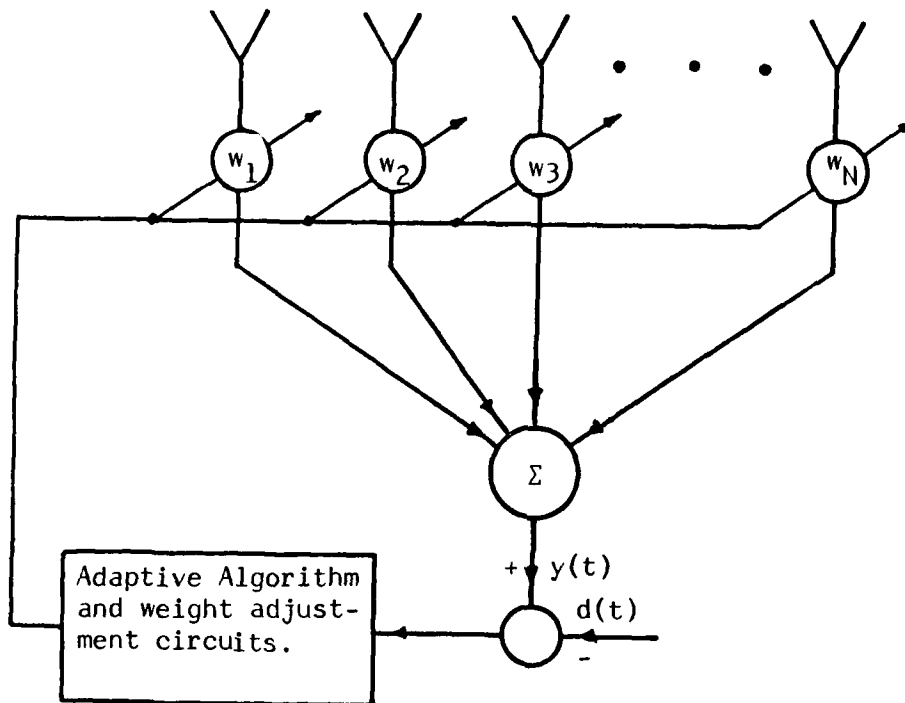


Fig. 1. Basic adaptive system utilizing mean square error criterion.

way that the MSE is minimized. Mathematically this can be written as follows :

The error signal at the jth sample is

$$\epsilon(j) = d(j) - W^T X(j) \quad (1)$$

where $d(j)$ is the desired signal

W is the weight vector

$X(j)$ is the input signal vector.

The superscript T means transpose. Both W and X have N -component each.

Squaring both sides of Eq.(1) and taking the averages we get¹

$$\xi_k(W) = E |\epsilon^2(k)| = \overline{d^2(k)} - 2 W^T r_{xd} + W^T R_{xx} W \quad (2)$$

where $R_{xx} = E |XX^T|$ is the covariance matrix of the input signal, $r_{xd} = E |dX|$ is the crosscorrelation vector between the input signal and the desired response.

Equation (2) is the objective function to be minimized. This can be found directly by equating the gradient of Eq. (2) to zero. This will lead to the following solution

$$W_{opt} = R_{xx}^{-1} r_{xd} \quad (3)$$

This equation is called the Wiener-Hopf equation. The corresponding minimum mean square error (MMSE) is given by

$$\xi_{\min} = \overline{d^2(k)} - W_{\text{opt}}^T r_{\text{xd}} \quad (4)$$

Direct solution of Eq.(3) has its own difficulties of computational problems and hardware implementation. Thus recursive methods is usually adopted.

The conjugate gradient (CG) algorithm depends on the idea of getting a finite set of directions $P(i)$ in such a way that they are covariance matrix conjugate to each other, i.e.

$$P^T(i) R_{\text{xx}} P(j) = 0 \quad i \neq j \quad (5)$$

The objective function, Eq.(2), is quadratic in W ; and if R_{xx} , r_{xd} , and $\overline{d^2(k)}$ are known exactly, the method of conjugate gradients guarantees, apart from rounding errors, to locate the minimum in at most N iterations⁶.

According to Fletcher and Reeves⁶ version of the conjugate gradient algorithm, the conjugate directions are generated recursively for iteration $k+1$ as follows :

$$P(k+1) = -g(k+1) + \beta_k P(k) \quad (6)$$

where
$$\beta_k = \frac{\|g(k+1)\|^2}{\|g(k)\|^2}$$

$g(k)$ is the gradient of $\xi_k(W)$ with respect to W , and $\|\cdot\|$ is the vector norm.

It is clear from Eq.(6) that generation of R_{xx} conjugate directions does not need explicit knowledge of R_{xx} , it depends only on the gradient of $\xi_k(W)$.

As far as the application of the CG algorithm under stochastic signal environments an exact knowledge of the gradient is not possible, instead an estimate for the gradient, $\hat{g}(k)$, is used. The most widely used estimate for the gradient is the unbiased estimate of Widrow¹ and is given by

$$\hat{g}(k) = - 2 \epsilon(k) X(k) \quad . \quad (7)$$

Thus, $\hat{g}(k)$ is used in the present algorithm instead of $g(k)$.

The general steps for the CG algorithm can be summarized as follows :

1. Starting with an arbitrary weight vector $W(0)$ find $\hat{g}(0)$ utilizing Eq.(7), let $P(0) = - \hat{g}(0)$ and put the iteration index $k=0$.

2. Find $W(k+1)$ as follows :

$$W(k+1) = W(k) + \mu_k P(k) \quad , \quad (8)$$

where μ_k is the minimizing step size for $\xi_k(W(k)+\mu P(k))$ in the direction $P(k)$. It is found by equating the gradient of $\xi_k(W(k)+\mu P(k))$ with respect to μ to zero. The corresponding value of μ is then given by

$$\mu_k = - \frac{P^T(k) \hat{g}(k)}{2 P^T(k) R_{xx} P(k)} \quad (9)$$

3. Find $\hat{g}(k+1)$, then calculate β_k ,

$$\beta_k = \frac{||\hat{g}(k+1)||^2}{||\hat{g}(k)||^2} \quad . \quad (10)$$

4. Calculate a new conjugate gradient direction according to

$$P(k+1) = - \hat{g}(k+1) + \beta_k P(k) \quad (11)$$

5. Test for termination condition, this could be

a) $\xi_k(W) \leq$ predetermined estimate for the minimum $\xi_k(W)$.

b) $||W(k+1) - W(k)|| \leq \delta$, where δ is an allowable error.

If either condition is satisfied, then stop the iteration process, if not put $k=k+1$ and go to step 2 and repeat the process.

Since this algorithm depends on the use of the gradient in a complicated manner and the gradient estimate used is usually noisy, the use of an averaging scheme is highly recommended. Thus, in both Eqs.(9) and (10) $\hat{g}(k)$ is replaced by its average value $\text{Av}\{\hat{e}(k)X(k)\}$. Also the numerator of Eq.(9) is approximated by $\text{Av}\{(P^T X)(X^T P)\}$ as an average for the quantity $P^T(k) R_{xx} P(k)$. The averaging process is taken over a specific number of K data samples.

3. CONVERGENCE AND MISADJUSTMENT

3.1 Convergence :

It will be shown that as the number of iterations increase, the expected value of the weight vector converges to the Wiener solution of Eq.(3). The following assumptions are made :

1. $\lim_{k \rightarrow \infty} \mu_k = 0$, $\mu_k < 1$
2. $\lim_{k \rightarrow \infty} \beta_k = 0$, $\beta_k < 1$
3. The time between successive iterations is long enough such that the signal vectors $X(k)$ and $X(k+1)$ are uncorrelated.

Taking the expectation of Eq.(8)

$$E \{W(k+1)\} = E \{W(k)\} + \mu_k E\{P(k)\} \quad , \quad (12)$$

from Eq.(11), $E \{P(k)\}$ can be written as

$$\begin{aligned} E \{P(k)\} &= -2 E \{X(k) | d(k) - X^T(k)W(k) | \} + \beta_{k-1} E \{P(k-1)\} \\ &= -2 | r_{xd} - R_{xx} E \{W(k)\} | + \beta_{k-1} E \{P(k-1)\} \end{aligned} \quad (13)$$

Proceeding through Eqs. (12) and (13) and taking into account that $P(0) = -\hat{g}(0)$, also assume $\mu_k = \mu$ and $\beta_k = \beta$ for simplicity. Starting with an initial guess $W(0)$, we get after $k+1$ iterations :

$$\begin{aligned} E|W(k+1)| &= |I - 2\mu R_{xx}|^{k+1} E|W(0)| + 2\mu \sum_{i=0}^k |I - 2\mu R_{xx}|^i r_{xd} \\ &\quad - 2\mu\beta R_{xx} \left| \sum_{k>0} 2I - 4\mu R_{xx} \right|^{k-1} E W(0) \\ &\quad + 2\mu\beta \left| \sum_{k>0} 2I - 4\mu R_{xx} \right|^{k-1} r_{xd} + \text{higher order terms in} \\ &\quad \beta \quad \text{and} \quad \mu \end{aligned} \quad (14)$$

The higher order terms in β and μ can be neglected since β and μ are both less than 1 and tend to zero as k tends to infinity.

Since the matrix R_{xx} is real symmetric and positive definite, it can be diagonalized by the unitary matrix Q such

that

$$R_{xx} = Q^{-1} \Lambda Q \quad (15)$$

where Λ is the diagonal matrix of eigenvalues and Q is the modal square matrix of eigenvectors. Eq.(14) can be written as

$$\begin{aligned} E | W(k+1) | &= Q^{-1} | I - 2\mu \Lambda |^{k+1} Q E | W(0) | \\ &+ 2\mu Q^{-1} \sum_{i=0}^k | I - 2\mu \Lambda |^i Q r_{xd} \\ &- 2\mu \beta Q^{-1} \Lambda \sum_{k>0} | 2I - 4\mu \Lambda |^{k-1} Q E | W(0) | \\ &+ 2\mu \beta Q^{-1} \sum_{k>0} | 2I - 4\mu \Lambda |^{k-1} Q r_{xd} + \dots \quad (16) \end{aligned}$$

Taking the limit as $k \rightarrow \infty$. If all the elements of the diagonal matrix are taken to be less than unity, we get

$$\begin{aligned} \lim_{k \rightarrow \infty} | 1 - 2\mu \Lambda |^{k+1} &\rightarrow 0 \\ \lim_{k \rightarrow \infty} \sum_{i=0}^{\infty} | I - 2\mu \Lambda |^i &= \frac{1}{2\mu} \Lambda^{-1} \\ \lim_{k \rightarrow \infty} | 2I - 4\mu \Lambda |^{k-1} &\rightarrow 0 \end{aligned}$$

Thus Eq. (16) reduces to

$$\begin{aligned} \lim_{k \rightarrow \infty} E | W(k+1) | &= 2\mu Q^{-1} \left(\frac{1}{2\mu} \Lambda^{-1} \right) Q r_{xd} \\ &= R_{xx}^{-1} r_{xd} \end{aligned}$$

which is the Wiener solution of Eq.(3).

3.2 Misadjustment :

The misadjustment is the term used to express the extent to which the actual MSE exceeds the minimum mean square error (MMSE). The excess in the MSE is due to the use of estimates for the signal statistics which are not known a priori. The misadjustment M is defined as¹ :

$$M \triangleq \frac{\text{Excess MSE}}{\text{MMSE}} = \frac{\xi_{\text{actual}} - \xi_{\text{min}}}{\xi_{\text{min}}} . \quad (17)$$

The misadjustment can be calculated in terms of the step size for the weight μ_k and that for the conjugate directions β_k . After sufficient number of iterations k such that M adaptive process has converged to the steady state near the MSE minimum point, the gradient-estimation noise of the adjustment algorithm at the minimum point is the gradient estimate itself. The analysis presented here follows a procedure similar to that of Widrow and McCool⁴ for the LMS.

The MSE ξ_k given by Eq.(2) can be written in terms of its minimum ξ_{min} of Eq.(4) as

$$\xi_k = \xi_{\text{min}} + |W(k) - W_{\text{opt}}|^T R_{xx} |W(k) - W_{\text{opt}}| \quad (18)$$

To simplify the analysis, $|W(k) - W_{opt}|$ is replaced by $V(k)$, utilizing the diagonalization of R_{xx} of Eq.(15) to transform to the primed coordinate, such that

$$V'(k) = \Lambda V(k) \quad . \quad (19)$$

Eq.(18) can be written as

$$\xi_k = \xi_{min} + V'^T(k) \Lambda V'(k) \quad . \quad (20)$$

The excess MSE is

$$\begin{aligned} \xi_{actual} - \xi_{min} &= V'^T(k) \Lambda V'(k) \\ &= \sum_{i=1}^N \lambda_i v_i'^2(k) \end{aligned} \quad (21)$$

where λ_i is the ith eigenvalue of R_{xx} .

The average excess MSE is thus

$$E |V'^T(k) \Lambda V'(k)| = \sum_{i=1}^N \lambda_i E |v_i'^2(k)| \quad . \quad (22)$$

Thus the misadjustment depends mainly on the covariance of $V(k)$.

According to the CG algorithm $W(k)$ is updated according to

$$W(k+1) = W(k) + \mu_k P(k).$$

Subtracting W_{opt} from both sides, we get

$$V(k+1) = V(k) + \mu_k P(k) \quad . \quad (23)$$

The direction of search, $P(k)$, is given by Eq.(11)

$$P(k) = - \hat{g}(k) + \beta_{k-1} P(k-1) \quad . \quad (24)$$

The covariance of the gradient estimation noise can be written in the primed coordinats as :

$$\text{Cov} | \hat{g}'(k) | = 4 \xi_{\min} \Lambda \quad . \quad (25)$$

Equation (24) can be written as

$$\begin{aligned} P(k) &= - g(k) - \hat{g}(k) + \beta_{k-1} P(k-1) \\ &= - 2r_{xd} - 2 R_{xx} | W_{\text{opt}} + V(k) | - \hat{g}(k) + \beta_{k-1} P(k-1). \end{aligned} \quad (26)$$

Which can be simplified to

$$P(k) = - 2 R_{xx} V(k) - \hat{g}(k) + \beta_{k-1} P(k-1) \quad . \quad (27)$$

Using Eq.(27) in Eq.(23)

$$V(k+1) = | I - 2 \mu_k R_{xx} | V(k) - \mu_k \hat{g}(k) + \mu_k \beta_{k-1} P(k-1) \quad . \quad (28)$$

In primed coordinates Eq.(28) can be written as

$$V'(k+1) = | I - 2 \mu_k \Lambda | V'(k) - \mu_k \hat{g}'(k) + \mu_k \beta_{k-1} P'(k-1) \quad . \quad (29)$$

To find the covariance matrix of Eq.(29) consider

$$\begin{aligned}
 V'(k+1)V'^T(k+1) &= |I - 2\mu_k \Lambda| V'(k) V'^T(k) |I - 2\mu_k \Lambda| \\
 &+ \mu_k^2 |-\hat{g}'(k) + \beta_{k-1} V'(k-1)| |-\hat{g}'(k) + \beta_{k-1} V'(k-1)|^T \\
 &+ \mu_k |I - 2\mu_k \Lambda| V'(k) |-\hat{g}'(k) + \beta_{k-1} V'(k-1)|^T \\
 &+ \mu_k |-\hat{g}'(k) + \beta_{k-1} V'(k-1)| V'^T(k) |I - 2\mu_k \Lambda|. \quad (30)
 \end{aligned}$$

Taking the expected value of Eq.(30) and noting that $\hat{g}'(k)$ and $V'(k)$ are uncorrelated, and after some mathematical manipulations, we get

$$\begin{aligned}
 \text{Cov} |V'(k)| &= 2\mu_k \mu_{k-1} \beta_{k-1} |4\mu_k \Lambda - 4\mu_k^2 \Lambda^2|^{-1} |I - \\
 &- 2\mu_k \Lambda| \{ \text{Cov} | \hat{g}'(k-1) | + \beta_{k-2}^2 \text{Cov} | \hat{g}'(k-2) | + \dots \\
 &+ \beta_{k-2}^2 \beta_{k-3}^2 \dots \beta_1^2 \beta_0^2 \text{Cov} | \hat{g}'(0) | \} + \mu_k^2 |4\mu_k \Lambda \\
 &- 4\mu_k^2 \Lambda^2|^{-1} \{ \text{Cov} | \hat{g}'(k) | + \beta_{k-1}^2 \text{Cov} | \hat{g}'(k-1) | + \dots \\
 &+ \dots + \beta_{k-1}^2 \beta_{k-2}^2 \dots \beta_1^2 \beta_0^2 \text{Cov} | \hat{g}'(0) | \}. \quad (31)
 \end{aligned}$$

During the implementation of the algorithm $\mu_k^2 \Lambda^2 \ll I$, and the higher order terms of β 's are neglected, Eq.(31) is simplified to

$$\text{Cov } |V'(k)| = \mu_k \xi_{\min} I + 2 \mu_{k-1} \beta_{k-1} \xi_{\min} I \quad . \quad (32)$$

Therefore, the average excess MSE is

$$\begin{aligned} E|V'^T(k) \Lambda V'(k)| &= (\mu_k + 2 \mu_{k-1} \beta_{k-1}) \xi_{\min} \sum_{i=1}^N \lambda_i \\ &= (\mu_k + 2 \mu_{k-1} \beta_{k-1}) \xi_{\min} \text{tr}(R_{xx}). \end{aligned} \quad (33)$$

$\text{Tr}(R_{xx})$ is the trace of the covariance matrix. Thus M becomes

$$M = (\mu_k + 2 \mu_{k-1} \beta_{k-1}) \text{tr}(R_{xx}) \quad . \quad (34)$$

This expression for M shows that M gets very small as the number of iterations k gets very large, according to the assumption for μ_k and β_k . This value of M is better than that obtained with the LMS where M is given by¹ : $\Delta_s \text{tr}(R_{xx})$, a constant value

4. SIMULATION RESULTS AND DISCUSSIONS

To test the CG algorithm, an array geometry and a signal environment is selected. A 4-element linear array whose element spacing is $\lambda/2$ is chosen as shown in Fig. 2.

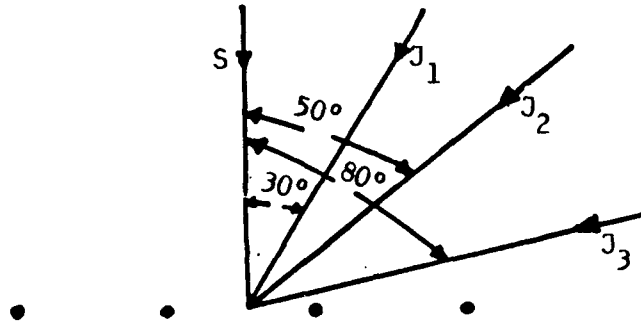


Fig. 2: 4-element linear array with signal and jammer locations.

The desired signal is taken to be sinusoidal having random phase between 0 and 2π . The jammers are located at 30° , 50° , and 80° . Each jammer is considered to be narrowband Gaussian whose variance is equal to the jammer power. White Gaussian thermal noise power of 10^{-3} is added to the signal vector. Different eigenvalue spread is considered. Averaging for the CG algorithm is taken over 3 samples.

Figure 3 shows the learning curves (MSE vs. number of iterations) for both the LMS and CG algorithm for eigenvalue spread $\frac{\lambda_{\max}}{\lambda_{\min}} = 402$, the jammers power are all equal to 100. After 300 iterations (900 samples) the CG algorithm is within 6 dB from the MMSE value while the corresponding LMS (after 900 iterations) is within 11 dB from the MMSE value. This shows the higher convergence speed of the CG algorithm

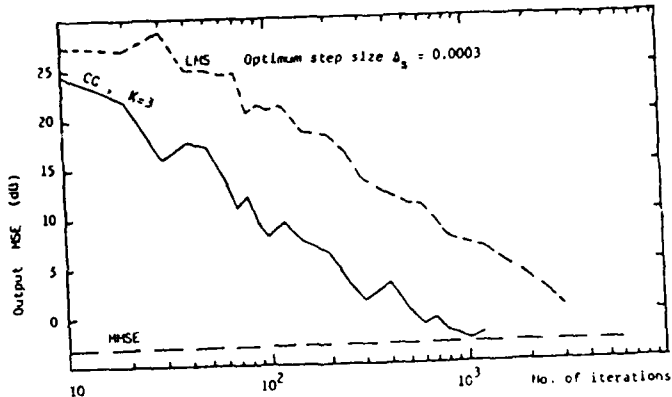


Fig. 3. Learning curves for a comparison between LMS and CC with $\lambda_{\max}/\lambda_{\min} = 402$

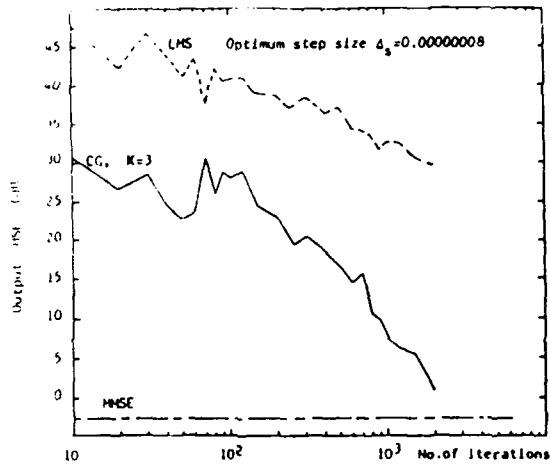


Fig. 4. Learning curves for a comparison between LMS and CG with $\lambda_{\max}/\lambda_{\min} = 2796.7$

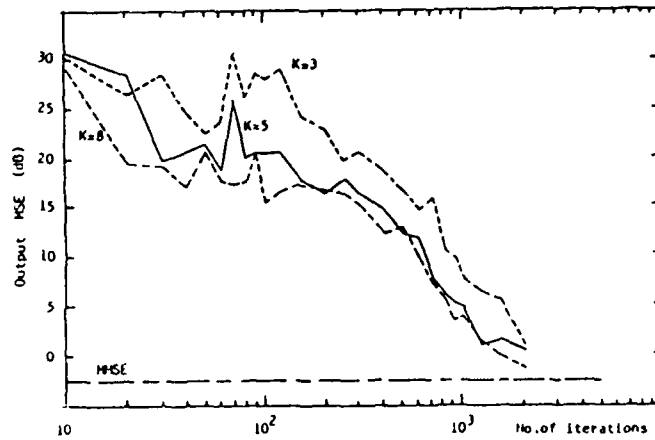


Fig. 5. Learning curves for CG with number of samples - 3, 5, and 8.

compared with the LMS. Note the lower value of the excess MSE for the CG algorithm.

Figure 4 shows the learning curves for large eigenvalue spread $\frac{\lambda_{\max}}{\lambda_{\min}} = 2796.7$. The jammer powers are $J_1 = 200$, $J_2 = 15500$, $J_3 = 6240$. The CG algorithm is within 10 dB from the MMSE after 1000 iterations (3000 samples) while the LMS is within 35 dB from the MMSE after 3000 iterations. It is clear that as the eigenvalue spread gets large the CG algorithm has better convergence characteristics. Note also the lower value of the misadjustment for the CG algorithm.

Figure 5 shows the effect of increasing the number of samples K over which averaging is taken for the CG algorithm. It is clear from the figure that as K increases, higher convergence speed and more smoothing is obtained.

5. CONCLUSION

This paper introduced an analysis for the conjugate gradient algorithm to be used in adaptive antenna systems. It is shown that the expected value of the MSE tends to the Wiener solution as the number of iterations tends to be very large. The excess MSE is analyzed and is found to be smaller than

that of the LMS. Simulation results is presented which show the higher convergence speed of the CG algorithm as compared with the LMS. Different eigenvalue spread are considered. It is shown that as the eigenvalue spread gets large the CG algorithm gives better convergence speed. The effect of the averaging on the CG convergence characteristics is also studied. It is found that as the number of averaging samples is increased, better convergence and more smoothing is obtained.

REFERENCES

1. Widrow, B., Mantoy, P.E., Griffiths, L.J., and Goode, B.B. (1967) Adaptive antenna systems, Proc. IEEE 55: 2143-2158.
2. Kalman, R.E. (1960) A new approach to linear filtering and prediction problems, Trans. ASME 82 : 35-45.
3. Reed, L.S., Mallett, J.D., and Brennan, L.E. (1974) Rapid convergence rate in adaptive arrays, IEEE Trans. Aerosp. Electron. Syst. 10 : 853-863.
4. Widrow, B. and McCool, J.M. (1976) A comparison of adaptive algorithms based on the methods of steepest descent and random search, IEEE Trans. Antennas Propagat. 24 (No. 5) : 615-637.

5. Hestenes, M.R. and Stiefel, E.(1952) Methods of conjugate gradients for solving linear systems, J. Res. Nation.Bureau of Standards 29 : 409-439.
6. Fletcher, R. and Reeves, C.M. (1964) Function minimization by conjugate gradients, Comp. J. 7 : 149-154.

ADAPTIVE TRANSFORM FEED TEST RESULTS

Michelle S. Hayes, Capt, USAF
Rome Air Development Center
Electromagnetics Directorate
Hanscom AFB, MA 01731

ABSTRACT

Rome Air Development Center has built an Adaptive Transform Feed (ATF) for use in conjunction with Grumman Aerospace Corporation's TA-3 phased array lens, as part of the Phased Array Lens Demonstration (PALDEM) Test Program. The purpose of this program was to demonstrate the advantages of transform feeds for use in a space-based radar system. This report describes the overall concept and design of the ATF, and presents the results of tests made on the feed independent of the lens. It also describes the results of some early tests made in conjunction with the lens.

1. INTRODUCTION

This report describes the design and testing of an adaptive transform feed (ATF) which was constructed at Rome Air Development Center as part of the Phased Array Lens Demonstration (PALDEM) Test Program. The objective of the PALDEM program was to perform RF tests utilizing Grumman's Test Article 3 (TA-3) space-fed lens membrane with various feed configurations. The results of these tests will be used to

establish design criteria for a full-sized phased array lens antenna for a Space-Based Radar system.

The PALDEM program called for testing the TA-3 lens with three feed configurations. The first feed configuration was a pyramidal horn built by Grumman. This feed was used for initial testing of the lens to determine its characteristics. Following this, the lens was tested with a corporate fed array built by RADC. The corporate feed was designed to illuminate the lens with a tailored amplitude distribution to produce a low sidelobe pattern. The third feed, and the subject of this report, was an adaptive transform feed which was also designed and constructed by RADC. This feed, shown in Figure 1, was to provide both a tailored amplitude distribution and an adaptive null-steering capability. The purpose of this phase of the project was to demonstrate the advantages of a transform feed, including the ability to produce low sidelobes in both the sum and difference patterns, and the ability to perform adaptive nulling.

Before we delivered the transform feed to Grumman, we thoroughly tested it to ensure that it would meet the design criteria and produce the desired patterns. The results of these tests, as well as the overall concept and design of the ATF are the subject of this report.

2. CONCEPT AND DESIGN

2.1 Transform Feed Concept

In general, a transform fed antenna consists of an objective lens which forms the primary radiating aperture and a

beamforming network which forms the feed. The general principle is illustrated in Figure 2. When the beamformer inputs are excited, the beamformer radiates a pattern which illuminates the objective lens. The lens re-radiates the received energy to the far field.

The objective lens generally consists of two arrays facing in opposite directions. The back face of the lens is illuminated by the feed and the received energy is transferred to the front face via transmission lines. Phase shifters are often inserted in the transmission lines to provide beam-steering capability at the lens. The front face of the lens forms the primary aperture which re-radiates the waveform to the far field.

The beamformer is a Fourier transforming device such as a Butler matrix, a Blass array or a Rotman lens. When a single input of the beamformer is excited, the outputs are uniformly illuminated. If these outputs are connected to the elements of a feed array, the feed will radiate a $\sin(u)/u$ ($u=kds\sin\Theta$) pattern to the lens. This will be re-radiated to the far field as a flat-topped, rectangular beam.

Each input to the beamformer creates an individual $\sin(u)/u$ beam which is spatially separated from the other subarray beams. Although separated in angle, each subarray beam overlaps and is orthogonal to the other beams (i.e. the peak of its beam coincides with the nulls of the other beams). When multiple inputs are excited, the beamformer radiates a sum of the orthogonal subarray beam patterns. If appropriate amplitude and

phase weights are applied to the subarray beam inputs, the sum of these contributions creates a smooth amplitude taper at the backface of the lens. This is re-radiated as a low sidelobe pattern in the far field.

In the ATF, the beamformer consists of two sets of Butler matrices which produce a set of 24 beams in both azimuth and elevation. The orientation of the subarray beams on the lens back face is shown in Figure 3. These 24 beams add to create a two-dimensional circularly-symmetric amplitude taper which should produce a low-sidelobe pattern in the far field. The amplitude taper is designed to approximate a -40 dB Taylor distribution at the lens. This ability to create a low sidelobe amplitude taper is one of the major advantages of a transform feed which we hoped to demonstrate during this program.

The objective lens in this project is Grumman's Test Article 3 (TA-3) circular space-fed lens antenna. The lens consists of two dipole arrays connected by 4-bit phase shifter modules on an aluminum mesh ground plane. The phase shifter modules provide collimation of the received beam as well as beam-steering. The dipole arrays have opposite polarizations to provide maximum isolation between the front and back faces. The lens has an active diameter of 58' and is programmed for a focal length also of 58' for an F/D of 1.

One of the advantages of the transform feed which we hoped to demonstrate in this effort is the ability to produce low sidelobe patterns in the monopulse difference pattern by a simple phase reversal across the feed. As shown in Figure 4,

reversing the phases on one side of a corporate feed creates an abrupt discontinuity in the center of the aperture distribution, resulting in high sidelobes. To get a low sidelobe pattern, an additional feed network is required. In a transform feed, however, the pattern is formed from the sum of subarray beam patterns, so that a similar phase reversal gives a smooth amplitude transition across the aperture center. This should produce a low sidelobe difference pattern in the far field.

Another advantage of an adaptive transform feed is its ability to adaptively form nulls in the antenna pattern. While this is an important feature of the ATF, it will not be discussed in this report.

2.2 Feed Design

The design of the ATF was done by McGrath and has been described in detail in earlier reports. The design was based largely on the characteristics of the TA-3 lens and on the availability of commercial beamforming and adaptive weight components. The ATF was designed for S-band operation with a center frequency of 3.4 GHz. In this report I will not discuss the details of the design, but will merely outline the major components of the ATF and their functions.

Figure 5 is a schematic of the RF components of the ATF. At the far right is a corporate feed structure which is virtually identical to the corporate feed previously delivered to Grumman. A single common input at the right feeds a 24-way corporate feed network. Fixed attenuators in the corporate feed establish the quiescent amplitude weighting applied to the 24 subarray beams.

The corporate feed network is followed by a set of adaptive weights, consisting of 24 programmable attenuators and 24 programmable phase shifters. The 10-bit attenuators have a range of 0 to -51 dB. The 10-bit RF vector modulator phase shifters have a full 360° range with a resolution of $.35^\circ$. Although the individual bit settings of the adaptive weights were not very accurate, this was not considered critical because the weights are used primarily for adaptive nulling. However, we were concerned about the effect of these units on the quiescent subarray beam patterns. Variations in the relative subarray beam amplitudes or phases could significantly alter the lens illumination and raise the sidelobe levels. In testing these units, we found an average insertion loss of about 2 dB. Although this insertion loss was undesirable, it was fairly uniform across all the subarray beams which should reduce its effect on the overall amplitude pattern. However, the insertion phases varied widely among the adaptive weights. To eliminate this problem a phase alignment procedure was developed to initialize the phase shifters to cancel the phase differences between the subarray beams. This procedure is described in section 3.2 of this report.

Between the adaptive weights and the Butler matrix beam ports are 24 bidirectional couplers. These units enable us to measure the signal path from the beam port to free space or from the adaptive weights to the corporate feed input. The latter connections are accessible on the outside of the feed for monitoring and troubleshooting the active components of the

feed. The directional couplers had near-ideal performance specifications.

Following the directional couplers is the two-stage Butler matrix transform section. The first stage consists of 6 8x8 Butler matrix boards which perform the spatial Fourier transform in the horizontal dimension. The second stage consists of 8 8x8 Butler matrix boards which perform the vertical transform. These boards were thoroughly tested to determine the insertion losses, phase gradients and RMS errors. The specifications were well within our requirements.

The 64 second stage Butler matrix outputs feed the center elements of a 10x10 microstrip patch array. The array was designed by McGrath with the aid of a computer routine. The outer elements of the array are to suppress edge effects and are terminated with 50Ω loads. Although the elements have a relatively narrow bandwidth, they provide a relatively uniform radiation pattern in the angular area covered by the lens and they are impedance matched.

The electronics which control the adaptive weights form another important part of the ATF. The electronics are designed for control by a Hewlett Packard 9836 computer with a General Purpose Input/Output (GPIO) card. A 16-bit word output through the GPIO is used to control the feed. Six bits of the output word determine which of the adaptive weights is selected, and the remaining 10 bits contain data for the selected weight. The control electronics are contained on the 6 circuit boards shown in Figure 6. The line driver board, located near the computer,

conditions the control signals so that they can be transferred to the feed over a relatively long distance. The main board contains the line receivers and the decoding circuitry which selects the individual phase shifter or attenuator to be controlled. Each of the four latch boards contains six sets of latch chips (one for each phase shifter/attenuator pair) which hold the data while the computer performs other functions. The feed also contains four power supplies which provide DC voltage to the control circuitry and to the cooling fans.

3. TEST RESULTS

3.1 Test Setup

Perhaps the most difficult problem we faced in testing the ATF was establishing a phase reference which would allow measurement of the relative phases of the individual subarray beams. This procedure was necessary to ensure that the ATF was properly aligned. This problem was overcome by using the setup shown in Figure 7. The center of the feed's radiating array was positioned directly above the pedestal's center of rotation so that the azimuth patterns could be measured. The transmit source was a horn positioned 58' in front of the feed, the same distance as the TA-3's focal length. Thus, when rotating the antenna in azimuth, we effectively measured the feed's pattern in amplitude and phase along a circle with a radius equal to the focal length of the lens. Unfortunately, the elevation positioner would change the distance between the feed array's center and the source, so a pivot and pulley apparatus was constructed so that the feed could be rotated in elevation

about the array's horizontal axis. This limited our measurements to azimuth cuts at fixed elevations. All patterns discussed here are azimuth cuts, and unless otherwise noted, are for the 3.4 GHz center frequency.

3.2 Feed Alignment

As mentioned earlier, the insertion phases of the adaptive weights in their quiescent states varied considerably from unit to unit. Since the proper phase distribution of the subarray beams is critical to obtaining the desired illumination of the lens, we were forced to develop a phase alignment procedure for the feed. The alignment procedure would establish the phase shifter settings which give a particular phase distribution among the subarray beams. One of the center subarray beams was chosen as the phase reference for the alignment. Its phase was measured at beam center and set to a reference value of zero degrees. In turn, each of the other beams was measured by orienting the feed so that the beam's peak was in the direction of the transmitting source. The computer was used to read the phase and adjust the phase shifter until the beam phase was as desired. The resulting phase shifter settings for all 24 subarray beams were then stored in a datafile for the particular phase distribution. The alignment procedure was used to determine the phase settings for both the sum pattern and the azimuth difference pattern. We also recorded the aligned phase values at the directional coupler ports, so that future alignments could be done directly at these ports using a network analyzer.

3.3 Subarray Beam Patterns

Subarray beam patterns were measured by fully attenuating all but the selected beam. Azimuth cuts of a few typical beams are shown in Figure 8. The patterns exhibit the expected $\sin(x)/x$ shape, although some distortion is apparent at low amplitude levels. This is caused by the fact that even though all other beams are attenuated, the maximum attenuation setting is -52 dB, so that there is still some residual power leaking through the other beams. Since the outside beams are -32 dB below the center beams, even the fully attenuated center beams will have some effect on the outside beam patterns.

The relationship between beams in a given azimuth cut was as expected, illustrated in Figure 9: the center beams cross over at their -3 dB points, each main lobe coincides with the nulls of the other beams, and the beams are located at the correct angular locations.

After the final alignment discussed in the previous section, the phase and amplitude of each beam were measured at the beam's peak, with results shown in Table 1. The RMS phase error for the final alignment was 1.5° . Phases measured for the outside beams were generally worse because their amplitudes are so low that they were corrupted by noise. However, those beams have little impact on the overall sum pattern and lens amplitude distribution because they fall outside the TA-3's aperture.

3.4 Sum and Difference Patterns

The feed's sum pattern was measured by exciting all 24 subarray beams in phase. Amplitude patterns taken at 0°

Table 1. Measured Phases and Amplitudes of Subarray Beams

Beam#(Calc. Amp.)					
Meas. Amp.,	Meas. Phase				
(dB)	(deg)				
		#1(-30.1)	#2(-30.1)		
		-48.0, -11.0	-33.5, 3.0		
		#9(-16.2)	#10(-6.7)	#11(-6.7)	#12(-16.2)
		-15.7, -1.8	-6.3, 0.4	-6.2, 0.1	-16.0, -1.2
#3(-30.1)	#4(-6.7)	#5(0.0)	#6(0.0)	#7(-6.7)	#8(-30.1)
-32.0, -1.8	-6.0, -0.4	-0.7, 0.0	-0.5, -1.9	-6.5, 1.0	-32.5, 1.5
#22(-30.1)	#21(-6.7)	#20(0.0)	#19(0.0)	#18(-6.7)	#17(-30.1)
-32.0, 2.5	-6.5, 1.7	-0.6, 1.2	-0.5, 2.5	-6.6, 0.4	-32.1, 3.0
		#16(-16.2)	#15(-6.7)	#14(-6.7)	#13(-6.2)
		-15.7, 0.6	-6.5, 0.0	-6.2, -1.0	-16.2, 1.4
		#24(-30.1)	#23(-30.1)	RMS Errors:	
		-35.6, 1.0	-31.0, -0.7	1.25 dB, 1.5 deg.	

elevation are shown in Figures 10a-c for 3.3, 3.4 and 3.5 GHz.

Figure 11 shows expanded plots of those patterns, along with the desired pattern, which would produce a -40 dB Taylor distribution on the lens. Clearly, the ATF succeeded in synthesizing the desired low-sidelobe taper. Figure 12 is a cross-polarization pattern taken at 3.4 GHz and 6° elevation, showing that the minimum isolation is -27 dB.

In addition to the low-sidelobe amplitude taper, the feed should illuminate the lens with a quadratically-varying phase, which projects to a uniform phase over a sphere of 58' radius centered about the feed's radiating face. The dashed lines of Figure 13 show that this specification is also met--they are the measured phase of the sum pattern, and are very near to uniform.

Difference patterns of the feed were measured by setting the right side beams 180° out of phase with the left side beams. The solid lines in Figure 13 show the measured phases of the difference patterns at $+6^\circ$ and -6° elevations. These phase patterns show the resulting phase reversal in the center of the feed's pattern. Figure 14 is the difference amplitude pattern for those two elevation cuts.

3.5 Preliminary Lens/Feed Tests

Some preliminary tests of the transform fed lens were conducted by RADC when the feed was delivered to the Grumman Aerospace Corp facilities in Bethpage, NY. At the time of the tests, the feed had been mechanically aligned with the lens, but had not been electrically aligned. This resulted in a small amount of squint in the patterns, but the overall results were still good.

Figure 15 shows the sum pattern with all 24 subarray beams active. The peak sidelobe level was about -20 dB. Although this sidelobe level is relatively high, it is comparable to that achieved with the corporate feed, and is probably due to errors in the lens. Figure 15 also shows the sector pattern produced by one of the center subarray beams. It demonstrates the flat-topped shape which was predicted for a single beam illumination of the lens.

Figure 16 shows the difference pattern of the transform fed lens, produced by reversing the phases of the right and left sides of the feed. As predicted, there is no appreciable

difference in the sidelobe levels between the sum and difference patterns.

5. CONCLUSIONS

Our in-house program on the adaptive transform feed was completed in Oct. 1986 when the feed was delivered to Grumman. Grumman completed their tests of the ATF with the lens this summer. We are awaiting their final report.

The results of the ATF tests were very good. After some initial troubleshooting of the control electronics, we were able to control the feed remotely to produce a number of different feed radiation patterns, including the sum, difference and individual subarray patterns. The location and weighting of the subarray beams was very close to the design. After establishing a phase alignment procedure for the sum pattern, we were able to very closely approximate a -40 dB Taylor distribution at the 58' focal length of the lens. We also demonstrated the ability to synthesize a low sidelobe monopulse difference pattern by reversing the phase of the subarray beams on the right or left half of the feed.

Although the initial tests of the feed with the lens did not have the low sidelobes which were predicted, we suspect that this was due to errors in the lens. At the time of the tests, the lens and feed had not been electrically aligned, and there were a large number of phase shifter module failures within the lens. Quantization errors in the lens modules may also have contributed to the higher than expected sidelobe levels. No

definite conclusions on the combined lens/ATF performance can be made until the final test results are reported by Grumman.

The adaptive transform feed built for this project would not be suitable for an operational system. It has a relatively narrow bandwidth, fairly high losses in some of the components, and it is not capable of handling high power levels. However, the purpose of this project was to demonstrate the basic capabilities of a transform feed. Future projects should concentrate on improvements to the lens and feed which will enable their use in an operational system.

ACKNOWLEDGEMENTS

This report is largely based on an earlier report written by Capt Daniel T. McGrath, Mr. Otho E. Kerr, Jr., and myself. Since Capt McGrath and Mr. Kerr are no longer with RADC, they were unable to participate in writing this report. However, I wish to acknowledge their role in the complete design and construction of the feed. I would also like to thank the many other RADC/EEA engineers and technicians who contributed to the success of this project.

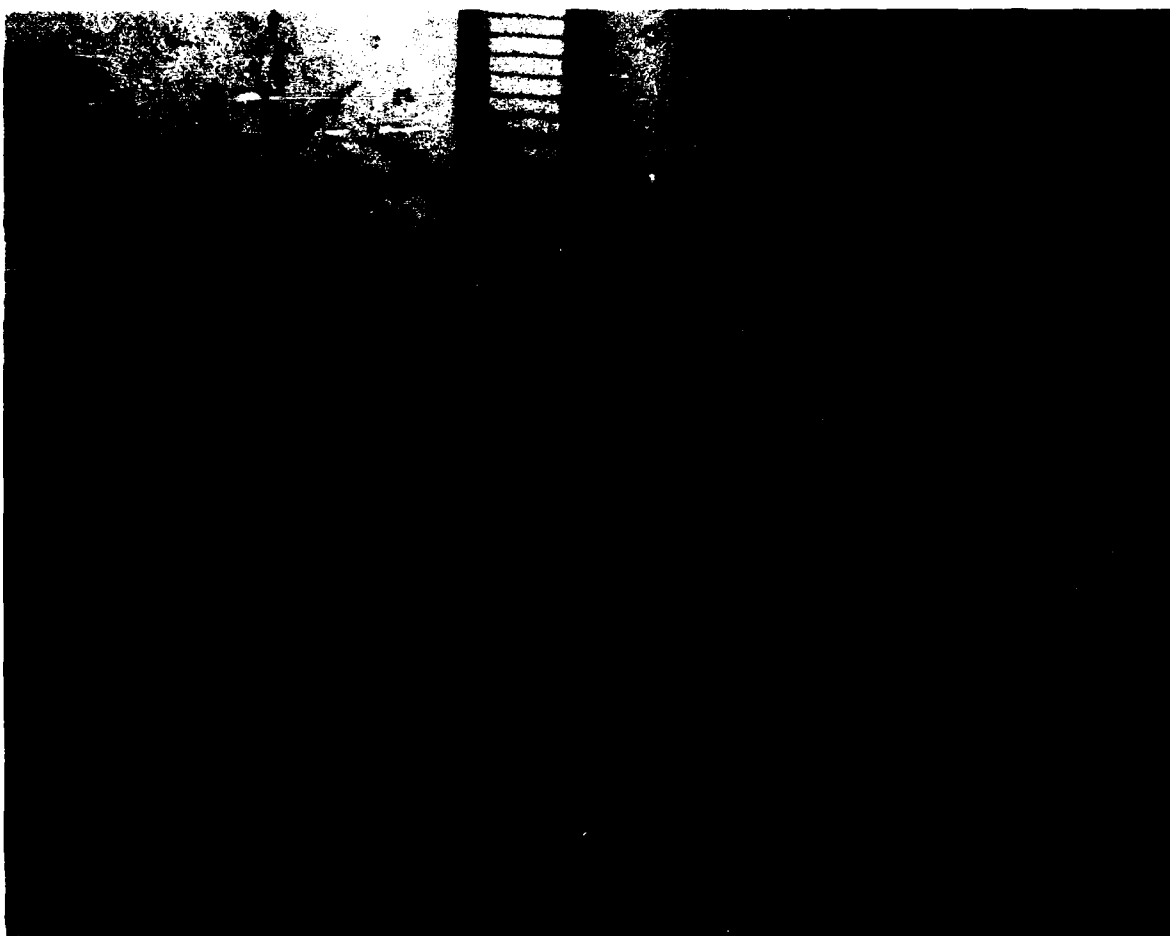


Figure 1. Rome Air Development Center's Adaptive Transform Feed

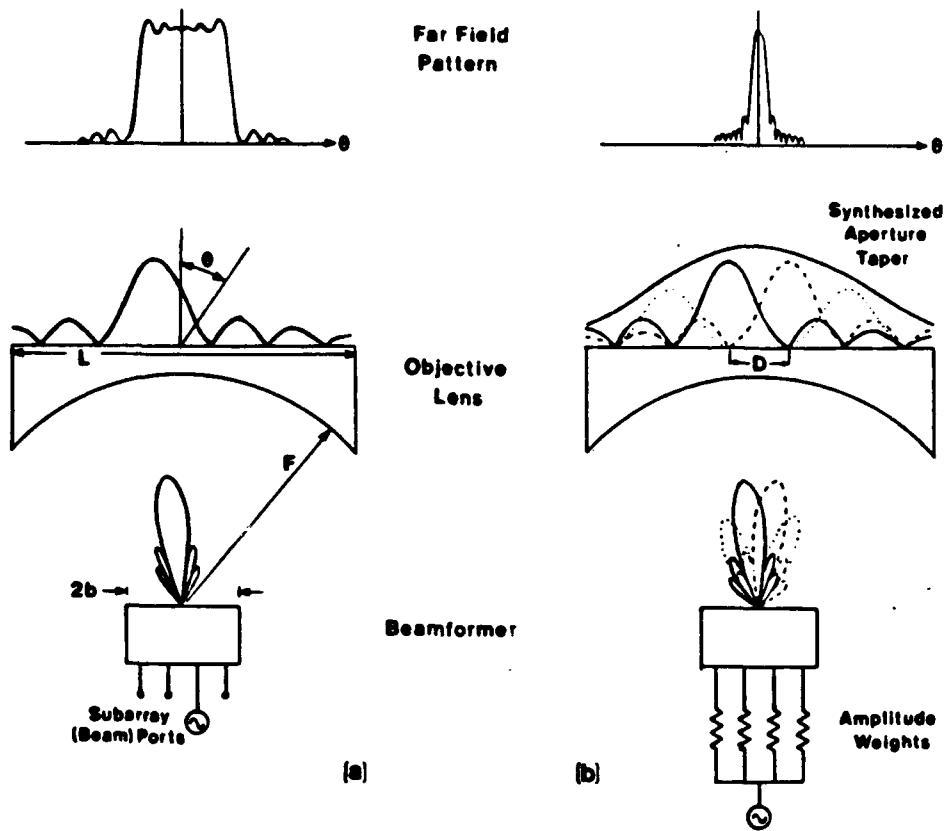


Figure 2. General Structure and Radiation Pattern Properties of Transform Feed Antennas

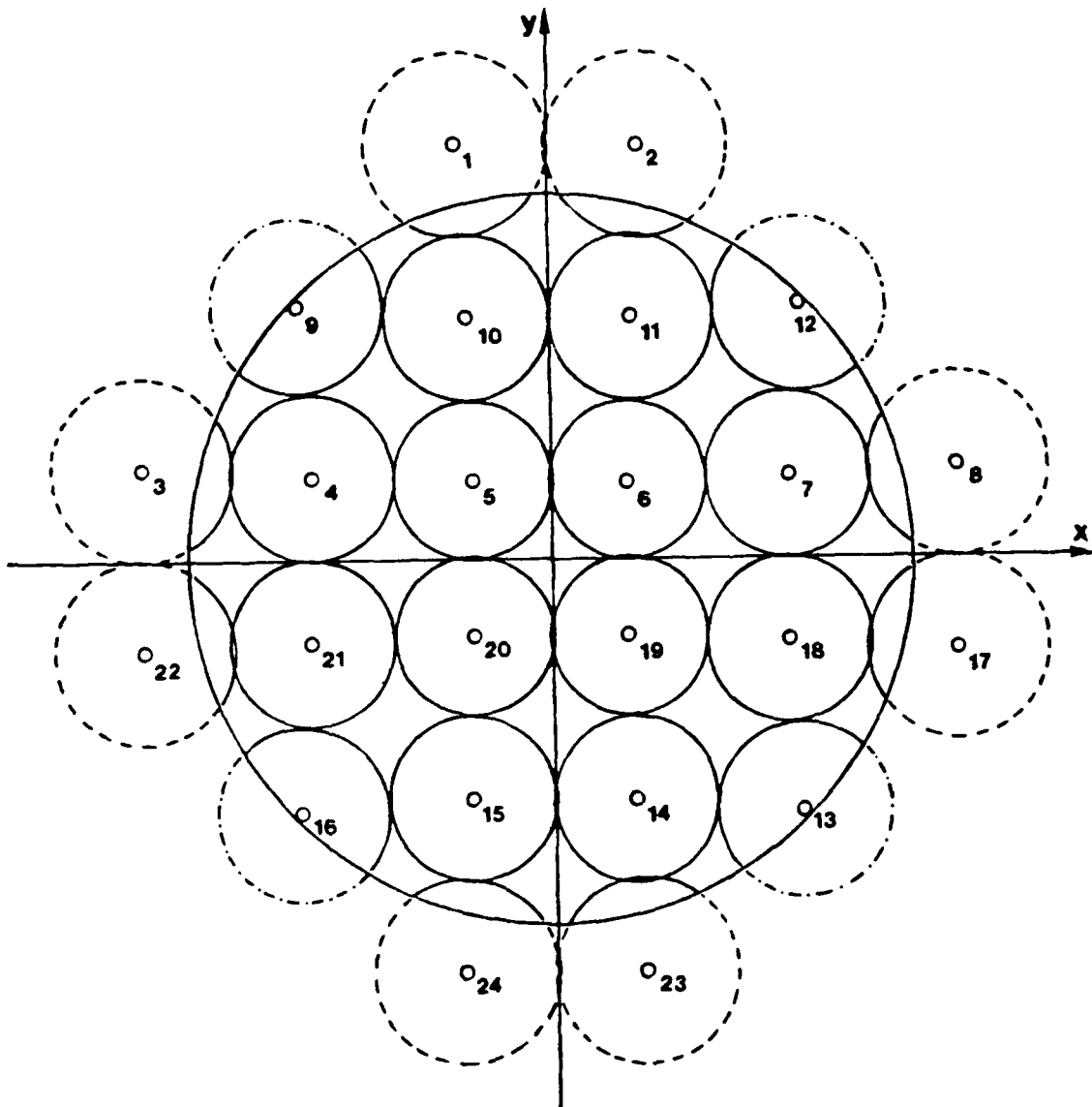


Figure 3. Subarray Beam Illumination of Lens Back Face (-3 dB Contours)

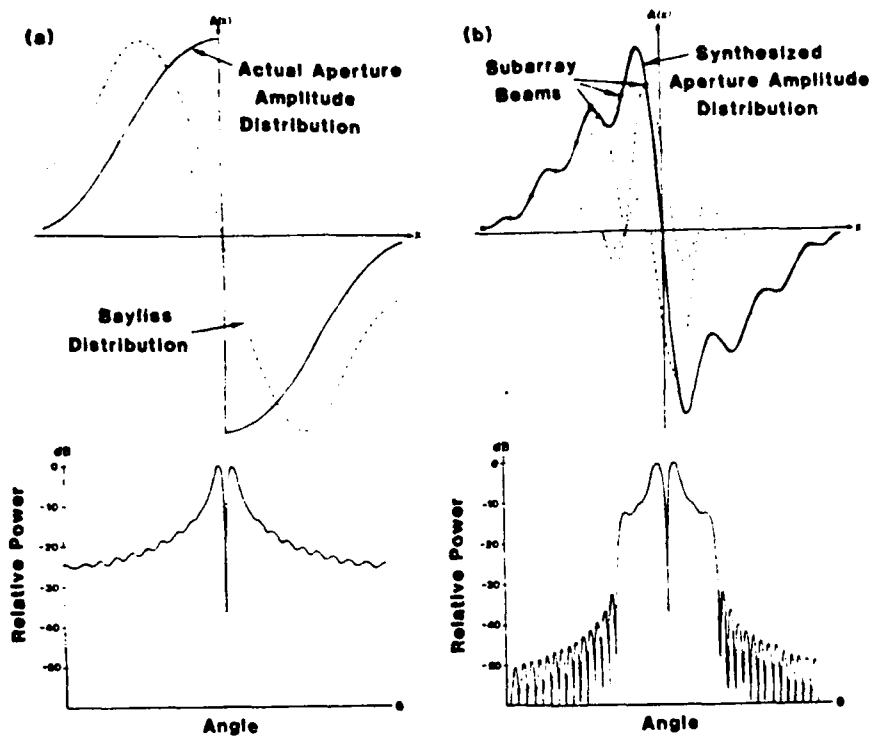


Figure 4. Difference Patterns Formed by Reversing Phases of One Side of the Feed Network: (a) Conventional Corporate Feed; (b) Transform Feed

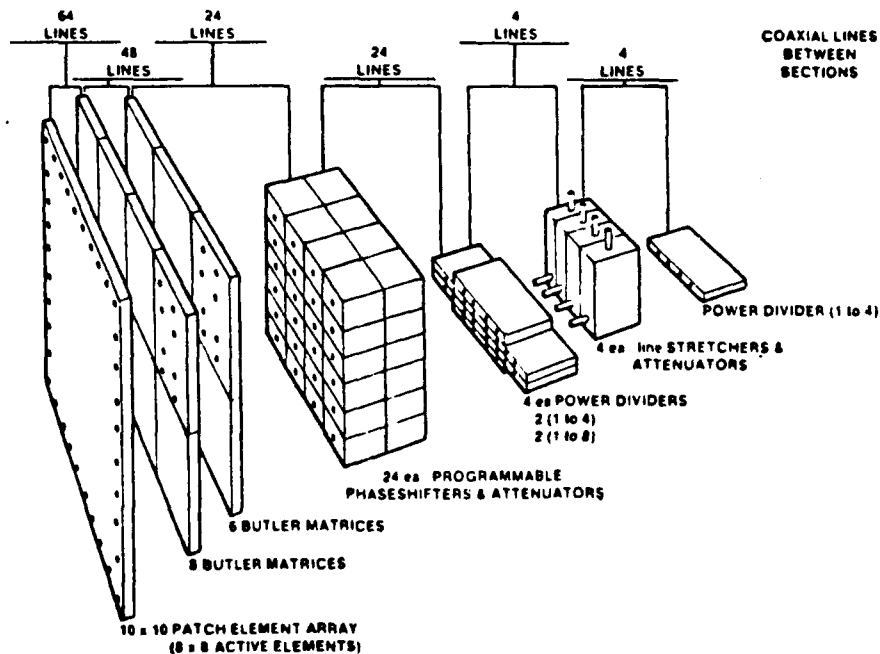


Figure 5. Adaptive Transform Feed Components and Arrangement

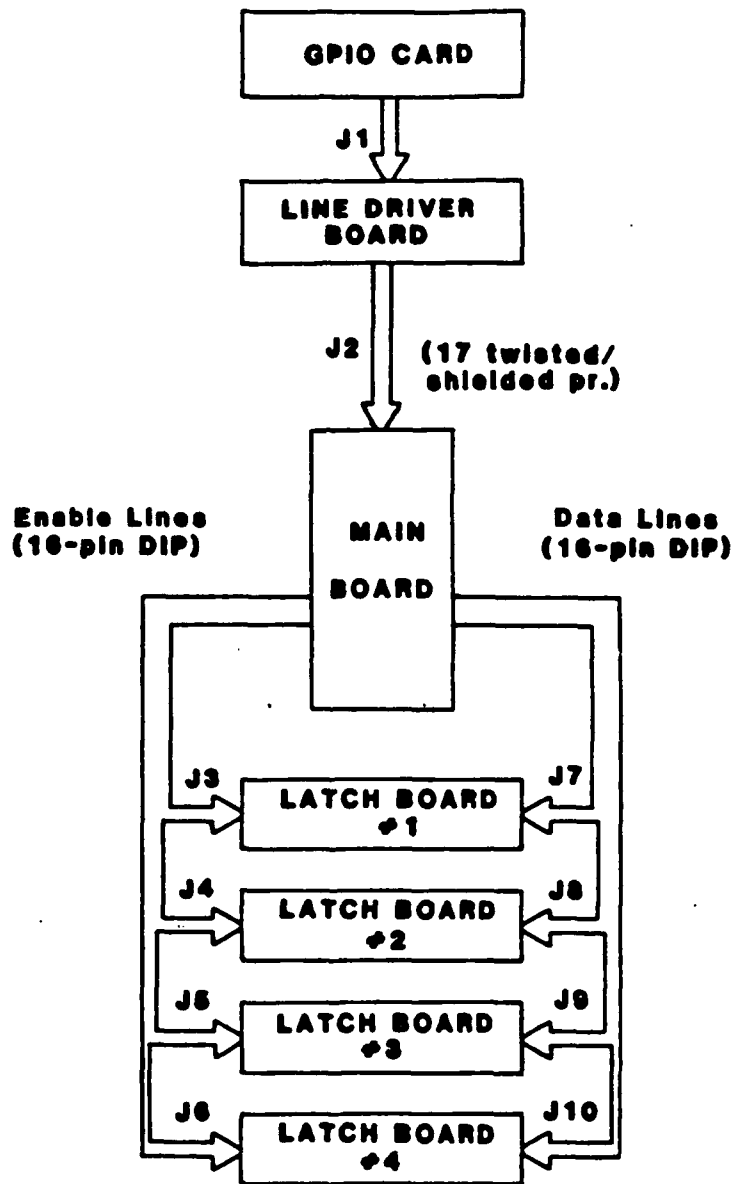


Figure 6. Adaptive Weight Control Electronics

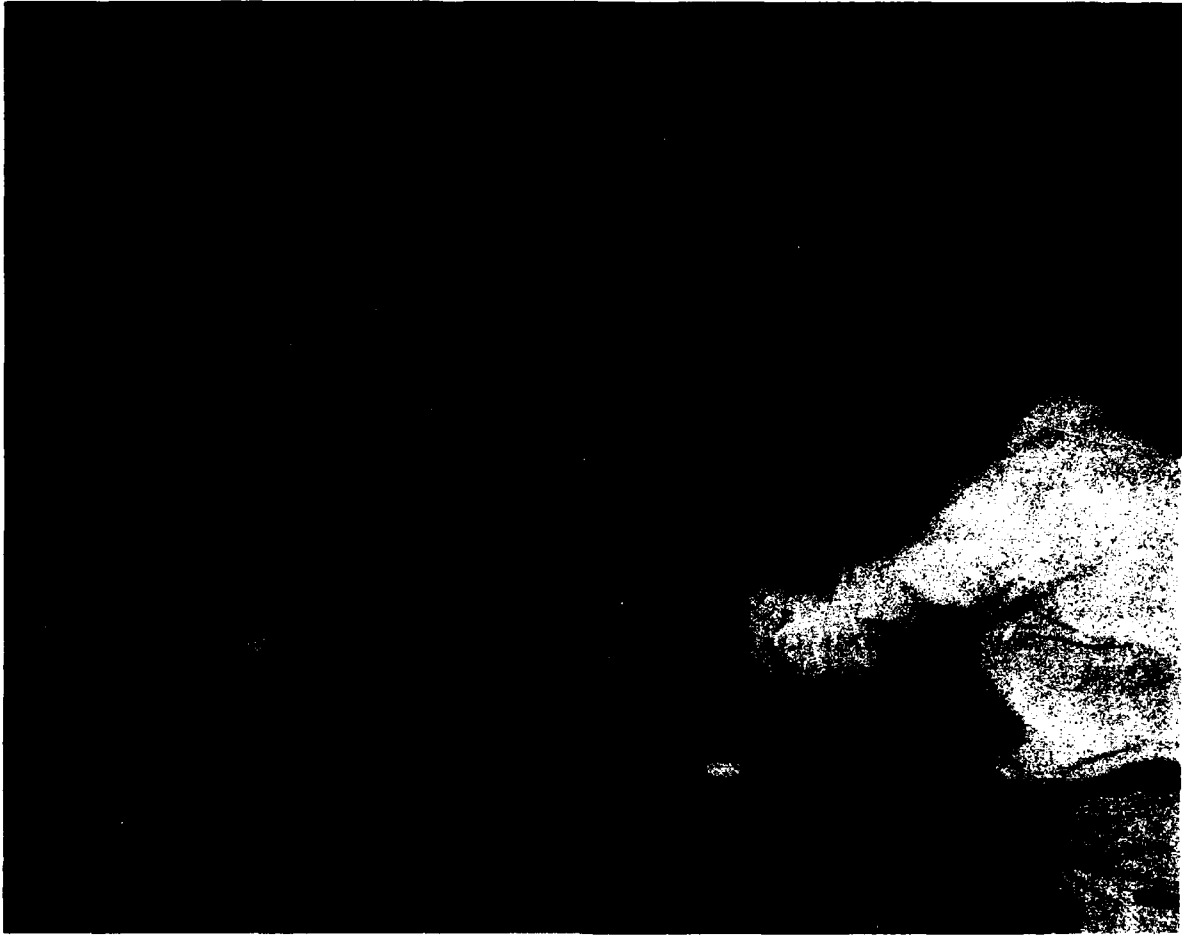
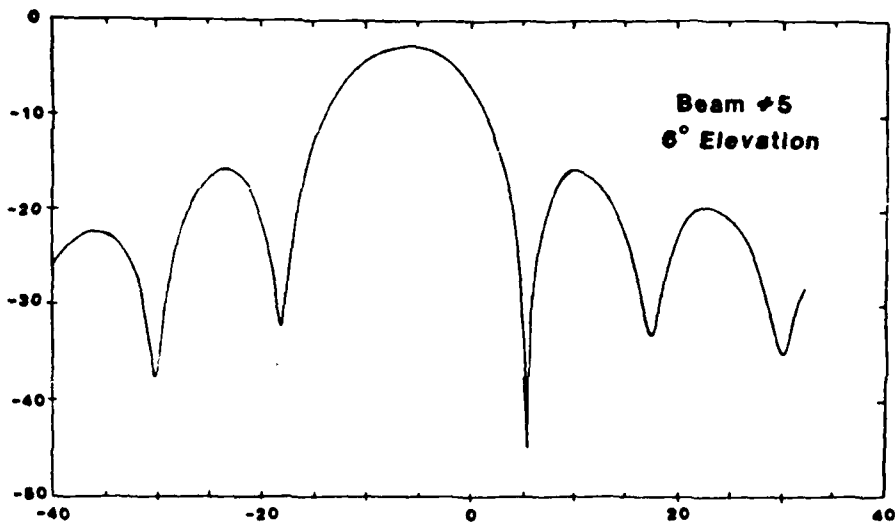
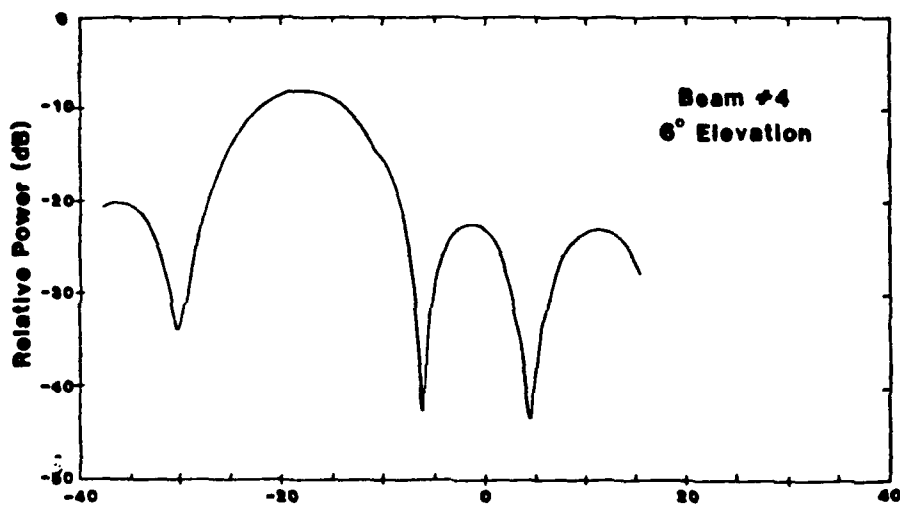


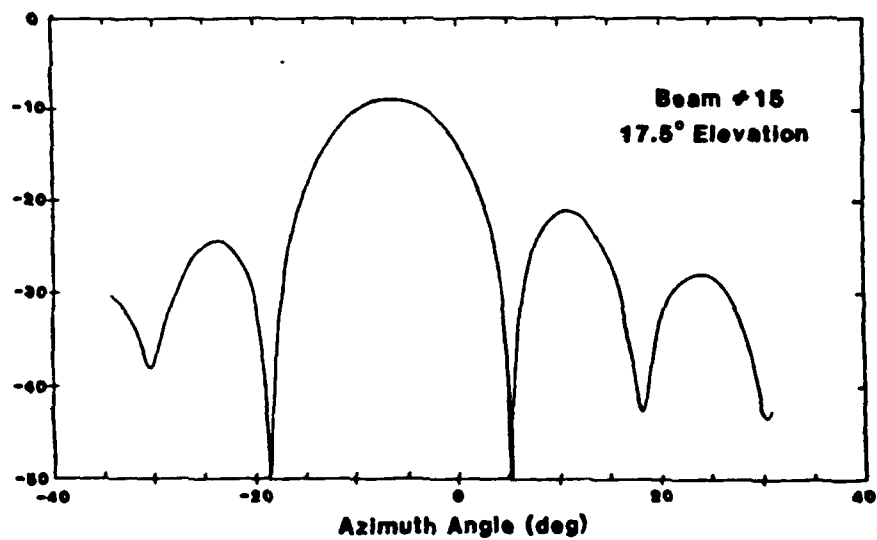
Figure 7. Test Setup



(a)



(b)



(c)

Figure 8. Typical Feed Beam Patterns

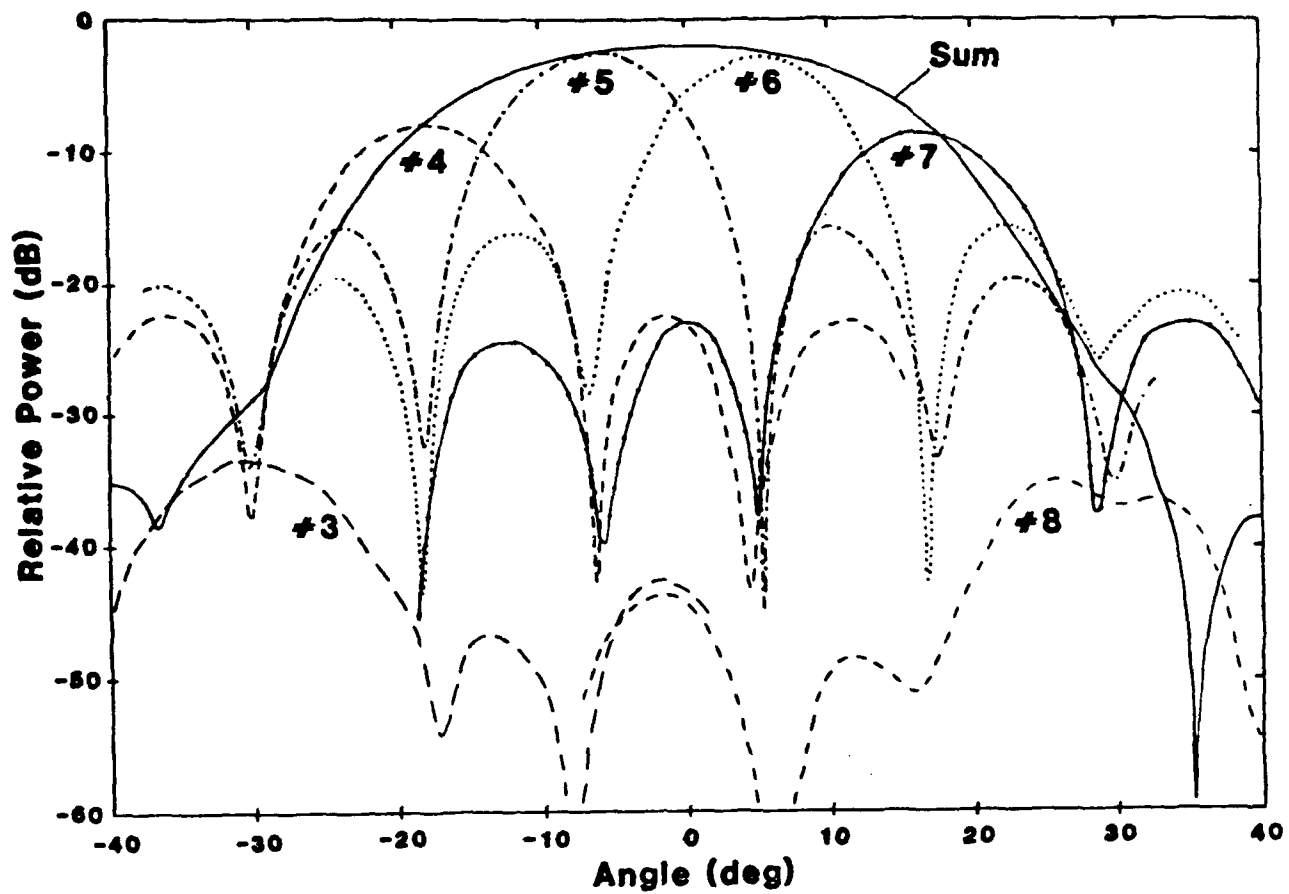


Figure 9. Overlay of Beams #3-8 and Sum Pattern, 3.4 GHz, 6° Elevation

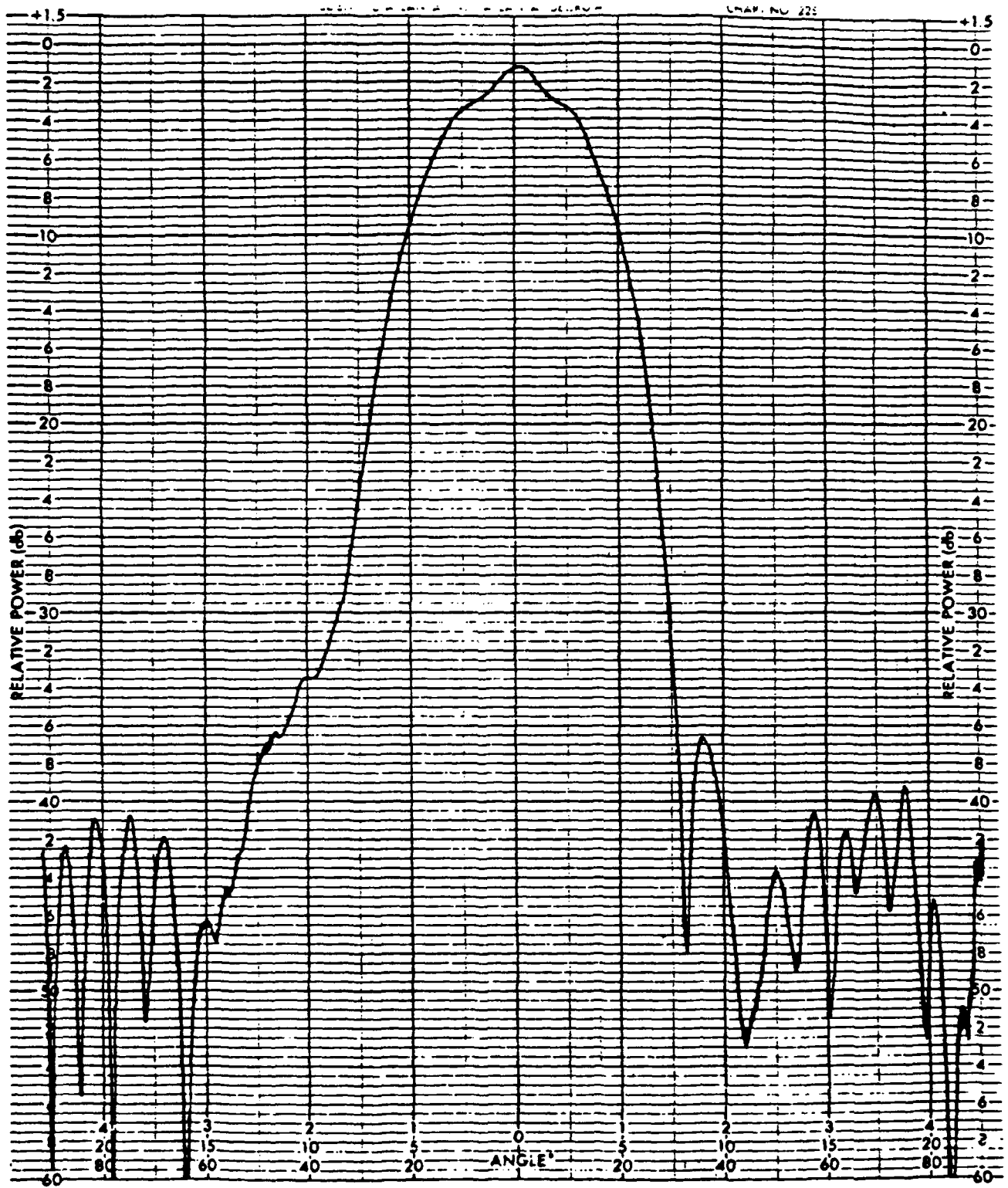


Figure 10a. Feed Sum Pattern, 0° Elevation, 3.3 GHz

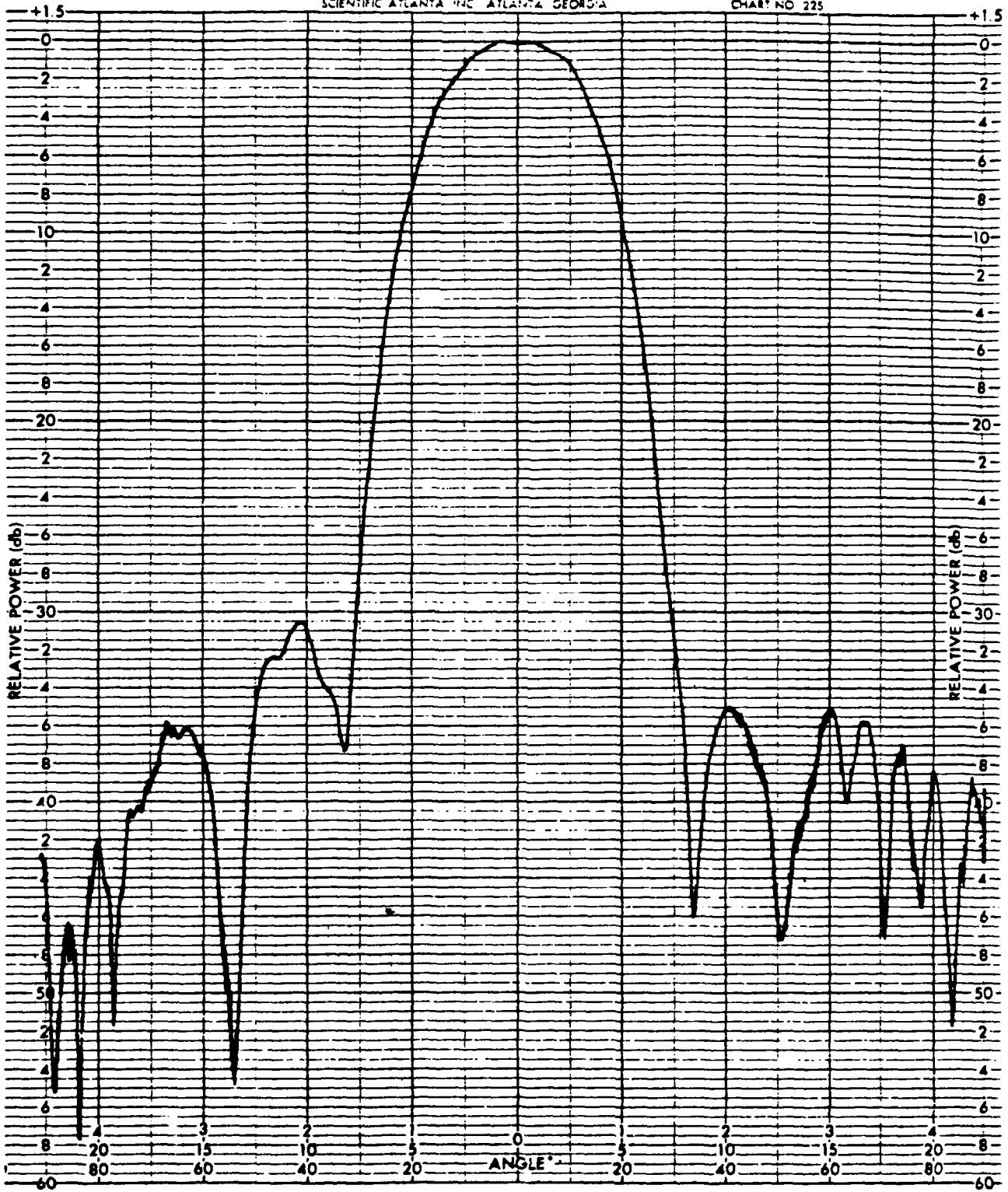


Figure 10b. Feed Sum Pattern, 0° Elevation, 3.4 GHz

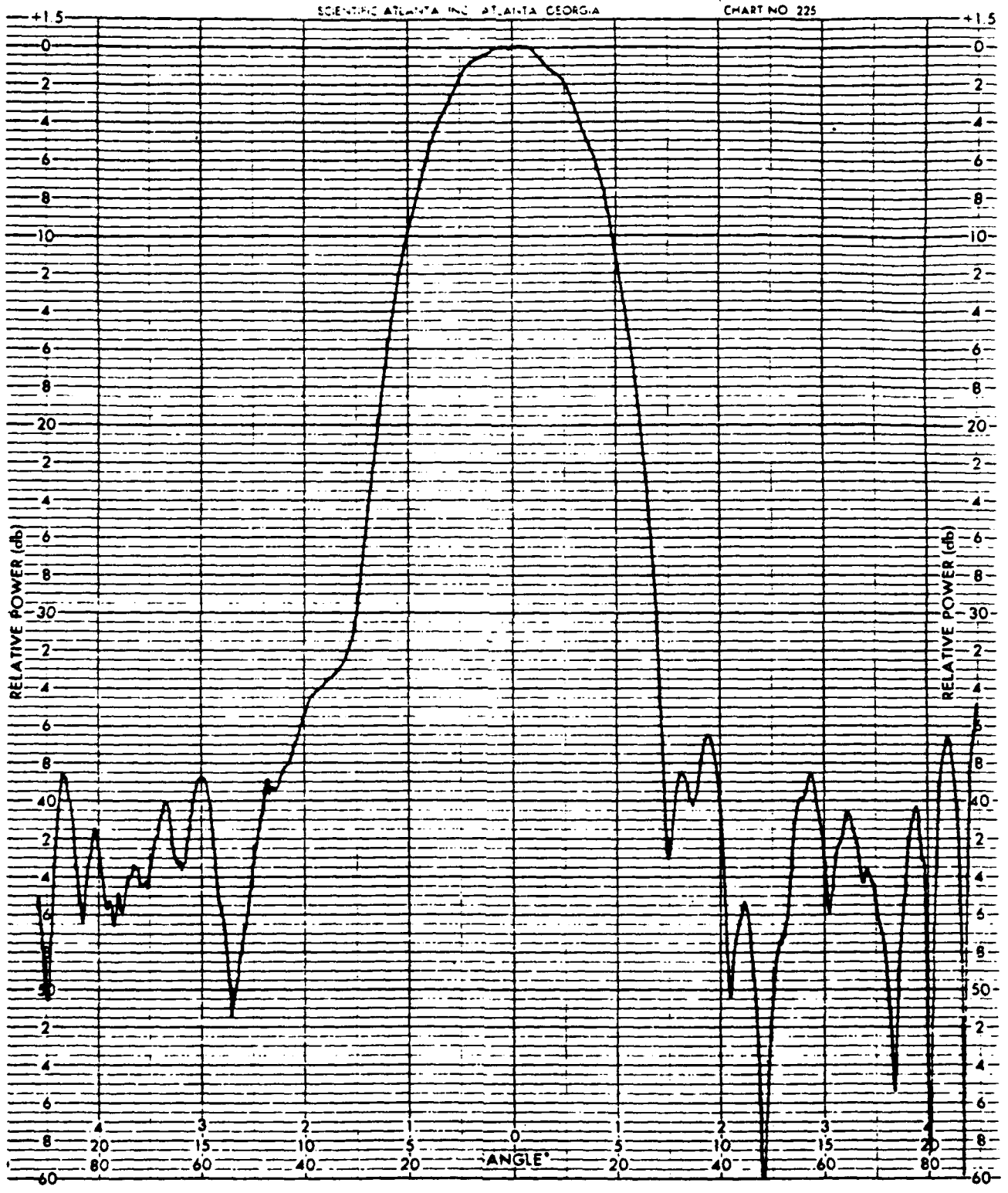


Figure 10c. Feed Sum Pattern, 0° Elevation, 3.5 GHz

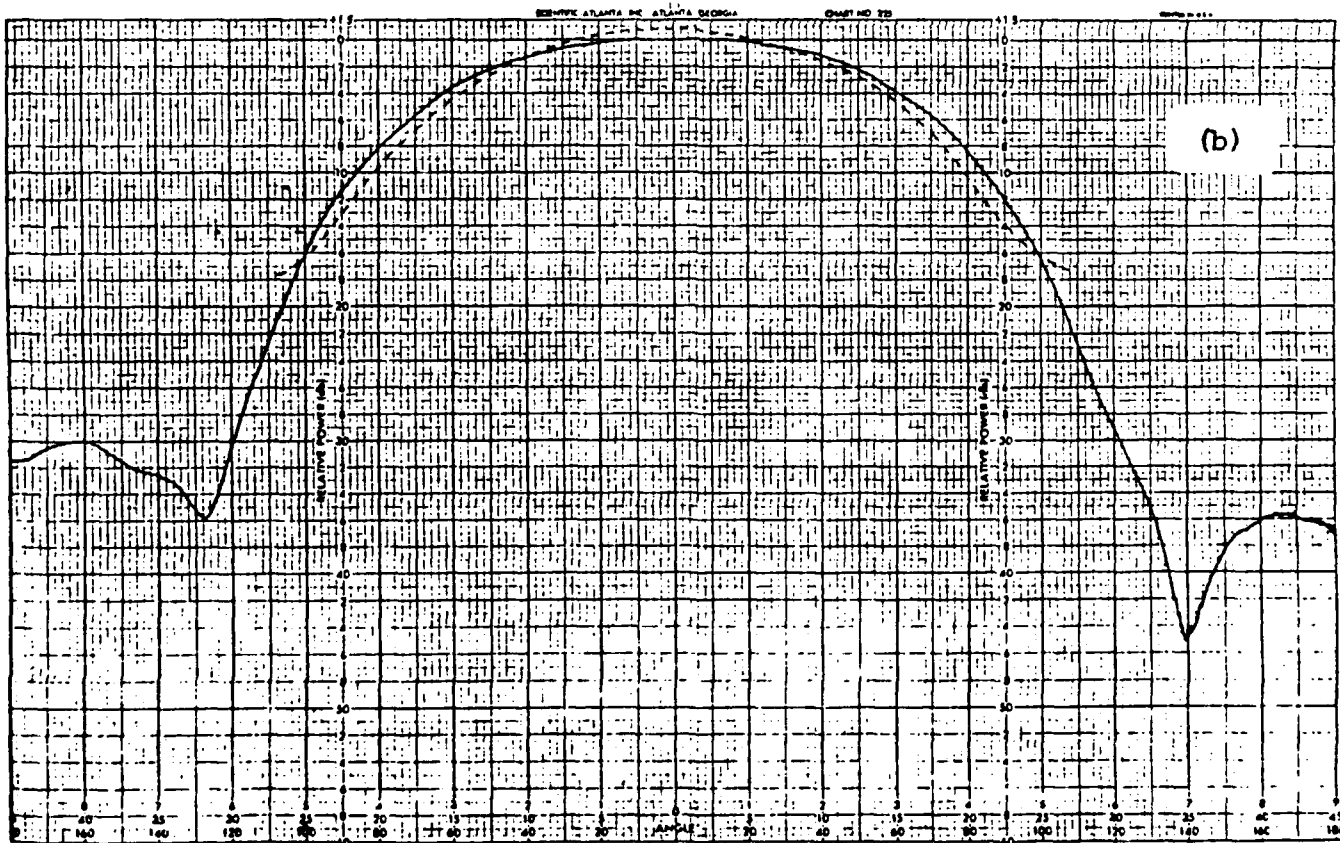
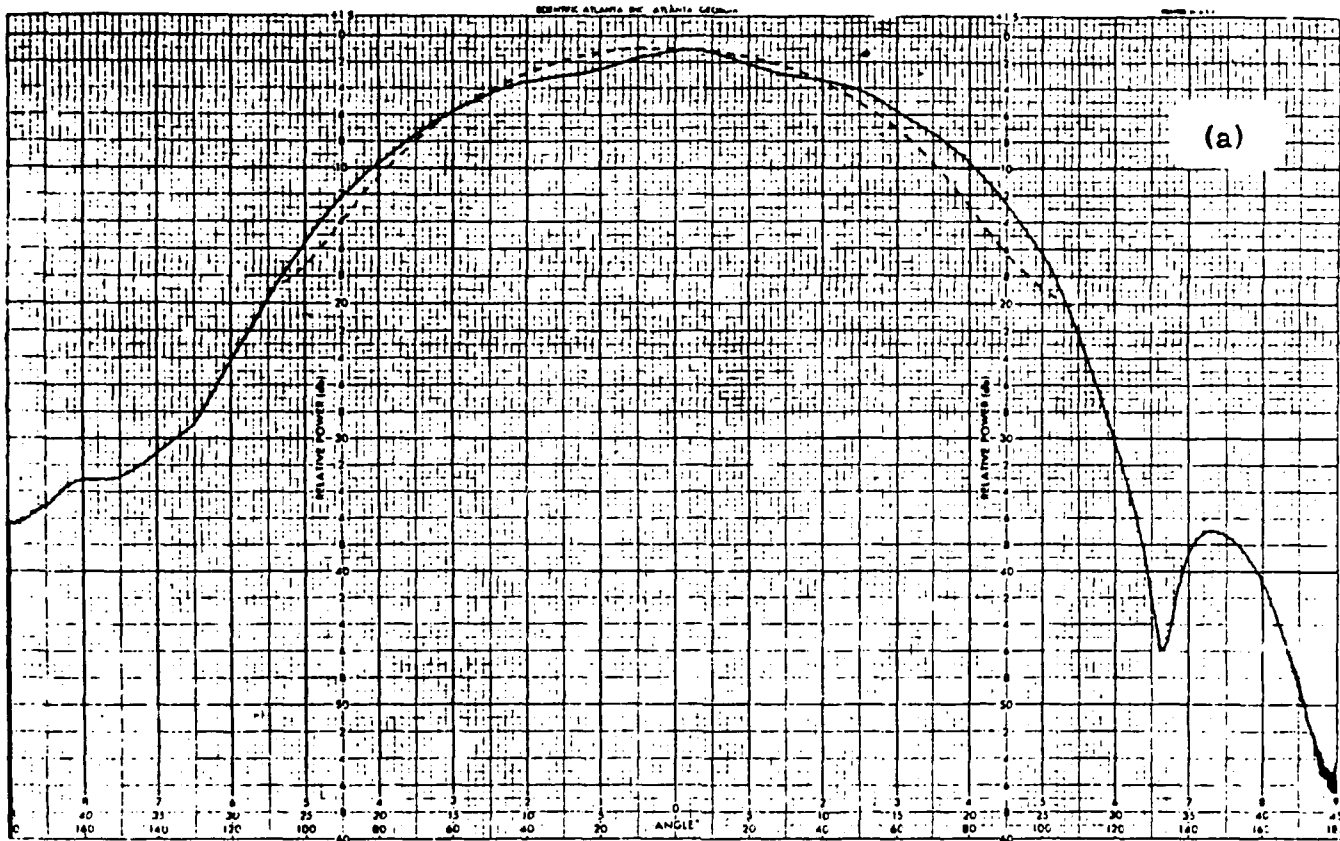


Figure 11. Expanded Plots of Sum Patterns, With Superimposed -40 dB Taylor Distribution (Dashed): (a) 3.3 GHz, (b) 3.4 GHz

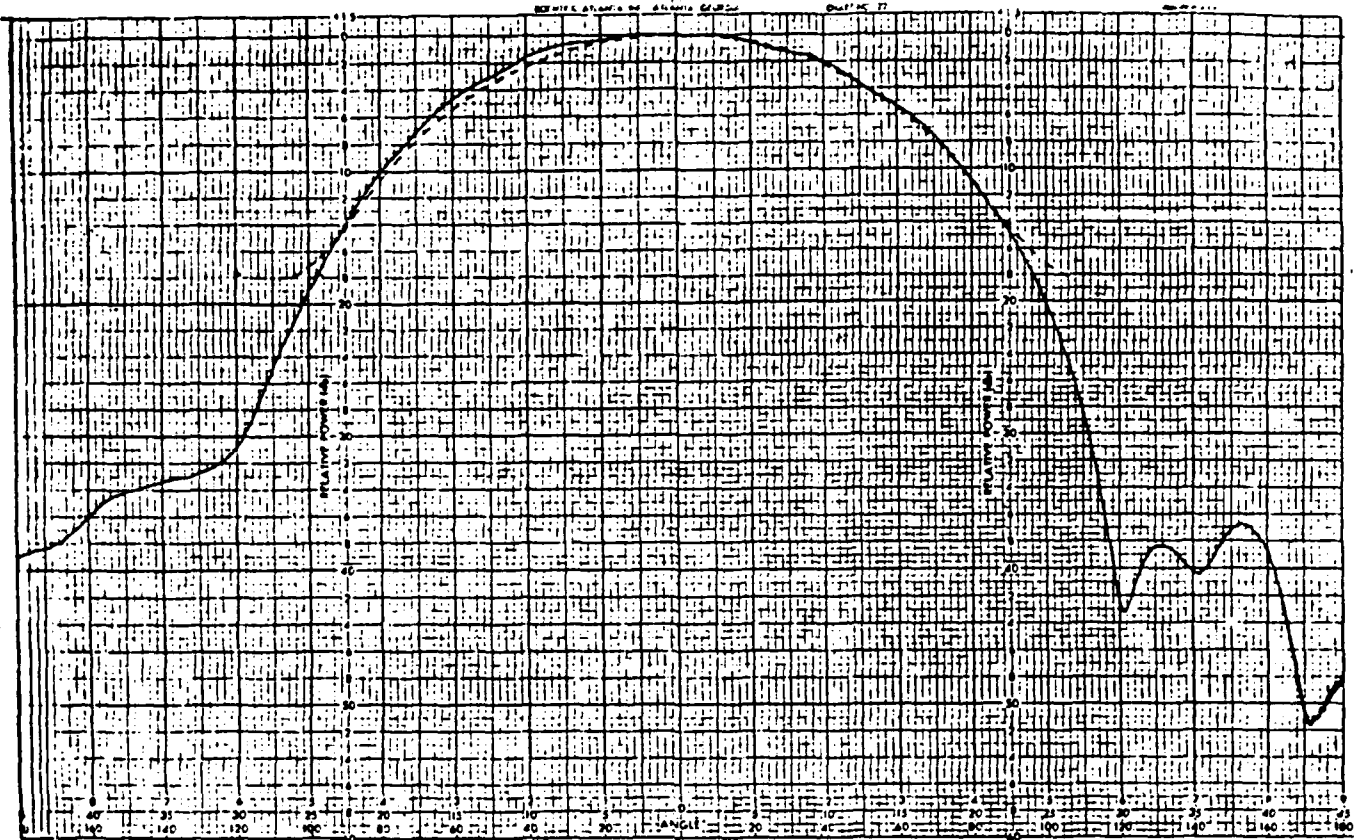


Figure 11c. Expanded Plots of Sum Pattern, With Superimposed -40 dB Taylor Distribution (Dashed), 3.5 GHz

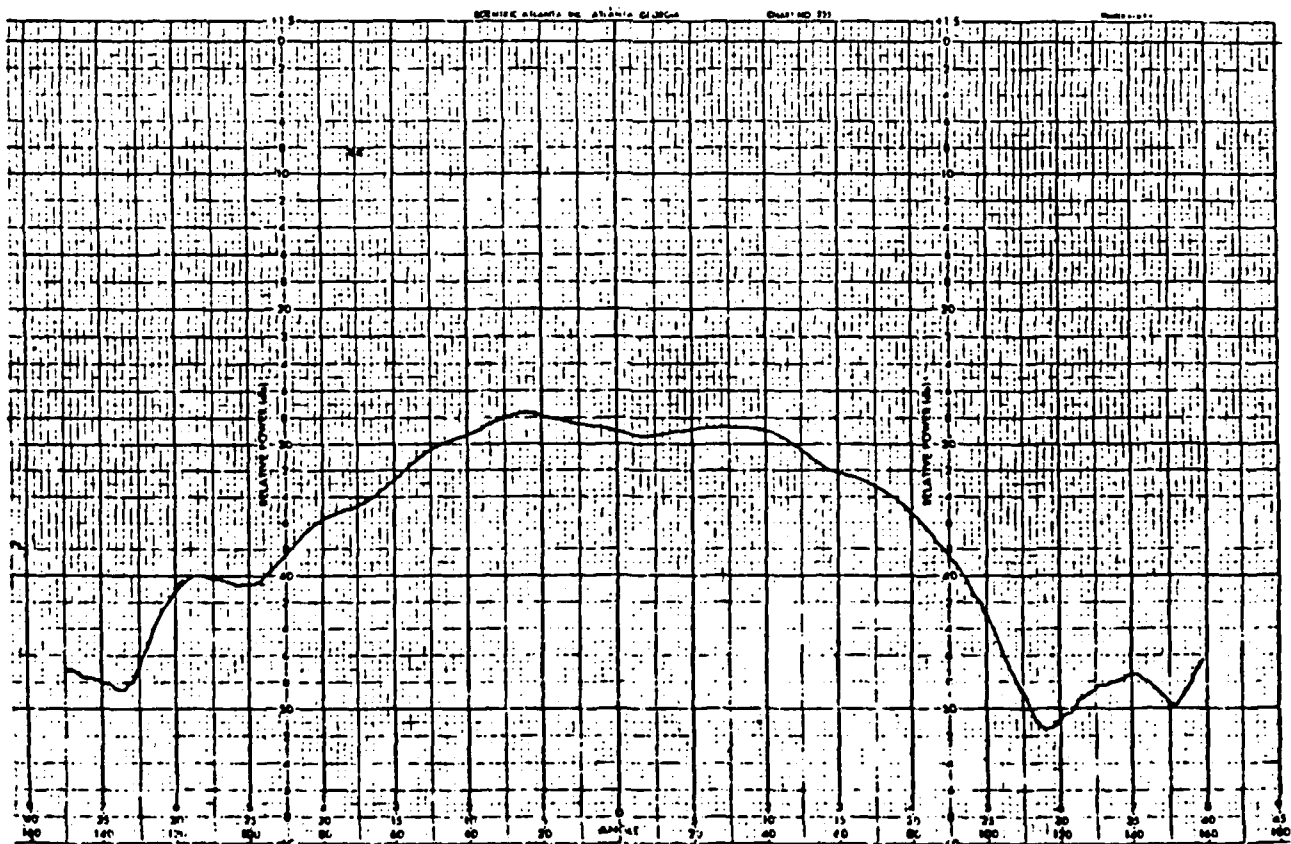


Figure 12. Cross-Polarized Pattern, 3.4 GHz, 6° Elevation

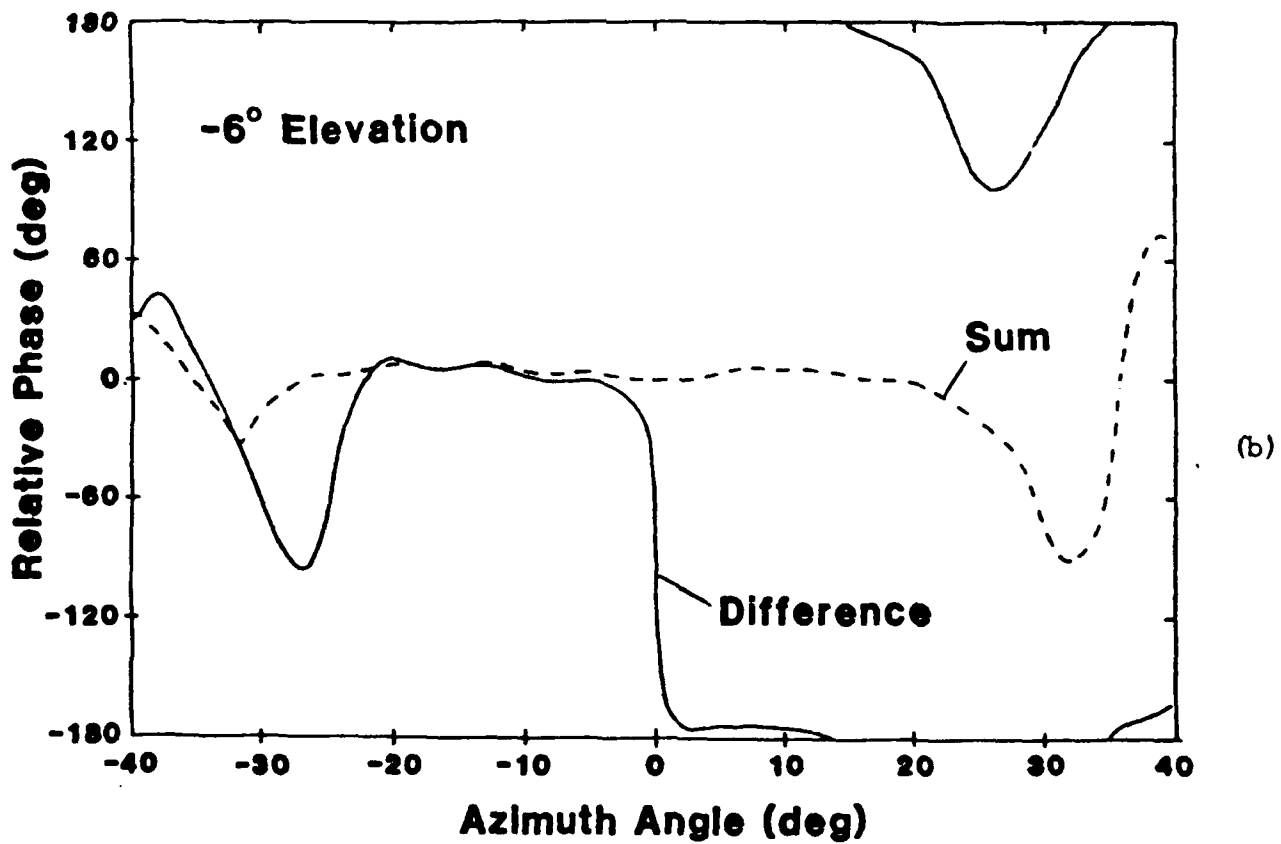
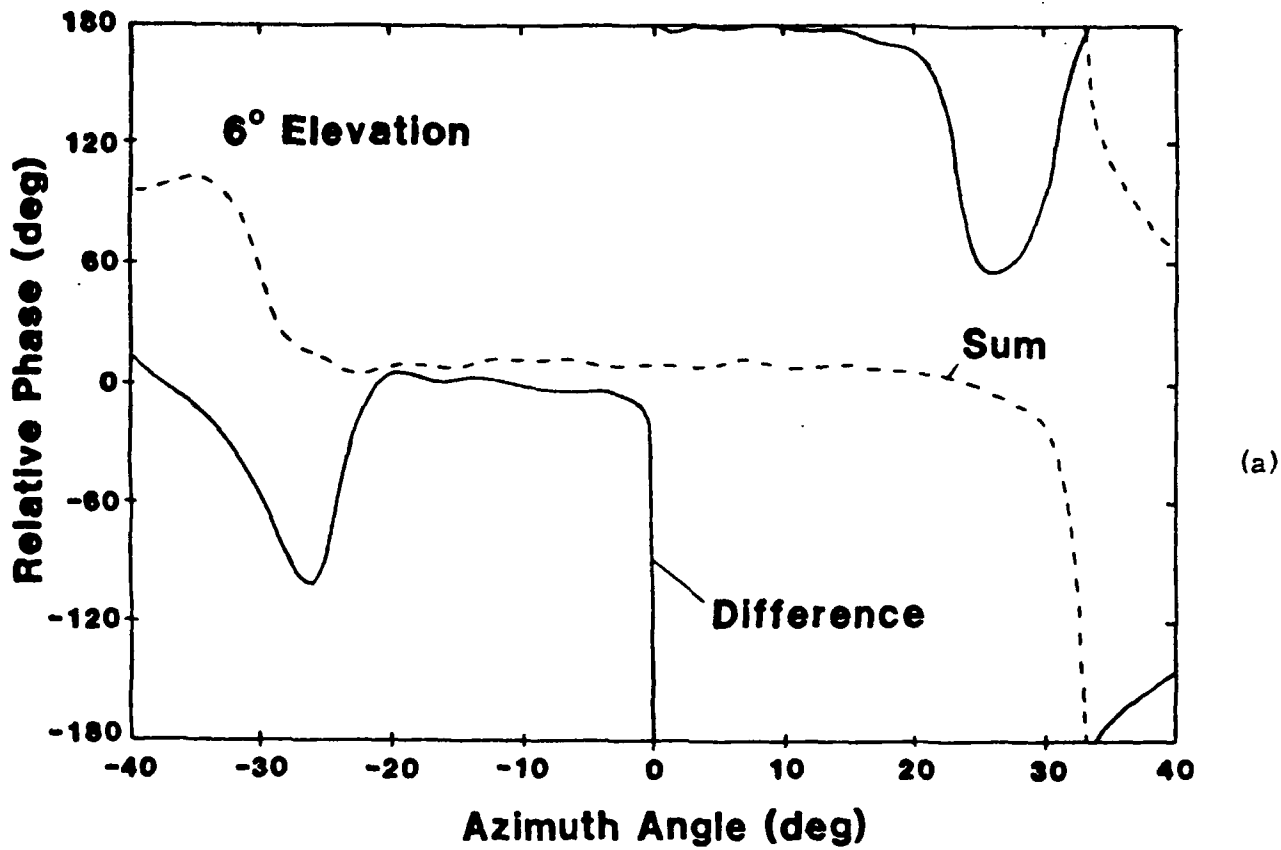
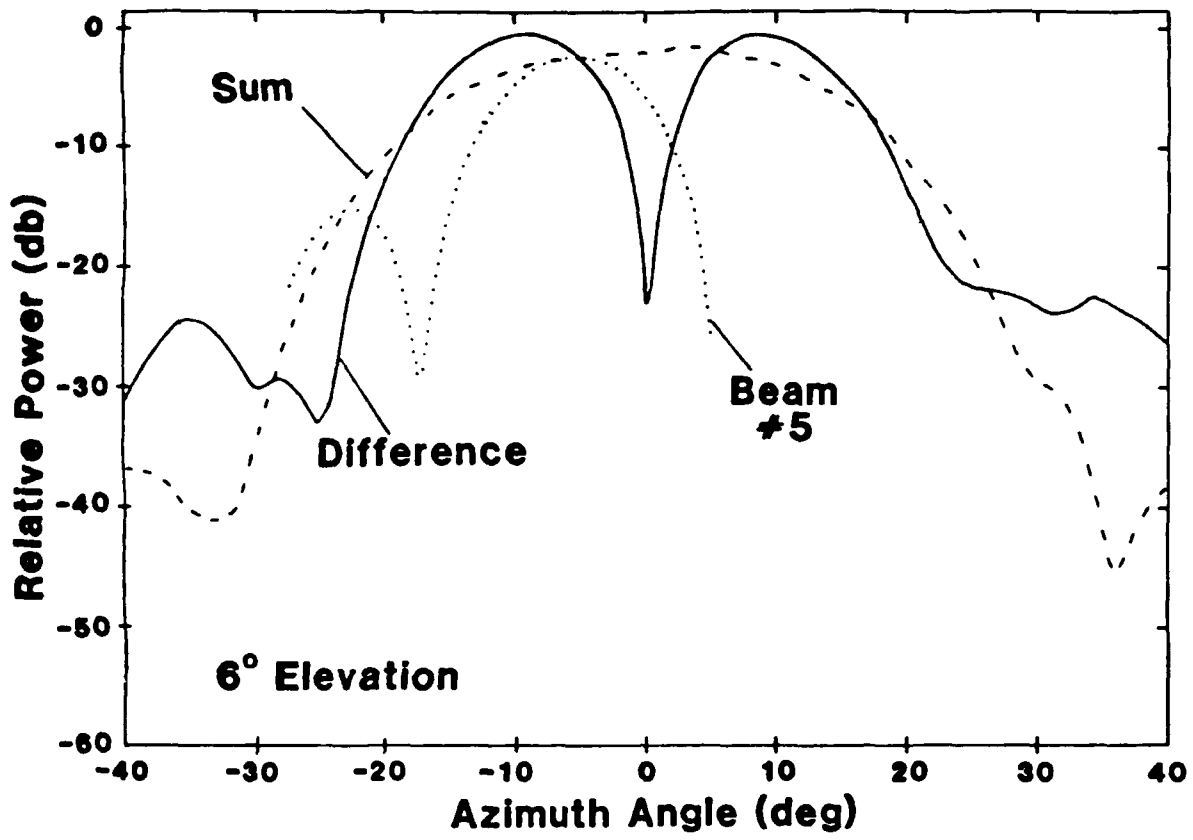
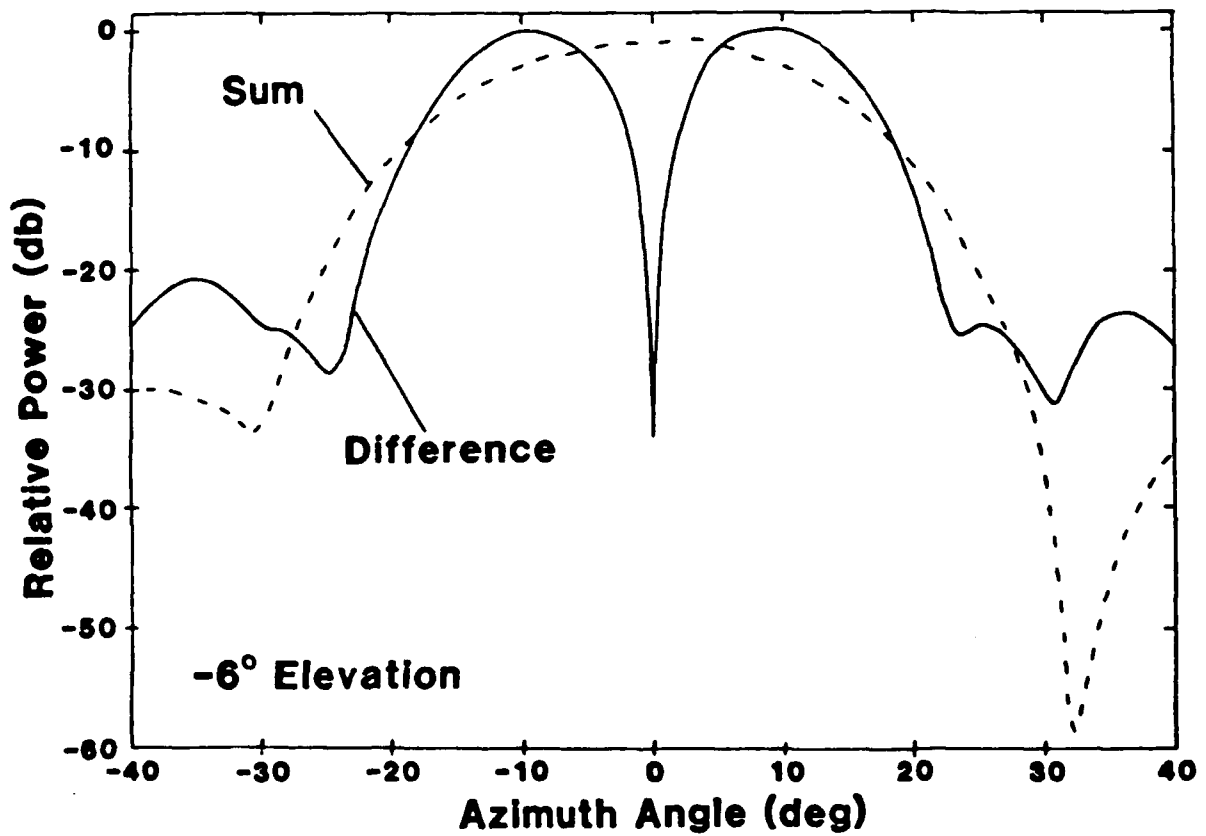


Figure 13. Phase Patterns Taken at +6° (a) and -6° (b) in Elevation: Solid--Difference Pattern Phase; Dashed--Sum Pattern Phase



(a)



(b)

Figure 14. Difference Patterns: (a) +6° Elevation; (b) -6° Elevation

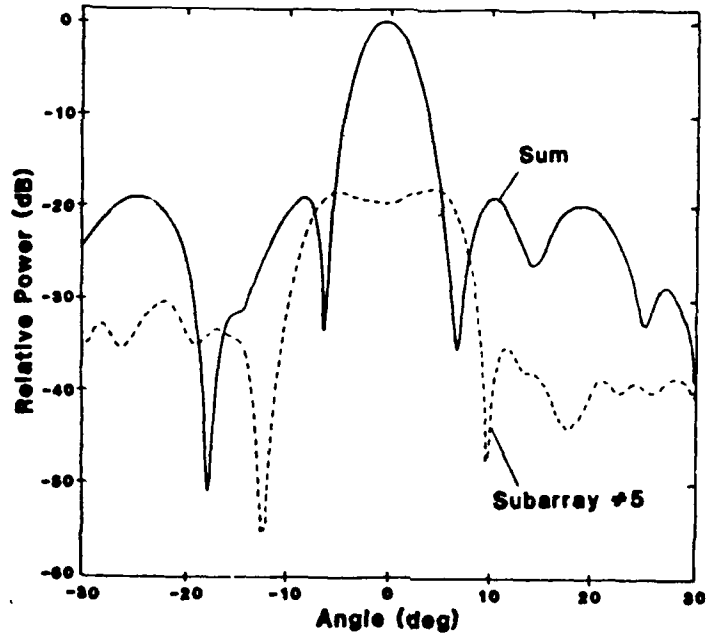


Figure 15. TA-3 Lens Patterns With Adaptive Transform Feed: Sum Pattern and Subarray #5 Pattern

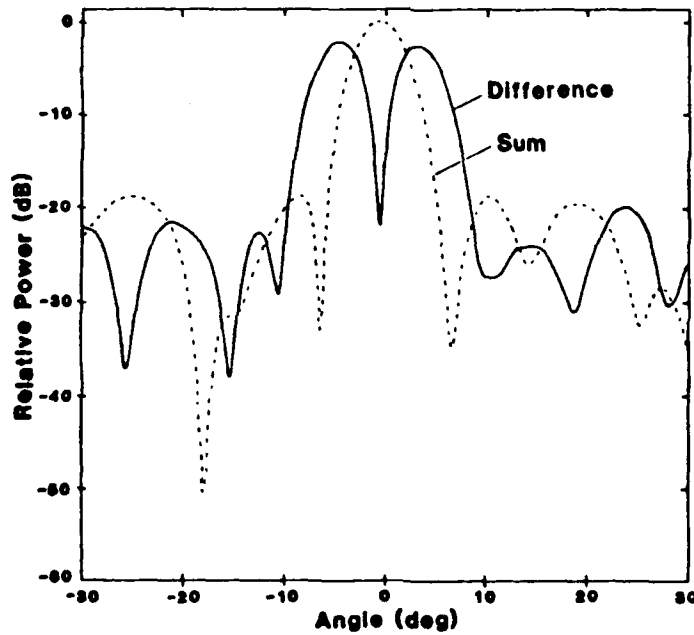
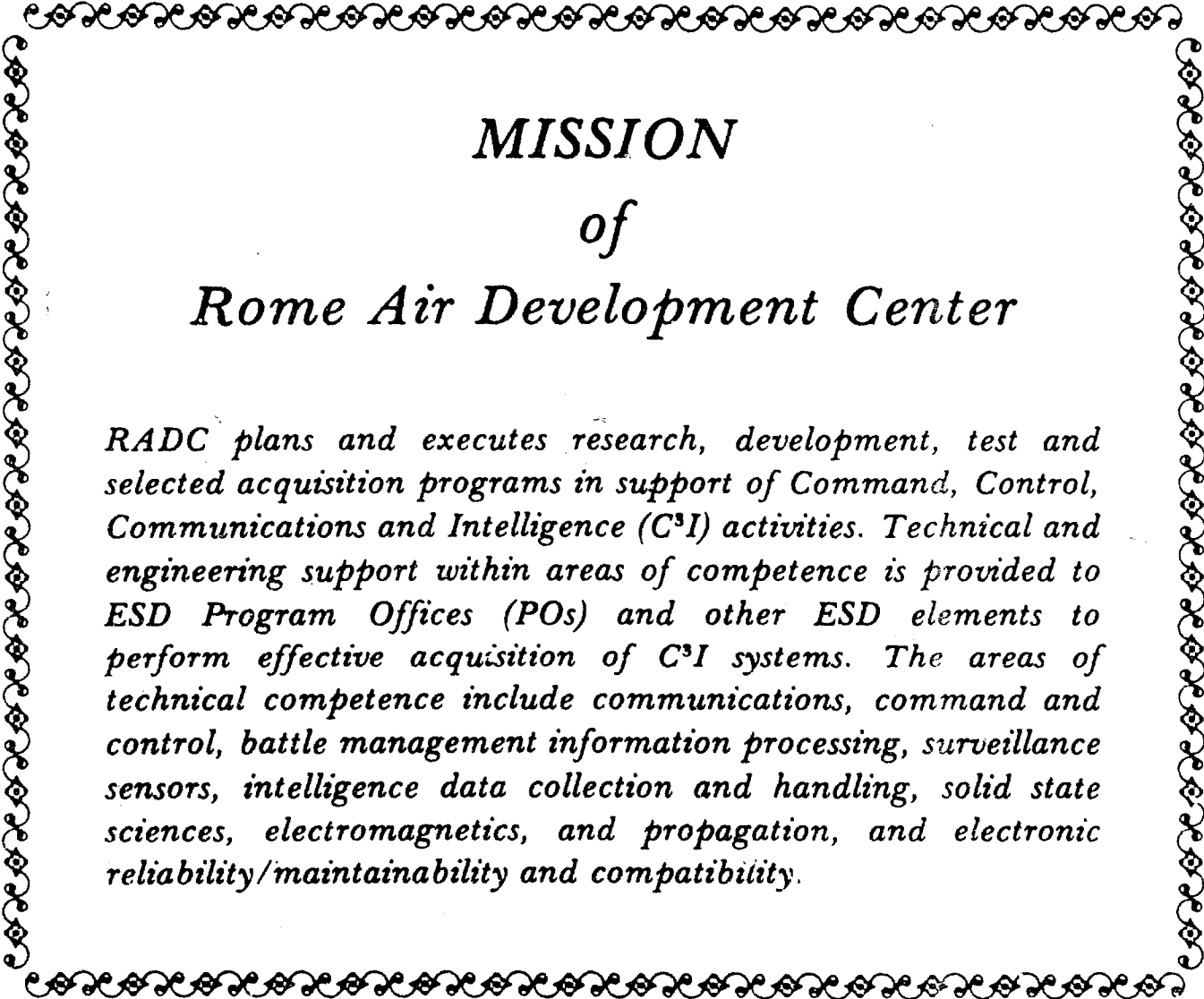


Figure 16. TA-3 Lens Difference Pattern Synthesized by the Transform Feed



MISSION
of
Rome Air Development Center

RADC plans and executes research, development, test and selected acquisition programs in support of Command, Control, Communications and Intelligence (C³I) activities. Technical and engineering support within areas of competence is provided to ESD Program Offices (POs) and other ESD elements to perform effective acquisition of C³I systems. The areas of technical competence include communications, command and control, battle management information processing, surveillance sensors, intelligence data collection and handling, solid state sciences, electromagnetics, and propagation, and electronic reliability/maintainability and compatibility.